Ice-stream dynamics: the coupled flow of ice sheets and subglacial hydrology

Teresa M. Kyrke-Smith

University College

University of Oxford

Thesis submitted in support of an application for leave to supplicate for the degree of

Doctor of Philosophy

Trinity 2014

Ice-stream dynamics: the coupled flow of ice sheets and subglacial hydrology

Teresa M. Kyrke-Smith

University College
University of Oxford

Thesis submitted in support of an application for leave to supplicate for the degree of
Doctor of Philosophy
Trinity 2014

Ice sheets are among the key controls on global climate and sea level. A detailed understanding of their dynamics is crucial to make accurate predictions of their future mass balance. Ice streams are the dominant negative component in this balance, accounting for up to 90% of the Antarctic ice flux into ice shelves and ultimately into the sea. Despite their importance, our understanding of ice-stream dynamics is far from complete.

A range of observations associate ice streams with meltwater. Meltwater lubricates the ice at its bed, allowing it to slide with less internal deformation. It is believed that ice streams may appear due to a localisation feedback between ice flow, basal melting and water pressure in the underlying sediments.

This thesis aims to address the instability of ice-stream formation by considering potential feedbacks between the basal boundary and ice flow. Chapter 2 considers ice-flow models, formulating a model that is capable of capturing the leading-order dynamics of both a slow-moving ice sheet and rapidly flowing ice streams. Chapter 3 investigates the consequences of applying different phenomenological sliding laws as the basal boundary condition in this ice-flow model. Chapter 4 presents a model of subglacial water flow below ice sheets, and particularly below ice streams. This provides a more physical representation of processes occurring at the bed. Chapter 5 then investigates the coupled behaviour of the water with the sediment, and Chapter 6 the coupled behaviour of the water with the ice flow. Under some conditions this coupled system gives rise to ice streams due to instability of the internal dynamics.

Extended Abstract

Ice sheets are among the key controls on the global climate system, both through the ice-albedo feedback and their potential contribution to sea-level change. An urgent question today is how ice sheets will respond to the perturbations of a changing climate. Increasing average temperatures in the atmosphere and ocean will lead to more rapid melting of ice sheets and shelves, but there is also the question of what the dynamical response of the ice to warming and melting will be. A detailed understanding of ice-sheet dynamics is crucial to make accurate predictions of their future mass balance. Ice streams are the dominant negative component in this balance, accounting for up to 90% of the Antarctic ice flux into ice shelves and ultimately into the sea. Nevertheless, despite their importance, our understanding of ice-stream dynamics is far from complete.

A range of observations associate ice streams with meltwater. Meltwater lubricates the ice at its bed, allowing it to slide with less internal deformation. It is believed that ice streams may appear due to a localisation feedback between ice flow, basal melting and water pressure in the underlying sediments, but there remains considerable uncertainty surrounding these fundamental controls.

This thesis aims to address the instability of ice-stream formation by considering potential feedbacks between the basal boundary and ice flow. Ice flows as a viscous fluid, and can accurately be modelled by the Stokes equation. Due to the large aspect ratio of ice sheets, together with the computational cost of solving for Stokes flow, thin-film approximations to Stokes flow are commonly used in ice-sheet modelling. While distinct thin-film models provide accurate flow descriptions for ice frozen to the bed, and for ice sliding extremely rapidly, neither are capable of accurately describing the spatial and temporal transitions from ice-sheet to ice-stream flow. In Chapter 2 we address this with a new, vertically integrated, higher-order formulation for ice-sheet

dynamics that captures the leading-order physics of low aspect ratio, viscous fluid flow, regardless of the amount of slip at the bed. The theory introduces a parameter λ that approximates the ratio of the basal stress to the shear stress scale, providing a measure of the relative importance of sliding and internal deformation. Our model is able to simultaneously describe the dynamics of both a slow-moving sheet and rapidly flowing ice streams. In Chapter 3, to test the formulation, we apply a triple-valued sliding law as the basal boundary condition and obtain numerical solutions that can be compared with previous work. We proceed to investigate the sensitivity of flow regimes and shear margin width to parameter variation, deriving a scaling for the latter. We also consider a double-valued sliding law, which enforces a constant, low basal stress beneath the ice stream. Comparisons of the resultant stress fields illustrate the different stress balances that can maintain ice-stream flow.

Sliding laws are purely phenomenological and we therefore move on to consider the basal boundary more explicitly. In Chapter 4 we present a model of subglacial water flow over a layer of saturated sediments, as observed below ice streams. The base-level flow is fed by subglacial melting; it is presumed to take the form of a rough-bedded film in which the ice is supported by larger clasts, but there is a millimetric water film which submerges the smaller particles. A model for the film is given by two coupled, partial differential equations, representing mass conservation of water and ice closure. We assume there is no sediment transport, and solve the equations for water film depth and effective pressure. Shock formation occurs in certain cases and we carry out a basic analysis of the structure of the shock front.

In Chapter 5 we consider the coupled behaviour of the water film with the deformable sediment layer below. We assume that sediment transport is possible, either as fluvial bedload or, more significantly, by ice-driven shearing and by internal squeezing (due to gradients in effective pressure). This provides an instability mechanism for rivulet formation; in the model, downstream sediment transport is compensated

by lateral squeezing of till toward the incipient streams. We show that the model predicts the formation of shallow, swamp-like streams, with a typical depth of the order of centimetres. These swamps are stable features, typically with a width of the order of tens to hundreds of metres.

Finally, in Chapter 6 we couple our water-film model to the vertically integrated, higher-order model for ice sheet dynamics. If there is sufficiently small amount of meltwater produced (e.g. if ice flux is low), the distributed film and ice sheet are stable, while for larger amounts of melt, the ice-water system can become unstable and ice streams form spontaneously as a consequence. We show that this can be explained as a result of a multivalued flux law, which arises from a simplified, one-dimensional analysis of the coupled model. From this analysis it is also possible to predict the parameter regimes for which ice-streaming occurs. We also consider the characteristic size and spacing of ice streams that form in the model, discussing the important role that one of the non-dimensional model parameters plays in this. To conclude we investigate the consequences of variations in bed topography on resultant ice-stream formation.

Acknowledgements

This thesis would not have been possible without the help, support and encouragement of many people:

Firstly, both my supervisors, Richard Katz and Andrew Fowler. Although like chalk and cheese in many ways, I am immeasurably grateful to both for their input and guidance over the past 3 and a half years. Rich has been a constant source of advice and ideas, and extremely generous with his time. He has offered help and direction in every part of my work, from the fundamentals that form the basis of the thesis, to the intricacies of debugging code and putting together presentations. 'Rich by name, rich by nature', as Andrew says, he has also given me every opportunity to go to conferences, workshops and summer schools, allowing my skills as a researcher to develop enormously. Andrew's wealth of knowledge has also brought a lot to this thesis, and despite frequently getting away with referring me to his latest book, he has always been happy to dedicate time to sharing his expertise. Moreover, he has provided me with many a 'scrummy lunch' in Pierre Victoire and copious gin and tonics in the Lamb and Flag, feeding both the body and the mind.

The many people I have met at conferences and summer schools. Through these trips I have gained a much broader picture of research within glaciology and had many interesting conversations with people from the field. In particular I would like to thank Dorthe Dahl-Jensen, for inviting Rich and I to join a workshop at the Svartisen Subglacial Laboratory, Christian Schoof, for hosting me for a few days in Vancouver, and Roiy Sayag, Ian Hewitt and Tony Payne for particularly useful and thought-provoking discussions at various points over the past years. I must also mention those I met on the Karthaus summer school back in 2010, where I learnt so much about the field before I had even begun work on this thesis.

The Earth Sciences department, which has provided me with a base throughout my DPhil. Although I often feel conscious of my rather mathematical stance, there are still some people who have taken me seriously. In particular I want to thank my various office mates over the years. Firstly those in the Seismolab: Andrew (it was brief), David (you introduced me into the life of not-so-brief high-table dinners), Sam (thank you for never losing patience with my PETSc questions), Tom (with that thunderous laugh to keep us all awake), Cedric ('tak' for being such a good tea/coffee/alcohol-drinking companion, and the constant source of amusement you provided after your 'French lunches' on a Friday), Owen (I'll always be in awe of your collection of strange awards, often awarded after giving talks to old people), Chao (you're the first person I know to step on a pigeon) and Forest (it was a cold night outside when you left me locked out of the office without my belongings). And every since we were moved to our sardine offices, I have had the pleasure of sharing an

office with Harriet ('Young geoscientist of the year'), Harry (maybe Nozzler will have children one day), Fran (your collection of plastic knives disconcerts me slightly) and Jonathan (I'm still trying to 'swallow my vowels' when I speak). Every one of you have provided me with both company and entertainment, in differing ways—thank you all.

All those who I have spent time with at AGU. Despite taking some of our other comrades too seriously, Dan has been an excellent travel-companion each year and was the epitome of tolerant when searching for a burger restaurant. Every year had something unique about it: the road trip in first year with David and Cedric (memorable in so many ways that I could not begin to go into here), Jie's masterclass in how to spend money in second year, and Victoria's demonstration of skills in glaciologist seduction in third year.

Outside of the department, Univ allowed me to meet people who don't wear walking boots at every waking hour. To my housemates: pitter-patter-furrowed-brow-Jess, I-squeeze-my-oranges-electronically-Claudia and none-of-my-housemates-are-in-Lucy. Thanks for having me as a housemate for the past 3 years, and for helping with the removal of spiders whenever needed. I must also thank some of those who don't have the pleasure of living in Stanley Road. Jenny, your emails never cease to surprise me with their surplus of incorrect grammar, but you did take us all to Greece, where I learnt a lot about Greek inefficiency. Your disrespect for the British monarchy is one of the reasons I am probably unable to stay friends with you, but it's been nice knowing you. 'My hero' Lyle, on the other hand, is a keeper. Visiting you in South Africa wasn't a bad way to spend NY 2013. I'm just pleased that I didn't get eaten by a lion like that poor Rhodesian Ridgeback. And finally, Adam. My bike and I would probably both be dead under a bus by now without you. Not only have you 'saved my life' on countless occasions but you are there whether I'm merrily squiffy, or sucking on a lemon/chewing on a wasp etc. Oxford would have been so very different without you; thank you for always making me smile.

Last of all, my family and friends from outside Oxford. I have enjoyed many trips to London over the years to visit my one remaining Devonshire friend, Jess, all the old Nonsuch girls (nattering-Nathalie, loyal-Lisa, la-di-da-Lara, exogamous-Emma, aghast-Anna, evaporative-Emily and pseudoNonsuch-plucky-Patch) and all my friends from Cambridge, who are now busy making their millions. It is always refreshing to get out of the Oxford bubble. Most importantly though I must thank my parents, for their love and support through everything. I would have never applied to do a DPhil in Oxford without their encouragement and I am eternally grateful for that. And my siblings: Nick, Ali and Rosie. Having Ali around in Oxford for the first two years of my DPhil provided some light relief from the graduate scene. And Nick and Rosie, both of you like to tell me that Oxford is full of weirdos whom I should stay well clear of. So thank you for that informative advice—it does sometimes come in handy.

Contents

List of Figures

List of Tables

Symbol	Description	Typical value
ρ_i	ice density	$917\,\mathrm{kg\,m^{-3}}$
ρ_w	water density	$1000\,\mathrm{kg\,m^{-3}}$
ρ_s	sediment density	$2.6 \times 10^3\,\mathrm{kg\,m^{-3}}$
g	gravity	$9.81\,\mathrm{m\,s^{-2}}$
η_w	water viscosity	$1.8 \times 10^{-3}\,\mathrm{Pa\,s}$
η_i	ice viscosity	$10^{14}\,\mathrm{Pa\,s}$
η_s	sediment viscosity	$2.7 \times 10^9\,\mathrm{Pa\,s}$
A	Glen's flow law rate	$6.8 \times 10^{-24}\,\mathrm{s^{-1}\,Pa^{-3}}$
		$\approx 3\,\mathrm{bar^{-3}\,y^{-1}}$
n	Glen's flow law exponent	1 (Newtonian)
		3 (non-Newtonian)
L	latent heat of water	$3.3 \times 10^5\,\mathrm{J\,kg^{-1}}$
c_p	specific heat capacity	$2.1 \times 10^3\,\mathrm{J\,kg^{-1}\,K^{-1}}$
G	geothermal heat flux	$60\,\mathrm{mW\,m^{-2}}$
ΔT	surface cooling	$20\,\mathrm{K}$
k	thermal conductivity of ice	$2.1\,\mathrm{W\,m^{-1}\,K^{-1}}$
D_s	grain size of sediment	$3 \times 10^{-5}\,\mathrm{m}$
μ	coefficient of inter-particle friction in sediment	0.6
ϕ	sediment porosity	0.4
c	sliding law coefficient	$6.8 \times 10^4\,\mathrm{Pa^{2/3}\,s^{2/3}\,m^{-1/3}}$
p	velocity exponent in sliding law	1/3
q	effective pressure exponent in sliding law	1/3

Table 1: Definitions and values of physical constants in thesis.

Variable	Description
$[x, y]$	horizontal coordinates
z	vertical coordinate
h	ice depth
s_i	ice surface elevation
$\Omega = \frac{\partial s_i}{\partial x}$	ice surface slope
b	bed elevation
$\mathbf{u}_b = (u_b, v_b)$	horizontal ice basal velocity
t	time
a	accumulation rate
p_i	ice pressure
$\boldsymbol{\tau}_b$	basal shear stress
H	meltwater depth
$s_w = b + H$	ice base elevation
l^*	clast spacing
p_w	water pressure
$N = p_i - p_w$	effective pressure
q	meltwater flux
ψ	hydraulic potential
Γ	melt rate
B	sediment transport coefficient
h_A	depth of deformable sediment
$a_b(x, y)$	background accumulation in Chapter 3
$a_p(x, y)$	accumulation perturbation in Chapter 3
A_0	magnitude of perturbation accumulation in Chapter 3

Table 2: Definitions of variables in thesis.

Chapter 1

Introduction

1.1 Ice sheets

Ice sheets are vast expanses of thick, glacial ice resting on land. There are two ice sheets on Earth today; between them they contain over 99% of the ice on Earth (the remaining 1% being contained in ice caps and glaciers) (Cuffey and Paterson, 2010). The Antarctic ice sheet is by far the largest of the two, extending over almost 14 million km^2 and containing 30 million km^3 of ice. The Greenland ice sheet is relatively small in comparison, extending 1.7 million km^2 and containing 2.8 million km^3 of ice (Greve and Blatter, 2009).

Understanding how the ice sheets will evolve into the future is a problem of crucial importance since they are among the key controls on global climate and sea-level. Not only do ice sheets reflect a lot of the sun's heat back into space, keeping the planet cool, but they also store approximately 90% of the world's freshwater, corresponding to over 60 m of global sea level rise (Lemke *et al.*, 2007). It is therefore vitally important to make accurate predictions about how they evolve, so to be able to project future climate and sea-level change. This requires an understanding of the mass balance of the ice sheet. The ice sheet spreads out over land as a viscous fluid, gaining mass by snowfall, and losing mass by melting and/or calving at the margins. Whether these processes are in equilibrium governs whether the ice sheet is growing or shrinking.

Figure 1.1 shows maps of the surface mass balance for both ice sheets, and Figure

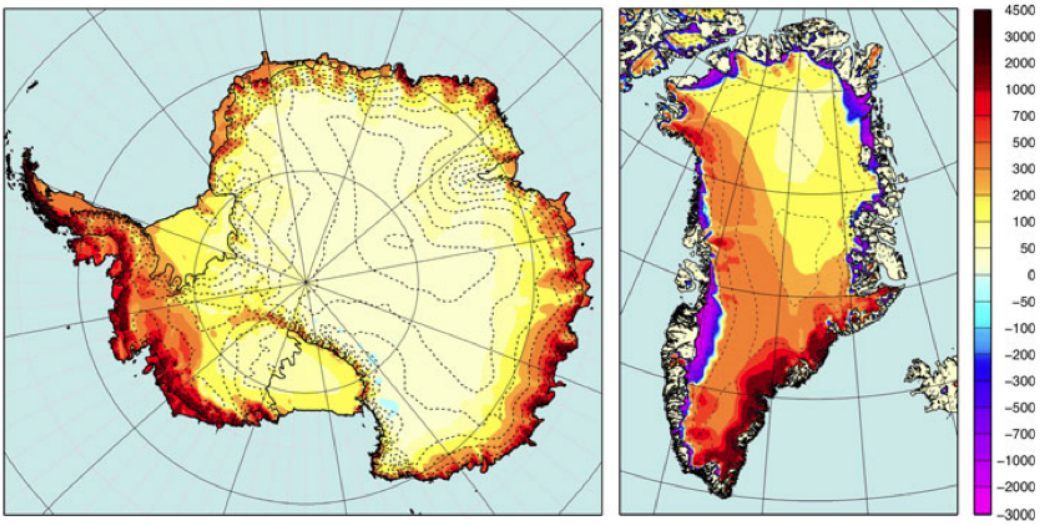

Figure 1.1: Surface mass balance maps of Antarctica and Greenland from the Regional Atmospheric Climate Model (RACMO2), given in units $\mathrm{kg\,m^{-2}\,year^{-1}}$ (Van den Broeke *et al.*, 2011).

1.2 the flow rates. From Figure 1.1 it is clear that Greenland has a well-defined marginal ablation zone around most of the ice sheet, due to high summertime melt and run-off (Van den Broeke *et al.*, 2011). The exception is in southeast Greenland where there are accumulation rates of over $3000\,\mathrm{kg\,m^{-2}\,year^{-1}}$ in the marginal zone. Furthermore, in Figure 1.2 we see that around much of the coast, the ice flows rapidly out into the ocean. While the interior of the ice sheet is approximately in mass balance, the coastlines are rapidly losing ice (Velicogna and Wahr, 2005).

Antarctica, however, exhibits some contrasting behaviour. One particularly notable distinction is the presence of ice shelves around the ice sheet. Their presence is attributed to the fact that near the coast much of the ice rests on a bed that is below sea level (see Figure 1.2). The lesser density of ice than water means that it reaches a point where the ice will begin to float, and so detach from the bed to form a floating ice shelf. From here the ice is released into the ocean either by iceberg calving or basal melting (Depoorter *et al.*, 2013). Since there is no surface melting on the ice sheet due to the low surface temperatures, this is the main mechanism by

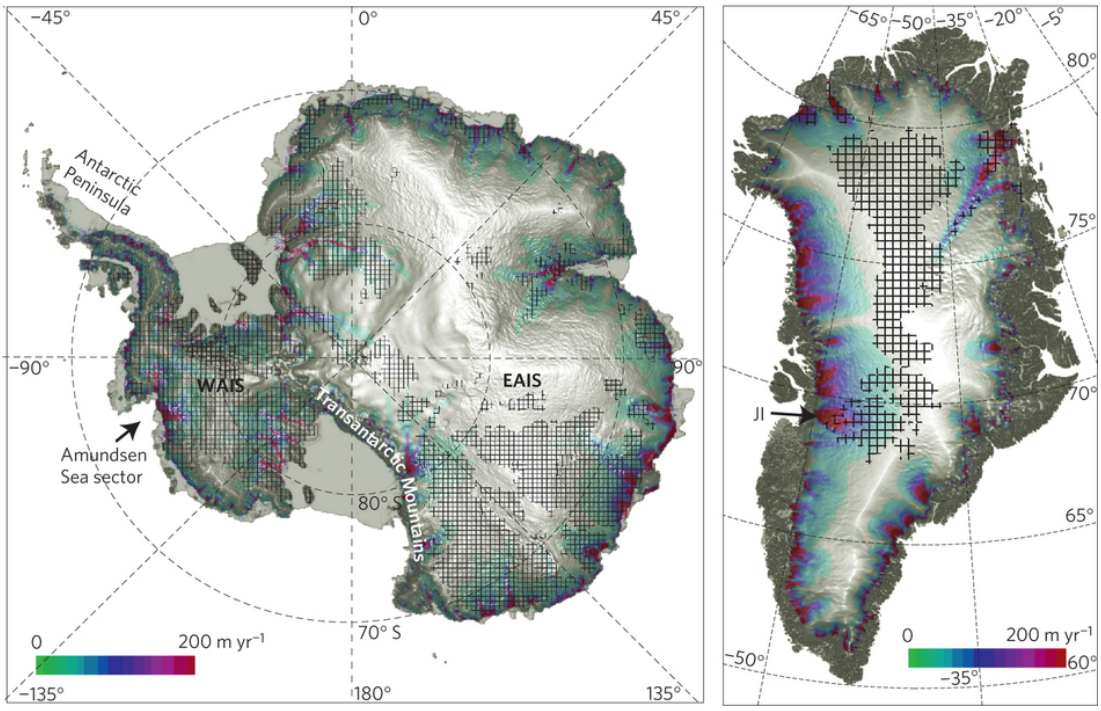

Figure 1.2: Shaded relief maps of Antarctica and Greenland showing regions of enhanced flow and areas of the ice sheets grounded below sea (hatched) (Bamber and Aspinall, 2013).

which the Antarctic ice sheet loses its mass. By far the largest ice shelves are the Ross Ice Shelf and Filchner-Ronne Ice Shelf, which are contained in large bays in the Western part of Antarctica. This part of Antarctica is of particular interest, since although the East Antarctic Ice Sheet (EAIS) contains nearly 90% of the ice volume, it rests on a land mass which is largely above sea level and appears to currently have a positive mass balance (e.g. Davis *et al.*, 2005). In contrast, the West Antarctic Ice Sheet (WAIS) has a bed which is up to 2500 m below sea level in places (Fretwell *et al.*, 2013) and observations and the associated calculations show it is losing mass (e.g. Rignot and Thomas, 2002; Zwally *et al.*, 2005; Rignot *et al.*, 2008).

Figure 1.3 is an ice velocity map for West Antarctica. It is evident that there is a complex flow pattern in the region. While much of the area is only moving slowly, there are distinct bands of fast flowing ice moving at 2-3 orders of magnitude faster

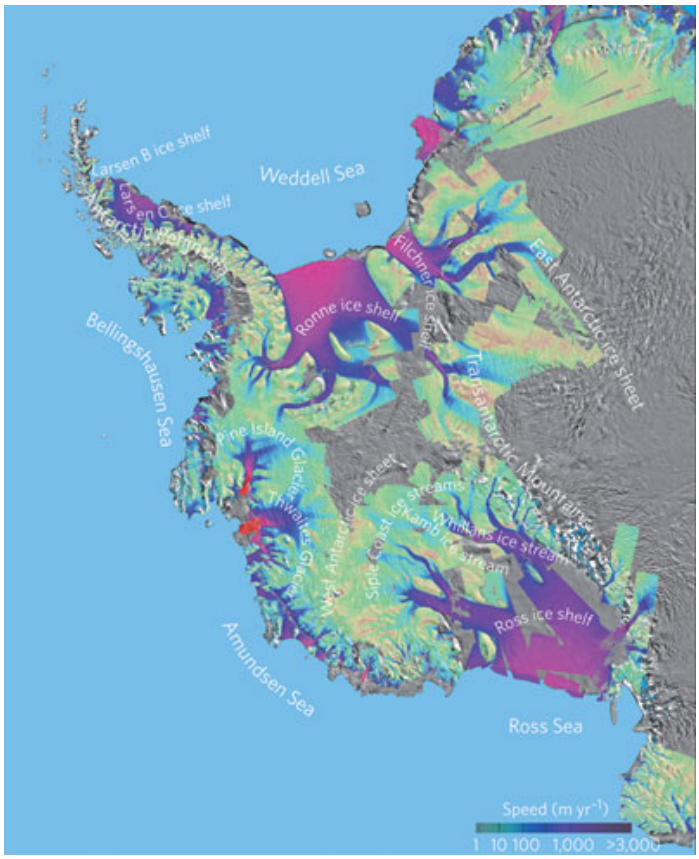

Figure 1.3: Map of ice flow velocities for West Antarctica (Joughin and Alley, 2011).

than the surrounding ice. These are termed ice streams, and it has been estimated that they transmit up to 90% of discharge from the ice sheet (Bamber, 2000; Rignot *et al.*, 2011; Bamber and Aspinall, 2013). Due to this dominant role in ice sheet drainage the stability of the ice sheet is strongly dependent on the stability of the ice streams, and it is therefore of utmost importance to improve understanding of ice streaming. This is the focus of my thesis.

1.2 Ice streams

An ice stream is a region of an inland ice sheet where the ice flows much more rapidly than the surrounding ice (Swithinbank, 1954). The reasons for the existence of some ice streams is clear; large variations in bedrock topography cause ice to be

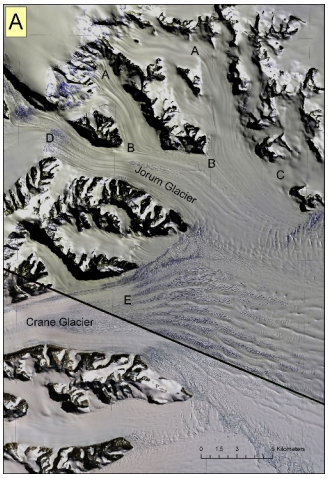

(a) Satellite image of topographically constrained fast flow.

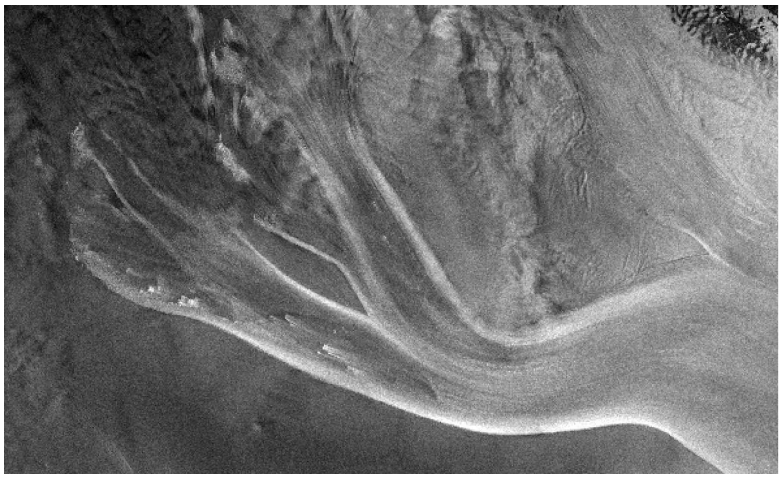

(b) Satellite image of a pure ice stream.

Figure 1.4: (a) ASTER image from 2001 showing Crane and Jorum glaciers on the Antarctic Peninsula flowing onto the former Larsen B ice shelf (Glasser and Gudmundsson, 2012). The flow is clearly constrained by the surrounding topography. (b) Radarsat image of Whillans Ice Stream, West Antarctica (http://www.earthzine.org/2008/03/27/keeping-an-eye-on-antarctica/). The image is approximately 400 km wide. There is no constraining topography governing the ice flow pattern; the margins of the ice stream are identifiable as the brightest areas due to crevassing.

channelised into bedrock troughs. The thicker ice then leads to larger shear stresses and hence faster flow (e.g. Rutford ice stream, West Antarctica (Doake *et al.*, 2001), and Jakobshavn Isbrae, Greenland (Clarke and Echelmeyer, 1996)). This is the same concept as for an outlet glacier, except that for a common outlet glacier one expects the bedrock walls of the topographic low to be exposed (Truffer and Echelmeyer, 2003). As Swithinbank (1954) pointed out, there exist some ice streams draining an ice sheet basin where topography does not appear to be the only control. These are known as pure ice streams; the most prominent example being the five distinct streams flowing out to the Ross ice shelf in the Siple Coast region of Antarctica (Shabtaie and Bentley, 1987; Cuffey and Paterson, 2010; Joughin and Tulaczyk, 2002; Bennett, 2003). Shear zones mark their boundaries and these margins are often highly crevassed due to the horizontal shear stresses exceeding the tensile strength of the

ice (Echelmeyer *et al.*, 1994; Bindschadler *et al.*, 2001; Raymond *et al.*, 2001). Figure 1.4(b) shows a satellite image from the Siple Coast of the Whillans Ice Stream, and the shear margins are clearly visible.

Evidence suggests that in many of these fast moving streams, basal sliding is a dominant component of the motion, driven by the presence of meltwater and deformable, wet, sediment slurries at the base of the sheet (e.g. Alley *et al.*, 1987; Clarke, 2005; Lemke *et al.*, 2007). There are, however, many questions about these processes yet to be answered, both because the bed of an ice sheet is a relatively inaccessible environment, and because the physics governing the coupled behaviour of the ice with meltwater drainage through the bed is a relatively underdeveloped area of research. Furthermore, while we can obtain some observations from the bed of paleo-ice streams, these are not consistent across all locations. For example, the presence of bedforms in the vicinity of some paleo-ice streams points to bed deformation having played an important role in the rapid ice flow (e.g. Cofaigh *et al.*, 2002; Dodswell *et al.*, 2004), while in the vicinity of other paleo-ice streams evidence for such soft-bedded deformation is lacking (e.g. Payne and Baldwin, 1999; Piotrowski *et al.*, 2001; Stokes and Clark, 2003). This therefore suggests the existence of a variety of controlling processes on ice-stream flow.

In the following subsections we identify and review some of these potential mechanisms for allowing ice streaming in regions with few topographic constraints. We start by discussing thermomechanical feedbacks, which occur as a result of internal ice dynamics, before considering effects at the basal boundary (meltwater lubrication and till deformation), which may allow the ice to slide very rapidly at its base. Having addressed internal and basal effects, we also briefly consider effects at the outflow boundary (ice shelf buttressing) that may contribute to ice-stream behaviour.

1.2.1 Thermomechanical feedbacks

Thermomechanical feedbacks can occur by a creep instability mechanism where large strain rates in the ice cause heating that reduces ice viscosity, further increasing the strain rates. Areas with large strain rates become weaker, deforming more easily, and a thermoviscous fingering instability may develop (a symmetry-breaking instability where fast-flowing 'fingers' emerge as a result of coupled thermal and viscous effects). This idea was initially proposed by Clarke *et al.* (1977) who considered a parallel-sided slab of ice and showed that a cold, slow-moving state could co-exist with a warm, fast-moving state under certain combinations of ice thickness and surface inclination. However, as discussed in detail in Schoof and Hewitt's review of thermally induced streaming (Schoof and Hewitt, 2013), there are many potential complications that this mechanism does not capture, relying on a fixed geometry, a fast temperature timescale in comparison with the ice, and the neglect of any lateral stresses and lateral diffusion of heat. Many authors have carried out more detailed studies on this idea (e.g. MacAyeal, 1992; Payne, 1995; Payne and Dongelmans, 1997; Hindmarsh, 2006a, 2009), and although earlier studies such as Clarke's were ill-posed due to the shallow ice model used (Hindmarsh, 2011), the instability does appear to be robust. Nevertheless, it is known that some ice streams flow almost entirely by basal sliding (e.g. Engelhardt and Kamb, 1997) and this suggests that thermoviscous fingering isn't a sufficient explanation for all ice streams.

We expect, nevertheless, that there are thermomechanical effects playing a role at the bed; the base of ice streams have been found to be at melting point (Engelhardt *et al.*, 1990; Iken *et al.*, 1993). Both geothermal and frictional heating are responsible for this increase in temperature at the base, and the resulting meltwater lubricates the bed, allowing the ice to slide rapidly over the interface. The rapid sliding means that frictional heating further increases, producing more melt, and there is a resulting positive feedback. However, if this was the only mechanism playing a role, ice

streams would shut down solely due to basal freezing, which cannot be true since water has been found at the bed of some stagnant ice streams (Retzlaff and Bentley, 1993; Catania *et al.*, 2003). Therefore, while thermomechanical effects are likely to be of importance in producing the melt in the first place, we require an in depth understanding of how the meltwater at the bed behaves so to examine the feedbacks between the water and ice in more detail.

1.2.2 Basal lubrication

Observations suggest that the temporal and spatial evolution of the subglacial drainage system may play an important role in ice-stream dynamics. For example, the stagnation of some ice streams has been attributed to the re-routing of subglacial meltwater at the bed (e.g. Anandakrishnan and Alley, 1997; Vaughan *et al.*, 2008). The presence of water affects ice velocities through the effective pressure; this is the difference between ice pressure (a function of ice thickness) and water pressure. If the basal water pressure is close to the ice overburden pressure, the effective pressure is small and the local ice sheet velocity may increase. However, to calculate the effective pressure we must know the water pressure, which depends on the mechanism of water flow.

There are two contrasting types of subglacial drainage system commonly discussed in the literature. If there is little meltwater production the bed can effectively be drained by a distributed system of cavities (Walder, 1986; Kamb, 1987), through thin, patchy films (Alley, 1989), by porous flow through sediment (Boulton *et al.*, 1995), or by canals incised downwards into a deformable, erodible bed (Walder and Fowler, 1994). In these cases, with increasing meltwater production water pressure beneath the ice increases, lowering the effective pressure and hence resulting in more rapid sliding (e.g. Lliboutry, 1968). In contrast, some subglacial water transport occurs through large-scale channels incised upwards into the ice (Röthlisberger, 1972). These provide efficient drainage for the meltwater, resulting in low water pressure at the bed

and hence lower sliding velocities. Transition between distributed and channelised drainage systems can occur, for example when the accumulation of meltwater results in the distributed system becomes over-pressurised, initialising channelised drainage (Hewitt, 2011).

In the context of ice-streams, a soft bed has become the paradigmatic assumption; there is evidence for the presence of a layer of water-saturated till at the base of some ice streams (e.g. Alley *et al.*, 1986, 1987; Blankenship *et al.*, 1986; Tulaczyk *et al.*, 2000b). Till comprises of saturated sediments generated by the ice sheet eroding the bed, and so it is logical to expect a particularly thick layer of till in ice-streaming regions due to the fast velocities eroding the bed. As a granular material, till deforms with Coulomb-plastic behaviour (e.g. Iverson *et al.*, 1998; Tulaczyk *et al.*, 2000b; Kamb, 2001; Joughin *et al.*, 2004; Schoof, 2004), and its behaviour depends on the effective pressure, which is determined by the drainage system. It is therefore important to understand the drainage mechanism at the bed, which, in the context of ice streams, is expected to be mostly in the form of soft-bedded drainage systems, i.e., patchy films and channels in the sediment, rather than cavities or Röthlisberger channels.

1.2.3 Till deformation

Another contributing factor to ice-stream flow may come about from deformation of the till itself at the ice-bed interface, due to the ice exerting shear stress on the till (Alley *et al.*, 1986; Greve and Blatter, 2009). This idea is illustrated in Figure 1.5. Alley *et al.* (1986) argued that at the upstream end of Ice Stream B (Whillans), the till porosity, force balance and water balance all suggest that till deformation provides the primary mechanism allowing the fast flow. In other regions, such as underneath the Rutford Ice Stream, radar and seismic data result in certain areas of fast flow being attributed to basal deformation, and others to basal sliding over a lubricated

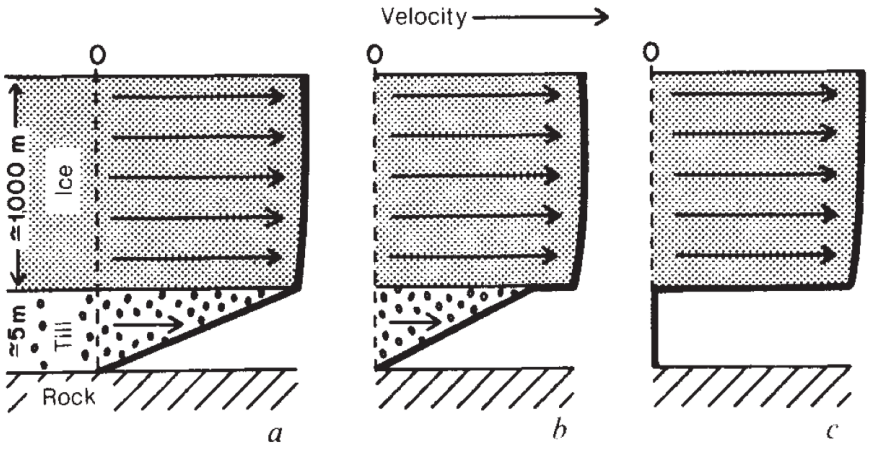

Figure 1.5: Possible models for an ice stream bed. (a) till deformation only; (b) till deformation plus basal sliding; (c) basal sliding only. Figure from Alley *et al.* (1986).

bed (Murray *et al.*, 2008).

Within areas of basal deformation, the extent of till deformation must depend on the till strength (Iverson *et al.*, 1994; Hart *et al.*, 2011). This is intrinsically linked to the subglacial hydrology, since the behaviour of the meltwater will determine the effective pressure in the till. Murray *et al.* (2008) noticed distinct contrasts in the hydrology between a region of basal deformation and one of basal sliding; in sliding regions he observed distributed water flow over the bed, while features more consistent with discrete canals in the sediment are present in regions of deforming till. It is therefore important to emphasise that what we term 'sliding' throughout the rest of this thesis as the basal ice movement occurring as a result of the combination of basal sliding and till deformation.

1.2.4 Longitudinal stresses and ice shelves

The buttressing of ice shelves provides a stabilising effect to the interior ice sheet (e.g., Thomas, 1979; Hindmarsh, 2006b; Goldberg and Holland, 2009); the presence of the ice shelf resists flow across the grounding line through transmission of longitudinal stresses. Iceberg calving can therefore have potentially large destabilising

consequences on an ice stream (e.g. Hughes, 1992), reducing the buttressing effect and therefore allowing flow acceleration. This acceleration can be enhanced by the large longitudinal stresses within the ice reducing the ice viscosity, allowing further flow acceleration (this is akin to the thermomechanical feedbacks discussed in Section 1.2.1, but with an added contribution from the shear-thinning rheology of ice (Glen, 1955)). As an example, the collapse of the Larsen B ice shelf in 2002 is thought to have played a significant contribution to the subsequent flow acceleration of glaciers on the Antarctic Peninsula (De Angelis and Skvarca, 2003; Rignot *et al.*, 2004).

1.3 Outlook

The aim of this thesis is to improve understanding of the feedbacks between subglacial hydrology and ice flow. We do this by considering the coupled behaviour of the ice sheet and subglacial water flow, in order to see if this can provide a mechanism for explaining ice-stream behaviour.

In Chapter 2 we describe how ice is modelled, discussing commonly used approximations, before deriving a hybrid approximation to ice flow that is suitable for modelling the emergence and stagnation of ice streams. In Chapter 3 we use this hybrid approximation together with different basal boundary conditions to examine the necessary stress balances across ice streams that will maintain ice stream flow. Chapter 4 moves on to consider the subglacial hydrology. We present a description of a distributed drainage system over a saturated, impermeable till layer and consider solutions to the governing equations de-coupled from the ice flow. In Chapter 5 we then discuss coupling the water flow with sediment evolution at the bed, and show that swamp-like streams may form in the sediment. Finally, in Chapter 6 we present results from coupling the subglacial hydrology and ice flow, and show that the coupled behaviour can result in the development of ice streams.

Chapter 2

Ice flow model

2.1 Introduction

A significant challenge in ice sheet dynamics is in accurately capturing the transition from ice sheet to ice stream flow; this is critically important in modelling the temporal emergence and stagnation of ice streams. Most of an ice sheet is frozen to the bed and vertical shear stresses are dominant in the stress balance. However, in ice streams the ice slips rapidly over the bed; this introduces significant horizontal stress gradients. An appropriate model for ice flow must be able to describe both types of behaviour. Under the assumption that ice is an incompressible, viscous fluid, Stokes flow provides a suitable description of all flow regimes. However, these equations are computationally expensive to solve in 3D and approximations are commonly used. Two such approximations, representing end-member models, are the shallow ice approximation (SIA) (Hutter, 1983; Fowler and Larson, 1978; Morland and Johnson, 1980) and shallow shelf approximation (SSA) (MacAyeal, 1989; Weis and Greve, 1999). The SIA assumes that the ice is frozen to the bed or only slipping very slowly; vertical shear stresses are supported by the basal drag in the stress balance. The approximation is valid only in regions of low basal slip and its accuracy decreases significantly as the amount of basal slip increases (Gudmundsson, 2003; Hindmarsh, 2004). The SSA, on the other hand, assumes longitudinal stresses dominate over vertical shear stresses, and horizontal velocities therefore do not vary with depth. It

can accurately describe the dynamics within an ice stream, but provides an inaccurate flow description outside of ice streams and in regions where there is strong basal friction balancing vertical shear stresses.

One approach to accurately describing all flow regimes within an ice sheet is to use both the above end-member models, coupling them together by imposing jump conditions at stream and shelf boundaries (Hulbe and MacAyeal, 1999; Ritz *et al.*, 2001; Schoof, 2006). It is convenient, however, to describe the flow of an ice sheet using the same set of partial differential equations over the whole domain. Hybrid approximations provide a way of computing the leading order flow dynamics for all flow regimes within an ice sheet without the numerical challenges of solving a full Stokes system (e.g., Blatter, 1995; Schoof and Hindmarsh, 2010; Bueler and Brown, 2008; Goldberg, 2011; Winkelmann *et al.*, 2011). In this chapter we derive a shallow-ice hybrid approximation, taking a similar approach to Schoof and Hindmarsh (2010) by introducing a scaling parameter related to the proportion of velocity due to slip at the bed. Other authors have taken different approaches; in particular Bueler and Brown (2008) solve the nonlinear SIA and SSA separately and then add the solutions together using an arbitrary weighting function.

The chapter is organised as follows. In Section 2.2 we outline the Stokes equations for describing ice flow and discuss suitable boundary conditions. In Section 2.3 we discuss classical approximations to Stokes flow, in particular the SIA and the SSA. We outline the assumptions made in deriving these approximations and this leads us to derive a hybrid approximation in Section 2.4. The approximation provides an accurate flow description both in ice streams and in the surrounding slow-moving ice. Section 2.5 presents some simple numerical solutions and we make some concluding remarks in Section 2.6.

2.2 Ice flow

2.2.1 Governing equations

Assuming that ice is an incompressible, viscous fluid, an ice sheet moving under gravity is accurately described by Stokes flow. The governing equations are those of mass and momentum conservation,

$$\boldsymbol{\nabla} \cdot \mathbf{v} = 0, \tag{2.1a}$$

$$\boldsymbol{\nabla} \cdot \boldsymbol{\sigma} = -\mathbf{f}. \tag{2.1b}$$

where $\mathbf{v} = (u, v, w)$ is the ice velocity, $\mathbf{f} = (0, 0, -\rho_i g)$ is the gravitational body force acting on the fluid, and

$$\sigma_{jk} = -p\delta_{jk} + \tau_{jk} \tag{2.2}$$

is the stress tensor. τ_{jk} is the deviatoric part of the stress tensor and is given by

$$\tau_{jk} = 2\eta_i \dot{\epsilon}_{jk} \tag{2.3}$$

where η_i is the ice viscosity and $\dot{\epsilon}_{jk} = \frac{1}{2}\left(\frac{\partial v_j}{\partial x_k} + \frac{\partial v_k}{\partial x_j}\right)$ is the strain rate.

The deformation of ice is usually modelled with a constitutive relation known as Glen's flow law (Glen, 1955; Cuffey and Paterson, 2010; Greve and Blatter, 2009)

$$\dot{\epsilon}_{jk} = A\tau^{n-1}\tau_{jk}, \tag{2.4}$$

where A is a temperature-dependent rate factor and τ is the second invariant of the deviatoric stress tensor i.e. $2\tau^2 = \tau_{jk}\tau_{jk}$. Ice is therefore a non-Newtonian fluid with viscosity

$$\eta_i = \frac{1}{2A\tau^{n-1}}. \tag{2.5}$$

2.2.2 Boundary conditions

Boundary conditions are required at the ice surface, $z = s_i$, and bed, $z = b$.

We apply a balance in normal stress (assuming no applied traction) at the ice surface,

$$\boldsymbol{\sigma} \cdot \mathbf{n}^s = -p_a \mathbf{n}^s \quad \text{at} \quad z = s_i, \tag{2.6a}$$

where $\mathbf{n}^s \propto (-\partial s_i/\partial x, -\partial s_i/\partial y, 1)$ is the normal to the surface. We also have the free surface kinematic boundary condition (Acheson, 1990), which says that fluid particles at the free surface remain at the boundary,

$$w(s) = \frac{\partial s_i}{\partial t} + \mathbf{u} \cdot \boldsymbol{\nabla} s_i - a_s \quad \text{at} \quad z = s_i, \tag{2.6b}$$

where $\mathbf{u} = (u, v)$ is the horizontal velocity vector (here evaluated at the surface) and $a_s(x, y, t)$ is the accumulation rate over the ice, which can be either positive or negative depending on the contribution of snowfall versus ablation.

At the bed the kinematic condition is

$$w(b) = \mathbf{u} \cdot \boldsymbol{\nabla} b - a_b \quad \text{at} \quad z = b, \tag{2.7a}$$

where the velocity is evaluated at the bed and $a_b(x, y, t)$ is the melt rate of the ice (negative if basal freeze-on is occurring). As the other condition we assign the velocity at the boundary, taking

$$\mathbf{u} = \mathbf{u}_b \quad \text{at} \quad z = b, \tag{2.7b}$$

where $\mathbf{u}_b = (u_b, v_b)$ is a defined basal sliding velocity. Assumptions about what value this sliding velocity takes lead to different approximations to Stokes flow, as discussed in the following section.

2.3 Classical approximations

Antarctica is thousands of kilometres in horizontal extent, with an average thickness of only a few kilometres and so its aspect ratio $\varepsilon = h_0/x_0 \sim 10^{-3}$ (where a subscript 0 represents a variable's scale). This low aspect ratio of ice sheets allows simplifications to be made to the 3D nonlinear equations describing Stokes flow. In particular, we have from (2.1a) that $w_0 \sim \varepsilon u_0$—vertical velocity is negligible in magnitude compared with horizontal velocities. Furthermore, integrating the expression for mass conservation (2.1a) over depth, with (2.6b) and (2.7a) as the boundary conditions, we obtain

$$\frac{\partial h}{\partial t} + \boldsymbol{\nabla} \cdot \mathbf{q} = a, \tag{2.8}$$

where $\mathbf{q} = \int_b^{s_i} \mathbf{u}\,\mathrm{d}z$ is the ice flux and $a(x, y, t) = a_s - a_b \approx a_s$, since accumulation rates are generally an order of magnitude larger than melt rates at the bed.

For clarity, we are able to separate the ice velocity $\mathbf{u}$ into two components, one being the basal velocity $\mathbf{u}_b$ from (2.7b), and the other being a deformational component $\mathbf{u}_d$, due to internal deformation of the ice. The ice flux can then be written as

$$\mathbf{q} = h\mathbf{u}_b + \int_b^{s_i} \mathbf{u}_d\,\mathrm{d}z. \tag{2.9}$$

Two end-member approximations to Stokes flow are then the result of considering the two limits– $|\mathbf{u}_b| \ll |\mathbf{u}_d|$ and $|\mathbf{u}_b| \gg |\mathbf{u}_d|$.

2.3.1 Shallow Ice Approximation

The shallow ice approximation (SIA) is a classical lubrication approximation, valid in the regime where $|\mathbf{u}_b| \ll |\mathbf{u}_d|$, i.e. if the ice is frozen to the bed or only sliding very slowly. In this case the flow will be dominated by vertical shear stresses and other stresses can be neglected in (2.1b) (Fowler and Larson, 1978; Morland and Johnson,

1980; Hutter, 1983). This allows us to find an expression for the ice velocity,

$$\mathbf{u} = \mathbf{u}_b + 2A(\rho_i g)^n |\boldsymbol{\nabla} s_i|^{n-1} \left[\frac{(s_i - z)^{n+1} - h^{n+1}}{n+1} \right] \boldsymbol{\nabla} s_i,$$

where the ice has been taken as isothermal (as is assumed throughout the thesis). Integrating this gives an expression for $\mathbf{q}$ and substituting into (2.8) gives an equation governing the depth h of the ice sheet,

$$\frac{\partial h}{\partial t} + \boldsymbol{\nabla} \cdot \left[h\mathbf{u}_b - \frac{2A(\rho_i g)^n |\boldsymbol{\nabla} s_i|^{n-1} h^{n+2}}{n+2} \boldsymbol{\nabla} s_i \right] = a. \tag{2.10a}$$

We further have that the basal stress is given by

$$\boldsymbol{\tau}_b = -\ \rho_i g h \boldsymbol{\nabla} s_i. \tag{2.10b}$$

2.3.2 Shallow Shelf Approximation

In contrast with the SIA, the shallow-shelf approximation (SSA) is a valid flow description in the case when the longitudinal stresses dominate over vertical shear stresses and $|\mathbf{u}_b| \gg |\mathbf{u}_d|$ e.g. in ice streams or on ice shelves. The ice velocity can be approximated as being constant with depth i.e.

$$\mathbf{u}(x, y) = \mathbf{u}_b(x, y)$$

at all ice depths. Depth-integrated conservation of mass is therefore given by the simple equation

$$\frac{\partial h}{\partial t} + \boldsymbol{\nabla} \cdot [h\mathbf{u}_b] = a, \tag{2.11a}$$

while the expression for the basal shear stress now includes a contribution from the longitudinal stresses, and the components can be written as

$$\boldsymbol{\tau}_b = \left(-\rho_i g h \frac{\partial s_i}{\partial x} + \frac{\partial}{\partial x}\left[2h\eta_i \left(2\frac{\partial u_b}{\partial x} + \frac{\partial v_b}{\partial y} \right) \right] + \frac{\partial}{\partial y}\left[h\eta_i \left(\frac{\partial v_b}{\partial x} + \frac{\partial u_b}{\partial y} \right) \right], \right.$$
$$\left. -\rho_i g h \frac{\partial s_i}{\partial y} + \frac{\partial}{\partial y}\left[2h\eta_i \left(2\frac{\partial v_b}{\partial y} + \frac{\partial u_b}{\partial x} \right) \right] + \frac{\partial}{\partial x}\left[h\eta_i \left(\frac{\partial u_b}{\partial y} + \frac{\partial v_b}{\partial x} \right) \right] \right) \tag{2.11b}$$

where η_i is given by (2.5) (MacAyeal, 1989; Weis and Greve, 1999).

2.4 Hybrid formulation of the ice flow model

The SIA is an accurate approximation over the vast majority of an ice sheet, where the ice is frozen to the bed, or only sliding very slowly. Ice streams are one of few areas where it does not provide a valid flow description; the flux is largely due to to sliding at the bed in ice streams and so the SSA provides a more accurate approximation to the flow. However, in this thesis we are interested in the emergence and stagnation of ice streams, and neither the SIA or the SSA accurately describe the transition between sheet and stream flow, temporally or spatially. We therefore consider a hybrid approximation of Stokes flow, which takes into account both vertical shear stresses and longitudinal stresses (Fowler, 2011a; Kyrke-Smith *et al.*, 2013).

2.4.1 Non-dimensionalisation and reduction

We first define the scales h_0, x_0, u_0, η_0, t_0, a_0 and $\tau_0 \sim \rho_i g h_0^2/x_0$, $p_0 \sim \rho_i g h_0$ (the latter from the z-cmpt of (2.1b)). Original variables are defined in Table 2. To derive the hybrid approximation we then non-dimensionalise the Stokes flow equations (2.1), scaling the variables as $z = h_0 z^*$, $x = x_0 x^*$ etc.

In the SIA equilibrium at the ice-sheet bed is from the basal drag, τ_b, resisting

the local driving stress. If, however, there is basal sliding, it is necessary to consider additional stress gradients in the model. In light of this we introduce a new dimensionless parameter λ, which is the ratio of the magnitude of the basal stress to the viscous shear stress scale, providing an estimate of slip,

$$\lambda = \frac{\tau_0 h_0}{\eta_0 u_0} \leq 1. \tag{2.12}$$

In the instance that $\lambda \sim \mathcal{O}(1)$ the flow is shear dominated (basal stresses are of similar magnitude to the vertical shear stresses) while for $\lambda \ll 1$, basal stresses are small compared to vertical shear. In this case the driving stress is greater than the drag provided by the bed, which increases the stretching rate in the ice as it is able to slide over the bed; longitudinal stresses start to play a more dominant role in the stress balance. λ is never greater than 1 since τ_0 is less than $\eta_0 u_0/h_0$ at all times, and equal if and only if the ice sheet is frozen to the bed and no slip is occurring (i.e. if the static basal stress is locally in balance with the driving stress, as in the SIA).

With λ and

$$\varepsilon = h_0/x_0 \tag{2.13}$$

as the two control parameters, we derive a set of non-dimensional equations for h, u_b and v_b. In terms of these dimensionless variables (dropping the * for simplicity), the individual components of the governing equations become

$$\frac{\partial \tau_{13}}{\partial z} = \frac{\partial p}{\partial x} - \frac{\varepsilon^2}{\lambda}\left(\frac{\partial \tau_{11}}{\partial x} + \frac{\partial \tau_{12}}{\partial y}\right), \tag{2.14a}$$

$$\frac{\partial \tau_{23}}{\partial z} = \frac{\partial p}{\partial y} - \frac{\varepsilon^2}{\lambda}\left(\frac{\partial \tau_{12}}{\partial x} + \frac{\partial \tau_{22}}{\partial y}\right), \tag{2.14b}$$

$$\frac{\partial p}{\partial z} = \frac{\varepsilon^2}{\lambda}\frac{\partial \tau_{33}}{\partial z} - 1, \tag{2.14c}$$

$$0 = \frac{\partial u}{\partial x} + \frac{\partial v}{\partial y} + \frac{\partial w}{\partial z}, \tag{2.14d}$$

having neglected terms of $\mathcal{O}(\varepsilon^2)$ (since we assume the ice is thin).

Similarly, non-dimensionalising the boundary condition at $z = s_i$ (2.6a), gives us

$$\tau_{13}(s_i) = -(p - p_a)\frac{\partial s_i}{\partial x} + \frac{\varepsilon^2}{\lambda}\left(\tau_{11}(s_i)\frac{\partial s_i}{\partial x} + \tau_{12}(s_i)\frac{\partial s_i}{\partial y}\right), \tag{2.15a}$$

$$\tau_{23}(s_i) = -(p - p_a)\frac{\partial s_i}{\partial y} + \frac{\varepsilon^2}{\lambda}\left(\tau_{12}(s_i)\frac{\partial s_i}{\partial x} + \tau_{22}(s_i)\frac{\partial s_i}{\partial y}\right), \tag{2.15b}$$

$$\frac{\varepsilon^2}{\lambda}\tau_{33}(s_i) = p - p_a + \mathcal{O}(\varepsilon^2), \tag{2.15c}$$

and we again neglect $\mathcal{O}(\varepsilon^2)$ terms.

Integrating (2.14c) over z, and applying the boundary condition (2.15c) gives us an expression for the static pressure at depth z,

$$p = p_a + (s_i - z) + \frac{\varepsilon^2}{\lambda}\tau_{33}. \tag{2.16}$$

Substituting into (2.14a) and (2.14b) we are left with

$$\frac{\partial \tau_{13}}{\partial z} = \frac{\partial s_i}{\partial x} - \frac{\varepsilon^2}{\lambda}\left(2\frac{\partial \tau_{11}}{\partial x} + \frac{\partial \tau_{12}}{\partial y} + \frac{\partial \tau_{22}}{\partial x}\right), \tag{2.17a}$$

$$\frac{\partial \tau_{23}}{\partial z} = \frac{\partial s_i}{\partial y} - \frac{\varepsilon^2}{\lambda}\left(\frac{\partial \tau_{11}}{\partial y} + \frac{\partial \tau_{12}}{\partial x} + 2\frac{\partial \tau_{22}}{\partial y}\right) \tag{2.17b}$$

where τ_{33} has been re-written as $-\tau_{11} - \tau_{22}$. These are the governing equations for the hybrid approximation.

We are further able to write these equations in terms of ice velocities, given Glen's flow law describing the deformation of ice, as outlined in Section 2.2. Taking the vertical shear stresses to scale as $\tau_{13} \sim \tau_{23} \sim \tau_0$ and the longitudinal stresses to scale as $\tau_{11} \sim \tau_{12} \sim \tau_{22} \sim \tau_{33} \sim \eta_0 u_0/x_0$, we can take the second invariant of the deviatoric stress tensor to scale as $\tau^2 \sim \tau_0^2$ and so we have

$$\tau^2 = \tau_{13}^2 + \tau_{23}^2 + \frac{\varepsilon^2}{\lambda^2}\left(\frac{1}{2}\tau_{11}^2 + \frac{1}{2}\tau_{22}^2 + \frac{1}{2}\tau_{33}^2 + \tau_{12}^2\right). \tag{2.18}$$

From (2.5) we further have that $\mu_0 \sim \left(2A_0\tau_0^{n-1}\right)^{-1}$, and so the non-dimensional components of the constitutive relation (2.4) can thus be expressed as

$$\frac{\partial u}{\partial z} + \varepsilon^2\frac{\partial w}{\partial x} = \lambda A\tau^{n-1}\tau_{13}, \tag{2.19a}$$

$$\frac{\partial v}{\partial z} + \varepsilon^2\frac{\partial w}{\partial y} = \lambda A\tau^{n-1}\tau_{23}, \tag{2.19b}$$

$$\frac{\partial u}{\partial y} + \frac{\partial v}{\partial x} = A\tau^{n-1}\tau_{12}, \tag{2.19c}$$

$$2\frac{\partial u}{\partial x} = A\tau^{n-1}\tau_{11}, \tag{2.19d}$$

$$2\frac{\partial v}{\partial y} = A\tau^{n-1}\tau_{22}, \tag{2.19e}$$

$$2\frac{\partial w}{\partial z} = A\tau^{n-1}\tau_{33}, \tag{2.19f}$$

Initially we consider the limit $\lambda \ll 1$. From (2.19a) and (2.19b) we have that $\mathbf{u} \approx \mathbf{u}_b$ in this limit and $\mathbf{u}$ is therefore a function of just x and y. Further assuming that $\tau_{11}, \tau_{12}, \tau_{22}$ are also functions of just x and y (i.e. evaluating (τ_{13}, τ_{23}) at the bed in the expression for τ^2 (2.18)), we can integrate the components of (2.17) with respect to z. Together with non-dimensional boundary conditions (2.15a) and (2.15b) we have

$$\boldsymbol{\tau}_s = -(s_i - z)\boldsymbol{\nabla} s_i + \frac{\varepsilon^2}{\lambda}\boldsymbol{\nabla}\cdot\left((s_i - z)\mathbf{S}\right), \tag{2.20}$$

where $\boldsymbol{\tau}_s = (\tau_{13}, \tau_{23})$ and $\mathbf{S}$ is the resistive stress tensor (Van der Veen, 1999; Hindmarsh, 2012), given by

$$\mathbf{S} = \boldsymbol{\tau} + \mathbf{I}\mathrm{trace}\left(\boldsymbol{\tau}\right) = \begin{bmatrix} 2\tau_{11} + \tau_{22} & \tau_{12} \\ \tau_{12} & \tau_{11} + 2\tau_{22} \end{bmatrix}. \tag{2.21}$$

Having considered the $\lambda \ll 1$ limit, we also consider the case $\lambda \sim \mathcal{O}(1)$, when shearing is dominant. The terms of $\mathcal{O}\left(\varepsilon^2/\lambda\right)$ are now very small $(\mathcal{O}(\varepsilon^2))$ unless horizontal gradients of the longitudinal stresses ($\partial\tau_{11}/\partial x$ etc) are very large, i.e. if

the horizontal velocities u, v change very rapidly in space. In regions where such a rapid change is occurring, gradients in $\mathbf{u}$ can be approximated by those of the sliding velocity, $\mathbf{u}_b$; in regions where the sliding velocity is not changing rapidly the corrective terms are small. Hence the equations (2.20) remain valid for all sliding regimes.

Since in this study we are considering an isothermal ice mass, we take the temperature dependent rate factor in Glen's flow law, A, to be a constant. Evaluating (2.20) at the bed we have a closed model for the sliding velocity, in the form

$$\boldsymbol{\tau}_b = -h\boldsymbol{\nabla} s_i + \frac{\varepsilon^2}{\lambda}\boldsymbol{\nabla}\cdot(h\mathbf{S})\,, \tag{2.22}$$

where h is the ice depth and $\boldsymbol{\tau}_b$ is the basal stress,

$$\boldsymbol{\tau}_b = (\tau_{bx}, \tau_{by}) = (\hat{\boldsymbol{\imath}}\cdot\boldsymbol{\tau}(b)\cdot\hat{\mathbf{n}}_b,\ \hat{\boldsymbol{\jmath}}\cdot\boldsymbol{\tau}(b)\cdot\hat{\mathbf{n}}_\mathbf{b}). \tag{2.23}$$

with $\mathbf{n}_b = (-\partial b/\partial x, -\partial b/\partial y, 1)$ and $\boldsymbol{\tau}$ given by (2.3).

It is possible to simplify this even further if we consider removing the depth terms from inside the derivatives in (2.20). In doing so we are assuming that the ice surface does not change abruptly—we do not expect it to in the case of rapid sliding, and in the case of shear-dominant flow we expect that the $\mathcal{O}(\varepsilon^2/\lambda)$ term is small in (2.20) and so it is reasonable to remove the depth term from inside the derivative. In this case we can write (2.20) as

$$(\tau_{13}, \tau_{23}) \approx (s_i - z)\boldsymbol{\gamma} \tag{2.24}$$

where

$$\boldsymbol{\gamma} = -\boldsymbol{\nabla} s_i + \frac{\varepsilon^2}{\lambda}\boldsymbol{\nabla}\cdot\mathbf{S}. \tag{2.25}$$

To obtain an equation governing the evolution of the ice depth, and therefore close the system of equations for ice velocities and depth, we can integrate the expression

for mass conservation (2.14d) over depth, as for (2.8) in Section 2.3. We have

$$\frac{\partial h}{\partial t} + \boldsymbol{\nabla} \cdot \mathbf{q} = a, \tag{2.26}$$

where $\mathbf{q} = \int_b^{s_i} \mathbf{u} \, \mathrm{d}z$ is the ice flux. When $\lambda \ll 1$ this becomes

$$\frac{\partial h}{\partial t} + \boldsymbol{\nabla} \cdot (h\mathbf{u}_b) = a. \tag{2.27}$$

A correction only becomes significant when shear stresses play an important role in the ice motion i.e. when sliding is small. In this case (2.18) becomes

$$\tau^2 \simeq \tau_{13}^2 + \tau_{23}^2 = (s_i - z)^2 \left|\boldsymbol{\gamma}\right|^2, \tag{2.28}$$

by (2.24). Furthermore, (2.19a) and (2.19b) $\Rightarrow (\partial u/\partial z, \partial v/\partial z) = \lambda \tau^{n-1} (\tau_{13}, \tau_{23})$, giving

$$\begin{aligned} \frac{\partial \mathbf{u}}{\partial z} &= \lambda \tau^{n-1} (s_i - z) \boldsymbol{\gamma} \\ &\approx -\lambda \tau^{n-1} (s_i - z) \boldsymbol{\nabla} s_i, \end{aligned} \tag{2.29}$$

to $\mathcal{O}(\varepsilon^2)$ accuracy again.

Finally, substituting (2.28) into (2.29) and integrating over depth gives us the mass flux

$$\mathbf{q} = \int_b^{s_i} \mathbf{u} \, \mathrm{d}z = h\boldsymbol{u}_b - \lambda \frac{h^{n+2}}{n+2} \left|\boldsymbol{\gamma}\right|^{n-1} \boldsymbol{\nabla} s_i. \tag{2.30}$$

We hence obtain the governing equations:

$$\frac{\partial h}{\partial t} + \boldsymbol{\nabla} \cdot \left(h\mathbf{u}_b - \lambda \frac{h^{n+2}}{n+2} \left|\boldsymbol{\gamma}\right|^{n-1} \boldsymbol{\nabla} s_i \right) = a, \tag{2.31a}$$

$$\boldsymbol{\tau}_b = h\boldsymbol{\gamma}, \tag{2.31b}$$

where $\boldsymbol{\gamma}$ is given by (2.25) with $\mathbf{u} = \mathbf{u}_b$. This is the most general form of the equations.

Note that since the $\mathcal{O}(\lambda)$ correction to $\mathbf{q}$ in (2.30) is only important when shear stresses are dominant ($\lambda \sim \mathcal{O}(1)$), $\tau^2 \simeq \tau_{13}^2 + \tau_{23}^2$ does not vary rapidly with x or y. It can therefore be removed from inside the divergence term in (2.25) when written out with the components of $\boldsymbol{\tau_b}$ substituted in from Glen's flow law for $\mathbf{S}$. Furthermore, expanding $|\boldsymbol{\gamma}|^{n-1}$, retaining terms greater than $\mathcal{O}(\varepsilon^2)$, shows that if $\lambda > \mathcal{O}(\varepsilon^2)$, then $\boldsymbol{\gamma} = -\boldsymbol{\nabla} s_i$ to $\mathcal{O}(\varepsilon^2)$ accuracy.

We therefore have the simplification that in (2.31a), $\boldsymbol{\gamma}$ can be taken to be

$$\boldsymbol{\gamma} = \begin{cases} -\boldsymbol{\nabla} s_i + \frac{\varepsilon^2}{\lambda \tau^{n-1}} \left(\nabla^2 \mathbf{u}_b + 3 \boldsymbol{\nabla} \left(\boldsymbol{\nabla} \cdot \mathbf{u}_b \right) \right) & \text{for all } \lambda \\ -\boldsymbol{\nabla} s_i & \text{if } \lambda > \mathcal{O}(\varepsilon^2) \end{cases} \tag{2.32}$$

to $\mathcal{O}(\varepsilon^2)$ accuracy.

Finally, by substituting the components of Glen's law (2.19a)-(2.19f) into (2.18), together with expressions for $\partial u/\partial z$ and $\partial v/\partial z$ from (2.29), we get

$$\tau^{2n} = |\boldsymbol{\nabla} s_i|^{2n} h^{2n} + \left(\frac{\varepsilon}{\lambda} \right)^2 \left[2 \left(\frac{\partial u}{\partial x} \right)^2 + 2 \left(\frac{\partial v}{\partial y} \right)^2 + 2 \left(\frac{\partial u}{\partial x} \right) \left(\frac{\partial v}{\partial y} \right) + \left(\frac{\partial u}{\partial y} + \frac{\partial v}{\partial x} \right)^2 \right]. \tag{2.33}$$

However, note that it is only valid to approximate τ^2 as $\tau_{13}^2 + \tau_{23}^2 = |\boldsymbol{\nabla} s_i|^2 h^2$ in (2.31a); the correction to $\boldsymbol{\gamma}$ in (2.31b) is important in the limit of small λ and so the longitudinal stress terms cannot be neglected.

2.5 Numerical Solution

The solution method and discretisation of the governing equations is outlined in Appendix A1. We use a staggered, Cartesian, two-dimensional grid with $n_i \times n_j$

discrete points. The nonlinear system of equations is solved using a Newton-Krylov solver, provided by the Portable Extensible Toolkit for Scientific Computation (Balay *et al.*, 1997, 2013, 2014). The fully coupled system is inverted at each time-step, and the solution is accepted when the absolute size of the nonlinear system residual is $< 10^{-8}$. We outline here a couple of simple test solutions to check the accuracy of the numerical solver.

2.5.1 SIA steady-state solution with zero sliding

We first consider the case when $\lambda = 1$ and there is no sliding at the bed ($\mathbf{u}_b = \mathbf{0}$). From (2.31a) we have that

$$\boldsymbol{\nabla} \cdot \left(\frac{h^{n+2}}{n+2} \left| \boldsymbol{\nabla} s_i \right|^{n-1} \boldsymbol{\nabla} s_i \right) + a = 0, \tag{2.34}$$

as for the non-dimensional SIA.

In the case on a flat bed ($\Rightarrow \boldsymbol{\nabla} s_i = \boldsymbol{\nabla} h$) this reduces to

$$\boldsymbol{\nabla} \cdot \left(\frac{h^{3}}{n+2} \left| \boldsymbol{\nabla} h \right|^{n-1} \boldsymbol{\nabla} h \right) + a = 0. \tag{2.35}$$

2.5.1.1 Newtonian solution with two Dirichlet boundary conditions

If we consider a solution to this on a square domain, with no flow variation in the y-direction, and the Dirichlet boundary conditions

$$h = h_s \quad \text{at} \quad x = 0,$$
$$h = h_e \quad \text{at} \quad x = 1,$$

in the Newtonian case ($n = 1$) there exists an analytic solution

$$h = \left[h_s^4 + \left(h_e^4 - h_s^4 + 6a \right) x - 6ax^2 \right]^{1/4}. \tag{2.36}$$

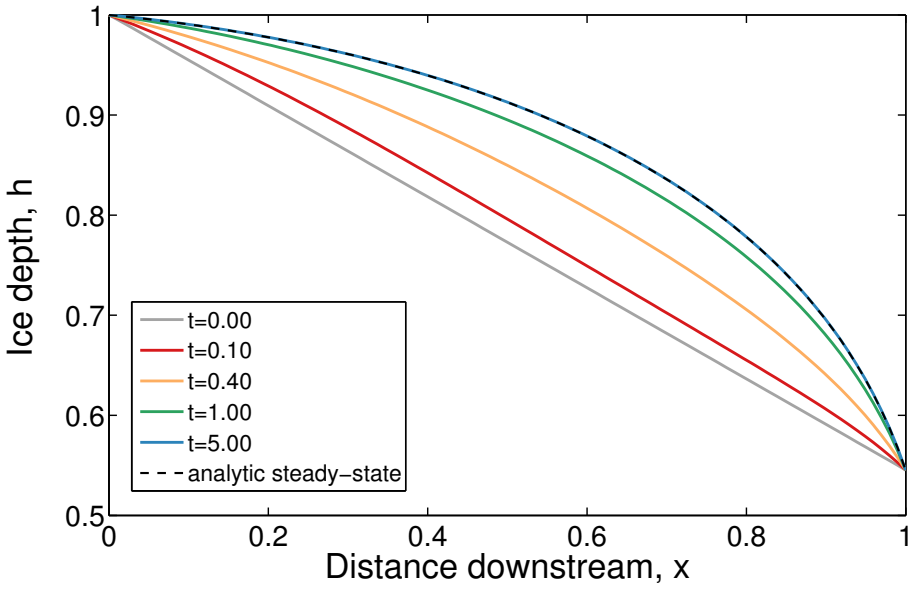

Figure 2.1: Downstream ice depth profile plotted at various times for a simulation with $\lambda = 1$, $\varepsilon = 0.001$ and a constant accumulation rate $a = 0.1$. The boundary conditions are given by (2.37). The simulation evolves to reach the steady-state solution given by (2.36).

Figure 2.1 shows the evolution of a solution to reach the analytic solution in this case with the boundary conditions

$$h = 1.0 \qquad \text{at} \quad x = 0, \tag{2.37a}$$

$$h = -\frac{\rho_w}{\rho_i} b \quad \text{at} \quad x = 1, \tag{2.37b}$$

where $b = -0.5$ is the non-dimensional basal elevation. The latter (2.37b) is the condition for hydrostatic equilibrium at the grounding line.

Furthermore, in Figure 2.2 we plot the numerical error in the steady-state solution found in the simulation shown in Figure 2.1. The error increases downstream, only decreasing again close to the outflow boundary where the depth is defined. There are four curves plotted, corresponding to the same simulation run at four different resolutions; it is evident that the accuracy of the result improves as the grid spacing decreases.

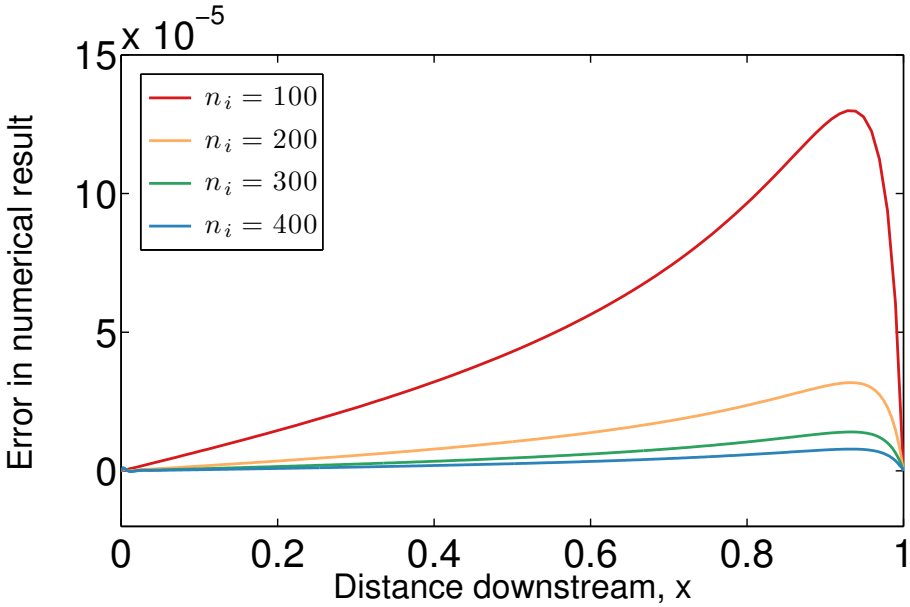

Figure 2.2: The numerical error in the steady-state found by numerical solution of the Newtonian hybrid ice flow model. This is plotted for four different grid resolutions, where the grid spacing is given by $dx = 1/n_i$.

2.5.1.2 Non-Newtonian solution with two Dirichlet boundary conditions

We also consider a non-Newtonian example ($n = 3$) with the same Dirichlet boundary conditions. An analytic solution in the case of zero accumulation rate ($a = 0$) is given by

$$h = \left[h_s^{8/3} - \left(h_s^{8/3} - h_e^{8/3}\right) x\right]^{3/8}. \tag{2.38}$$

Figure 2.3 shows the evolution of a solution to reach the analytic solution in this case with the boundary conditions (2.37).

Furthermore, in Figure 2.4 we plot the numerical error in the steady-state solution found in the simulation shown in Figure 2.3. As in the Newtonian case the error increases downstream, only decreasing again close to the outflow boundary where the depth is defined. There are four curves plotted, corresponding to the same simulation run at four different resolutions; once again it is evident that the accuracy of the result improves as the grid spacing decreases.

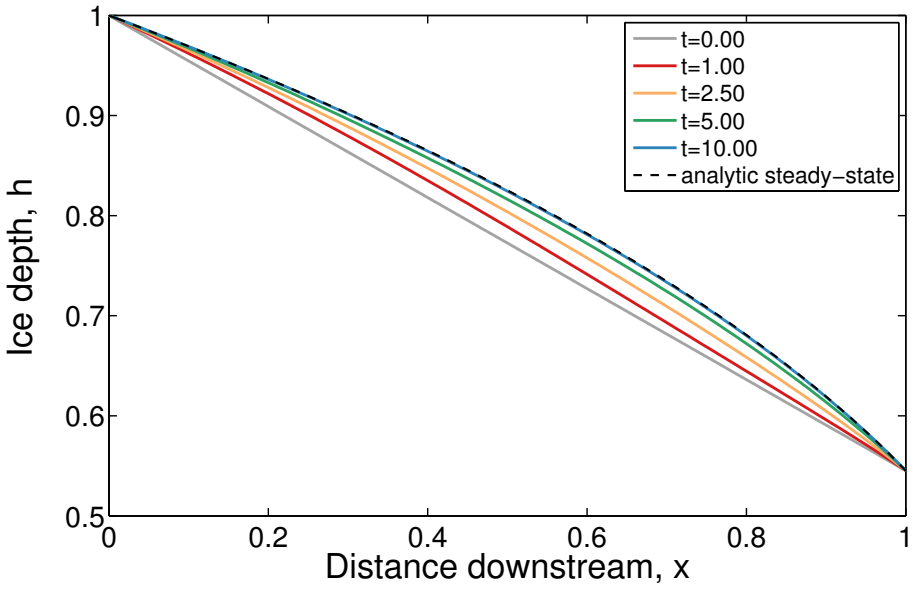

Figure 2.3: Downstream ice depth profile plotted at various times for a simulation with $\lambda = 1$, $\varepsilon = 0.001$ and a constant accumulation rate $a = 0.1$. The boundary conditions are given by (2.37). The simulation evolves to reach the steady-state solution given by (2.38).

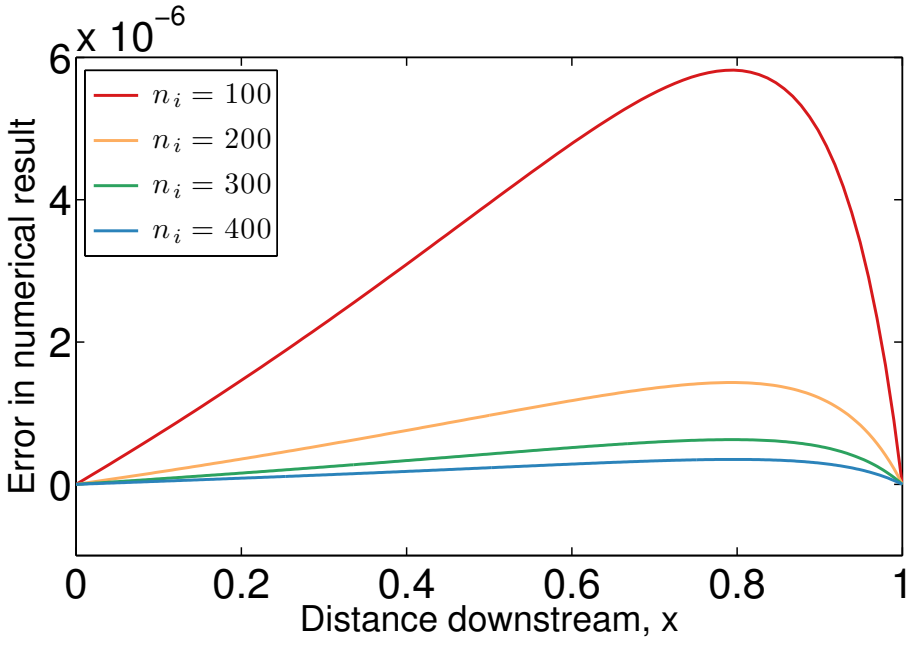

Figure 2.4: The numerical error in the steady-state found by numerical solution of the hybrid ice flow model. This is plotted for four different grid resolutions, where the grid spacing is given by $dx = 1/n_i$.

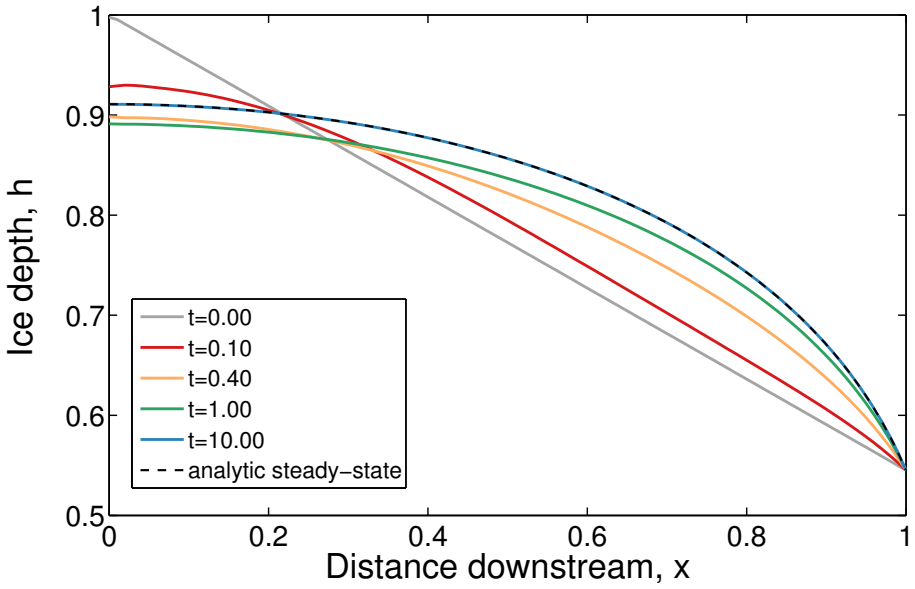

Figure 2.5: Downstream ice depth profile plotted at various times for a simulation with $\lambda = 1$, $\varepsilon = 0.001$ and a constant accumulation rate $a = 0.1$. The boundary conditions are a Neumann inflow condition (2.39a) and a Dirichlet outflow condition (2.37b). The simulation evolves to reach the steady-state solution given by (2.40).

2.5.1.3 Newtonian solution with a Neumann inflow and a Dirichlet outflow boundary condition

An analytic solution to (2.35) also exists in the Newtonian ($n = 1$) SIA limit with a Neumann boundary condition at the inflow,

$$\frac{\partial h}{\partial x} = 0 \quad \text{at} \quad x = 0, \tag{2.39a}$$

$$h = h_e \quad \text{at} \quad x = 1. \tag{2.39b}$$

It is given by

$$h = \left[h_e^4 + 6a\left(1 - x^2\right)\right]^{1/4}. \tag{2.40}$$

Figure 2.5 shows the evolution to reach the analytic solution in this case with a Neumann inflow boundary condition (2.39a) and the flotation criterion as the Dirichlet outflow condition again (2.37b).

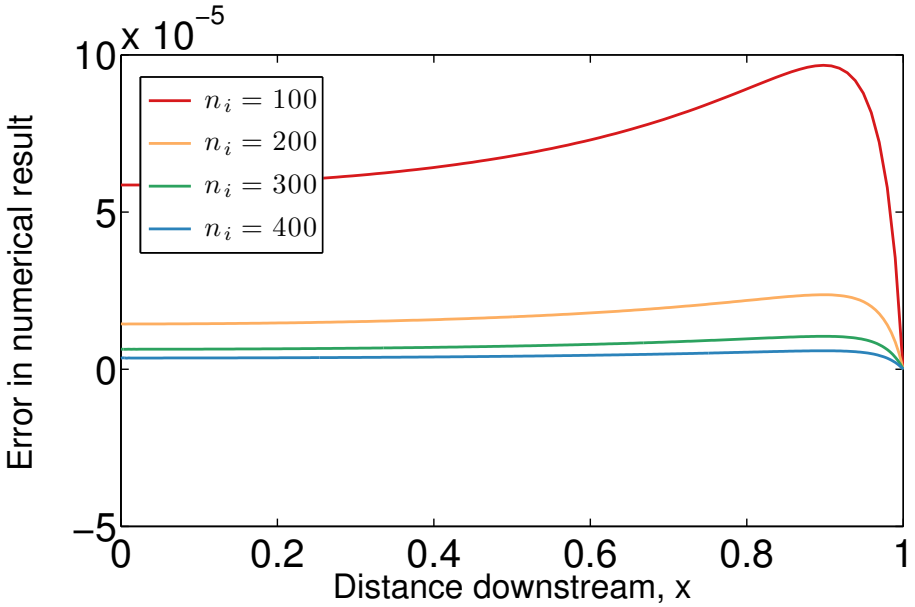

Figure 2.6: The numerical error in the steady-state solution found by numerical solution of the hybrid ice flow model. This is plotted for four different grid resolutions, where the grid spacing is given by $dx = 1/n_i$.

Figure 2.6 illustrates the numerical error in the steady-state solution found in the simulation shown in Figure 2.5. There are four curves plotted, corresponding to the same simulation run at four different resolutions; it is evident that again the accuracy of the result improves as the grid spacing decreases. Furthermore, the Neumann inflow condition means that there is error in the accuracy of the solution at the inflow boundary (compare with Dirichlet case in Figure 2.2 where there is zero error at both boundaries). The Neumann case also takes a longer time to evolve to its steady state.

2.5.2 SSA steady-state solution

We also consider the case when $\lambda \ll 1$ and there is now sliding at the bed. In an effort to find a simple analytic solution we assume there is no flow variation in the y direction and take a constant depth field i.e. we have $h(x, y) = 1$, $v_b(x, y) = 0$,

$u(x, y) = u(x)$. The governing equations (2.31) become

$$\frac{\partial u_b}{\partial x} = a, \tag{2.41a}$$

$$\tau_{bx} = -\frac{\partial b}{\partial x} + 4\frac{\varepsilon^2}{\lambda}\frac{\partial^2 u_b}{\partial x^2}. \tag{2.41b}$$

We choose a simple linear relationship between τ_b and u_b,

$$\tau_b = cu_b,$$

and take the accumulation rate to satisfy (2.41a). Given a constant bedslope, such that $\partial b/\partial x = -1$, the system reduces to a second-order ordinary differential equation, with constant coefficients,

$$u_b = 1 + 4\frac{\varepsilon^2}{\lambda}\frac{\partial^2 u_b}{\partial x^2}, \tag{2.42}$$

where c has been taken as unity for simplicity. This has a general solution

$$u_b = A\exp\left(\frac{\sqrt{\lambda}}{2\varepsilon}x\right) + B\exp\left(-\frac{\sqrt{\lambda}}{2\varepsilon}x\right) + 1. \tag{2.43}$$

Taking there to be zero inflow into the domain and constant velocity flow out of the domain,

$$u_b = 0 \quad \text{at} \quad x = 0, \tag{2.44a}$$

$$\frac{\partial u_b}{\partial x} = 0 \quad \text{at} \quad x = 1, \tag{2.44b}$$

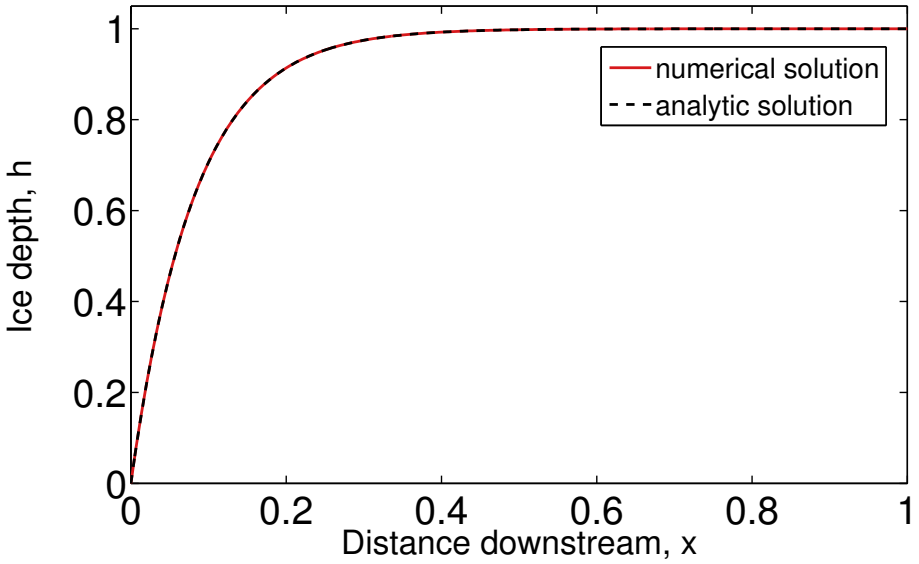

Figure 2.7: Downstream ice velocity profile for a simulation with $\lambda = 0.015$, $\varepsilon = 0.001$ and an accumulation rate satisfying (2.41a) . The boundary conditions are zero inflow into the domain (2.44a) and a Neumann outflow condition (2.44b). The result is plotted against the analytic solution given by (2.43).

the values of A and B in (2.43) are

$$A = -\frac{1}{\exp\left(\sqrt{\lambda}/\varepsilon\right) + 1}, \tag{2.45a}$$

$$B = -\frac{\exp\left(\sqrt{\lambda}/\varepsilon\right)}{\exp\left(\sqrt{\lambda}/\varepsilon\right) + 1}. \tag{2.45b}$$

This provides us with an analytic solution to compare with numerical results; Figure 2.7 shows a numerical solution of the hybrid ice flow model in this limit plotted against the analytic solution.

Once more we solve the equations with a range of grid resolutions, and Figure 2.8 illustrates how the numerical error of the solution again decreases with grid spacing.

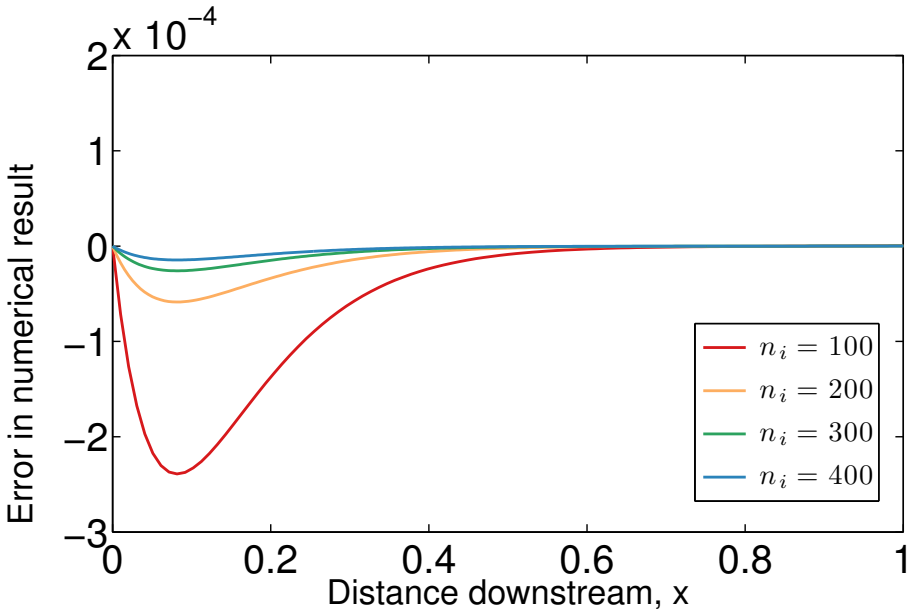

Figure 2.8: The numerical error in the solution found by numerical solution of the hybrid ice flow model. This is plotted for four different grid resolutions, where the grid spacing is given by $dx = 1/n_i$.

2.6 Summary and conclusions

In this chapter we have outlined the governing equations for ice flow and discussed common approximations used in ice-sheet modelling. Since these are not suitable for describing ice stream emergence and stagnation, we consider a higher-order model and derive a set of non-dimensional equations for ice depth, h, and ice velocity $\mathbf{u}_b = (u_b, v_b)$. We make the thin-film assumption, meaning that horizontal gradients of the vertical shear stresses are neglected. We assume that there are no abrupt spatial changes in basal or surface elevation, as is consistent with observations of pure ice streams. Moreover, membrane stresses are accurately approximated by using the sliding velocity to compute them; if the horizontal velocities (u, v) change rapidly in space, then this must be due to rapid changes in sliding velocity (u_b, v_b).

There are two non-dimensional parameters in the governing equations, ε and λ. The first is the aspect ratio of the ice sheet, assumed small. The parameter λ is

the ratio of basal to shear stress. It is similar to the traction number of Schoof and Hindmarsh (2010) and the slip ratio of Gudmundsson (2003). More specifically, if we define a deformational velocity scale due to vertical shear, $[u_d] \sim A\,[\tau_b]^n\,[d]$ (Schoof and Hindmarsh, 2010), then our parameter λ can be written as $\lambda = [u_d]/[u]$, which is the inverse of the slip ratio used by Gudmundsson (2003) and is closely related to the stress ratio used by Schoof and Hindmarsh (2010). An advantage of our formulation is that $0 < \lambda \leq 1$, making it easier to consider the whole range of sliding regimes, as is the purpose of using a higher-order formulation.

The discretisation and numerical solution of the governing equations is presented in an appendix to the chapter and we have considered a couple of simple test solutions to the equations in Section 2.5, in both the SIA and the SSA limit. The work presented here therefore provides us with a tool with which we can accurately compute ice flow dynamics in regions where there is both rapidly flowing ice and near-stagnant ice.

Chapter 3

Stress balances across ice streams

3.1 Introduction

In the previous chapter we presented an approximation to Stokes flow that is suitable for describing ice flow both in and outside of ice streams. However, regardless of the model used for the ice flow, the accuracy of the flow description is largely due to correct computation of the basal velocity. This is reliant on knowledge of the frictional resistance at the bed ($\boldsymbol{\tau}_b$ in the stress balance equation (2.31b)), which in turn is intrinsically linked to bed characteristics and the subglacial hydrology (e.g., Clarke, 2005; Iken and Bindschadler, 1986). It is common to represent this response of the basal velocity to changes in basal shear stress through a sliding law of the form $\boldsymbol{\tau}_b = f(\mathbf{u}_b)$ (e.g., Cuffey and Paterson, 2010; Fowler, 2011b). This allows the stress equation to be written as an equation just in terms of $\mathbf{u}_b$ and h, and so together with conservation of mass (2.31a) we have three equations for the three unknowns h, u_b and v_b. Since the subglacial hydrologic system is complex, and relatively little is known about it due to its inaccessibility, such sliding laws are typically phenomenological—they are consistent with the theory of processes governing the relationship, rather than directly derived from the physics. Simple sliding laws where basal velocity increases with basal shear stress (e.g. $u_b = A\tau_b^n$) are long-established and still commonly used (e.g., Weertman, 1972; Fowler, 1981), but more detailed considerations of the subglacial hydrologic system can be suggestive of a variety of different relationships,

The two contrasting types of subglacial drainage systems commonly discussed in the literature, outlined in the introduction to this thesis, are distributed drainage and channelised drainage. The former is relevant when there is little meltwater production. With increasing meltwater production, water pressure beneath the ice increases, lowering the effective pressure and hence resulting in more rapid sliding (Lliboutry, 1968; Kamb *et al.*, 1985; Walder, 1986; Fountain and Walder, 1998). In contrast, channelised drainage occurs through larger-scale Röthlisberger channels, which provide efficient drainage for the meltwater, resulting in low water pressure at the bed and hence slower sliding velocities (Röthlisberger, 1972). The physics governing these drainage mechanisms has motivated the use of multivalued sliding laws as the basal boundary condition (Lliboutry, 1968; Hutter, 1982; McMeeking and Johnson, 1986; Fowler, 1987b,a; Kamb, 1987). In these the basal velocity is a double or triple valued function of the basal shear stress. More specifically, Fowler and Johnson (1995, 1996) demonstrated that a 'hydraulic runaway' mechanism is suggestive of a triple-valued sliding law, based on the positive destabilising feedback between basal friction and increased meltwater production in a distributed drainage system. Sayag and Tziperman (2009) invoked a switch in drainage system as motivation for a triple-valued sliding law, suggesting that each of two stable branches (where basal stress increases with basal velocity) correspond to different drainage patterns at the bed.

Beneath Antarctica, however, there is generally more evidence for high-water-pressure, distributed drainage (Kamb and Engelhardt, 1991). Therefore, although there is evidence that before an ice stream forms the bed is already at the pressure-melting point in the onset region (e.g., Bindschadler *et al.*, 2000), a switch in drainage systems seems an unlikely reason for ice stream formation. In fact, the Siple coast appears to be underlain by a layer of till (Alley *et al.*, 1986; Blankenship *et al.*, 1986; Tulaczyk *et al.*, 2000a). While the driving stress on Siple coast ice streams is $10 - 20\,\mathrm{kPa}$ (Cuffey and Paterson, 2010; Truffer and Echelmeyer, 2003), Kamb

and Engelhardt (1991) showed through lab tests that the yield stress of underlying sediment is an order of magnitude smaller, and hence the till is unable to support the driving stress. The driving stress must therefore be resisted elsewhere. Physical reasoning suggests lateral shear in the ice stream margins must provide some of this resistance, with only a small fraction balanced by friction at the bed (Kamb, 2001; Jackson and Kamb, 1997; Echelmeyer *et al.*, 1994; Raymond, 1996; Truffer *et al.*, 2001; Hulbe, 2001; Schoof, 2004; Sayag and Tziperman, 2008). A triple-valued sliding law has two stable branches so that the driving stress is balanced by the basal stress in both the slow and fast flow regimes. In contrast, a double-valued sliding law enforces a low basal stress beneath the whole ice stream. One therefore wonders if a double-valued sliding law also allows for ice stream behaviour in a numerical model.

In this chapter we examine the effect these two different sliding laws have on ice stream formation. We use the hybrid model of ice flow that takes into account both membrane stresses and vertical shear stresses, providing a suitable description of ice flow both within and outside of ice streams. Although we do not explicitly model subglacial hydrologic features here, hydrologic mechanisms are an important motivating factor for the relationships between basal stress and basal velocity used. The aim is to learn more about the fundamental stress balances in ice streams.

The chapter is organised as follows: Section 3.2 provides details of the model, describing the basal boundary condition, the model setup and the numerical approach. In Section 3.3 we benchmark the model by applying a triple-valued sliding law at the bed. We extend Sayag and Tziperman's work (Sayag and Tziperman, 2009), investigating the triple-valued sliding law and the flow behaviour it produces in more detail. Section 3.4 considers behaviour under a double-valued sliding law. We find a relationship between governing parameters that allows for the formation of a stable ice stream, held back primarily by membrane stresses. In Section 3.5 we compare results under the two sliding laws and discuss the implications of the vertically integrated,

Symbol	Description	Typical value
x_0	horizontal length scale	200 km
h_0	vertical length scale	1 km
$\varepsilon = \frac{h_0}{x_0}$	aspect ratio of ice sheet	5×10^{-3}
u_0	horizontal velocity scale	$500\,\mathrm{m\,yr^{-1}}$
$t_0 \sim \frac{x_0}{u_0}$	time scale	400 yr
$\tau_0 \sim \rho g h_0 \varepsilon$	basal shear stress scale	45000 Pa
$a_0 \sim \varepsilon u_0$	accumulation rate scale	$2.5\,\mathrm{m\,yr^{-1}}$
$\lambda = \frac{[\tau_b][d]}{[\eta][u]}$	basal to shear stress ratio	0.015

Table 3.1: List of variable scales and non-dimensional parameters in the governing equations. Typical ice sheet scales provide a natural choice of depth, horizontal extent and velocity scales. Remaining scales are chosen by balancing terms in the governing equations. Values of constants are given in Table 1 at the start of the thesis.

higher-order formulation in comparison with the SSA. We make some final comments in Section 3.6.

3.2 Model description

3.2.1 Ice flow equations

We consider the simplification to Stokes flow derived in the previous chapter. The governing equation for conservation of mass is

$$\frac{\partial h}{\partial t} + \boldsymbol{\nabla}\cdot\left(h\mathbf{u}_b - \lambda\frac{h^{n+2}}{n+2}\left|\boldsymbol{\gamma}\right|^{n-1}\boldsymbol{\nabla}s_i\right) = a, \tag{3.1}$$

where

$$\boldsymbol{\gamma} = -\boldsymbol{\nabla}s_i + \frac{\varepsilon^2}{\lambda}\boldsymbol{\nabla}\cdot\mathbf{S}, \tag{3.2}$$

and $\mathbf{S}$ is the resistive stress tensor (Van der Veen, 1999; Hindmarsh, 2012), given by

$$\mathbf{S} = \boldsymbol{\tau} + \mathbf{I}\,\mathrm{trace}\,(\boldsymbol{\tau}) = \begin{bmatrix} 2\tau_{11} + \tau_{22} & \tau_{12} \\ \tau_{12} & \tau_{11} + 2\tau_{22} \end{bmatrix}. \tag{3.3}$$

Equation (3.1) is a depth-integrated equation for conservation of mass. It shows that a change in depth of ice at some point is caused by divergence of the ice flux and the accumulation rate at that point. If $\lambda \to 0$ then ice flux approximates as $h\mathbf{u}_b$ (plug flow) whereas if $\lambda = 1$ the flux corresponds to that for free-surface lubrication flow (as in the SIA).

Conservation of momentum is given by

$$\begin{aligned} \boldsymbol{\tau}_b &= h\boldsymbol{\gamma} \\ &= -h\boldsymbol{\nabla} s_i + \frac{\varepsilon^2}{\lambda} h\boldsymbol{\nabla}\cdot\mathbf{S}, \end{aligned} \tag{3.4}$$

which describes the force balance at the bed. The three terms correspond to basal stress, driving stress and membrane stress contributions respectively. For $\lambda \sim \mathcal{O}(1)$, the membrane stress contribution is small and the balance is largely between the basal and driving stress; for $\lambda \ll 1$ the membrane stress correction plays a more significant role in the stress balance.

3.2.2 Constitutive sliding law

Sliding laws of the form $\boldsymbol{\tau}_b = f(\mathbf{u}_b)$ are long-established. However, because of the strong dependence of basal friction on the effective pressure at the bed, sliding laws of the form $\boldsymbol{\tau}_b = f(\mathbf{u}_b, N)$, where N is the effective pressure at the bed, provide a better description. In the current framework we do not model the basal water pressure; hence we use the first kind, although some dependence on effective pressure is implicitly included in our choice of f.

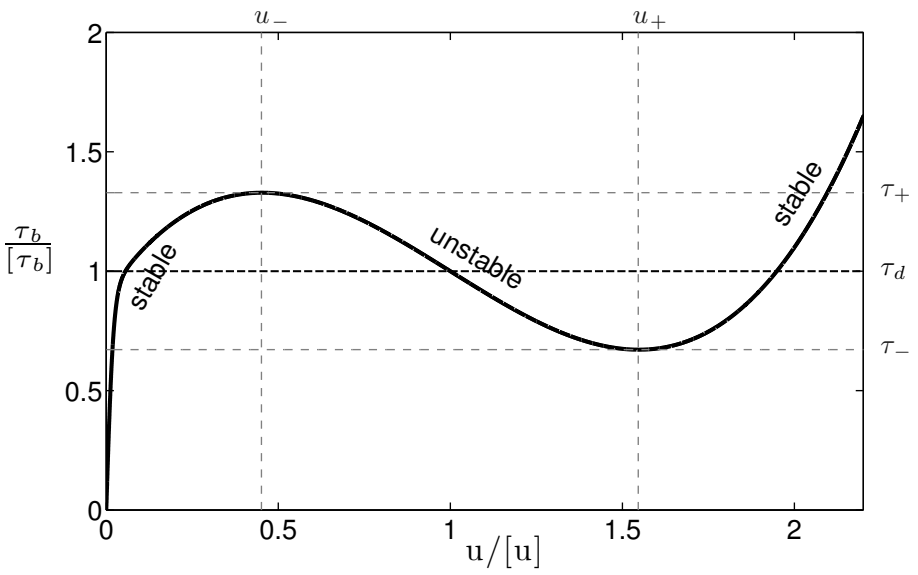

Figure 3.1: A cross-section of the triple valued sliding law, $\tau_b(u, v = 0)$. Based on Sayag and Tziperman (2009), Figure 4.

More specifically, in the first part of this chapter we consider a triple-valued sliding law. Sayag and Tziperman (2009, 2011) developed ideas behind such a sliding law and we adopt their implementation, which is obtained analytically from a simple one-dimensional force balance based on the cross-flow structure of an ice stream. Figure 3.1 illustrates the resulting non-dimensional relationship, given by

$$\boldsymbol{\tau}_b = \frac{\mathbf{u}_b}{|\mathbf{u}_b|}\left[(|\mathbf{u}_b| - 1)^3 + a\,(|\mathbf{u}_b| - 1) + 1\right]\tanh\left(\beta\,|\mathbf{u}_b|\right), \tag{3.5}$$

where a and β are parameters taken to be -0.9 and 50 respectively.

A multivalued sliding law is expected to be unstable on its middle branch where $\partial\tau_b/\partial u_b < 0$ (Lliboutry, 1968, p.55). Consequently, if the stress is gradually increased while on the lower branch to the first maximum in Figure 3.1, a transition must then occur to the upper branch, and this transient must involve the rapid variation of some other dynamical quantity which is implicitly involved in the sliding law. Commonly, this hidden variable is taken to be the subglacial effective pressure, which is also presumed to be the underlying cause of the multi-valuedness (c.f. Fowler, 1987a). We

therefore introduce a new variable ν such that

$$\delta \frac{\partial \nu}{\partial t} = |\mathbf{u}_b| - \nu, \tag{3.6}$$

where δ is a parameter that describes the time scale on which ν relaxes to $\mathbf{u}_b$ i.e. a time scale for the evolution of the subglacial drainage system. This time scale introduces a limit to how rapidly velocities can transition between u_- and u_+.

By replacing $\mathbf{u}_b$ with ν in the part of the triple-valued sliding law that governs the positioning of the unstable branch (the cubic part), we obtain a relationship between basal stress and velocity with some time dependence in it, defining a time scale over which velocity changes in response to changes in basal stress. In particular, taking $\delta = 10^{-3}$ gives a time scale of evolution for the system of 0.4 yrs, given the other scales in Table 3.1.

The triple-valued sliding law hence becomes

$$\boldsymbol{\tau}_b = \frac{\mathbf{u}_b}{|\mathbf{u}_b|} \left((\nu - 1)^3 - \frac{9\,(\nu - 1)}{10} + 1 \right) \tanh\left(50\,|\mathbf{u}_b|\right). \tag{3.7}$$

We propose that sliding laws of the form $\boldsymbol{\tau}_b = f(\mathbf{u}_b)$ which express a physically unstable relationship between τ_b and u_b should be replaced with those of the form $\boldsymbol{\tau}_b = f(\mathbf{u}_b, \nu)$. This also helps with numerical solves of the system, since introducing this time sale for evolution prevents rapid transitions in velocity with time, which are difficult to capture numerically.

3.2.3 Model setup

Figure 3.2 shows the 3D model setup. There is zero inflow into the domain at $x = 0$, implemented by setting $u_b = 0$ and $\partial s_i / \partial x = 0$; the latter imposes zero flow due to vertical shear at $x = 0$. Free slip is allowed along the boundary ($\tau_{12} = 0$). To avoid considering grounding-line behaviour, we treat $x = 1$ as an open outflow boundary

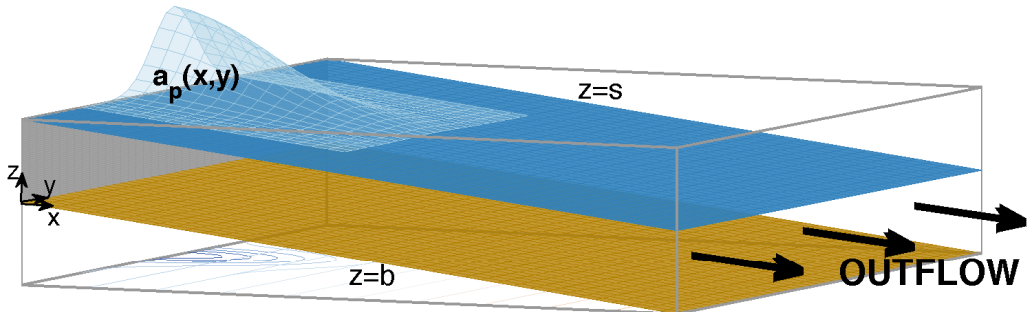

Figure 3.2: Schematic illustrating the model setup. The bed is flat, and with constant slope. The surface is also flat initially before a constant perturbation to the accumulation field is applied in the form of a Gaussian blob, $a_p(x, y)$, as illustrated. There is zero inflow at the $x = 0$ boundary.

(Papanastasiou *et al.*, 1992; Sayag and Tziperman, 2009), where the upper surface is free to evolve and $\partial u/\partial x = 0$. The domain is periodic in the y-direction.

The simulations are initialised in a steady state that is uniform in the cross-flow direction. Downstream of the inflow boundary the ice has a constant thickness $h = 1$. There is no variation in velocity in the cross-flow direction i.e. $(u, v) = (u(x), 0)$. Under these conditions, the velocity field can be computed from (3.4), with $\nu = |\mathbf{u}_b|$ in the steady state. A background 'balance' accumulation, $a_b(x)$, is required to maintain the steady state. This balance accumulation is the steady-state solution of (3.1), given by

$$a_b(x, y) = \frac{\partial u_b}{\partial x}. \tag{3.8}$$

A forcing is required to produce ice stream behaviour. A perturbation accumulation, $a_p(x, y)$, is therefore also applied, in the form of a truncated Gaussian at the upper boundary, motivated by Sayag and Tziperman (2009). More specifically, $a_p(x, y)$ is given by

$$a_p(x, y) = A_0 \exp\left(-25x^2 - 100\left(y - \frac{1}{2}\right)^2\right), \tag{3.9}$$

where A_0 is the magnitude of the perturbation. The magnitudes used are necessarily large, but can be thought of as representing the sum of accumulation rates from upstream. Use of such a forcing provides a simple way of reproducing ice stream behaviour, which allows us to study the resulting downstream flow regimes.

3.2.4 Numerical Solution

We discretise the governing equations and boundary conditions using a finite-volume scheme with semi-implicit time stepping. We use a two-dimensional, staggered, Cartesian grid with $n_i \times n_j$ discrete points (Rommelaere and Ritz, 1996; Sayag and Tziperman, 2009). An upwind difference scheme is implemented at the open outflow boundary together with the condition $\partial u_b/\partial x = 0$ (Sayag and Tziperman, 2009). The nonlinear system of equations is solved using a Newton-Krylov solver, provided by the Portable Extensible Toolkit for Scientific Computation (Balay *et al.*, 1997, 2013, 2014). The fully coupled system is inverted at each time step, and the solution is accepted when the absolute size of the nonlinear system residual is less than 10^{-8}. To aid numerical solution, if this condition is not satisfied after 50 iterations, we split the equations into two groups ((3.1) and (3.6) in one, and the components of (3.4) in the other) and solve them iteratively using a Picard iteration with a subspace correction (Hindmarsh and Payne, 1996).

Values of constants are given in Table 3.1. The value of the maximum time step must always be smaller than the relaxation time scale defined by δ so that changes in velocity are not limited by the size of the time step.

Note that an alternative setup, together with some basic results, is discussed in appendix A2.

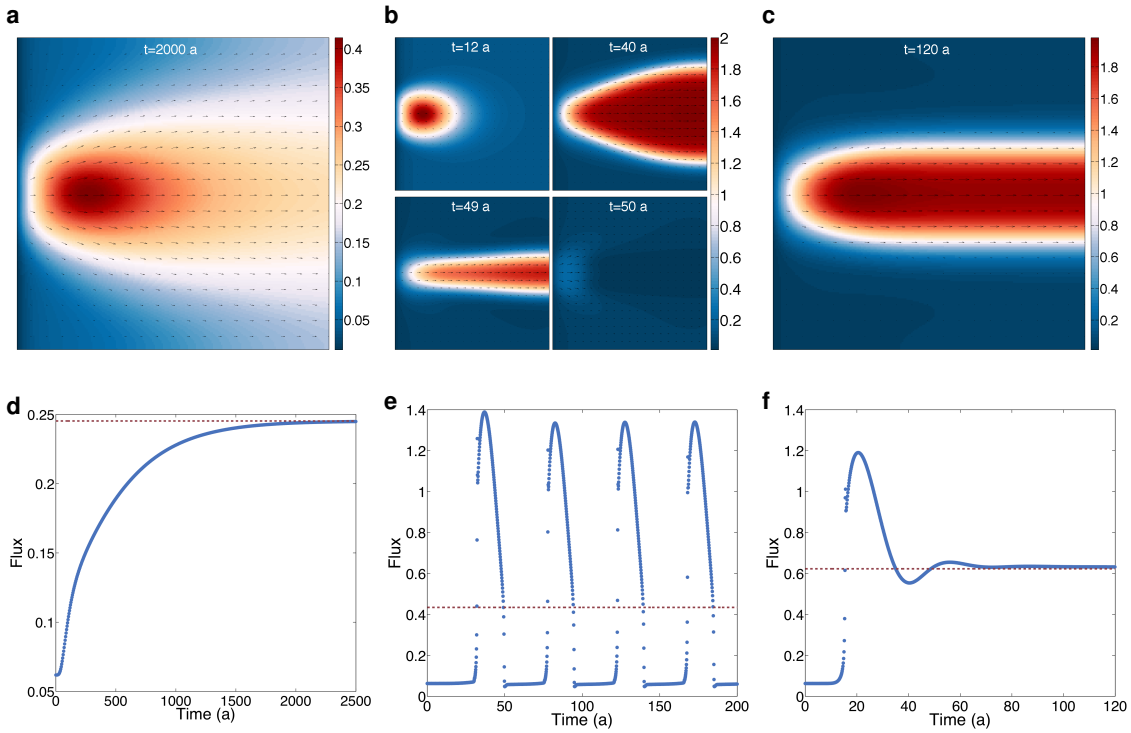

Figure 3.3: Simulation results for three different incoming mass flux values ($A_0 = 15, 30, 45\,\mathrm{m\,yr^{-1}}$ respectively). The plots in the top row are illustrations of the velocity fields and the plots on the bottom row show time series of the total flux out of the solution domain (blue dots plotted at regular time intervals) with the total incoming flux also plotted (red dashed line).

3.3 Results with a triple-valued sliding law

3.3.1 Reference flow regimes at small λ

In order to assess the suitability of the model for describing ice dynamics in and outside of ice streams, we apply the triple-valued sliding law as the basal boundary condition in the set-up described in Section 3.2.3. The ice rheology is taken to be Newtonian, to compare results with Sayag and Tziperman (2009).

Figure 3.3 shows the three distinct flow regimes that occur as a result of varying the magnitude of the perturbation accumulation A_0. Other parameter values are given in Table 3.1.

In Figure 3.3a, for a small value of A_0, the solution reaches a steady state in which

the velocities all fall on the slow, stable branch of the sliding law and the influx is dispersed across the domain. Figure 3.3d shows the evolution of the total flux out of the domain, which reaches a steady-state after approximately 2000 yrs.

In Figure 3.3b, for a slightly larger value of A_0, solutions oscillate between slow-flow and fast-flow behaviour. Initially the velocity field falls entirely on the slow branch of the sliding law. As the accumulation builds up near the inflow boundary, increasing the surface slope, the velocity moves to the fast stable branch of the sliding law and an ice stream forms downstream of the perturbation. The ice stream evolves, drawing down the additional upstream mass-accumulation until there is no longer a driving stress sufficient to maintain the stream. The ice stream narrows before collapsing back to its no-stream state. The cycle then repeats.

Finally, in Figure 3.3c, increasing the magnitude of the perturbation accumulation A_0 further results in sustained flow on the fast, stable branch of the sliding law. A steady-state stream forms, with different regions of the domain on different branches of the sliding law.

These are the same three distinct flow regimes that were reported by Sayag and Tziperman (2009), who used the same setup but solved the shallow shelf approximation. The regimes illustrated in Figures 5-7 in their work directly correspond to those shown in Figure 3.3 here. We have neglected to include the depth fields and cross-stream velocity profiles as the most interesting behaviour is captured in the plots included here. Quantitative differences occur between our results and theirs for a given accumulation perturbation, due to the use of a higher-order formulation in our work, which accounts for vertical variation in horizontal velocities. Particularly in regions of low basal velocity, the added component of velocity at the ice surface due to vertical shear is significant, and results in larger outflow from the domain for a given basal velocity. A further difference arises from the addition of the parameter ν into the sliding law (equation 3.7). It makes our solver convergence more rapid and

more robust. Moreover, the jumps in velocity in the solutions are less rapid and the overall behaviour is smoother, as can be seen by direct comparison of Figures 3.3e and 3.3f with Figures 7a and 6a respectively in their paper. Setting $\delta = 0$ (i.e. taking $\nu = |\mathbf{u}_b|$), results in behaviour as seen in Sayag and Tziperman (2009), with rapid jumps in flux when the solution moves across the unstable branch of the sliding law (e.g. in the region $11 - 12\,\text{yrs}$ in Figure 6a of their paper).

3.3.2 Effect of variations in λ

Having verified in Section 3.3.1 that our formulation reproduces the three flow regimes obtained by Sayag and Tziperman (2009), we diverge from their study to look at the effect of including vertical variation in horizontal velocity due to gravity-driven shear. We do so by varying the scaling parameter λ, corresponding to the basal-to-shear-stress ratio, and looking at the impact on emergent ice stream behaviour. A value of $\lambda \ll 1$ corresponds to attributing most of the movement to sliding when considering the stress balance (as in the SSA), while $\lambda = 1$ corresponds to assuming that all velocity is due to vertical shear, as in the SIA. Intermediate values correspond to various different proportions of the velocity being attributed to sliding when considering the stress balance.

3.3.2.1 Shear margin width

The value of λ affects the characteristics of an ice stream that forms under this formulation. We consider a simple model of an ice stream where the cross-stream velocity component v is zero, and u only varies in the cross-stream direction (Sayag and Tziperman, 2011). Figure 3.3c shows this to be a fair description for a steady state ice stream downstream of the onset zone.

Under these simplifications, the only non-trivial, non-dimensional governing equa-

tion is

$$\tau_{bx} = -h\frac{\partial s_i}{\partial x} + \frac{\varepsilon^2}{\lambda}h\frac{\partial}{\partial y}\left(\frac{1}{\tau^{n-1}}\frac{\partial u_b}{\partial y}\right), \tag{3.10}$$

where

$$\tau^2 = \tau_{13}^2 + \frac{\varepsilon^2}{\lambda^2}\tau_{12}^2, \tag{3.11}$$

Assuming that vertical shear is negligible compared with lateral shear in the stream itself, we have $\tau_{13} \ll \frac{\varepsilon}{\lambda}\tau_{12}$. This assumption means τ^2 can be approximated as $(\varepsilon^2/\lambda^2)\,\tau_{12}^2$, giving

$$\tau^{n-1} = \left|\frac{\varepsilon}{\lambda}\frac{\partial u_b}{\partial y}\right|^{1-\frac{1}{n}}. \tag{3.12}$$

We now seek the distance W_m corresponding to the velocity drop ΔU across the shear margin. Assuming a balance between the driving stress and horizontal shear in the margins, we obtain the relation

$$(W_m)^{1+\frac{1}{n}} \sim \frac{\varepsilon^{1+\frac{1}{n}}}{\lambda^{\frac{1}{n}}}\,(\Delta U)^{\frac{1}{n}}\,. \tag{3.13}$$

Now the value of ΔU is enforced by the triple-valued sliding law (and corresponds to $(u_+ - u_-)$ in Figure 3.1). The shear margin must therefore obey

$$W_m(n,\lambda) = \varepsilon K_1^{\frac{n}{n+1}}\left(\frac{K_2}{\lambda}\right)^{\frac{1}{1+n}} \tag{3.14}$$

for constants K_1 and K_2.

Taking logarithms of (3.14) gives

$$\log(W_m) = \log(\varepsilon) + \frac{n}{n+1}\log(K_1) + \frac{1}{n+1}\log(K_2) - \frac{1}{n+1}\log(\lambda) \tag{3.15}$$

suggesting that a logarithmic plot of W_m against λ should give a straight line with gradient $-1/(n+1)$.

Figure 3.4 is a plot of margin width against λ from results from simulations run

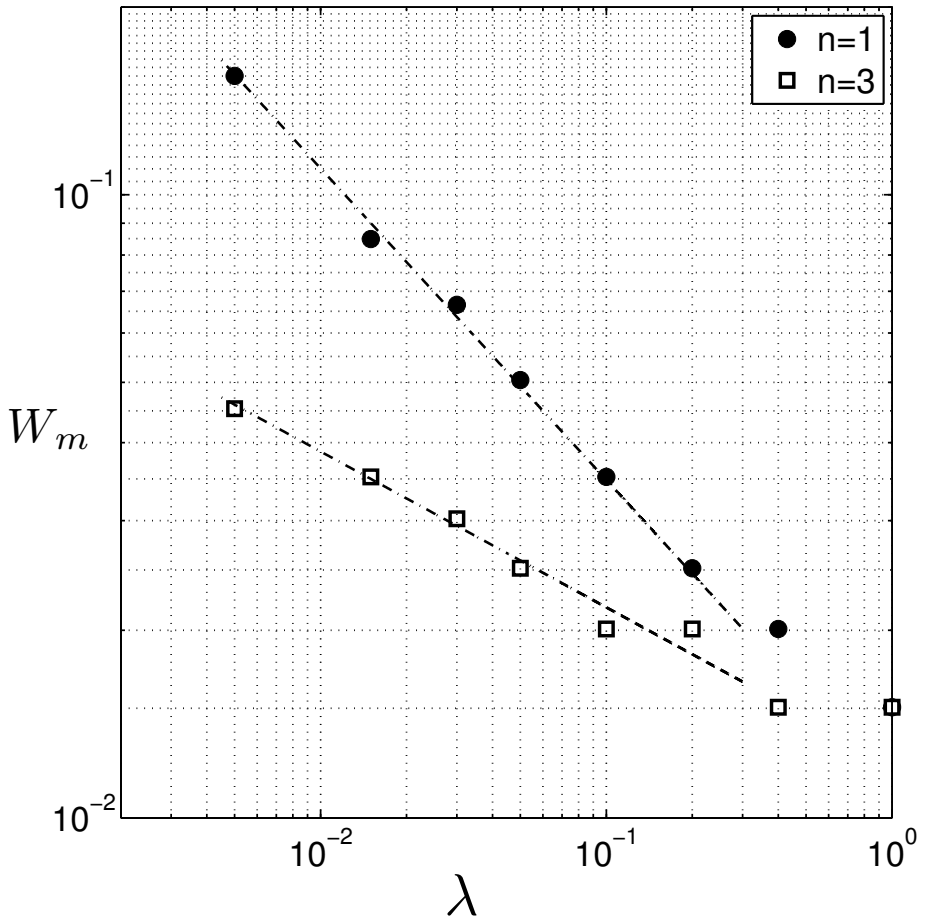

Figure 3.4: A plot illustrating the relationship between the width of the shear margin of an ice stream varies and the scaling parameter λ. Results from simulations run with $n = 1$ and $n = 3$ are both plotted, where n is Glen's flow law exponent. Dashed lines with gradient $-1/(n + 1)$ are also plotted.

on a 200×200 grid. The margin width is estimated by counting the number of grid cells with velocity in the range $u_- < |\mathbf{u}_b| < u_+$ through a cross-section of the domain, and calculating the width accordingly. The circles correspond to Newtonian viscosity ($n = 1$), and the squares to non-Newtonian viscosity ($n = 3$). Lines with gradients $-1/2$ and $-1/4$ are plotted through the Newtonian and non-Newtonian points respectively. The horizontal grid lines are plotted at intervals of the grid spacing in the simulations. The margin width decreases as λ increases, since membrane stresses play a less dominant role in the stress balance. Without membrane stresses, large jumps in velocity are allowed to occur over a small distance. Moreover, when the margin width is small and spans only two or three grid points, it can only take one of a few discrete values, given the choice of resolution. We therefore see that the lines with gradient $-1/(n+1)$ in Figure 3.4 are a very good fit to the plotted points, only losing accuracy for numerically unresolved margin widths.

3.3.2.2 Flow regimes

We also address the question of how the choice of λ affects flow behaviour across all flow regimes with an ensemble of simulations. Values of λ and A_0 are different in each simulation. Figure 3.5 maps the resulting flow regimes for different parameter combinations. All three distinct flow regimes occur, each plotted with a different marker; the divides between flow regimes in parameter space are shaded and labelled numerically. We discuss each of these boundaries and explain the physical processes that govern where the boundaries lie in parameter space.

Boundaries 1 and 2 separate solutions that remain at all times on the slow stable branch of the sliding law (dark circles in Figure 3.5) and those that exhibit some oscillatory or streaming behaviour (grey diamonds and white squares in Figure 3.5, respectively). The minimum perturbation to the accumulation field large enough to cause the flow to move onto the fast branch of the sliding law occurs at $\lambda \approx 0.1$. For

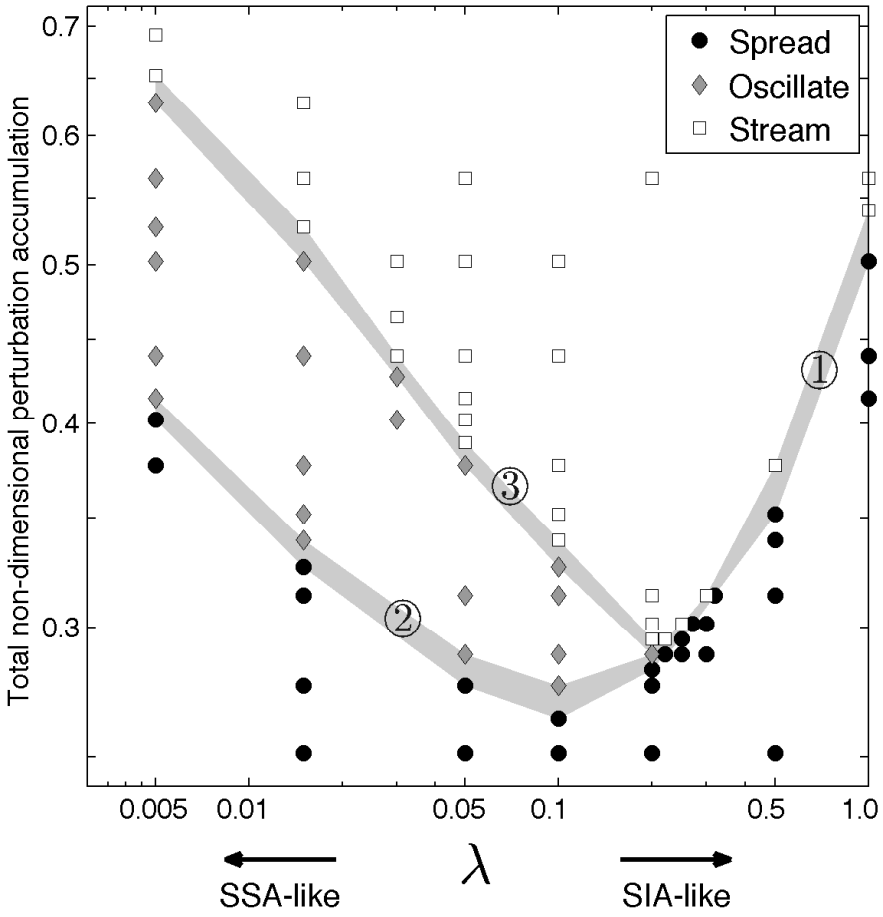

Figure 3.5: Phase diagram showing three discrete regions for slow, fast and oscillatory behaviour. Each point plotted represents one simulation that was run with specified values of λ and A_0.

$\lambda < 0.1$ the required size of the perturbation accumulation increases as λ decreases further (divide 2) and similarly, for $\lambda > 0.1$, the size of a_p must be increased further for there to be any solutions that exhibit fast-flow behaviour (divide 1).

In a bid to explain these observations we must ask what the necessary conditions for the flow to enter the fast-flow regime are. As a result of implementing the triple-valued sliding law, the basal stress must reach a critical value τ_+ (see Figure 3.1) before transitioning onto the unstable branch of the sliding law. Equation (3.4) describes a balance between basal stress and driving stress, with a correction of $\mathcal{O}(\varepsilon^2/\lambda)$ due to membrane stresses. For expository simplicity, we write it as

$$(\text{basal stress}) = (\text{driving stress}) + \frac{\varepsilon^2}{\lambda}\,(\text{depth-integrated membrane stress gradients})\,. \tag{3.16}$$

When $\lambda \sim 1$ the correction for membrane stress effects is $\mathcal{O}(\varepsilon^2)$ and so to $\mathcal{O}(\varepsilon^2)$ accuracy the balance is between driving and basal stress, as in the SIA. When the driving stress in the onset region reaches the critical value τ_+ the transition onto the unstable branch of the sliding law occurs and there is resulting fast-flow behaviour. The correction for membrane stresses, however, becomes more significant for smaller values of λ and so influences how large the driving stress ($-h\partial s_i/\partial x$) needs to become before the basal stress reaches the critical value. In turn, the rate at which the accumulation builds up in the onset zone controls this increase in driving stress. The build-up further depends on the rate at which the incoming ice is drawn downstream. We hence consider the non-dimensional flux out of the domain, which in the Newtonian case, with $\partial b/\partial x = -1$ and non-dimensional depth $h \approx 1$ (an accurate approximation for ice streams which form in this suite of simulations), is given by

$$\begin{aligned} q_x &= \int_0^1 \left[u_b(1,y) + \frac{\lambda}{3}\right] \mathrm{d}y \\ &\approx U_s W_s + \frac{\lambda}{3} \end{aligned} \tag{3.17}$$

where U_s is the transversley-averaged stream velocity and W_s the width of the ice stream. It is evident that, when $\lambda \sim \mathcal{O}(1)$, the increased flux due to vertical shear can be significant, whereas when λ is small this effect is insignificant.

For boundary 1 in Figure 3.5, $\lambda \gtrsim 10^{-1}$, and hence the membrane stress correction in (3.16) is negligible. Equation 3.17 shows that as λ increases there will be a resultant increase in outflow from the domain for a given basal velocity. For a given basal velocity field, more ice is therefore removed with higher values of λ; hence less ice accumulates in the onset region where the accumulation perturbation is applied. A larger a_p is required at higher λ for the driving stress to reach the critical value to cause transition onto the unstable branch of the sliding law (τ_+ in figure 3.1). This explains the positive gradient of curve 1 for $\lambda \gtrsim 10^{-1}$.

The curve defining boundary 2 in Figure 3.5, in contrast, has a negative gradient. For smaller values of λ, the flow velocities remain completely on the slow branch of the sliding law for much larger accumulation rates. At these lower values of λ, $\lambda/3$ is small and so the outflow (3.17) depends only on u_b. It is necessary then to consider the effect of the membrane stress correction in the stress balance (3.16). While for $\lambda \gtrsim 10^{-1}$ the dominant balance is between the basal stress and the driving stress, as λ decreases further, the $\mathcal{O}(\varepsilon^2/\lambda)$ correction in (3.16) becomes more significant. The greater accumulation in the onset region causes the driving stress to increase. The increasing velocity in the onset region results in large negative gradients in the longitudinal stress, since the velocities downstream are lower. The $\mathcal{O}(\varepsilon^2/\lambda)$ correction is therefore negative, meaning that the driving stress needs to reach larger values before the RHS of (3.16) will reach the critical value τ_+ at which the transition to the unstable branch of the sliding law will occur. This effect is only further amplified as λ decreases further, and so larger perturbations to the accumulation field are required to reach the higher driving stresses that result in oscillatory/streaming behaviour. This explains the negative gradient of the curve separating the slow flow

behaviour and oscillatory/streaming behaviour for $\lambda \lesssim 10^{-1}$. Since lower values of λ correspond to a stress balance where membrane stresses are of increased significance, this result emphasises the important effect membrane stresses can play in inhibiting the emergence of ice streams.

Finally we consider what governs boundary 3, which separates flow that periodically surges from those solutions that form a steady-state stream. There is no oscillatory flow once this boundary intersects boundary 1, for $\lambda \gtrsim 0.2$. For a steady-state stream to exist, the outflow from the domain must balance the incoming mass accumulation perturbation $\int\int a_p(x,y)\,\mathrm{d}x\,\mathrm{d}y$. Equation (3.9) gives an expression for a_p that can be integrated:

$$\begin{aligned} \int\int a_p(x,y)\,\mathrm{d}x\,\mathrm{d}y &= \int_0^1\int_0^1 A_0 e^{-25x^2-100\left(y-\frac{1}{2}\right)^2}\,\mathrm{d}x\,\mathrm{d}y \\ &\approx \frac{\pi A_0}{100}, \end{aligned} \tag{3.18}$$

giving the total incoming perturbation accumulation.

Equating the outflow (3.17) and the incoming mass accumulation (3.18) gives

$$\frac{\pi A_0}{100} = U_s W_s + \frac{\lambda}{3}. \tag{3.19}$$

Equation (3.19) gives the necessary condition that must be satisfied for a solution to form an ice stream. As mentioned previously, U_s is determined by the triple-valued sliding law, therefore the solution will only form a steady-state stream if there is enough incoming mass accumulation to maintain a stream of some width W_s; if there is not, the solution will oscillate. Given that the flux in a stream is given by (3.17), why then does a solution with a smaller value of λ need more accumulation before a steady-state stream can form? It is due to the fact that a smaller value of λ results in stresses being delocalised and so results in wider shear margins, as discussed

in Section 3.3.2.1. We therefore have a wider strip of the domain flowing at higher velocities and hence greater outflow from the domain at smaller λ. Consequently more incoming mass accumulation is required with smaller values of λ to be able to maintain the resulting wider streams.

3.4 Results with a double-valued sliding law

While there are physical mechanisms involving meltwater drainage feedbacks that motivate the choice of a triple-valued sliding law (Fowler and Johnson, 1995; Sayag and Tziperman, 2009), some of these effects are more common on a seasonal time scale and hence probably more relevant as controlling mechanisms for seasonal surges (e.g., Schoof, 2010). In Antarctica, studies suggest the till behaves more like a plastic material with a yield stress (Alley *et al.*, 1986; Blankenship *et al.*, 1986). The triple-valued sliding law does not represent such behaviour well; Figure 3.6 illustrates that under the triple-valued law, the modelled basal stress beneath an ice stream is as high as that outside the stream.

McMeeking and Johnson (1986) suggested a sliding law such as curve (2) in Figure 3.6a would be a good way of representing physical processes occurring at the bed. The existence of a critical velocity (u_-) at which the base fails was one possible explanation they provided, along with the possibility of the high stresses at a surge front disrupting the in situ drainage system, perhaps closing off a channelised system.

We run some simple experiments with a doubled-valued sliding law as our basal boundary condition to investigate the stress balances in ice streams that slide over a base capable of supporting only low stresses ($\leq \tau^Y$) at high velocities. One might think that the ice stream could now run away due to the low basal resistance at the bed, but in practice this does not happen; the driving stress is instead resisted by lateral shear stresses in the ice stream margins.

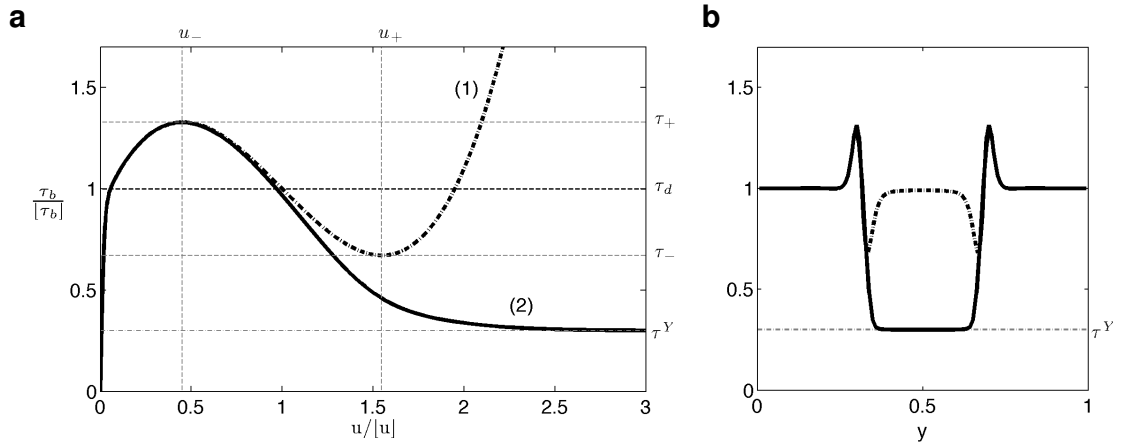

Figure 3.6: Comparisons between the triple-valued and double-valued sliding laws. In (a) cross-sections of the triple-valued sliding law (dashed line) and double-valued sliding law (solid line) are plotted. In (b) there is a schematic of the cross-stream basal stress profiles ($\tau_b(u, v = 0)$). They are taken across an ice stream formed with the triple-valued sliding law (dashed line) and the double-valued sliding law (solid line) as the basal boundary conditions.

For ease of comparison, and to enable use of the same model set-up, we formulate a sliding law using tanh functions to reshape the function given by equation (3.7). Given that our triple-valued law can be written as $\boldsymbol{\tau}_b = \frac{\mathbf{u}_b}{|\mathbf{u}_b|} f\left(\nu, |\mathbf{u}_b|\right)$, we have

$$\boldsymbol{\tau}_b = \frac{\mathbf{u}_b}{|\mathbf{u}_b|}\left[\frac{1}{2} f\left(\nu, |\mathbf{u}_b|\right)\left(1 - \tanh(3\nu - 4.5)\right) + \frac{1}{2}\tau^Y\left(1 + \tanh(3\nu - 4.5)\right)\right], \tag{3.20}$$

where ν is as defined in equation 3.6. Figure 3.6a is a plot of this function alongside the original triple-valued function (dashed line).

3.4.1 Steady-state ice stream solutions

To see the effect of using a double-valued sliding law on ice stream formation, we ran a set of simulations similar to those in Section 3.3. For small accumulation perturbations these exhibit the same behaviour as with a triple-valued sliding law (as expected

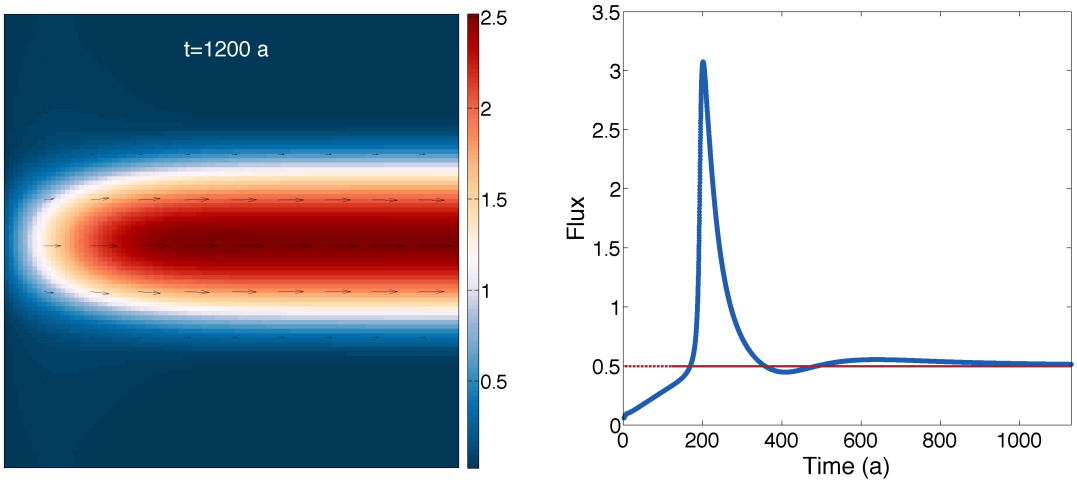

Figure 3.7: An example simulation for which a steady state stream forms with $n = 1$, $\lambda = 0.005$, $\tau^Y = 0.3$, $A_0 = 35\,\mathrm{m\,yr^{-1}}$, $\delta = 0.1$ and all other parameter values given in table 1.

due to the sliding laws overlying each other at low velocities). It is the behaviour on the unstable branch that is of interest; under what parameter combinations can a stable stream-like solution be maintained?

Experimentation shows that a solution to the governing equations resulting in a steady-state stream is not always possible, given certain combinations of parameters. Streams that form increase in velocity rapidly (there are insufficient stresses to hold them back) and since there is limited incoming accumulation a balance is not possible—i.e. (3.19) cannot be satisfied and so the code stops converging unless membrane stresses increase quickly enough to hold back the stream. As such, only under very specific combinations of parameters does a fully coupled non-linear evolution of the governing equations with the double-valued sliding law (3.20) reach a steady-state stream solution. Figure 3.7 gives an example of one solution resulting in a steady state Newtonian stream.

Note that there are a number of parameters in the sliding law neither constrained by observations or directly related to the physics, for example: the smoothing parameter δ and the magnitude of the accumulation perturbation. Other parameters

such as τ_Y and τ_+ (the high velocity basal stress limit and the value of the basal stress at the peak of the sliding law respectively) can be somewhat constrained by observations and associated calculations of basal stress values in ice-streaming regions (e.g. Joughin *et al.*, 2004). Nevertheless, the large parameter space means it is difficult to choose the most representative values of all the parameters.

3.4.2 A simple model for an ice stream underlain by weak till

To determine the parameter combination needed for a steady-state stream to form under the double-valued sliding law, we consider a simple model of an ice stream and ascertain the balance of terms when the basal stress is not providing full resistance to the stream. The cross-stream velocity component is taken to be zero ($v = 0$) and u is taken to vary only in the cross-stream direction (i.e. u is just a function of y, as for the shear-margin-width scaling in Section 3.3.2.1). The domain is taken to be of constant depth $h = 1$ and so $\boldsymbol{\nabla} s_i = \boldsymbol{\nabla} b = (-\alpha, 0)$. $\alpha = 1$ is used for the simulations run in this paper but we carry out this scaling analysis for the most general case.

Under these simplifications the only non-trivial governing equation is

$$\tau_{bx} = \alpha + \frac{\varepsilon^2}{\lambda} \frac{\partial}{\partial y} \left(\frac{1}{\tau^{n-1}} \frac{\partial u_b}{\partial y} \right), \tag{3.21}$$

where

$$\tau^2 = \tau_{13}^2 + \frac{\varepsilon^2}{\lambda^2} \tau_{12}^2. \tag{3.22}$$

As for the shear-margin-width scaling, vertical shear within the stream is taken to be negligible compared with lateral shear across the margins, meaning that τ^2 can be approximated as $(\varepsilon^2/\lambda^2)\,\tau_{12}^2$ and

$$\tau^{n-1} \approx \left| \frac{\varepsilon}{\lambda} \frac{\partial u_b}{\partial y} \right|^{1-\frac{1}{n}}. \tag{3.23}$$

We also assume a yield stress of the basal sediment beneath the ice stream, denoted by τ^Y. Hence $\tau_{bx} = \tau^Y$ in

$$\tau^Y \approx \alpha + \frac{\varepsilon^{\frac{1}{n}+1}}{\lambda^{\frac{1}{n}}} \frac{\partial}{\partial y} \left(\left| \frac{\partial u_b}{\partial y} \right|^{\frac{1}{n}-1} \frac{\partial u_b}{\partial y} \right). \tag{3.24}$$

Integrating (3.24) in y and applying the centreline condition ($\partial u_b/\partial y = 0$ at $y = 0$), we get

$$\left| \frac{\partial u_b}{\partial y} \right|^{\frac{1}{n}-1} \frac{\partial u_b}{\partial y} = \left(\frac{\lambda}{\varepsilon} \right)^{\frac{1}{n}} \frac{1}{\varepsilon} \left(\tau^Y - \alpha \right) y. \tag{3.25}$$

Assuming the fastest velocity is at the centre of the ice stream, this simplifies to

$$\frac{\partial u_b}{\partial y} = -\frac{\lambda}{\varepsilon^{n+1}} \left| \tau^Y - \alpha \right|^n |y|^{n-1} y, \tag{3.26}$$

and so we now have

$$u_b = u_b(0) - \frac{\lambda}{\varepsilon^{n+1}} \frac{\left| \tau^Y - \alpha \right|^n |y|^{n+1}}{n+1}. \tag{3.27}$$

This describes a velocity profile across an ice stream under our model formulation with a double-valued sliding law.

Furthermore, defining W_s to be the width of an ice stream, $u_b\left(\pm\, W_s/2\right) = u_\infty$ to be the basal velocity outside of that ice stream (usually close to zero), and taking $\Delta U = u(0) - u_\infty$, results in

$$\Delta U = \frac{\lambda}{\varepsilon^{n+1}} \frac{\left| \tau^Y - \alpha \right|^n}{n+1} \left(\frac{W_s}{2} \right)^{n+1} \tag{3.28}$$

as a relationship between the non-dimensional velocity change between the inside and outside of the stream and the non-dimensional width of the ice stream, the basal yield stress of the underlaying till, the bedslope, and the controlling parameters λ and ε. This is the well-known result for the parabolic velocity cross-profile of an ice stream (e.g., Van der Veen, 1999; Raymond, 1996), but also includes the dependence on the

controlling model parameters ε and λ.

For example, given ice with non-Newtonian rheology ($n = 3$), and taking our typical scalings for an ice sheet $\varepsilon = 0.005$ and $\lambda = 0.015$ (see table 1) we have

$$\Delta U = \left(3.75 \times 10^5\right) \left|\tau^Y - \alpha\right|^3 W_s^4. \tag{3.29}$$

Typical driving stresses for pure ice streams are in the region of $10 - 20\,\mathrm{kPa}$ (Raymond, 1996; Truffer and Echelmeyer, 2003) with basal stresses of $\sim 1 - 10\,\mathrm{kPa}$ (Sayag and Tziperman, 2009). Taking $\left|\tau^Y - \alpha\right| \sim 10^{-1}$, we get the result that ice streams with velocities in the range $10^2 - 10^3\,\mathrm{m\,yr^{-1}}$, as in the Siple Coast, will be between approximately 30 km and 60 km wide, which is in agreement with observations (e.g., Cuffey and Paterson, 2010).

Furthermore, in Section 3.4.1 we experimented with simulations using Newtonian rheology ($n = 1$), $\alpha = 1$, $\tau^Y = 0.3$ and varying values of λ and accumulation magnitude. Equation (3.28) suggests they therefore should obey

$$\Delta U = 3500 \lambda W_s^2; \tag{3.30}$$

we therefore illustrate this behaviour with a plot of ΔU against λW_s^2 in Figure 3.8. The deviation from the scaling is due to numerical inaccuracies as the width of the ice stream is very sensitive to numerical resolution. The simulations for Figure 3.8 were run with $n_i = n_j = 100$.

It is important to note that the simulations run to create this figure do not all necessarily lie within physical parameter space—the velocities span a much wider range than that found in nature. Moreover, this scaling explains why there is such sensitivity to changes in parameters. Given a certain basal stress underneath the stream, the membrane stresses are only sufficient to hold back the stream if the combination of parameters chosen do satisfy (3.28). Given the limited size of our

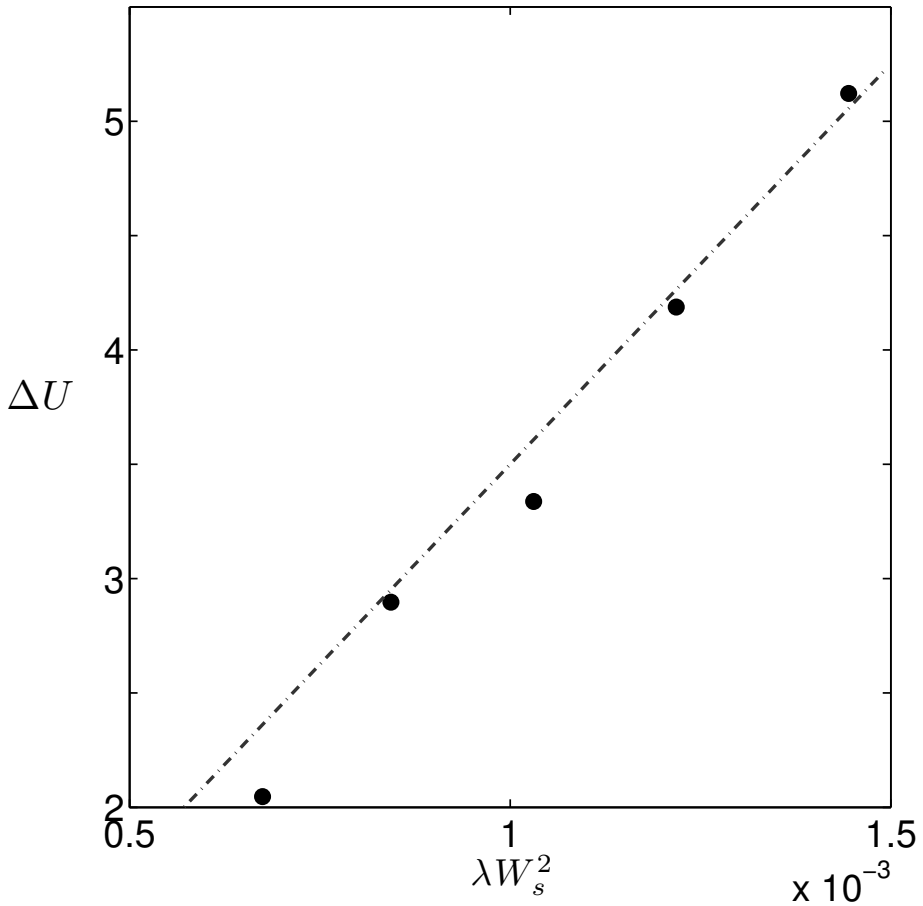

Figure 3.8: A plot of ΔU against λW_s^2 It shows the fit of our results to the scaling ($\Delta U = 3500\lambda W_s^2$ is the line plotted).

domain (with enforced periodicity across the domain) and the defined size of the accumulation perturbation (3.9), there is not much variation allowed in the width of an ice-stream that forms in our model. For example, if the accumulation perturbation is very large and the value of λ not set to be larger accordingly, then the system is unable to reach a steady-state as there is a limit to how wide the stream may become.

3.5 Discussion

3.5.1 Comparison of stress fields under the two sliding laws

We now consider in detail the stress balances in ice streams that occur as a result of contrasting sliding laws. Figure 3.9 shows cross-stream velocity profiles for streams formed under both triple-valued and double-valued sliding laws, and the corresponding plots of the magnitude of basal stress and lateral shear stress.

Figure 3.9a illustrates how the cross-stream velocity profile changes with variation in λ under the triple-valued sliding law. Narrowing of the shear margins at higher values of λ, as discussed in Section 3.3.2.1, can be clearly seen.

Figure 3.9b shows how the corresponding distribution of the basal stress changes with variations in λ. As λ decreases, increasing the significance of the membrane stresses in the stress balance, the delocalising effect of the membrane stresses means the basal stresses do not increase back to the stable value within the width of the ice stream. Only at higher values of λ, when the margins are narrower, do the basal stresses rapidly increase to be in balance with the driving stress. The behaviour of the basal stress within the shear margin itself is complex. The stress field at first increases while moving from the slow flow region into the stream, corresponding to an increase in τ_b from the intersection point of the stable branch of the triple-valued sliding law with the line $\tau_b = \tau_d$ to the value of τ_+ at the peak of the sliding law. It then decreases rapidly as the velocity increases to the inner ice stream velocity, consistent with a decrease in basal stress along the unstable branch of the sliding law. This does provide a physically plausible profile if we assume that outside of the ice stream the bed is frozen, and across the shear margin there is a transition to temperate bed conditions, due to the increased internal and frictional heating as velocities rapidly increase (Schoof, 2012). The fast-flowing ice in the stream results in large horizontal shear across the margin (seen in Figure 3.9c) and the basal friction increases due to the

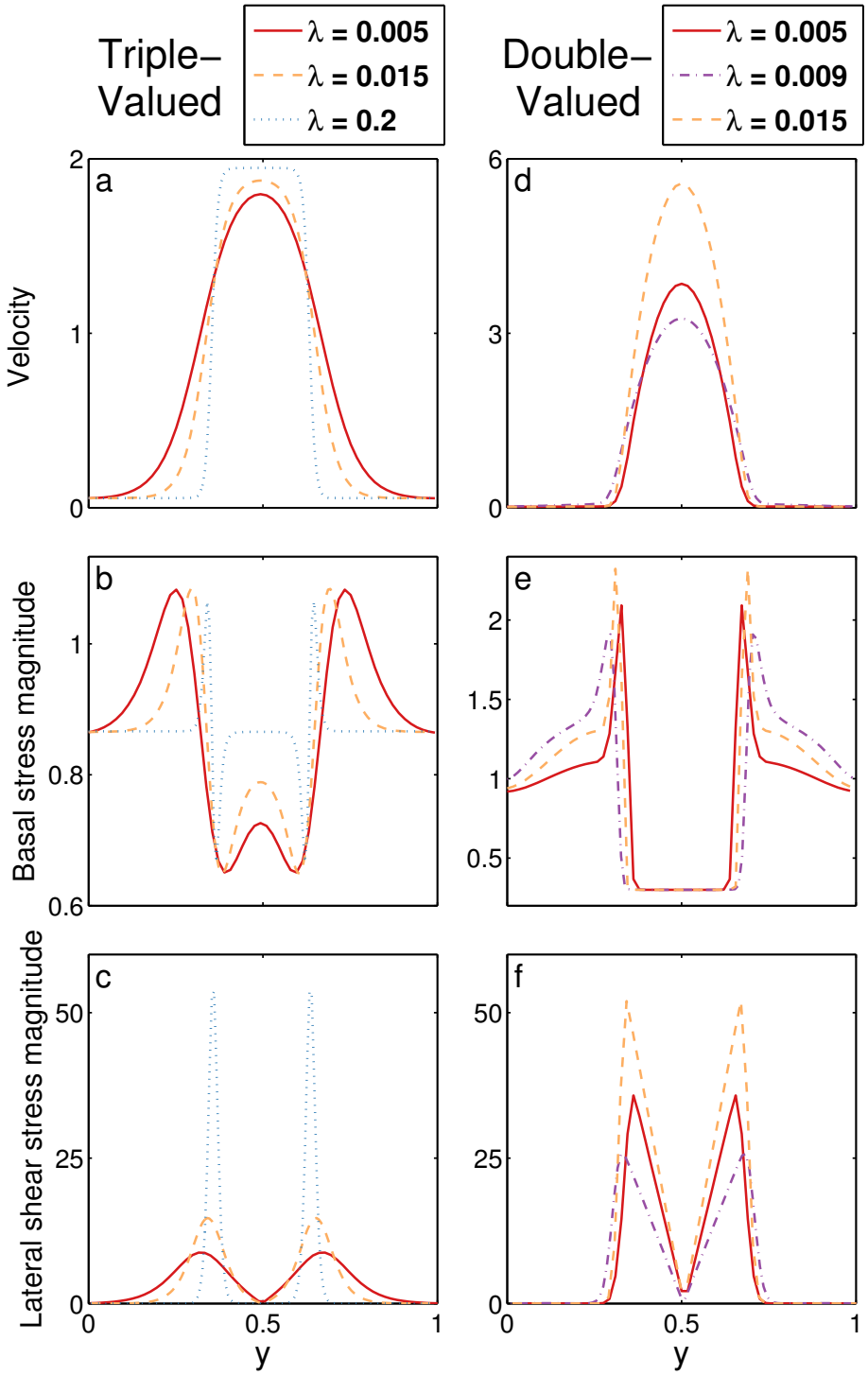

Figure 3.9: Cross-stream velocity and stress profiles for ice streams formed under a triple-valued sliding law (left column) and a double-valued sliding law (right column). Panels (a) and (d) in the top row show the cross-stream velocity profiles. (b) and (e) in the middle row show the corresponding profiles of basal stress magnitude, $\sqrt{|\boldsymbol{\tau}_{13}|^2 + |\boldsymbol{\tau}_{23}|^2}$ and (c) and (f) the corresponding lateral shear stress magnitude, $|\boldsymbol{\tau}_{12}|$. The legends are shown at the top of each column.

increasing velocity. These two effects would cause increased heating, both internally and at the bed, and so further into the margin the temperature would reach the melting point, resulting in internal and basal melting. The meltwater would lubricate the bed, causing a rapid decrease in basal friction while moving further into the ice stream, and reaching a minimum inside the shear margin.

Finally, Figure 3.9c shows the corresponding distribution of lateral shear stress through an ice stream with a triple-valued sliding law as the basal boundary condition. There are maxima in the lateral shear in the margins where the rapid transition from slow flow to streaming flow occurs. At high λ these peaks in longitudinal shear stress magnitude are restricted to narrower bands. As a consequence, the lateral shear stress is of larger magnitude in these bands because the same velocity change occurs over a smaller distance ($\partial u_b/\partial y$ is larger).

Figures 3.9d-f correspond to Figures 3.9a-c but are results with a double-valued sliding law. The velocity in the ice stream is no longer defined by the sliding law, but instead by the scaling (3.28). The velocity of a steady-state stream increases linearly with λ, given a specified ice stream width. The choice of λ is therefore critical in governing whether a stable stream can form in the model or not, once the magnitude of the forcing accumulation perturbation has been chosen (which in turn governs what width and velocity of ice stream can form, according to (3.19)).

Figure 3.9e shows the basal stress profiles across ice streams formed with the double-valued sliding law. At higher values of λ the peak of the sliding law (given by the value $\tau_b = \tau_+$ in Figure 3.6a) is increased and hence there are larger values of basal stress in the margins when compared with the triple-valued sliding law. If the maximum was only as large as for smaller values of λ, the membrane stresses would not be strong enough to hold the entire stream back. In Figure 3.9b for the triple-valued case, when λ is larger (and the margins therefore thinner), it is the basal stress that acts to stop run-away of the ice stream. In contrast, in the double-valued case

there is a constant, very low resistance provided by the bed underneath the stream, and so resistance in the margins must be larger so that the ice stream is in balance.

Figure 3.9f is a plot of the magnitude of the lateral shear stress throughout the stream. As λ increases, the lateral shear magnitude also increases due to the larger velocity change occurring over the margin. There is insufficient basal traction to support the stream, so membrane stresses play a more significant role in balancing the driving stress.

In summary, under a triple-valued sliding law, at lower values of λ the lateral shear and the basal drag both play an important role in the force balance of an ice stream while at higher values, the basal stress plays the dominant role in providing the resistive drag. A double-valued sliding law, however, enforces a low basal stress beneath the ice stream and so a restricted range of parameters is allowed, such that membrane stresses are large enough to hold back the ice stream throughout. For the membrane stresses to be large enough at higher values of λ, a larger velocity difference across the ice stream margins is required (hence larger values of $\partial u_b/\partial y$).

3.5.2 A suitable value of λ

Throughout this work we have presented models with various values of λ to explore the controls on stress balances in ice streams. How does the scale λ affect the proportion of velocity which is due to sliding both inside and outside of an ice stream? Figure 3.10a is a plot showing the fraction of the ice stream velocity that is due to sliding at the bed; Figure 3.10b illustrates the fraction of surface velocity due to sliding at the bed over the entire domain for various values of λ in both the Newtonian and non-Newtonian cases.

In the ice stream itself, increasing λ results in a smaller proportion of the stream flow due to sliding, since vertical shear is favoured in the stress balance. For $\lambda \sim \mathcal{O}(10^{-2})$ over 99% of the flow in the stream is due to sliding, as has been observed in

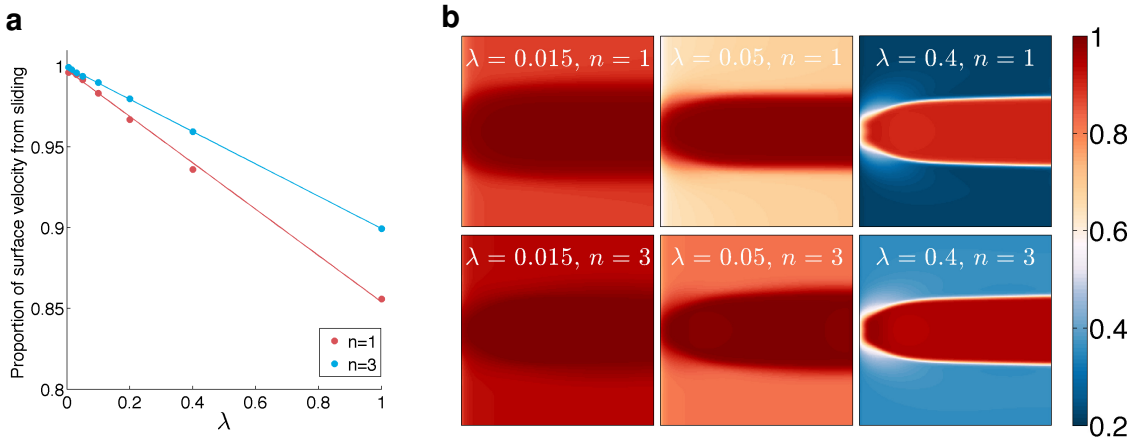

Figure 3.10: Plots illustrating the fraction of surface velocity due to sliding at the bed under a triple-valued sliding law. In (a) the fraction within the ice stream is plotted with different values of λ for both Newtonian and non-Newtonian rheology. In (b) this value is plotted over the domain for specific cases.

some Antarctic ice streams (e.g., Lüthi, 2010).

The triple-valued sliding law pre-defines the basal velocity both within and outside the ice stream. In particular, the sliding velocity outside the stream corresponds to the point where the slow stable branch intersects $\tau_b = \tau_d = 1$ in Figure 3.1. The high proportion of velocity outside the stream due to sliding for small λ is a consequence of this; the vertical shear adds only a very small proportion of velocity. If, however, there was no slip outside of the ice stream (if the ice was frozen to the bed) then there would still be some flow, all due to vertical shearing, outside of the ice stream. This is in contrast to the SSA, which would result in no flow.

A clear benefit, therefore, in using a hybrid formulation such as the one described in this paper is the fact that it can attribute varying degrees of surface velocity to sliding at the bed over a single domain. The SSA produces vertically uniform, plug-flow solutions, which may be accurate in the ice stream itself but do not accurately represent the transition to slow flow outside of the stream. The SSA also cannot be used to model the emergence of ice streams, since it provides an inaccurate description of the ice flow before the stream has developed. Of course, the SIA with added sliding

also allows different areas of the bed to have varying ratios of the surface velocity due to sliding (as in the high λ limit in these plots), but it is well known that the SIA rapidly loses its accuracy as sliding increases (e.g., Gudmundsson, 2003). The SIA does not include membrane stresses in the stress balance, which have been shown to have important stabilising effects on ice stream formation in this work.

The model formulation presented in this paper also has the potential to be applied to other regions of an ice sheet where there are no abrupt changes in basal or surface elevation. The main advantage of this formulation is the fact that it can accurately model ice that is sliding rapidly while also accrediting varying degrees of velocity to sliding over the domain; this is most useful in the region of ice streams where there are abrupt changes in the dominant motion.

3.5.3 Limitations of the model

The model used in this work is idealised so that it is possible to identify critical controlling mechanisms associated with ice-stream stress balances, to improve our understanding of ice stream stability.

An important limitation of the model is that we do not incorporate energy conservation, and so have assumed the ice to be at a constant temperature. It is well known, however, that thermal effects play an important role in ice stream dynamics—measurements have shown ice stream beds to be at melting point (Engelhardt *et al.*, 1990; Iken *et al.*, 1993), while the rest of the ice is much colder. There is also potential of a creep instability mechanism allowing for ice stream formation (e.g. Clarke *et al.*, 1977; Hindmarsh, 2006a), as discussed in more detail in Section 1.2.1 of Chapter 1. Therefore, while this work focuses on feedbacks relating to the basal boundary condition, for a more complete study it would be necessary to include thermal effects more comprehensively. Including them in the rheology would have significant effects at the margins; we would expect the shear thinning effect to be further increased (Suckale

et al., 2014).

Another important aspect neglected in this work is the stabilising effect of buttressing from ice shelves (e.g., Thomas, 1979; Hindmarsh, 2006b; Goldberg and Holland, 2009) and the corresponding destabilising effect that calving events can have on an ice stream (e.g., Hughes, 1992). In this study we have cut off our domain before the grounding line and so include no ice shelf–ice sheet interaction. We would not, however, expect these effects to significantly alter our results. The hybrid formulation would still provide an apt description of ice sheet flow and while buttressing might dampen instabilities (and similarly calving events might allow an instability to develop), this would only add some irregularity to results and some quantitative changes in the location of divides between flow regimes.

3.6 Summary and conclusions

The theoretical model outlined in Chapter 2 of this thesis introduces a new hybrid formulation suitable for describing ice flow dynamics both in, and in the vicinity of, ice streams. To benchmark the model we consider a setup based on Sayag and Tziperman (2009) and apply a triple-valued sliding law at the bed. We show our results to be in agreement with theirs. We then look at the interplay of the triple-valued sliding law with the hybrid approximation, demonstrating the importance of using a model that includes both vertical shear and longitudinal stresses. Variations in the choice of the scaling parameter λ, given a certain forcing, can alter the flow behaviour significantly. This value also governs shear margin width, as demonstrated with a simple scaling argument and by comparison of simulations with different values of λ. The hybrid approximation allows us to compare the significance of different stress components and study, in more detail, the relative importance they play in ice stream formation.

We have also examined the effect of using a double-valued sliding law in Section

3.4. Simple physical considerations justify experimenting with a law of this form. While the triple-valued sliding law might represent behaviour due to switching between drainage systems (Sayag and Tziperman, 2009), or a thermoviscous feedback mechanism (Fowler and Johnson, 1995, 1996), its properties mean that there is only a small difference in basal stress inside and outside of an ice stream (see Figure 3.9b). This is not the case under most ice streams, where the basal stress is considerably lower (e.g., Kamb, 2001; Joughin *et al.*, 2004) and there is evidence that the till deforms with Coulomb-plastic behaviour (e.g., Iverson *et al.*, 1998; Tulaczyk *et al.*, 2000b; Kamb, 2001; Joughin *et al.*, 2004; Schoof, 2004). We therefore experimented with a sliding law of the form (3.20) that specifies a low basal stress under fast-flowing ice. We found a scaling showing the critical dependence of the ice stream velocity on the width of an ice stream, the basal yield stress of the underlying till, the bedslope, and the parameters λ and ε for membrane stresses to be sufficient to balance the gravitational driving stress in an ice stream.

Our results demonstrate the benefits of using a hybrid of the SIA and SSA when describing ice flow in the region of ice streams. Varying the scaling parameter λ in the model results in behaviour variability given the same forcing; the stabilising effects of membrane stresses become apparent at low values of the stress ratio, while at $\lambda \sim \mathcal{O}(1)$ the increased flux due to the vertical shear inhibits the formation of ice streams.

Having considered two heuristic sliding laws in this study, the results further suggest that there are many potential hydraulic mechanisms occurring under the ice that can give rise to ice stream and surging behaviour. Winsborrow and Clark (2010) describe seven potential controls on ice stream location, all of which had been previously proposed in the literature, and suggest that topographic focusing, 'soft' subglacial geology, subglacial meltwater routing, and calving margins are the most common controlling factors. The spatiotemporal dynamics of ice streams will vary depending

on which of these controlling factors are dominant, and so it is important to work more on understanding each of them, and interaction between them. Using purely phenomenological sliding laws allows us to gain qualitative insight into the effect of different controlling mechanisms. For example, in this work, different assumptions about drainage behaviour and till plasticity lead us to formulate sliding laws of the form (3.7) and (3.20), and both result in characteristic streaming behaviour. Furthermore, although using idealised models (such as that considered in this chapter) may not accurately represent all of the complicated physical processes taking place at the bed, they do help to identify critical controlling mechanisms associated with the problem. In the rest of this thesis we try to represent the physics at the bed more directly, rather than through parameterised sliding laws. This will allow us to investigate the coupled behaviour in greater depth.

Chapter 4

Subglacial water layer

4.1 Introduction

In the previous chapter we looked at the consequences of applying multivalued sliding laws as the basal boundary condition for ice flow. We investigated the conditions under which ice streaming occurred, and the stress balances necessary to maintain resultant ice-stream flow. Nevertheless, while implementing a multivalued flux law as a boundary condition may produce ice-stream behaviour, in order to put the basal boundary condition into a more physical context we need to consider the water flow at the bed. There is much evidence suggesting the presence of an active subglacial water layer in West Antarctica (e.g. Fricker *et al.*, 2007), and using knowledge of the subglacial drainage system more directly should help to further improve understanding of the system.

As outlined in the introductory chapter to this thesis, there are two contrasting types of subglacial drainage systems beneath ice sheets that are commonly discussed in the literature. If there is little meltwater production, the bed can be effectively drained by a distributed system of cavities (Walder, 1986; Kamb, 1987), or through thin, patchy films (Alley, 1989). With this style of drainage, increasing meltwater production increases the water pressure beneath the ice, which lowers the effective pressure and hence results in more rapid sliding (Lliboutry, 1968; Kamb *et al.*, 1985; Walder, 1986; Fountain and Walder, 1998). In contrast, subglacial water transport

may occur through larger-scale channels. These provide efficient drainage for meltwater, resulting in low water pressure at the bed, corresponding to high effective pressure, and hence slower sliding velocities (Röthlisberger, 1972). Beneath Antarctica, however, there is more evidence for high water pressure, distributed drainage systems (e.g. Kamb and Engelhardt, 1991). More specifically, evidence from Antarctica suggests that rapid basal velocities in ice streams are enabled by the presence of a layer of till at the base of the sheet (Alley *et al.*, 1986, 1987; Blankenship *et al.*, 1986; Tulaczyk *et al.*, 2000a). For likely permeabilities and till thickness, Darcian porous flow through the sediment would be too slow to evacuate all the meltwater present at the bed (Boulton and Jones, 1979; Walder and Fowler, 1994) and the till is therefore water saturated and is thought to deform with Coulomb-plastic behaviour (e.g. Iverson *et al.*, 1998; Tulaczyk *et al.*, 2000b). Knowledge of the yield strength of the till is important, but more information than this is required about conditions of the hydrological system and how the water flows at the bed.

In this chapter we develop a more detailed and physically motivated model of the subglacial water layer than that used in other recent studies looking at coupled dynamics of ice streams and subglacial hydrology (e.g. Bougamont *et al.*, 2011; Bueler and Brown, 2008; Sayag and Tziperman, 2008; Van Pelt and Oerlemans, 2012). We consider meltwater flowing over saturated, relatively impermeable till. There is some distribution of supporting clasts over the bed and a water film exists as a stable configuration if it is shallow enough not to submerge all surrounding bed protrusions (Creyts and Schoof, 2009). The chapter is organised as follows. In Section 4.2 we describe the physical model and present the governing equations. Section 4.3 considers solutions to the non-dimensionalised equations; under some conditions the solutions are well-behaved but in other cases shocks form. In Section 4.4 we analyse the structure that these shocks take before making some concluding remarks in Section 4.5.

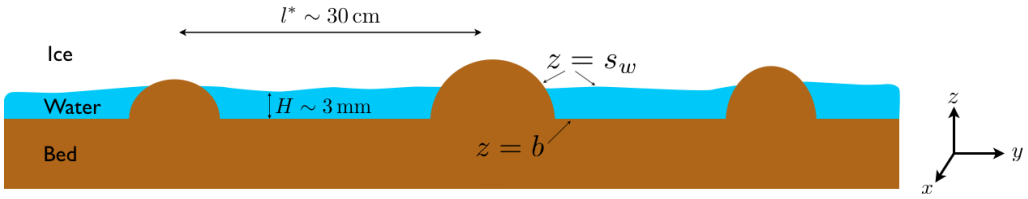

Figure 4.1: Geometry of subglacial flow in a thin film configuration with a distribution of supporting clasts over the bed.

4.2 Model

We conceive of water flowing at the base of an ice stream as illustrated in Figure 4.1. The ice is underlain by sediments that are saturated by water. Typically the water is at high pressure and the till is deformable. We presume the till is not very permeable, and expect that the water generated at the base might flow in some sort of distributed system. The simplest such flow is a thin film at the interface between the ice and the till. With a clean separation between the ice and the bed, as envisioned by Weertman (1972), the resulting flow is an unstable configuration (Walder, 1982). However, we can suppose such a film could exist stably if it is thinner than supporting clast size (Creyts and Schoof, 2009), which is reasonable if the water film thickness is of order millimetres. Of course, this film is still subject to instability if it grows deep enough to separate the ice and bed, and we might expect local-scale water streams to form once the water layer depth reaches some critical value at which surrounding bed protrusions are submerged (Walder and Fowler, 1994). Note, however, that we will consider a detailed analysis of the water and sediment interaction in the following chapter of this thesis; for now we analyse the water layer alone and do not consider effects from coupling with the ice or sediment.

We consider Cartesian axes (x, y, z) where x points in the ice flow direction, y is across-flow and z is vertically upwards. As shown in Figure 4.1, the till surface is denoted by $z = b$, the lower ice surface by $z = s_w$, and the resulting depth of the

water film is

$$H = s_w - b. \tag{4.1}$$

The upper ice surface is denoted by $z = s_i$. The hydraulic head driving water flow at the ice/till interface is

$$\psi = p_w + \rho_w g s_w \tag{4.2}$$

where p_w is water pressure, ρ_w is the density of water and g is acceleration due to gravity. Since water pressure is typically close to the ice overburden pressure, it is useful to re-write this expression in terms on the effective pressure, N, defined as

$$N = p_i - p_w. \tag{4.3}$$

Assuming the basal ice pressure is hydrostatic, i.e. $p_i = p_a + \rho_i g(s_i - s_w)$, where p_a is atmospheric pressure, we can then re-write the hydraulic potential as

$$\psi = p_a + \rho_i g s_i + \Delta\rho_{wi} g s_w - N, \tag{4.4}$$

where $\Delta\rho_{wi} = \rho_w - \rho_i$ is the difference between the density of water and ice. Water moves in the direction of decreasing gradients in ψ,

$$-\boldsymbol{\nabla}\psi = -\rho_i g \boldsymbol{\nabla} s_i - \Delta\rho_{wi} g \boldsymbol{\nabla} s_w + \boldsymbol{\nabla} N. \tag{4.5}$$

The first two terms can be viewed as the driving potential gradient, dependent only on ice geometry, and reflecting the well-known fact that basal water flow is driven primarily by the ice surface slope, and the basal slope only contributes $\sim 1/10$ to the flow direction. The contribution from gradients in effective pressure is the only term that depends on properties of the hydrologic system.

4.2.1 Governing equations

4.2.1.1 Mass conservation of water

Given that the water flows in a film of depth H, with area flux $\mathbf{q} = (q_x, q_y)$, mass conservation of water takes the form

$$\frac{\partial H}{\partial t} + \boldsymbol{\nabla} \cdot \mathbf{q} = \Gamma, \tag{4.6}$$

where Γ is the melt-rate of the ice (with units $\mathrm{kg\,m^{-2}\,s^{-1}}$). The melt rate includes contributions from local heat sources as well as from frictional water dissipation in the subglacial water flow. More specifically,

$$\Gamma = \frac{G + \mathbf{u}_b.\boldsymbol{\tau}_b - q_T + |\mathbf{q}.\boldsymbol{\nabla}\psi|}{\rho_w L}, \tag{4.7}$$

where L the latent heat, G is the geothermal heat flux, $\mathbf{u}_b$ the basal ice velocity, $\boldsymbol{\tau}_b$ the basal ice stress, and q_T the sensible heat flux into the overlying ice. An approximation for the latter is discussed in appendix A3, and it is found to increase with $u_b^{1/2}$. There is therefore potential for Γ to reach zero, and then become negative if $q_T > G + \mathbf{u}_b.\boldsymbol{\tau}_b$; our model does still apply when the water film thickness vanishes. However, we take G and τ to be sufficiently large to prevent re-freezing in this work.

It is also important to note that the frictional heat source $\mathbf{u}_b.\boldsymbol{\tau}_b$ arises from an integration of the ice viscous dissipation term over the basal sliding region, and $\boldsymbol{\tau}_b$ and $\mathbf{u}_b$ here refer to conditions near the base of the far-field ice sheet flow, but far from the actual interface (Fowler, 1981); they are the quantities used in the ice sheet sliding law. At this stage we are also neglecting dissipation in the ice due to lateral shear—an effect that could be significant in the regions around ice stream shear margins (Schoof, 2012; Perol and Rice, 2014).

For a thin layer of water we expect that the flow would be laminar, and so assume

a local Poiseuille flow in the water film, which implies that

$$\mathbf{q} = -\frac{H^3}{12\eta_w}\boldsymbol{\nabla}\psi, \tag{4.8}$$

where η_w is the viscosity of water and $\boldsymbol{\nabla}\psi$ is given by (4.5).

4.2.1.2 Closure Relations

While mass conservation of water tells us how the water moves in response to a hydraulic potential gradient, we also require an equation to describe the evolution of the subglacial hydraulic system. By analogy with the closure equation of Röthlisberger (1972), we consider a balance between the opening and closure rates of the system; we take

$$\frac{\partial H}{\partial t} = \frac{\rho_w}{\rho_i}\Gamma - W_c, \tag{4.9}$$

where the melt rate, Γ, is given by (4.7). The water film thickens as melt is produced, and thins by closure due to the excess ice overburden pressure. In the present situation, we conceive of the ice as being supported by load-bearing clasts, and W_c represents the viscous creep of ice around these supporting clasts. Under the assumption that clasts have spacing l^* (see Figure 4.1), we expect that

$$W_C \propto \frac{Nl^*}{\eta_i}. \tag{4.10}$$

There is an inverse correlation between creep rate and ice viscosity; higher ice viscosity will slow the creep rate. However, the creep rate increases with both the effective pressure and the spacing between supporting clasts, l^*. This latter quantity is analogous to the channel width in the closure equation of Röthlisberger (1972), assuming a single (wide) channel. Furthermore, as the film thickness increases, the spacing between protruding clasts will increase as more of them become submerged; l^* will

therefore be an increasing function of H.

More specifically, based on Creyts and Schoof (2009), we take the rate of closure due to viscous creep as

$$W_C = AN^n l^*(H). \tag{4.11}$$

A is the rate factor and n the exponent from Glen's flow law, which describes the rheological behaviour of ice (Cuffey and Paterson, 2010). There is, however, little to constrain our choice for the functional dependence of $l^*(H)$. We assume there is some film depth H_c at which all the clasts would become submerged and the ice would become locally clear of the bed. We hence define

$$l^*(H) = \frac{l_0}{\Lambda(H)}, \tag{4.12}$$

where l_0 is a length scale that represents the typical clast spacing in the absence of water, and will be chosen to be consistent with observed effective pressures on the Whillans ice stream (B). We are then left to choose a function for $\Lambda(H)$. The most simple choice, for illustrative purposes, would be a function such as

$$\Lambda(H) = \begin{cases} 1 - \frac{H}{H_c}, & 0 < H < H_c, \\ \\ 0, & H \geq H_c, \end{cases} \tag{4.13}$$

as illustrated by the dashed grey line in Figure 6.1. When H reaches H_c, the ice separates from the bed. From (4.9) with (4.11) and (4.12) we have that

$$N = \left[\frac{\Lambda(H)}{Al_0} \left(\frac{\rho_w}{\rho_i} \Gamma - \frac{\partial H}{\partial t} \right) \right]^{1/n}, \tag{4.14}$$

and it is clear that with the above choice of $\Lambda(H)$, $N = 0$ when $H = H_c$, implying that once the ice separates from the bed there is no basal stress. In this context there

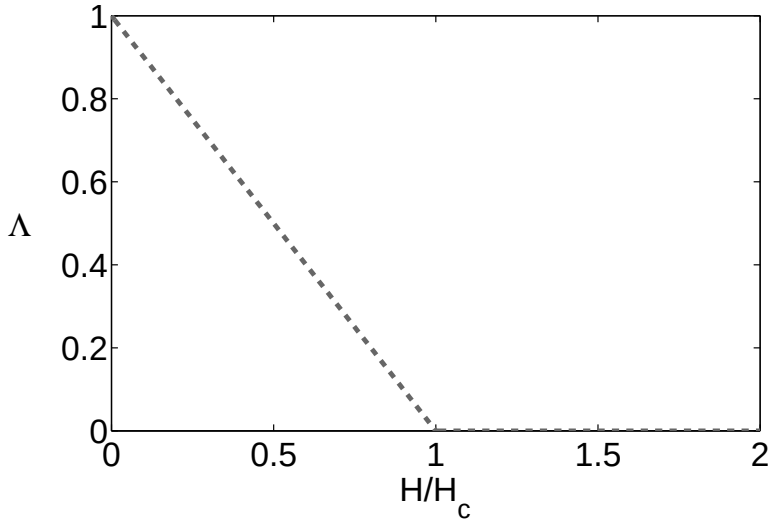

Figure 4.2: Plots of $\Lambda(H)$. The dashed grey line is given by (6.9).

is then no reason that H cannot increase further locally, with the effective pressure remaining zero.

It is also worth noting that, since we are considering water flow over sediment rather than hard bedrock, there should also be a description of bed evolution in the model. This would require a second closure relation for the bed elevation b, based on an Exner equation incorporating sediment transport (e.g. Fowler, 2011a). In this chapter, however, we assume that there is no sediment transport so that b is fixed and $H = s_w - b$. We therefore require only one closure equation. This is not an unreasonable assumption so long as there is no net change in bed elevation. There can still be some transport of sediment by virtue of the shear induced by the sliding of basal ice, but if the sliding is a uniform motion in the downflow direction, we would expect the deposition and erosion rates to be in equilibrium. Other work specifically considers bed evolution in an effort to explain the evolution of subglacial bedforms (e.g. Clark, 2010), but we postpone including details of these processes until the next chapter of the thesis when we will consider a simple representation of sediment-water interaction.

4.2.2 Coupling of the water and ice

It is clear from the equations describing the water layer that the behaviour of the water is directly coupled with that of the ice. Most notably, the leading order contribution to the gradient in hydraulic potential is from ice surface gradients (4.5). The creep closure of the ice (4.11) as well as terms in the expression for the melt rate also depend on ice flow. For the moment we take these ice flow variables as constant, so we can consider the behaviour of the water layer below ice moving at a constant velocity, with constant surface gradient and viscosity. This assumption will be relaxed in Chapter 6 when we solve for the coupled ice-water behaviour.

4.2.3 Non-dimensionalisation and reduction

Mass conservation of water (4.6) and the creep closure equation (4.9) provide two equations to solve for the two unknowns, water depth, H, and effective pressure, N. Values of the dimensional constants are given in Table 1 at the start of the thesis.

To make the subglacial water model dimensionless we guess approximate scales for some variables based on observations/physical intuition, and then use these to derive characteristic scales for other variables, as given in Table 4.1. We assume a characteristic value for the horizontal extent of the ice $x_0 \sim 500\,\mathrm{km}$, and depth of the ice $d_0 \sim 1\,\mathrm{km}$, based on length scales in ice-streaming regions such as the Siple Coast (e.g. Cuffey and Paterson, 2010). We also define an effective pressure scale $\sim 4 \times 10^4\,\mathrm{Pa}$ (e.g. Blankenship *et al.*, 1987).

The scale for melt rate is then chosen to balance geothermal heating.

$$\Gamma_0 \sim \frac{G}{\rho_w L} \sim 10^{-10}\,\mathrm{m\,s^{-1}}. \tag{4.15}$$

Other scales are chosen to balance dominant terms in equations (4.6) and (4.9). The scale for $\mathbf{q}$ is chosen based on the fact that the meltwater drives the divergence in

meltwater flux downstream i.e.

$$\begin{aligned} q_0 &\sim \Gamma_0 x_0 \\ &\sim 10^{-10}\,\mathrm{m\,s^{-1}} \times 5 \times 10^5\,\mathrm{m} = 5 \times 10^{-5}\,\mathrm{m^2\,s^{-1}}, \end{aligned} \tag{4.16}$$

and the hydraulic potential from (4.4)

$$\psi_0 = \rho_i g h_0 = 10^7\,\mathrm{Pa}. \tag{4.17}$$

The scale for the effective depth H is then chosen from the expression for $\mathbf{q}$ (4.8), based on the assumption that water flux 'downstream' will largely be driven by gradients in ψ i.e.

$$\begin{aligned} H_0^3 &\sim \frac{12\eta_w q_0 x_0}{\psi_0} \qquad (4.18) \\ &\sim \frac{12 \times 1.8 \times 10^{-3}\,\mathrm{Pa\,s} \times 5 \times 10^{-5}\,\mathrm{m^2\,s^{-1}} \times 5 \times 10^5\,\mathrm{m}}{10^7\,\mathrm{Pa}} \\ &\sim 3 \times 10^{-8}\,\mathrm{m^3} \\ \Rightarrow H_0 &\sim 3 \times 10^{-3}\,\mathrm{m}. \qquad (4.19) \end{aligned}$$

As for a scale for the clast spacing in the ice closure relation (4.9), we take $l^* \sim l_0$ and balance the opening and closure rate terms to get

$$l_0 \sim \frac{\rho_w \Gamma_0 \eta_i}{\rho_i N_0} \sim 0.3\,\mathrm{m}. \tag{4.20}$$

The ice flow scales (for variables considered as constant in this chapter) are fur-

Symbol	Description	Typical value
x_0	horizontal length scale	$500\,\mathrm{km}$
d_0	ice depth scale	$1000\,\mathrm{m}$
u_0	ice velocity scale	$100\,\mathrm{m\,yr^{-1}}$
Γ_0	melt rate scale	$10^{-10}\,\mathrm{m\,s^{-1}}$
H_0	meltwater depth scale	$3\times10^{-3}\,\mathrm{m}$
N_0	effective pressure scale	$4\times10^{4}\,\mathrm{Pa}$
q_0	meltwater flux scale	$5\times10^{-5}\,\mathrm{m^2\,s^{-1}}$
t_w	water time scale	$3.9\times10^{7}\,\mathrm{s}\approx1\,\mathrm{yr}$
τ_0	basal stress scale	$2\times10^{4}\,\mathrm{Pa}$
ψ_0	hydraulic potential scale	$10^{7}\,\mathrm{Pa}$
Ω_0	ice surface slope scale	2×10^{-3}
l_0	clast spacing	$0.3\,\mathrm{m}$
A_0	Glen's flow law rate scale	$1.25\times10^{-23}\,\mathrm{s^{-1}\,Pa^{-3}}$ $=3\,\mathrm{bar^{-3}\,y^{-1}}$

Table 4.1: List of variable scales in the governing equations for the subglacial water layer.

thermore defined by

$$\Omega_0 = \frac{d_0}{x_0}, \tag{4.21}$$

$$\tau_0 = \rho_i g d_0 \Omega_0, \tag{4.22}$$

$$A_0 = \frac{1}{2\eta_i \tau_0^{n-1}}, \tag{4.23}$$

and we take $u_0 \sim 100\,\mathrm{m\,yr^{-1}}$. Finally, the time scale for water flow is defined by

$$t_w = \frac{H_0 x_0}{q_0}. \tag{4.24}$$

Table 4.1 gives values of these model variable scales.

Symbol	Definition	Typical value
r	ρ_i/ρ_w	0.9
ω	$\Delta\rho_{wi}/\rho_i$	0.1
δ_{Hh}	H_0/h_0	3×10^{-6}
ν	$N_0/\left(\rho_i g \Omega_0 x_0\right)$	4×10^{-3}
μ	$\left(\tau_0 u_0\right)/G$	1
κ	$\left(\frac{\rho_i c_p k u_0}{\pi x_0}\right)^{1/2} \frac{\Delta T}{G}$	0.27
χ	$\left(q_0 \psi_0\right)/\left(x_0 G\right)$	10^{-2}

Table 4.2: Descriptions and typical values of non-dimensional parameters in the subglacial water layer equations (4.25a) - (4.25d).

We non-dimensionalise and the dimensionless form of the equations becomes

$$\frac{\partial H}{\partial t} + \boldsymbol{\nabla}.\mathbf{q} = \Gamma, \tag{4.25a}$$

$$r\frac{\partial H}{\partial t} = \Gamma - \frac{N^n}{\Lambda(H)}, \tag{4.25b}$$

where

$$\begin{aligned}\mathbf{q} &= -H^3 \boldsymbol{\nabla}\psi \\ &= H^3\left(-\boldsymbol{\nabla}s_i - \omega\boldsymbol{\nabla}b - \omega\delta_{Hh}\boldsymbol{\nabla}H + \nu\boldsymbol{\nabla}N\right),\end{aligned} \tag{4.25c}$$

and

$$\Gamma = 1 + \mu\mathbf{u}_b.\boldsymbol{\tau}_b - \kappa u^{1/2} + \chi H^3\left|\boldsymbol{\nabla}\psi\right|^2. \tag{4.25d}$$

Dimensionless parameters are given in Table 4.2 and $\Lambda(H)$ is the same function as in (4.13), only now a function of the dimensionless water depth.

4.2.4 Simplification of subglacial system

The parameters δ_{Hh}, ν and χ are all small. We thus neglect the terms of order δ_{Hh} and χ, representing gradients in water depth and melt due to meltwater dissipation,

respectively, but retain the term in ν, as it represents a singular perturbation. From (4.25b) we have

$$N = \left[\Lambda(H)\left(\Gamma - r\frac{\partial H}{\partial t}\right)\right]^{1/n}, \tag{4.26}$$

and the mass conservation of water equation (4.25a) can then be written as an equation for H:

$$\frac{\partial H}{\partial t} - \boldsymbol{\nabla}\cdot\left(H^3(\boldsymbol{\nabla}s_i + \omega\boldsymbol{\nabla}b)\right) = -\nu\boldsymbol{\nabla}\cdot\left[H^3\boldsymbol{\nabla}\left(\Lambda(H)\left(\Gamma - r\frac{\partial H}{\partial t}\right)\right)^{1/n}\right] + \Gamma. \tag{4.27}$$

Furthermore, to allow consideration of the behaviour of the hydraulic system on its own, we assume that the ice has a constant, uniform surface slope

$$\boldsymbol{\nabla}s_i = -\hat{\boldsymbol{\imath}}, \tag{4.28}$$

and zero basal slope, $\boldsymbol{\nabla}b = \mathbf{0}$. Equation (4.27) then reduces to

$$\frac{\partial H}{\partial t} + \frac{\partial}{\partial x}\left(H^3\right) = -\nu\boldsymbol{\nabla}\cdot\left[H^3\boldsymbol{\nabla}\left(\Lambda(H)\left(\Gamma - r\frac{\partial H}{\partial t}\right)\right)^{1/n}\right] + \Gamma. \tag{4.29}$$

Given that $\Lambda(H)$ is a decreasing function of H, the essential structure of the model can be described by

$$H_t + H_x = \boldsymbol{\nabla}^2 H + \boldsymbol{\nabla}^2 H_t, \tag{4.30}$$

which is closely related to that studied by Benjamin *et al.* (1972) as a model for long waves in shallow water; we may infer that the present equation is well-posed.

4.3 Solutions to the water layer equation

4.3.1 Zero melt-rate solutions

We first consider leading-order solutions of (4.29), with $\Gamma = 0$. Ignoring the $\mathcal{O}(\nu)$ term, gives

$$H_t + 3H^2 H_x = 0. \tag{4.31}$$

As there is no melt being generated we expect that water present at $t = 0$ will simply be advected out of the domain.

4.3.1.1 Analysis

Using the method of characteristics, solutions to (4.31) are described by $\dot{H} = 0$ on $\dot{x} = 3H^2$. With zero melt rate H is constant and therefore $\dot{x}$ is also constant. The characteristics must be straight lines.

More specifically, we first analyse the behaviour of solutions for the simple case where $H = mx$ (with m a positive real number) i.e. there is an initial water layer linearly increasing in depth across the domain. The boundary conditions for the solution of (4.31) are therefore

$$H = 0 \quad \text{at} \quad x = 0,\ t > 0 \tag{4.32}$$

$$H = mx \quad \text{at} \quad t = 0,\ x > 0. \tag{4.33}$$

Parametising the second boundary condition as $H = m\sigma$, $t = 0$, $x = \sigma$, we get that $x = 3\left(m\sigma\right)^2 t + \sigma$. Characteristic diagrams for $m = 0.5$ and $m = 2$ are shown in Figures 4.3(a) and 4.3(b) respectively. Solutions are well-behaved and no characteristics intersect.

How does this behaviour contrast with that if the initial water profile has a neg-

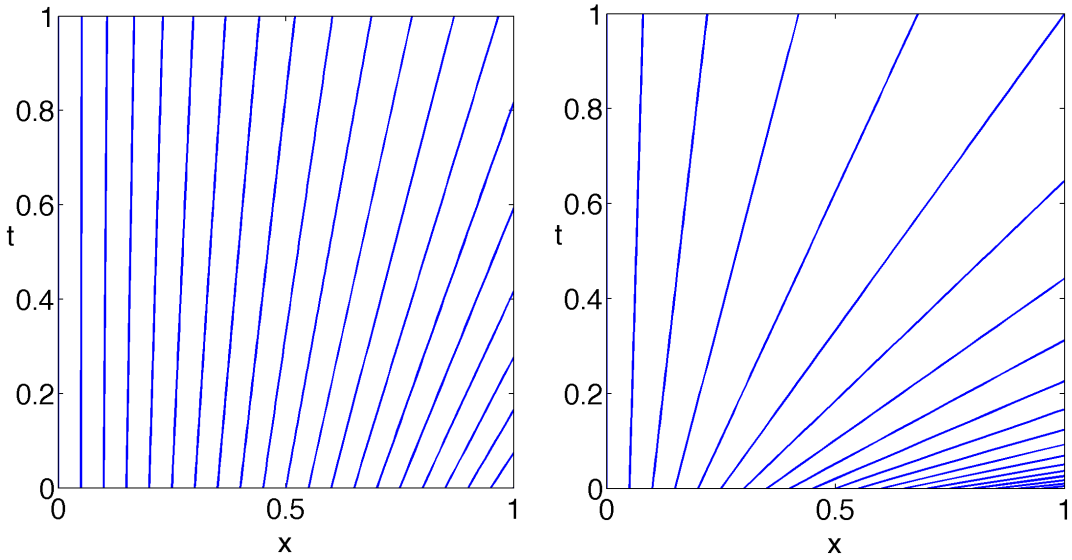

(a) Initial condition: $H = \frac{1}{2}x$.

(b) Initial condition: $H = 2x$.

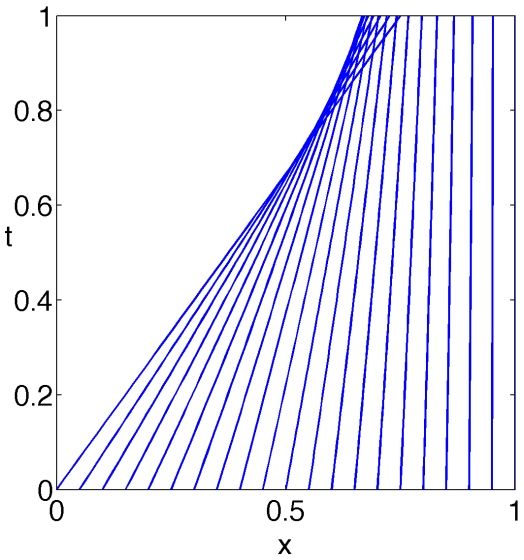

(c) Initial condition: $H = \frac{1}{2}(1 - x)$.

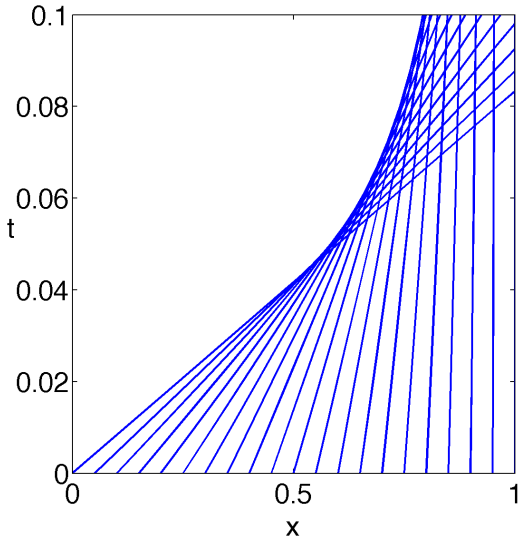

(d) Initial condition: $H = 2(1 - x)$.

Figure 4.3: Characteristic curves for solution of equation (4.31) in one dimension. Initial conditions are stated below each plot. In (a) and (b) the initial water depth has positive gradient and the solutions are well behaved. In (c) and (d) the initial water depth has a negative gradient and so the characteristics intersect, generating a shock wave.

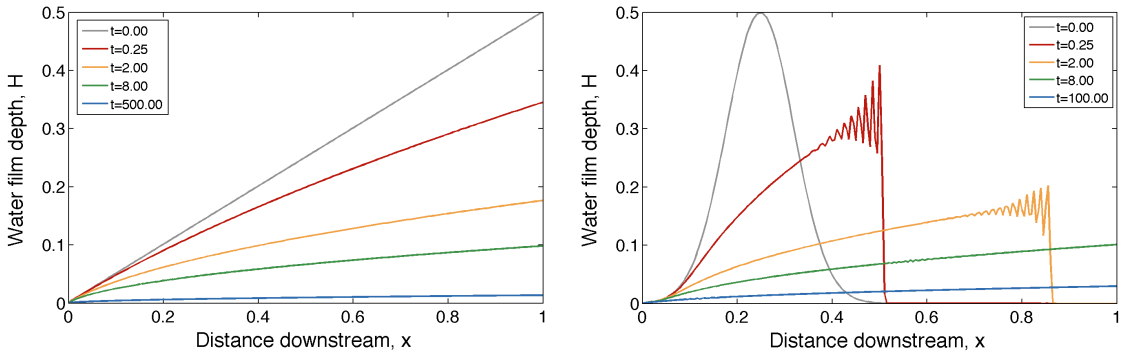

(a) (b)

Figure 4.4: Evolution of water depth profiles taken down the domain for the initial water depths plotted in grey. $H_c = 6\,\text{mm}$. The smooth increasing profile in (a) is well-behaved as the water is advected out of the domain. In contrast, the Gaussian bump in (b) introduces negative gradients and a shock forms, which is then advected out of the domain.

ative gradient? For example, we consider the case with

$$H = m(1-x) \quad \text{at} \quad t = 0,\ x > 0. \tag{4.34}$$

Parametising as $H = m(1-\sigma)$, $t = 0$, $x = \sigma$, we get that $x = 3\left[m(1-\sigma)\right]^2 t + \sigma$. Characteristic diagrams for $m = 0.5$ and $m = 2$ are shown in Figures 4.3(c) and 4.3(d) respectively. The characteristic curves intersect in this case, generating a shock wave. This is in agreement with other analyses of nonlinear wave equations, which result in shocks forming from any initial condition where the variable decreases in the direction of flow (e.g. Whitham, 1973; Spiegelman, 1993).

4.3.1.2 Numerical solutions

We run numerical simulations solving (4.31) to check that solutions agree with the above analysis. Figure 4.4(a) shows the solution of (4.31) plotted at discrete times for a simulation initialised with $H = \frac{1}{2}x$. The water is advected out of the domain. In Figure 4.4(b) we initialise the simulation with a Gaussian blob of water upstream,

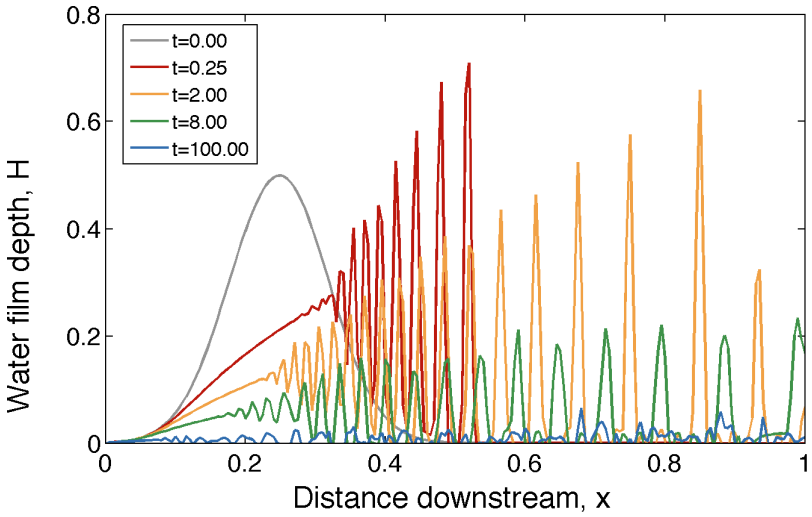

Figure 4.5: Evolution of a water depth profile for the initial water depth plotted in grey. The simulation has been solved using a semi-implicit time discretisation, rather than an implicit discretisation as in Figure 4.4(b). More numerical artefacts are seen here.

which introduces a negative gradient in water depth. A shock arises, as we expect from the analysis in Section 4.3.1.1. There is some numerical dispersion, which results in a small train of waves before the shock front. While the shock develops over a very short time scale, the time scale over which the water is advected out of the domain is much longer, as can be seen in both cases in Figure 4.4. This is because the advection velocity is $\sim 3H^2$, which is very slow for small H. Introducing a constant melt rate so that the steady-state solution is non-zero will allow the simulations to evolve into steady state over a much smaller time scale. This is what we consider in the following section.

Before considering non-zero melt rate, however, we comment on the numerical method. The presence of an advection term in (4.31) means it is very important to consider the discretisation of the equation carefully. Figure 4.5 shows an example of how the numerical inaccuracies increase under a semi-implicit discretisation of the time derivative, for the solution plotted in Figure 4.4(b) (there solved using an implicit discretisation). The spatial discretisation is also important and were we to consider

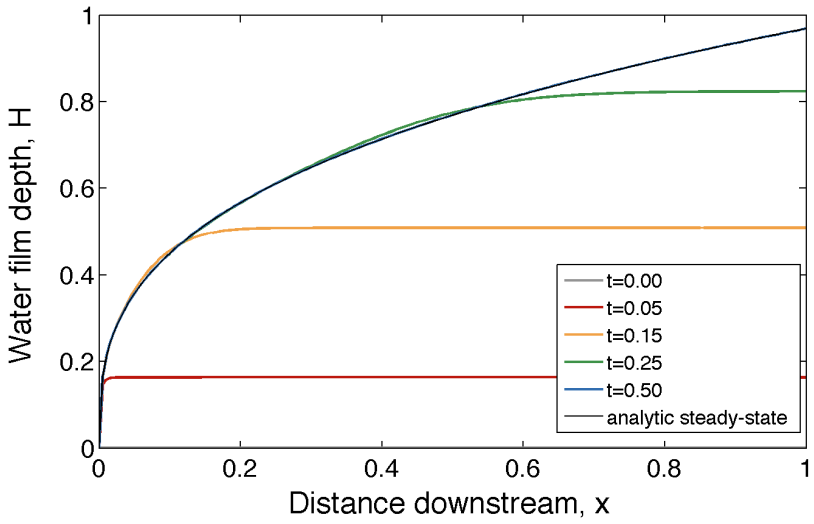

Figure 4.6: Evolution of a water depth profile for a simulation with $\Gamma = 1$ and initialised with zero water. A downstream profile is plotted at various times as the solution evolves to the steady state.

this zero melt rate case with $\nu = 0$ in more detail it would be necessary to consider different advection schemes, perhaps using a flux limiter. For the plots shown here we have simply used a cell-centred finite volume discretisation. Since this case is for illustrative purposes only, and later in the thesis we always have non-zero melt rate and non-zero ν, we do not consider the numerical method any further at this point.

4.3.2 Constant melt-rate solutions

With a non-zero constant melt rate, leading-order solutions of (4.29) must satisfy

$$H_t + 3H^2 H_x = \Gamma. \tag{4.35}$$

The stable, steady-state solution of (4.29) therefore satisfies

$$\left(H^3\right)_x = \Gamma. \tag{4.36}$$

We solve (4.35) and see the solution evolve to this steady state, given a prescribed constant melt rate. An example of this is in Figure 4.6, where $\Gamma = 1$ and the simulation has been initialised with zero water depth.

4.3.2.1 Analysis

As in section 4.3.1.1, we initially ignore the $\mathcal{O}(\nu)$ term in (4.29), and consider the equation

$$\frac{\partial H}{\partial t} + 3H^2 \frac{\partial H}{\partial x} = \Gamma, \tag{4.37}$$

with the boundary conditions

$$H = 0 \quad \text{at} \quad x = 0,\ t > 0 \tag{4.38}$$

$$H = 0 \quad \text{at} \quad t = 0,\ x > 0. \tag{4.39}$$

The characteristic solutions are described by

$$\dot{H} = \Gamma \tag{4.40}$$

$$\dot{x} = 3H^2. \tag{4.41}$$

We parameterise the initial data, $t = \tau, x = 0,\ H = 0$ and solve (4.40) to give $H = \Gamma(t - \tau)$. Substituting into (4.41) and solving we get $x = \Gamma^2(t - \tau)^3$ and so have the solution

$$H = (\Gamma x)^{1/3} \quad \text{for} \quad x \leq \Gamma^2 t^2 \tag{4.42}$$

We now consider the other boundary condition and parameterise it as $t = 0, x = \sigma, H = 0$. Solve (4.40) we have $H = \Gamma t$ and substituting into (4.41) and solving we

further get $x = \Gamma^2 t^3 + \sigma$. Combining these we find $H = [\Gamma(x - \sigma)]^{1/3}$ and so have

$$H = (\Gamma x)^{1/3} \text{ for } x \leq \Gamma^2 t^2 \tag{4.43}$$

$$H = \Gamma^{1/3}(x - \sigma)^{1/3} \text{ for } x > \Gamma^2 t^2 \tag{4.44}$$

The characteristics are plotted in Figure 4.7(a). These illustrate a well-behaved solution, as seen in Figure 4.6. Furthermore, the solution for $x > \Gamma^2 t^2$ can be written as $H = \Gamma t$, which explains why the solution for $x > \Gamma^2 t^2$ is constant (and the constant increases at each time step) in Figure 4.6.

We also consider the characteristics for the general initial condition $t = 0, x = \sigma, H = H(\sigma)$. The general solution becomes

$$H = (\Gamma x)^{1/3} \text{ for } x \leq \Gamma^2 t^2 \tag{4.45}$$

$$H = \left[\Gamma (x - \sigma) + (H(\sigma))^3\right]^{1/3} \text{ for } x > \Gamma^2 t^2 \tag{4.46}$$

along $x = \Gamma^2(t - \tau)^3$ and $x = (\Gamma t + H(\sigma))^3 / \Gamma - H(\sigma)^3 / \Gamma + \sigma$ respectively.

If we consider a sensible increasing function of x for $H(\sigma)$, the solutions are again well-behaved and shocks do not form e.g. in Figure 4.7(b), a characteristic diagram is plotted for $H(\sigma) = \frac{1}{2}x$.

However, if we initialise with a profile with negative gradients in H, then shocks might form. We consider the characteristic diagram for

$$H(\sigma) = A \exp\left(-100\left(x - \frac{1}{4}\right)^2\right) \tag{4.47}$$

where A is the magnitude of the Gaussian bump. The resultant characteristics for two values of A are plotted in Figures 4.7(c) and 4.7(d), and we can see that such a choice of $H(\sigma)$ can cause shock formation.

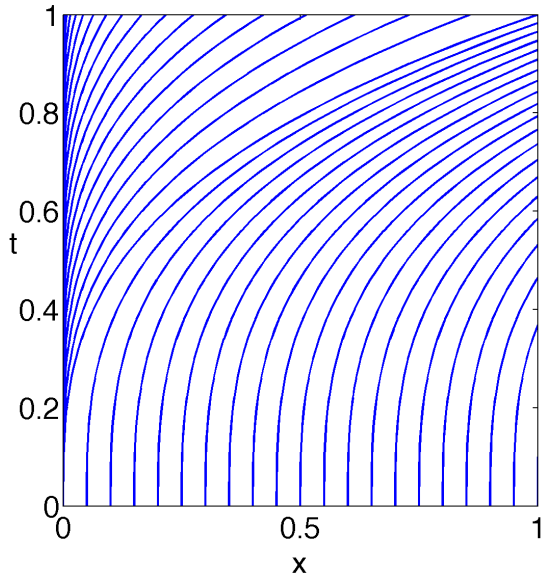

(a) Initial condition: $H = 0$.

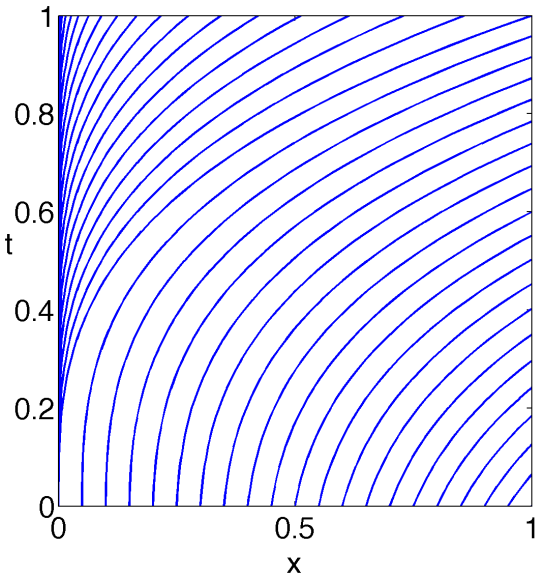

(b) Initial condition: $H = \frac{1}{2}x$.

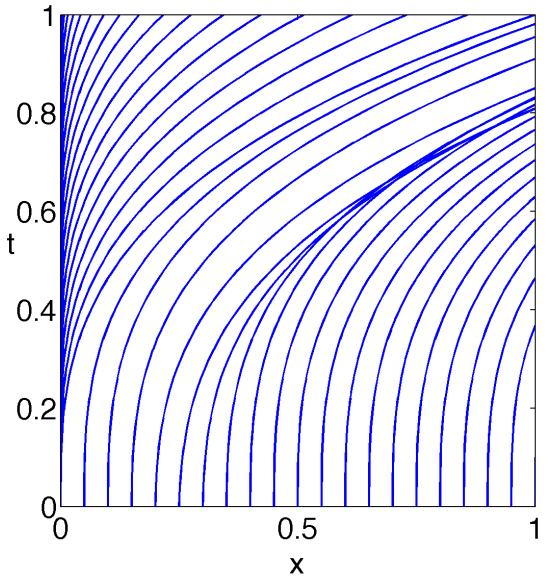

(c) Initial condition: eq (4.47) with $A = 0.1$.

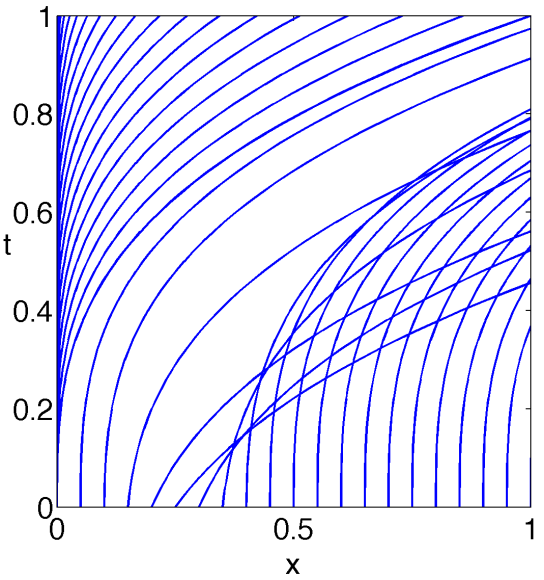

(d) Initial condition: eq (4.47) with $A = 0.5$.

Figure 4.7: Characteristic curves for solution of equation (4.37) in one dimension, with $\Gamma = 1$. Initial conditions are stated below each plot. In (a) and (b) the initial water depth has positive gradient and the solutions are well behaved. In (c) and (d) the initial water depth has a negative gradient and so the characteristics intersect, generating a shock wave.

4.3.2.2 Numerical solutions

We consider numerical solutions to (4.29) with a Gaussian blob of magnitude $A = 0.5$ as the initial condition (given by (4.47) and illustrated in Figure 4.8(a)). We want to investigate the effect of including the $\mathcal{O}(\nu)$ term (which has not been included in the above analysis), as well as looking at the behaviour under this perturbation in the $\nu = 0$ case (4.35).

We first solve (4.29) with $\nu = 0$. Figure 4.8(b) provides snapshots at four different times as the initially perturbed water layer evolves to the steady state. A shock front forms, and the perturbation is advected out of the domain.

If ν is non-zero, this alters the behaviour. Figure 4.8(c) shows snapshots in the case $\nu = 0.001$, with $H = 0$ at the inflow and $H_x = 0$ at the outflow. The solution does not converge as H grows large in the vicinity of the shock front and approaches the critical depth H_c (see the $t = 0.1$ a subplot). The effective pressure at the bed approaches zero as H approaches H_c.

If, however, we take $\nu > 10^{-3}$, the diffusive effect of the $\mathcal{O}(\nu)$ term is strong enough to smooth out the shock and prevent H growing to large values at the front. The shock front is not as abrupt as in the $\nu = 0$ case, and the perturbation is advected out of the domain.

To study the behaviour in the vicinity of where the shock forms in more detail, we also consider a cross-section down the centre of the domain. Figure 4.9 illustrates the water depth profile for the three cases up until the time at which the $\nu = 0.001$ case stops converging and H reaches the critical depth. Figure 4.10 then has plots of the cross sections of the two cases which go on to evolve to the steady state. It is clear that the $\mathcal{O}(\nu)$ term diffuses the shock front, and in doing so H reaches larger values in the vicinity of the shock. Note that if we chose a larger value for H_c, such that the water depth did not reach H_c in the solution domain, the $\nu = 0.001$ case could also evolve to steady state.

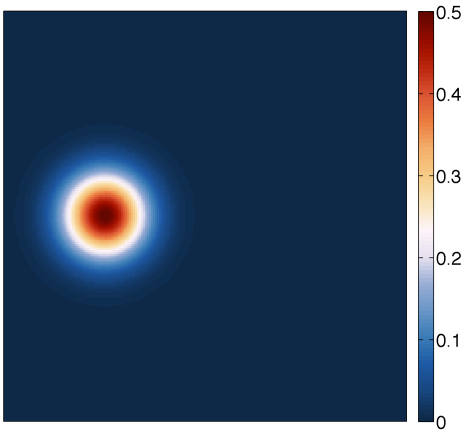

(a) Initial condition.

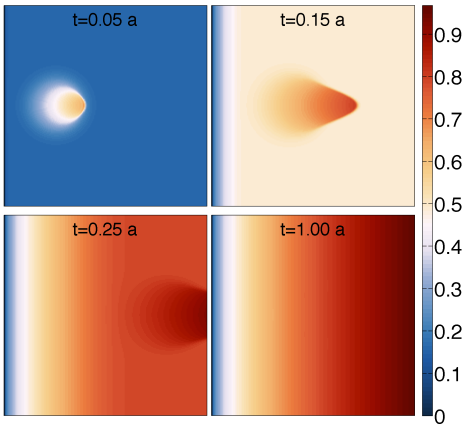

(b) $\nu = 0$.

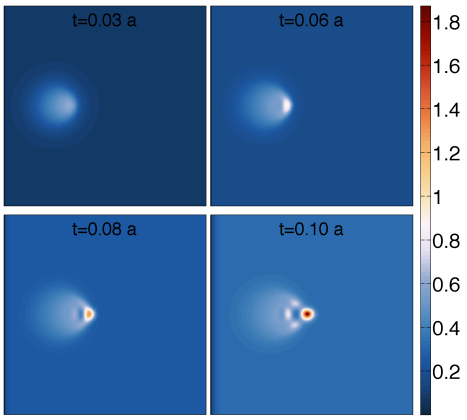

(c) $\nu = 0.001$.

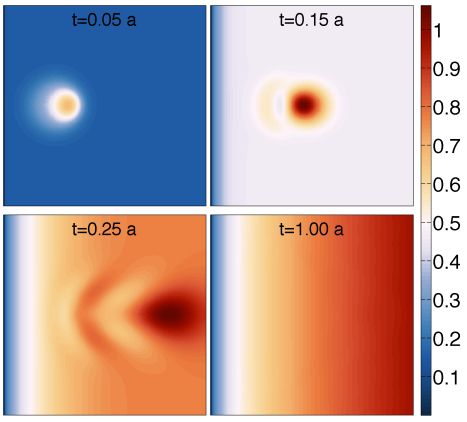

(d) $\nu = 0.01$.

Figure 4.8: Solutions of (4.29) with differing values of ν, with $\Lambda(H)$ given by (6.9) and $H_c = 2$. The initial condition is shown in (a) and the other subplots show snapshots of the domain as it evolves from the initial state. All units are non-dimensional.

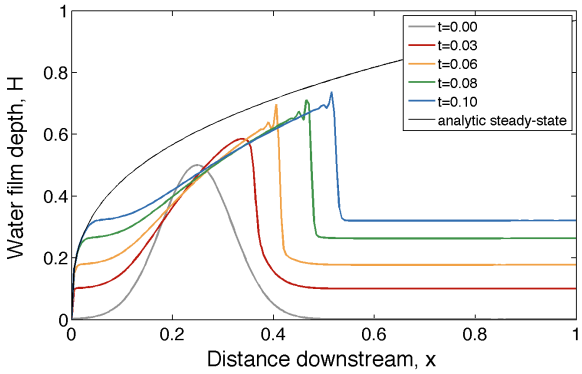

(a) $\nu = 0$.

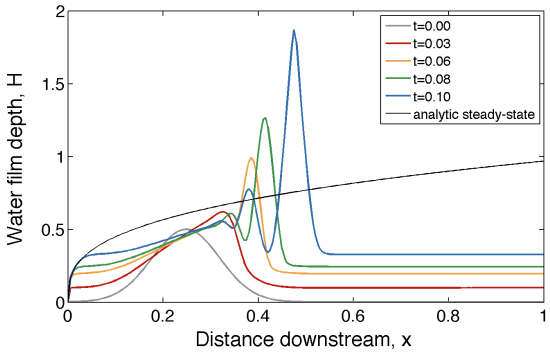

(b) $\nu = 0.001$.

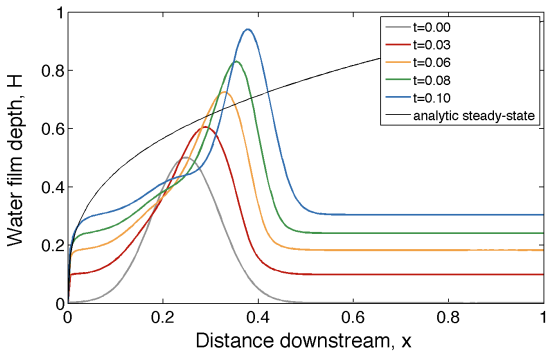

(c) $\nu = 0.01$.

Figure 4.9: Evolution of the water depth profile along the centreline of the domain for the three different cases illustrated in Figure 4.8. The solution with $\nu = 0.001$ stops converging at time $t = 0.1$ since H reaches $H_c = 2$. The dispersive effect of the $\mathcal{O}(\nu)$ term can be seen clearly.

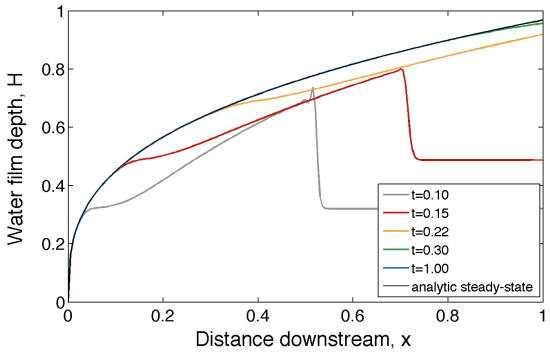

(a) $\nu = 0$.

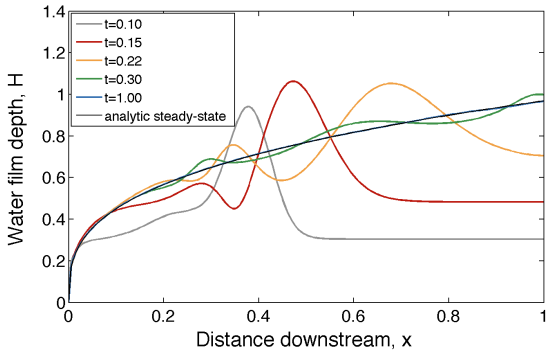

(b) $\nu = 0.01$.

Figure 4.10: Evolution of the water depth profile across the domain for the two cases which go on to evolve to the steady state. Both plots start at time $t = 0.10$ (the time at which the plots in Figure 4.9 end) and we see how the solution then evolves to the steady state for both the $\nu = 0$ and $\nu = 0.01$ case.

4.4 Shock structure

Can we quantify the behaviour of the shock analytically? We have observed that taking $\nu \neq 0$ introduces an oscillatory wave train behind the shock front that gets damped out. What more can be said about the structure of this shock front?

The 1D simplification of (4.29) in the Newtonian case with $\frac{\partial b}{\partial x} = 0$ and $\Lambda(H)$ given by (4.13) can be written as

$$H_t + \left(H^3\right)_x = -\nu \left[H^3 \left(\left(1 - \frac{H}{H_c} \right) (\Gamma - rH_t) \right)_x \right]_x + \Gamma \tag{4.48}$$

where subscripts x and t refer to partial derivatives of those variables, and $H < H_c$.

For simplicity, we take the source term to be zero, and initially consider the case where $\nu = 0$. At the front we consider a travelling wave solution to (4.48) in the form $H(x,t) = H(X)$, where

$$x = x_s + X, \tag{4.49}$$

$$\dot{x}_s = c, \tag{4.50}$$

so $X = x - ct$ and c is the wave's phase speed. Inserting this into (4.48) gives us

$$-cH_X + \left(H^3\right)_X = 0. \tag{4.51}$$

Given that

$$H \to H_\pm \text{ as } x \to \pm\infty \tag{4.52}$$

with $H_- > H_+$, we have that $K = cH_- - H_-^3 = cH_+ - H_+^3$, and so have a shock speed

$$c = \frac{[H^3]_-^+}{[H]_-^+}. \tag{4.53}$$

Now what is the effect of including the $\mathcal{O}(\nu)$ term and re-introducing the third derivative into the equation? To analyse what happens in this case, we write

$$x = x_s + \varepsilon X, \tag{4.54}$$

$$\dot{x}_s = c, \tag{4.55}$$

so $X = \frac{x-ct}{\varepsilon}$ and c is the wave's phase speed and ε some small parameter that we choose to take $\varepsilon = \nu^{1/2}$. Inserting this into (4.48), and again neglecting the source term, gives us

$$-cH_X + \left(H^3\right)_X = -\left[H^3\left(\left(1 - \frac{H}{H_c}\right)(\varepsilon\Gamma + rcH_X)\right)_X\right]_X. \tag{4.56}$$

Integrating the above expression gives

$$-K - cH + H^3 = -H^3\left[\left(1 - \frac{H}{H_c}\right)(\varepsilon\Gamma + rcH_X)\right]_X \tag{4.57}$$

The boundary condition (4.52) requires that the RHS $\to 0$ so again we have that $K = cH_- - H_-^3 = cH_+ - H_+^3$, and have a shock speed given by (4.53). Equation (4.57) is no longer a simple algebraic relationship, as in (4.51), so we consider what behaviour we expect this shock to exhibit.

We first define

$$\begin{aligned} \phi &= H - \frac{H^2}{2H_c} \\ \Rightarrow \phi_X &= \left(1 - \frac{H}{H_c}\right) H_X. \end{aligned} \tag{4.58}$$

Since $H < H_c$ there is also a critical ϕ value taken as $\phi_c = H_c/2$. This relationship is illustrated in Figure 4.11. We are also able to rearrange (4.58) to get an expression

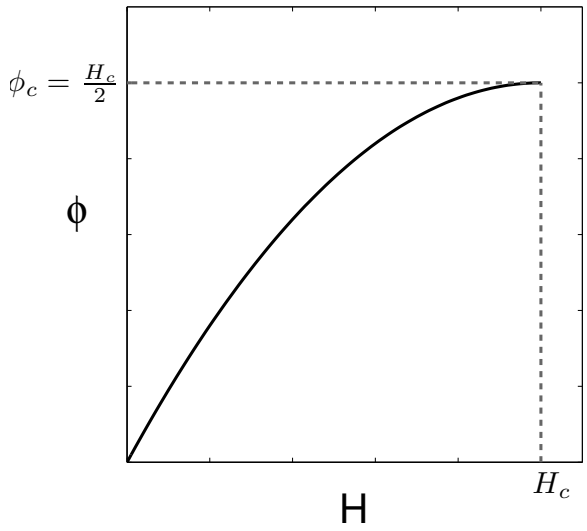

Figure 4.11: A plot of ϕ versus H.

for H in terms of ϕ,

$$H = H_c - \sqrt{H_c^2 - 2H_c\phi}, \tag{4.59}$$

which, on re-arrangement, gives

$$1 - \frac{H}{H_c} = \sqrt{1 - \frac{\phi}{\phi_c}}, \tag{4.60}$$

and so we can write H_X as

$$H_X = \frac{\phi_X}{\sqrt{1 - \phi/\phi_c}}. \tag{4.61}$$

Now, given all these expressions for H in terms of ϕ we can re-write (4.57) as an equation for ϕ,

$$\phi_{XX} - \delta\frac{\phi_X}{\sqrt{1 - \phi/\phi_c}} + V'(\phi) = 0, \tag{4.62}$$

where

$$V'(\phi) = \frac{K - cH + H^3}{rcH^3} \tag{4.63}$$

and $\delta = \varepsilon\Gamma/rcH_c$. This is as an equation for a damped non-linear oscillator. We plot $V'(\phi)$ in Figure 4.12(a) and also solve (4.63) together with (4.60) and plot a

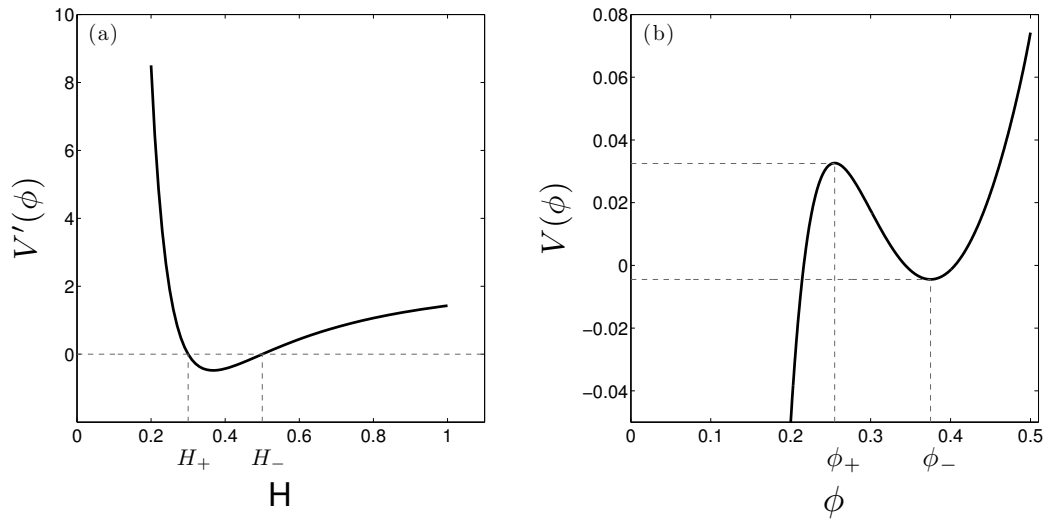

Figure 4.12: (a): Plot of $V'(\phi)$ versus H from (4.63). (b) A solution of (4.63), which gives us $V(\phi)$ as a function of ϕ. We have that $c = [H^3]_-^+ / [H]_-^+$ and $K = cH_- - H_-^3 = cH_+ - H_+^3$ in (4.63). We further take $H_c = 1.0$, $r = 0.9$, and $H_- = 0.5$, $H_+ = 0.3 \Rightarrow \phi_- = 0.375$ and $\phi_+ = 0.255$ for this set of plots.

solution for $V(\phi)$ in Figure 4.12(b). $V(\phi)$ is a multivalued function, suggesting that we can expect oscillatory solutions to (4.62). However, we do not expect the solution to oscillate continuously, since the term in δ is a damping term. As $X \to -\infty$ we expect that solutions will be damped out.

We finally solve the nonlinear oscillator equation (4.62) with boundary conditions that $\phi \Rightarrow \phi_-$ as $X \Rightarrow -\infty$ and $\phi \Rightarrow \phi_+$ as $X \Rightarrow +\infty$. In Figure 4.13 we plot this solution for two different values of the damping coefficient δ. It is clear that a larger value of δ results in the oscillations being damped out more rapidly.

This analysis agrees with solutions obtained to the equation for the water layer earlier in the chapter. In particular, Figures 4.9(b) and 4.10(b) illustrate solutions of (4.48) with $\nu = 0.001$ and $\nu = 0.01$ respectively. Oscillations are damped out. The amplitude and length of the wave train decreases for larger values of ν, which is in agreement with the solutions plotted in Figures 4.9 and 4.10 since the damping coefficient $\delta \propto \nu^{1/2}$. Furthermore, the wavelength of oscillations seen in simulations increases with ν, in agreement with the analysis where the shock width is $\varepsilon = \nu^{1/2}$.

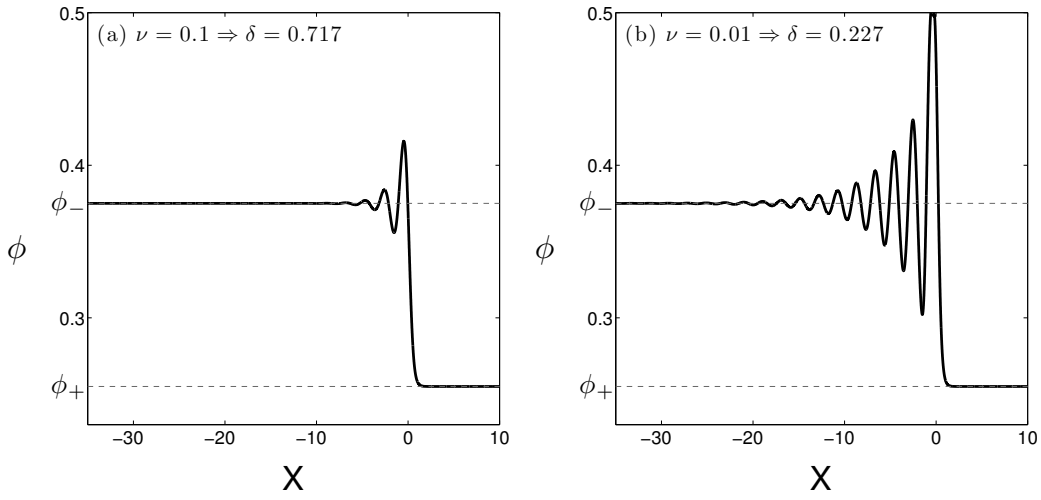

Figure 4.13: Plots of solutions of (4.62) for two different values of the damping term coefficient $\delta = \varepsilon\Gamma/rcH_c$, as labelled $H_c = 1.0$, $\Gamma = 1$, $\varepsilon = \nu^{1/2}$, $r = 0.9$, $c = [H^3]^+_- / [H]^+_-$ and $K = cH_- - H_-^3 = cH_+ - H_+^3$. For this plot we specifically take $H_- = 0.5$ and $H_+ = 0.3$, as for Figure 4.12, $\Rightarrow \phi_- = 0.375$ and $\phi_+ = 0.255$.

4.5 Summary and conclusions

The theory developed in this chapter provides a simplified model of subglacial water flow at the base of an ice sheet. We assume the meltwater flows in a Weertman-Creyts-Schoof style rough-bedded film (Weertman, 1972; Creyts and Schoof, 2009), where the roughness is taken into account by assuming some distribution of supporting clasts at the ice-bed interface. A water film can exist if it is thinner than the supporting clast size.

We have carried out a basic analysis of the behaviour of such a water film and investigated its inherent properties. By using the method of characteristics we see that the governing equation for water depth results in shock formation if there is an initial negative gradient in water depth in the direction of flow. An abrupt shock forms in the case where $\nu = 0$ in the governing equation (4.29), but when $\nu > 0$ this term diffuses out the shock front e.g. Figures 4.9(b),4.9(c). Analysis of the structure of the shock front shows that in the case of non-zero melt the effect of the $\mathcal{O}(\nu)$ term is to damp out oscillations that will occur behind the shock front. This is in agreement

with what we see in numerical solutions of the governing equation

The work done in this chapter paves the way for a detailed investigation of the coupling of the water with both the sediment and the ice, which are considered in subsequent chapters of the thesis. Given the interesting behaviour observed in this chapter, we expect that there is potential for significant nonlinear feedback in the coupled behaviour.

Chapter 5

Water-sediment interaction beneath ice streams

5.1 Introduction

Subglacial drainage systems commonly discussed in the literature, such as the linked cavity and the Röthlisberger systems are framed in the context of the classic hard glacial bed: cavities/thin patchy films form behind bedrock protrusions, while the channels are mostly thought of as rock-floored and incised into the ice. However, evidence suggests the observed rapid basal velocities in ice streams are facilitated by the presence of a layer of till at the base of the sheet (Alley *et al.*, 1986, 1987; Blankenship *et al.*, 1986; Tulaczyk *et al.*, 2000a), and therefore these hard-bed drainage systems may not be relevant to subglacial water flow beneath ice streams. In the previous chapter we have presented a model for a thin film of water flowing over till, but we have assumed that the till is stationary and does not deform, pretty much like hard bedrock. In this chapter we are therefore interested in studying the interaction between the water layer described in the previous chapter and a sediment layer.

For likely permeabilities and till thickness, Darcian porous flow through the sediment is likely to be insufficient to evacuate all the meltwater present at the bed (e.g., Boulton and Jones, 1979; Walder and Fowler, 1994), and as such the till is water-saturated. As a granular material the till is expected to deform with Coulomb-plastic

behaviour (e.g., Iverson *et al.*, 1998; Tulaczyk *et al.*, 2000b; Kamb, 2001; Joughin *et al.*, 2004; Schoof, 2004), and its behaviour depends on the effective pressure, which is determined by the drainage system. In an effort to understand the possible nature of subglacial water flow over a layer of saturated till, Walder and Fowler (1994) developed the concept of canals, which are in essence inverted Röthlisberger channels, incised in the underlying sediment. In their work they showed that these canals would form a distributed system due to the fact that effective pressure decreased with increasing water flux. However, their model can be criticised on a number of counts. For example, they assumed a pseudo-viscous flow law for till, an assumption that has led to debate (Iverson and Iverson, 2001; Fowler, 2003; Jop *et al.*, 2006), and is still an open question. More pertinently, Walder and Fowler's model was conceptually similar to that of Röthlisberger, insofar as it assumed a local channel surrounded by till and ice, and the resulting model was consequently essentially algebraic in nature. It also made assumptions concerning the shape of channels. One was that the canal depth was controlled by that necessary to enable bedload transport to remove sediment. The other was that whether a canal or channel formed depended on the relative softness of ice and till, and this depended on the effective pressure.

The aim of this chapter is therefore to develop a more sophisticated model of subglacial stream flow. In particular, we abandon the restrictive view of channels or canals as pre-formed, and we aim to describe their evolution from an initial spatially extensive rough water film. As an eventual aim, we hope to characterise sub-ice stream water flow sufficiently to allow for a useful parameterisation of its effect on the ice flow. This requires a suitable averaging over the presumably small scale dimensions of hydraulic stream flow to describe the larger scale ice stream flow. This would be a big improvement on recent work looking at ice stream formation over a Coulomb-plastic till, which simply uses a basic diffusion equation to describe the evolution of a water layer over saturated till, assuming the water diffuses from high to low effective

thickness (Bueler and Brown, 2008; Bougamont *et al.*, 2011; Van Pelt and Oerlemans, 2012).

In this work we assume that the water film is able to transport sediment, and so consider mass conservation of both water and sediment, as well as a closure relation for the ice, when deriving governing equations for the water film depth H, the bed elevation b, and the effective pressure N at the bed. We do not consider the ice flow in the work at this stage; we assume the ice is sat there moving at a constant velocity with constant surface slope.

The chapter is organised as follows. In Section 5.2 we present the coupled model for water and sediment transport that forms the basis of the rest of the study. The model is non-dimensionalised and simplified in Section 5.3 and a reduced version of it is solved in Section 5.4. A discussion of the results and their context follows in Section 5.5.

5.2 Setup and governing equations

We assume the water flow in a thin film configuration, as shown in Figure 4.1 in Chapter 4. We now, however, introduce a deformable sediment bed into the setup, and so might expect the sediment to deform such that water may flow in discrete channels for example, as illustrated in Figure 5.1. Our model will show that this may be possible.

5.2.1 Water layer equations

From Chapter 4, we have an equation for mass conservation of water (4.6) and for ice closure (4.9). These give us two equations for two unknowns—the water layer depth,

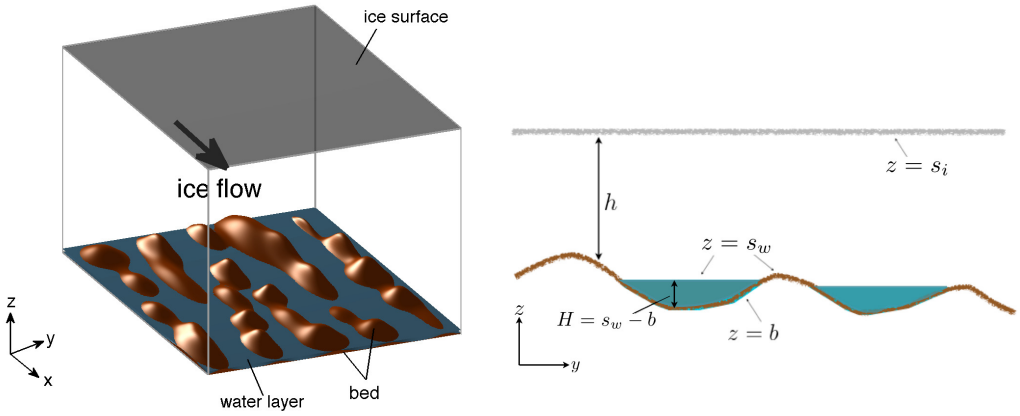

Figure 5.1: Geometry of the flow under consideration. A 3D schematic and a cross-section with notation labelled.

H, and the effective pressure, N. We also have that

$$H = s_w - b, \tag{5.1}$$

and since we took the bed elevation to be known, and constant, from this we knew the lower ice surface elevation, s_w. However, now we allow for an evolving sediment surface, and so we need to consider a further closure equation for the system. Note that strictly the ice closure equation should also have another term added into it to allow for the evolving bed elevation but we do not consider this here; this closure equation is something that we expect to evolve in the future.

5.2.2 Sediment closure equation

The evolution for the sediment surface at $z = b$ is given by the Exner equation,

$$\frac{\partial b}{\partial t} + \boldsymbol{\nabla} \cdot \mathbf{q}_c + \boldsymbol{\nabla} \cdot \mathbf{q}_b = -E, \tag{5.2}$$

where the volumetric sediment flux has two constituents, a bedload volume flux $\mathbf{q}_b$ and a creep flux $\mathbf{q}_c$. E represents erosion of the bed as suspended sediment.

We suppose

$$\mathbf{q}_c = \frac{1}{2} u_b h_A \hat{\boldsymbol{i}} - \frac{h_A^3}{12\eta_s} \boldsymbol{\nabla} N, \tag{5.3}$$

where $\boldsymbol{i}$ is the unit vector in the ice flow direction x, and h_A is the depth of the deformable sediment. The first term represents the shear-driven deformation by the ice, and the second represents till squeezing by the effective pressure gradient. The depth of the till h_A is determined by the horizon below which the effective pressure (which increases with depth) is sufficiently large that the yield stress is not exceeded. From Fowler (2009, 2010a) it can be taken as

$$h_A = \frac{[\frac{\tau}{\mu} - N]_+}{\Delta\rho_{sw} g(1-\phi)}, \tag{5.4}$$

where $\Delta\rho_{sw} = \rho_s - \rho_w$ (ρ_s being the sediment density), μ is the coefficient of inter-particle friction and ϕ the porosity of the bed. Also note that τ is the actual shear stress at the interface, rather than the 'far-field' basal stress τ_b used in the sliding law. The two are related (Fowler, 2009) if we suppose that the actual sliding law at the interface is

$$\tau = f(u_b, N),$$

by

$$\tau_b = \overline{f(u_b, N)},$$

where the overline denotes a local spatial average, over areas with zero effective pressure (i.e. where there are water streams in the sediment) and areas with non-zero effective pressure (i.e. inter-water-stream areas). For example, if the sliding law is of the form $\tau = c u_b^p N^q$, since we don't expect the sliding velocity u_b to be perturbed to

leading order at the interface, we can re-write (5.4) in terms of the basal stress as

$$h_A = \frac{[\frac{\tau_b N^b}{\mu \overline{N}^b} - N]_+}{\Delta \rho_{sw} g (1-\phi)}. \tag{5.5}$$

$\overline{N}$ is a local average; we not not delve into the details of how to define it mathematically since we end up taking h_A as constant in the work presented in this chapter.

The bedload transport is defined in terms of an effective stress, which combines the stress exerted by the water flow, $\boldsymbol{\tau}_w = -\frac{1}{2} H \boldsymbol{\nabla} \psi$, with the effect of bedslope. The effective stress can therefore be written

$$\boldsymbol{\tau}_e = -\frac{1}{2} H \boldsymbol{\nabla} \psi - \Delta \rho_{sw} g D_s \boldsymbol{\nabla} b \tag{5.6}$$

where D_s is the grain size of the sediment (Fowler, 2010a). Later, when we consider the bimodal nature of till, D_s will be taken to be the size of the smaller, hydraulically mobile grains. We then write

$$\mathbf{q}_b = B \boldsymbol{\tau}_e \tag{5.7}$$

where B is generally a function of τ_w, reflecting the idea that it is the water stress which determines the size of the motion, but direction is determined by $\boldsymbol{\tau}_e$. Typical forms, such as the Meyer-Peter/Muller law, involve measurements on turbulent flows, together with absence of transport below some critical yield stress, thus $B \propto [\tau_w - \tau_c]^{1/2}$. However, for thin films and relatively slow flows we may take a simple linear form, since we expect the flow to be laminar, and not necessarily well-described by sub-aerial formulae. Note also the specific requirement that $B = 0$ when $\tau_w = 0$ i.e. $H = 0$. Furthermore, the bedload is a constituent of the fluid flow, so that the water flux is really considered to comprise both water and mobile sediment. In particular, we must have $q_b < q$.

With these expressions for $\mathbf{q}_b$ and $\mathbf{q}_c$, the closure relation takes the form

$$\frac{\partial b}{\partial t} + \boldsymbol{\nabla}.\left[\frac{1}{2}u_b h_A \hat{\boldsymbol{\imath}} - \frac{h_A^3}{12\eta_s}\boldsymbol{\nabla}N\right] - \boldsymbol{\nabla}.\left[B\left(\frac{1}{2}H\boldsymbol{\nabla}\psi + \Delta\rho_{sw}gD_s\boldsymbol{\nabla}b\right)\right] + E = 0. \quad (5.8)$$

The erosion term E represents net erosion (erosion minus deposition). The suspended sediment load, if present at all, is likely to come into an equilibrium in which $E = 0$ and so we assume this to be the case throughout the rest of this work.

5.2.3 Boundary Conditions

We consider a rectangular domain where $0 < x < l$ and $-W < y < W$. In general, we assume that $x = 0$ might represent a divide, or a cold-temperate transition line, while $x = l$ would typically be a land-based terminus or a grounding line. For these cases, a suitable inflow boundary condition is

$$H = 0 \quad \text{at} \quad x = 0. \quad (5.9a)$$

When $H = 0$ there is no hydraulic sediment transport and so we must also choose $B = 0$ (it can't be taken as a constant). If the till is not deformable, then $h_A = 0$. If it is, however, the till flux is $\frac{1}{2}h_A u_b \mathbf{i}$, and then we have

$$\frac{\partial N}{\partial x} = 0 \quad \text{at} \quad x = 0, \quad (5.9b)$$

so that there is no till flux across the divide. Alternatively we could prescribe an inlet water mass flow.

At the outflow ($x = l$) in the case of a grounding line it is suitable to take

$$N = 0 \quad \text{at} \quad x = l. \quad (5.10a)$$

Alternatively, to avoid the possibility of boundary layers forming we could simply take

$$\frac{\partial H}{\partial x} = 0 \quad \text{at} \quad x = l. \tag{5.10b}$$

Finally, at the sides of the domain we may prescribe no transverse flux of water or sediment. We therefore have

$$\frac{\partial \psi}{\partial y} = \frac{\partial H}{\partial y} = 0 \tag{5.11}$$

at $y = \pm W$.

5.3 Non-dimensionalisation and reduction

We have four equations relating four unknowns—H, s_w, b and N.

$$H = s_w - b, \tag{5.12a}$$

$$\frac{\partial H}{\partial t} = \boldsymbol{\nabla}.\left[\frac{H^3}{12\eta_w}\boldsymbol{\nabla}\psi\right] + \Gamma, \tag{5.12b}$$

$$\frac{\partial H}{\partial t} = \frac{\rho_w}{\rho_i}\Gamma - \frac{N l_0}{\eta_i \Lambda(H)}, \tag{5.12c}$$

$$\frac{\partial b}{\partial t} = -\boldsymbol{\nabla}.\left[\frac{1}{2}u_b h_A \hat{\boldsymbol{\imath}} - \frac{h_A^3}{12\eta_s}\boldsymbol{\nabla}N\right] + \boldsymbol{\nabla}.\left[B\left(\frac{1}{2}H\boldsymbol{\nabla}\psi + \Delta\rho_{sw} g D_s \boldsymbol{\nabla} b\right)\right], \tag{5.12d}$$

where

$$\Gamma = \frac{G + \mathbf{u}_b.\boldsymbol{\tau}_b - q_T + \mathbf{q}.\boldsymbol{\nabla}\psi}{\rho_w L}, \tag{5.13a}$$

$$\psi = \rho_i g s_i + \Delta\rho_{wi} g s_w - N, \tag{5.13b}$$

$$h_A = \frac{[\frac{\tau_b N^b}{\mu \overline{N}^b} - N]_+}{\Delta\rho_{sw} g(1-\phi)}. \tag{5.13c}$$

Values of constants in the equations are given in Table 1 at the start of the thesis. The ice surface elevation, s_i, and ice velocity $\mathbf{u}_b$ are also unknowns (that in theory

could be solved for using the Stokes equations), but we assume they are known at this stage to avoid further complication. Their values are taken as the scale values in Table 5.1, with $s_i \sim h_0$.

Before non-dimensionalising, we refine our concept of the basal water layer. Following Creyts and Schoof (2009), we conceive of till as having a bimodal grain size distribution, and we suppose that the larger grains have a diameter D_M which is larger than the basic water film thickness, $D_M \gtrsim 5\,\mathrm{mm}$. The ice load is thus supported by by the larger clasts, while the smaller grains of size D_s may be transported by the flow. The shear stress exerted on the small particles is $\tau_w \approx \frac{1}{2}\rho_i g \Omega H$, and the consequent Shields stress is

$$\tau^* = \frac{\tau_w}{\Delta\rho_{sw} g D_s} = \frac{\rho_i \Omega H}{2\Delta\rho_{sw} D_s}, \tag{5.14}$$

and since sediment transport occurs for $\tau^* \gtrsim \tau_c^* \approx 0.05$, the basic water film will transport particles of size less than a critical value

$$D_c \approx \frac{10\rho_i \Omega H}{\Delta\rho_{sw}} \approx 30\,\mu\mathrm{m}, \tag{5.15}$$

corresponding to silt.

The effective pressure exerted on the bed will then vary with the water film thickness. When $H = 0$, then $N = \sigma_{nn} - p_w$, where σ_{nn} is the normal stress in the ice, and p_w is the pore water pressure in the sediment. As H increases, N will decrease until it reaches zero when $H = D_M$. For $H > D_M$, the ice is properly separated from the bed, and we term the consequent water flow a stream, as opposed to a film.

5.3.1 Scalings

As in the previous chapter, we assume typical length scales $x_0 \sim 500\,\mathrm{km} = 5 \times 10^5\,\mathrm{m}$, $s_i \sim h \sim 10^3\,\mathrm{m}$, and an effective pressure scale $N_0 \sim 4 \times 10^4\,\mathrm{Pa}$ (Blankenship *et al.*,

1987). We take the upper ice surface to have slope Ω in the downstream x direction, i.e. $\boldsymbol{\nabla} s_i = (-\Omega, 0)$, and also take the ice velocity scale as $u_0 \sim 100\,\mathrm{m\,yr^{-1}}$. Other scales are chosen to balance dominant terms in equations (5.12b), (5.12c) and (5.12d). The scales for Γ, $\mathbf{q}$, H, ψ and l_0 are therefore the same as in Section 4.2.3, but we consider a slightly different scale for bed elevation, from the expression for the hydraulic potential i.e.

$$S_0 \sim \frac{N_0}{\Delta\rho_{wi} g} \sim 49\,\mathrm{m}, \tag{5.16}$$

motivated by work considering subglacial bedforms and so also modelling sediment deformation Fowler (2010a,b).

Now, before considering all the scales in equation 5.12d, we need to determine a scale for the bedload volume flux $B \sim q_B/\tau_e$. Collins (1979) sees large fluctuations in sediment discharge when taking measurements from a turbulent Alpine proglacial stream during the glacier's ablation period. Values range between approximately $0.1\,\mathrm{g\,l^{-1}}$ and $2\,\mathrm{g\,l^{-1}}$. Furthermore, Knudsen *et al.* (2007) suggest a typical sediment discharge is of the order of $10\,\mathrm{g\,l^{-1}}$, for discharge that occurs after a major surge has occurred at Kuannersuit Glacier, Greenland. We expect this to be an overestimate in the context of ice streams and based on these studies take $1\,\mathrm{g\,l^{-1}}$ as a more sensible order of magnitude estimate. Given that $1\,\mathrm{g\,l^{-1}} = 1\,\mathrm{kg\,m^{-4}}$ and $\rho_s = 2.6 \times 10^3\,\mathrm{kg\,m^{-3}}$ (Fowler, 2010a), the proportion of sediment present in the meltwater is therefore $1/2.6 \times 10^3 = 3.85 \times 10^{-3}$. Furthermore, given $q_0 \sim 5 \times 10^{-5}\,\mathrm{m^2\,s^{-1}}$, we have that the sediment discharge, $q_s \sim 3.85 \times 10^{-4} \times 5 \times 10^{-5}\,\mathrm{m^2\,s^{-1}} = 1.925 \times 10^{-8}\,\mathrm{m^2\,s^{-1}}$ and we

Symbol	Description	Typical value
x_0	$[x]$- horizontal length scale	$5 \times 10^5\,\mathrm{m}$
h_0	$[z_i]$- vertical length scale for ice	$1000\,\mathrm{m}$
Ω_0	ice surface slope scale	2×10^{-3}
u_0	ice velocity scale	$100\,\mathrm{m\,yr^{-1}} = 3.17 \times 10^{-6}\,\mathrm{m\,s^{-1}}$
τ_0	ice sheet basal shear stress	$10^4\,\mathrm{Pa}$
H_0	meltwater depth scale	$3 \times 10^{-3}\,\mathrm{m}$
S_0	bed elevation depth scale	$49\,\mathrm{m}$
q_0	meltwater flux scale	$5 \times 10^{-5}\,\mathrm{m^2\,s^{-1}}$
N_0	effective pressure scale	$4 \times 10^4\,\mathrm{Pa}$
l_0	clast spacing scale	$0.3\,\mathrm{m}$
h_A	till deformation depth	$4.2\,\mathrm{m}$
t_0	time scale	$2 \times 10^8\,\mathrm{s} \sim 7\,\mathrm{yr}$
Γ_0	melt rate scale	$3.5\,\mathrm{mm\,yr^{-1}} = 10^{-10}\,\mathrm{m\,s^{-1}}$
B_0	sediment transport coefficient scale	$7.12 \times 10^{-7}\,\mathrm{kg^{-1}\,m^3\,s}$

Table 5.1: List of variable scales in the governing equations for the coupled sediment and water equations (5.12a) - (5.12d).

expect the bedload volume flux downstream to scale with this i.e.

$$\mathbf{q}_b = B\boldsymbol{\tau}_e = B\left(-\frac{1}{2}H\boldsymbol{\nabla}\psi - \Delta\rho_{sw}gD_s\boldsymbol{\nabla}b\right) \tag{5.17a}$$

$$\sim B\frac{H_0}{2}\rho_i g\Omega_0 \sim 1.925 \times 10^{-8}\,\mathrm{m^2\,s^{-1}}$$

$$\Rightarrow B \sim \frac{2 \times 1.925 \times 10^{-8}\,\mathrm{m^2\,s^{-1}}}{3 \times 10^{-3}\,\mathrm{m} \times 917\,\mathrm{kg\,m^{-3}} \times 9.81\,\mathrm{m\,s^{-2}} \times 2 \times 10^{-3}} \sim 7.12 \times 10^{-7}\,\mathrm{kg^{-1}\,m^3\,s} \tag{5.17b}$$

Finally, we can also determine the time scale t_0 by balancing the rate of change of water depth with the term representing the shear-driven deformation of the sediment by the ice. For this we need a scale for the till deformation depth, which comes from

(5.13c) and can be taken as

$$h_A \sim \frac{N_0}{\Delta\rho_{sw} g(1-\phi)} = \frac{4\times10^4\,\mathrm{Pa}}{1.6\times10^3\,\mathrm{kg\,m^{-3}}\times 9.81\,\mathrm{m\,s^{-2}}\times(1-0.4)} \sim 4.2\,\mathrm{m} \tag{5.18}$$

$$\begin{aligned} \frac{\partial b}{\partial t} &\sim \frac{\partial}{\partial x}\left(\frac{1}{2}u_b h_A \boldsymbol{i}\right) \\ \frac{H_0}{t_0} &\sim \frac{u_0 h_A}{2x_0} \\ &\sim \frac{100\,\mathrm{m\,yr^{-1}}\times 4.2\,\mathrm{m}}{2\times5\times10^5\,\mathrm{m}} \\ \Rightarrow t_0 &\sim \frac{3\times10^{-3}\,\mathrm{m}\times 2\times5\times10^5\,\mathrm{m}}{100\,\mathrm{m\,yr^{-1}}\times 4.2\,\mathrm{m}} \sim 7\,\mathrm{yr} \end{aligned} \tag{5.19}$$

A summary of the scales chosen is in Table 5.1.

5.3.2 Non-dimensionalisation

Using the scalings given above, the non-dimensional form of the governing equations (5.12a)-(5.12d) becomes:

$$H = \frac{1}{\delta_{HS}} s_w - b, \tag{5.20a}$$

$$\varepsilon \frac{\partial H}{\partial t} = \boldsymbol{\nabla}.\left[H^3 \boldsymbol{\nabla}\psi\right] + \Gamma, \tag{5.20b}$$

$$\varepsilon r \frac{\partial H}{\partial t} = \Gamma - \frac{N}{\Lambda(H)}, \tag{5.20c}$$

$$\frac{\partial b}{\partial t} = -\boldsymbol{\nabla}\cdot\left[u_b h_A \hat{\boldsymbol{\imath}} - \beta h_A^3 \boldsymbol{\nabla} N\right] + \sigma \boldsymbol{\nabla}\cdot\left[B\left(H\boldsymbol{\nabla}\psi + \lambda\boldsymbol{\nabla}b\right)\right], \tag{5.20d}$$

where

$$\psi = s_i + \nu\left(s_w - N\right), \tag{5.21}$$

Symbol	Description	Typical value
δ_{HS}	$\frac{H_0}{S_0}$	6×10^{-5}
ε	$\frac{H_0}{\Gamma_0 t_0}$	10^{-1}
ν	$\frac{N_0}{\rho_i g h_0}$	4×10^{-3}
r	$\frac{\rho_i}{\rho_w}$	0.9
β	$\frac{h_A^2 N_0}{6\eta_s x_0 u_0}$	2.7×10^{-5}
σ	$\frac{B_0 \rho_i g h_0 t_0}{2x_0^2}$	10^{-3}
λ	$\frac{2\Delta\rho_{sw} D_s}{\rho_i h_0}$	10^{-7}

Table 5.2: Descriptions and typical values of non-dimensional parameters in the coupled water and sediment evolution equations (5.20a) - (5.20d).

Definitions and values of the non-dimensional parameters are given in Table 5.2.

5.3.3 Simplification and reduction

Now we are interested in the possibility of a lateral, stream-forming instability where downstream sediment transport is compensated by cross-stream sediment transport. The ubiquitous presence of mega-scale glacial lineations (MSGL) suggests that in ice streams lateral variations of effective pressure occur over a length scale $l_{GL} \sim 300\,\mathrm{m}$ (in contrast to longitudinal variations occurring on the length scale $l_x \sim 1000\,\mathrm{km} = 10^6\,\mathrm{m}$). This observation motivates a similar analysis to the work presented here by Fowler (2010a). In his work he considers a slightly simpler version of (5.20a) - (5.20d), focusing on the interaction of water flow with ice deformation, and hence the formation of MSGL. Note, however, that the presence of these undulations is thought to be caused by the interaction of the ice flow with the underlying sediments (Fowler, 2010a) and in a complete theory we would need to study the interaction of the sediment, water and ice altogether (allowing for the evolution of b, s_i and s_w), so that these waveforms evolve naturally. However, here we are interested in the formation of finite depth streams in the sediment and we leave the fully coupled

behaviour to a later study.

We therefore want to simplify the non-dimensional model, keeping just the key ingredients that allow us to learn about the interaction of the water and sediment at the bed. For simplicity, we first define

$$\Psi = s_w - N. \tag{5.22}$$

We also take the melt rate of the ice to be constant i.e. $\Gamma = 1$.

Under these assumptions, our governing equations simplify down to

$$H = \frac{1}{\delta_{HS}} s_w - b, \tag{5.23a}$$

$$\varepsilon \frac{\partial H}{\partial t} + \frac{\partial}{\partial x}\left(\Omega H^3\right) = \nu \boldsymbol{\nabla} \cdot \left[H^3 \boldsymbol{\nabla} \Psi\right] + 1, \tag{5.23b}$$

$$\varepsilon r \frac{\partial H}{\partial t} = 1 - \frac{N}{\Lambda(H)}, \tag{5.23c}$$

$$\frac{\partial b}{\partial t} + \boldsymbol{\nabla} \cdot \left[u_b h_A \hat{\boldsymbol{\imath}} - \beta h_A^3 \boldsymbol{\nabla} N\right] = -\sigma \frac{\partial}{\partial x}\left(B \Omega H\right) + \sigma \boldsymbol{\nabla} \cdot \left[B\left(\nu H \boldsymbol{\nabla} \Psi + \lambda \boldsymbol{\nabla} b\right)\right], \tag{5.23d}$$

giving four equations for H, b, s_w and N.

An x-dependent uniform state exists where

$$\Psi = 0, \tag{5.24a}$$

$$N = \Lambda(H), \tag{5.24b}$$

$$\Omega H^3 = x, \tag{5.24c}$$

and the sediment surface will be given as a solution of

$$\frac{\partial b}{\partial t} = -\frac{\partial}{\partial x}\left(u_b h_A\right) + \beta \frac{\partial}{\partial x}\left(h_A^3 \frac{\partial N}{\partial x}\right) - \sigma \frac{\partial}{\partial x}\left(B \Omega H\right) + \sigma \frac{\partial}{\partial x}\left[B \lambda \frac{\partial b}{\partial x}\right]. \tag{5.25}$$

This will result in a slow subsidence of the bed, as the sediment is eroded, given

approximately by

$$b \approx -\left[\frac{\partial}{\partial x}\left(h_A u_b\right)\right] t, \tag{5.26}$$

since σ and β are both small. This solution corresponds to an erosion rate of approximately half a millimetre per year.

This basic state is unstable—a result analogous to that in Fowler (2010a). We denote the uniform state as H_0 and consider small perturbations around this basic state. Assuming s_w is constant, we have that $\frac{\partial b}{\partial x} = -\frac{\partial H}{\partial x}$, and $N \approx 1 - H$ (taking $H_c = 1$). The perturbation, $\hat{H}$, must therefore satisfy an equation of the form

$$\frac{\partial \hat{H}}{\partial t} = \beta \frac{\partial}{\partial x}\left(h_A^3 \frac{\partial \hat{H}}{\partial x}\right) + \sigma \frac{\partial}{\partial x}\left(B\Omega \hat{H}\right) + \sigma \frac{\partial}{\partial x}\left[B\lambda \frac{\partial \hat{H}}{\partial x}\right]. \tag{5.27}$$

By consideration of solutions of the form $\hat{H} = H' \exp(\alpha t + ikx)$, we see that instability may occur if $\frac{\partial}{\partial x}(B\Omega) > 0$. This is a more general condition than in Fowler (2010a) where the basic state was uniform with Ω taken as constant, and so instability occurred if $\frac{\partial B}{\partial x} > 0$. Instead, we can see here that instability may still occur if B is constant, so long as the surface slope increases down flow (analogous to the Smith and Bretherton (1972) situation for river flow). We would expect this to the the case near the grounding line in an ice stream.

Our interest, more specifically however, lies in the evolution of this instability as H increases to larger depths. We first rescale y so to get a scale separation of the derivatives. More explicitly we take

$$y_0 \sim \sqrt{\beta} x_0 \tag{5.28}$$

corresponding to a length scale of 2.5 km. On substitution into (5.23b) - (5.23d)

$$\varepsilon\frac{\partial H}{\partial t}+\frac{\partial}{\partial x}\left(\Omega H^3\right)=\frac{\nu}{\beta}\frac{\partial}{\partial y}\left[H^3\frac{\partial\Psi}{\partial y}\right]+\nu\frac{\partial}{\partial x}\left[H^3\frac{\partial\Psi}{\partial x}\right]+1, \tag{5.29a}$$

$$\varepsilon r\frac{\partial H}{\partial t}=1-\frac{N}{\Lambda(H)}, \tag{5.29b}$$

$$\frac{\partial b}{\partial t}+\frac{\partial}{\partial x}\left(u_b h_A\right)-\frac{\partial}{\partial y}\left(h_A^3\frac{\partial N}{\partial y}\right)-\beta\frac{\partial}{\partial x}\left(h_A^3\frac{\partial N}{\partial x}\right)=-\sigma\frac{\partial}{\partial x}\left(B\Omega H\right)$$
$$+\frac{\sigma\nu}{\beta}\frac{\partial}{\partial y}\left(BH\frac{\partial\Psi}{\partial y}\right)+\sigma\nu\frac{\partial}{\partial x}\left(BH\frac{\partial\Psi}{\partial x}\right)+\frac{\sigma\lambda}{\beta}\frac{\partial}{\partial y}\left(B\frac{\partial b}{\partial y}\right)+\sigma\lambda\frac{\partial}{\partial x}\left(B\frac{\partial b}{\partial x}\right). \tag{5.29c}$$

Neglecting the lowest order terms in ε, ν, β and σ, these can be simplified down to read

$$\frac{\partial}{\partial y}\left[H^3\frac{\partial\Psi}{\partial y}\right]=\frac{\beta}{\nu}\left[\frac{\partial}{\partial x}\left(\Omega H^3\right)-1\right], \tag{5.30a}$$

$$N=\Lambda(H), \tag{5.30b}$$

$$\frac{\partial b}{\partial t}+\frac{\partial}{\partial x}\left(u_b h_A\right)-\frac{\partial}{\partial y}\left(h_A^3\frac{\partial N}{\partial y}\right)=\frac{\sigma\nu}{\beta}\frac{\partial}{\partial y}\left(BH\frac{\partial\Psi}{\partial y}\right). \tag{5.30c}$$

In particular, since we are not interested in the moulding of the subglacial topography, for now we assume that the ice remains locally flat (i.e. $\frac{\partial s_w}{\partial y}\approx 0$). We could allow for subsidence of s_w, i.e.

$$\frac{\partial s_w}{\partial t}=-\delta_{HS}w_s, \tag{5.31}$$

where w_s should be chosen from the ice dynamics, but we do not consider this detail here since we are not explicitly modelling the ice. We therefore also take $\partial s_w/\partial t=0$.

Now the leading order approximation to (5.30a) tells us that

$$\frac{\partial}{\partial y}\left[H^3\frac{\partial\Psi}{\partial y}\right]=0, \tag{5.32}$$

which implies that Ψ must be constant cross-stream otherwise there would be net transverse flow. This prompts the neglect of the term on the RHS of (5.30c). Now strictly $\Psi_y = 0$ together with $(s_w)_y = 0$ implies that $N_y = 0$ also. However, in recent work that includes a simple representation of ice dynamics (Kyrke-Smith and Fowler, 2014), we see that Ψ has a further correction term in it, and that $(s_w)_y \neq 0$ either and so it is valid to take $\Psi_y = 0$ but not to then assume $N_y = 0$. We do not examine this in detail here, and refer the reader to Kyrke-Smith and Fowler (2014). We therefore simplify (5.30c) down to read

$$\begin{aligned} \frac{\partial H}{\partial t} &= \frac{\partial}{\partial x}\left(u_b h_A\right) - \frac{\partial}{\partial y}\left(h_A^3 \frac{\partial \Lambda}{\partial H}\frac{\partial H}{\partial y}\right) \\ &\approx \frac{\partial}{\partial x}\left(u_b h_A\right) + \frac{\partial}{\partial y}\left(h_A^3 \frac{\partial H}{\partial y}\right), \end{aligned} \tag{5.33}$$

under the simplest possible choice of $\Lambda(H)$ that represents the decrease in clast spacing as H increases i.e. $\Lambda(H) = 1 - H$.

Furthermore, since we prescribe no sediment or water flow through the sides of the domain (5.11), integrating (5.30a) across the domain yields

$$\frac{1}{2W}\int_{-W}^{W} \Omega H^3 \,\mathrm{dy} = x, \tag{5.34}$$

which needs to be solved in conjunction with (5.33).

5.4 Solutions of the reduced model

We wish to show here that the solution of the evolution equation (5.33), together with the boundary conditions (5.11) at the edge of the domain, and the conservation law (in the form of an integral constraint (5.34)), results in solutions that take the form of steady stream-like features incised in the sediment. Details of the solutions exactly will vary depending on choices of $\Lambda(H)$, h_A and B, but we propose that the

key ingredients are all contained in the following reduced version of the model:

$$\frac{\partial H}{\partial t} = 1 + \frac{\partial^2 H}{\partial y^2}, \tag{5.35a}$$

together with

$$\frac{\partial H}{\partial y} = 0 \quad \text{on} \quad y = \pm W, \tag{5.35b}$$

$$\frac{1}{2W}\int_{-W}^{W} H^3 \,\mathrm{dy} = x. \tag{5.35c}$$

For the boundary conditions, the only further assumption that has been made is that $\Omega = 1$ i.e. the downstream surface slope is constant. However, to reduce (5.33) to (5.35a) a couple more assumptions have been made. Firstly, for simplicity, we also take $W = 0$. Also, in ice streams we expect the ice velocity to increase downstream, presumably due to decreasing effective pressure in a distributed drainage system in which q is also increasing. Decreasing N also implies increasing h_A (from (5.13c)), so this advective term is positive and we take it to be a constant ($= 1$). The only potential problem with this assumption would be if h_A reached zero. This could occur if either till deformation ceases (no water, and the effective pressure becomes very large), or because separation of the bed from the ice occurs (if H too large and N reaches zero). The former occurs if $H = 0$, and so we state that the differential equation is only valid when $H > 0$, and otherwise we specify $H = 0$. For the latter, it is slightly different. If $h_A = 0$ because $N = 0$, then then this will be as a result of the water depth having reached the critical depth at which all supporting clasts are drowned. At this point we would then expect a stream to form, separating the bed from the ice, with the depth of the stream rapidly decreases to zero at its margins. At this point we would expect stream sediment transport to provide an alternative source and diffusive term, but we avoid such complications involved in

modelling this by assuming that in this case sufficiently coarse clasts exist to prevent N actually reaching zero. h_A therefore remains positive, and so $\frac{\partial}{\partial x}(u_b h_A) = 1$ is a valid assumption.

5.4.1 Single stream solution

A problem in the above model (which cannot be avoided—it is not caused by any of our simplifications) is that the solution for the differential equation with the boundary conditions is inconsistent with the integral constraint. This is because of the latent assumption that $H = 0$. The model for H should really be

$$\frac{\partial H}{\partial t} = 1 + \frac{\partial^2 H}{\partial y^2} \quad \text{or} \quad H = 0, \tag{5.36a}$$

$$H_y \to 0 \quad \text{as} \quad y \to \infty \quad \text{or} \quad H \to 0 \quad \text{as} \quad y \to \pm\infty \tag{5.36b}$$

$$\lim_{W\to\infty} \frac{1}{2W} \int_{-W}^{W} H^3 \,\mathrm{dy} = x. \tag{5.36c}$$

However, the solution must contain regions of finite support, and we expect there to be a steady state consisting of a number of streams. The simplest solution consists of a periodic array of streams, each of which (with a suitable choice of origin) satisfies the system

$$\frac{\partial H}{\partial t} = 1 + \frac{\partial^2 H}{\partial y^2} \quad \text{or} \quad H = 0, \tag{5.37a}$$

$$H = 0 \quad \text{on} \quad y = \pm\lambda, \tag{5.37b}$$

$$\int_{-\lambda}^{\lambda} H^3 \,\mathrm{dy} = \tilde{x}. \tag{5.37c}$$

where λ is the the width of the stream and $\tilde{x} = 2\lambda x$.

The steady symmetric solution is

$$H = \frac{1}{2}\left(y_m^2 - y^2\right), \qquad |y| < y_m,$$
$$H = 0, \qquad |y| > y_m \tag{5.38}$$

where

$$y_m = \left(\frac{35\tilde{x}}{4}\right)^{1/7}, \tag{5.39}$$

and we must have

$$\lambda > \left(\frac{35}{2}\right)^{1/6}, \tag{5.40}$$

i.e. $y_m > \lambda$. We show that this solution is stable by solving the problem numerically, as outlined in the following section.

5.4.2 Numerical methods

5.4.2.1 Change of Variables

This problem has a moving boundary. This can be numerically complex to solve for and so we follow a method devised by Fowler *et al.* (2007), where a very similar problem arises. We first suppose that the solution of (5.37) is symmetric so that $\frac{\partial H}{\partial y} = 0$ at $y = 0$ and we need only consider half the domain.

We change variables from y, t to X, T, defined by

$$T = t \tag{5.41a}$$
$$X = \int_0^y H^3(y', t)\,\mathrm{dy}. \tag{5.41b}$$

The chain rule gives

$$\frac{\partial}{\partial t} = \frac{\partial}{\partial T} + \frac{\partial X}{\partial t}\frac{\partial}{\partial X}, \tag{5.42a}$$

$$\frac{\partial}{\partial y} = H^3\frac{\partial}{\partial X}, \tag{5.42b}$$

and applying these to the inverse function $y(X,T)$, gives

$$0 = \frac{\partial y}{\partial T} + \frac{\partial X}{\partial t}\frac{\partial y}{\partial X}, \tag{5.43a}$$

$$1 = H^3\frac{\partial y}{\partial X}. \tag{5.43b}$$

Substituting these into (5.37), and writing $T = t$ results in

$$\frac{\partial H}{\partial t} - H^3\frac{\partial y}{\partial t}\frac{\partial H}{\partial X} = 1 + H^3\frac{\partial}{\partial X}\left(H^3\frac{\partial H}{\partial X}\right) \tag{5.44a}$$

$$\frac{\partial y}{\partial X} = \frac{1}{H^3}. \tag{5.44b}$$

We define

$$\frac{\partial y}{\partial t} = w, \tag{5.45a}$$

$$X_f = \frac{1}{2}\tilde{x}, \tag{5.45b}$$

$$(X_f - X)^{1/4} = \xi_f - \xi, \tag{5.45c}$$

$$\xi_f = X_f^{1/4}, \tag{5.45d}$$

and obtain an equation for w by differentiating (5.44b) and substituting for $\frac{\partial H}{\partial t}$ from (5.44a). Our governing equations therefore become

$$\frac{\partial H}{\partial t} = \phi, \tag{5.46a}$$

$$\frac{\partial w}{\partial \xi} = -\frac{12\left(\xi_f - \xi\right)^3\phi}{H^4}, \tag{5.46b}$$

where

$$\phi = 1 + \frac{w}{4}J + \frac{1}{16}A\frac{\partial J}{\partial \xi}, \tag{5.47}$$

with

$$A = \left(\frac{H}{\xi_f - \xi}\right)^3, \tag{5.48a}$$

$$J = \left(\frac{H}{\xi_f - \xi}\right)^3 \frac{\partial H}{\partial \xi} = A\frac{\partial H}{\partial \xi}. \tag{5.48b}$$

The boundary conditions are

$$w = \frac{\partial H}{\partial \xi} = 0 \quad \text{at} \quad \xi = 0, \tag{5.49a}$$

$$H = 0 \quad \text{at} \quad \xi = \xi_f, \tag{5.49b}$$

the second of which implies that $\phi = 0$ at $\xi = \xi_f$ by (5.46a).

The front position y_m where $H = 0$ is defined by

$$\frac{\partial y_m}{\partial t} = w\left(\xi_f, t\right). \tag{5.50}$$

5.4.2.2 Discretisation

To solve (5.46a), (5.46b) we step forward H explicitly, and then calculate w by quadrature. Although the equations appear degenerate, a local analysis of the behaviour near $\xi = \xi_f$ shows that

$$H = \alpha(t)\left(\xi - \xi_f\right) + \frac{4\left(w_f\alpha^4 - 4\right)}{5\alpha^6}\left(\xi - \xi_f\right)^2 + ..., \tag{5.51a}$$

$$w = w_f + \frac{12\dot{\alpha}}{\alpha^4}\left(\xi - \xi_f\right) + ..., \tag{5.51b}$$

where $w_f = w(\xi_f, t)$.

Nevertheless, there is still some awkwardness in making the finite-difference ap-

proximation near $\xi = \xi_f$. To overcome this awkwardness we introduce two simplifications. Firstly, we redefine

$$A = \begin{cases} \left(\frac{H}{\xi_f - \xi}\right)^3 & \text{if } \xi < \xi_f, \\ -\left[\left.\frac{\partial H}{\partial \xi}\right|_{\xi=\xi_f}\right]^3 & \text{if } \xi = \xi_f, \end{cases} \tag{5.52a}$$

$$J = \begin{cases} \left(\frac{H}{\xi_f - \xi}\right)^3 \frac{\partial H}{\partial \xi} & \text{if } \xi < \xi_f, \\ -\left[\left.\frac{\partial H}{\partial \xi}\right|_{\xi=\xi_f}\right]^4 & \text{if } \xi = \xi_f. \end{cases} \tag{5.52b}$$

We also replace w with $\theta = wH^3$ to make (5.46b) behave better near the boundary. Equations (5.46a)- (5.47) are therefore replaced by

$$\frac{\partial H}{\partial t} = \phi, \tag{5.53a}$$

$$\frac{\partial \theta}{\partial \xi} = -\frac{12H^2}{A}\left(1 + \frac{1}{16}A\frac{\partial J}{\partial \xi}\right), \tag{5.53b}$$

where

$$\phi = 1 + \frac{\theta}{4H^3}J + \frac{1}{16}A\frac{\partial J}{\partial \xi}, \tag{5.54}$$

The boundary conditions also become

$$\frac{\partial H}{\partial \xi} = \theta = 0 \quad \text{at} \quad \xi = 0, \tag{5.55a}$$

$$H = \theta = 0 \quad \text{at} \quad \xi = \xi_f, \tag{5.55b}$$

which helps prevent blow-up near the boundary.

A simple explicit finite-difference scheme results in (5.53a) and (5.53b) approxi-

mated as

$$\frac{H_i^{n+1} - H_i^n}{\Delta t} = \phi_i^n, \tag{5.56a}$$

$$\frac{\theta_{i+1} - \theta_i}{\Delta \xi} = 12 \frac{H_{i+\frac{1}{2}}^2}{A_{i+\frac{1}{2}}} \left(1 + \frac{1}{16} A_{i+\frac{1}{2}} \frac{J_{i+1} - J_i}{\Delta \xi}\right), \tag{5.56b}$$

with

$$\phi_i = \begin{cases} 1 + \frac{1}{4}\frac{\theta_i A_i}{H_i^3}\left(\frac{H_i - H_{i-1}}{\Delta \xi}\right) + \frac{1}{16} A_i \left(\frac{J_{i+1} - J_i}{\Delta \xi}\right), & i = 1, ..., N-1, \\ 0 & i = N, \end{cases} \tag{5.57}$$

where $\Delta\xi$ is the step size and $\xi_f = N\Delta\xi$. The backward difference for the advective term is used if $\theta_i > 0$, otherwise the forward difference is used. We further have

$$A_i = \begin{cases} \left(\frac{H_i}{\xi_f - i\Delta\xi}\right)^3 & i = 1, ..., N-1, \\ -\left(\frac{H_i - H_{i-1}}{\Delta \xi}\right)^3 & i = N, \end{cases} \tag{5.58a}$$

$$J_i = A_i \frac{H_i - H_{i-1}}{\Delta \xi} \tag{5.58b}$$

5.4.3 Numerical Results

We solve equations (5.56a) and (5.56b) for $H(\xi, t)$ and $\theta(\xi, t)$. We take $\tilde{x} = 2 \Rightarrow X_f = \xi_f = 1$.

From (5.45c), we have that $X = 1 - (1 - \xi)^4$, and so substitute this in to write $H(\xi, t)$ as $H(X, t)$. We then solve for $H(y, t)$ by integrating (5.44b) using the simple discretisation

$$y_{i+1} = y_i + \frac{X_{i+1} - X_i}{[0.5(H_{i+1} + H_i)]^3}. \tag{5.59}$$

y_m is taken as y at $i = N$. A slight inaccuracy is introduced due to this being an estimate of y half a grid point before the end of the grid but the inaccuracy decreases

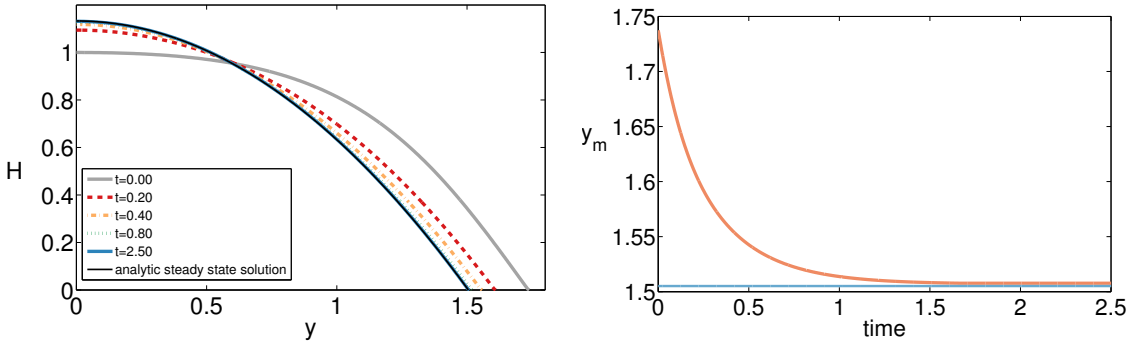

(a) Snapshopts of $H(y)$ at specified times

(b) Evolution of y_m to reach the steady-state illustrated by the blue line

Figure 5.2: Simulation results with initial condition $H(\xi) = \cos\left(\frac{\pi}{2}\xi\right)$, $N = 600$ and $\Delta t = 10^{-6}$.

as the grid spacing decreases.

We ran simulations for various different initial conditions, with a range of grid resolutions and time steps. Two examples of solutions are illustrated below. Figure 5.2 shows a solution initialised with a small perturbation from the steady state, and Figure 5.3 a solution initialised with a large perturbation from the steady state. For both we plot the depth profile and the evolution of the stream margin. The depth profile is in a sense inverted since the stream is incised downwards into the sediment. It can be seen that both relax to the steady state as time progresses.

Comparisons of the accuracy of the steady state solution shows that as grid resolution is increased the accuracy of the solution for the position of the stream edge increases. Figure 5.4 plots the steady state position of the edge of the stream for solutions at a range of grid resolutions.

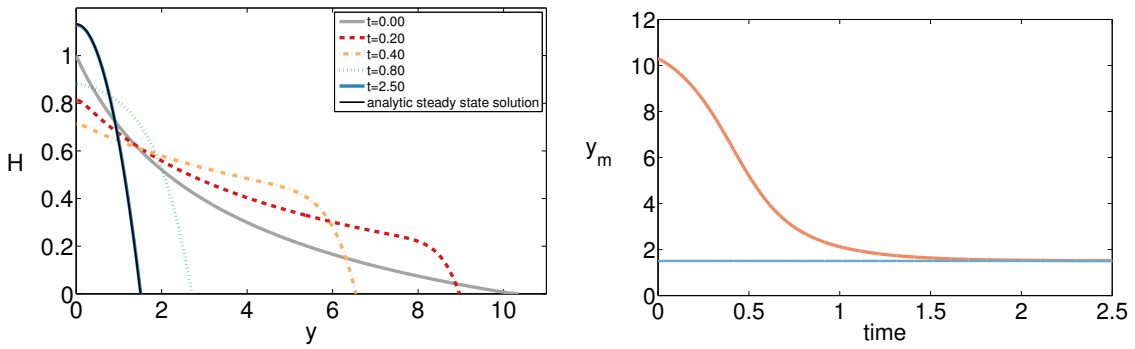

(a) Snapshopts of $H(y)$ at specified times

(b) Evolution of y_m to reach the steady-state illustrated by the blue line

Figure 5.3: Simulation results with initial condition $H(\xi) = \frac{e^{1-\xi}-1}{e-1}$, $N = 400$ and $\Delta t = 10^{-5}$.

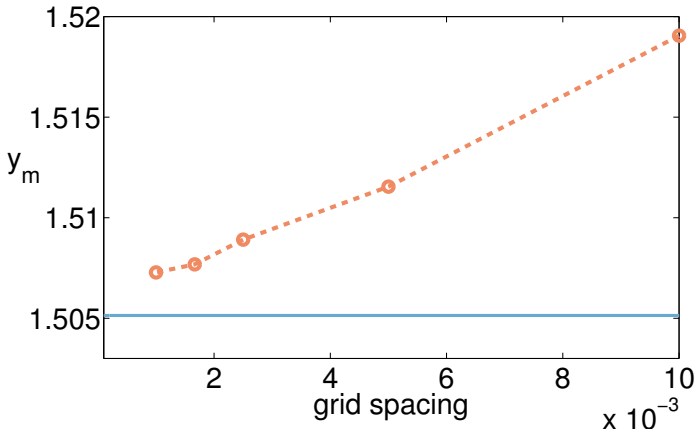

Figure 5.4: The position of the stream edge (y_m) plotted for various values of grid spacing. Individual points are shown with orange circles. The blue line represents the analytic value of y_m for the steady state.

5.5 Summary and Conclusions

The instant formation of finite width streams in the evolution of (5.37) is a singular solution, and we associate it with the neglect of the x derivative terms. Our expectation is that in reality, a smooth profile near $x = 0$ will develop pinch-out points where $H = 0$ downstream. To examine this we would need to re-introduce the x derivative terms into the equations and solve the system described by (5.20a)–(5.20d) in two dimensions. Given the complications of the numerical solve for the simplified system

described by (5.37), we do not attempt such a solve and leave this for future work. Furthermore, though the model is complicated, it does introduce simplifications that can be criticised. Examples of these are the assumptions of constant ice viscosity for ice, a rheology for till deformation that assumes a yield stress based on solid fraction and an effective viscosity that is prescribed and the use of a simple linear bedload sediment transport law. The closure relationship between water film depth and effective pressure is also shrouded with uncertainty, but we are simply aiming to capture the leading-order behaviour, and hope that more refined descriptions of such things will be included in the future.

Nevertheless the results of our simplified, one-dimensional study suggest that for a Creyts-Schoof water film of thickness $\approx 5\,\mathrm{mm}$ beneath an ice sheet, a uniform film is unstable, just as in the case for subaerial overland flow, and the model suggests that 'streams' of finite width will develop. Given the simplifying assumptions made in this chapter, these streams appear more like huge swamps, with a lateral extent of the order 1000 m and a depth barely deeper than the water layer. However, in a paper recently submitted (Kyrke-Smith and Fowler, 2014), we re-introduce a basic description of ice dynamics, and the re-scaling that results from this suggests that the streams will still be more like swamps, but with widths of tens to hundreds of metres, and depths of the order a centimetre. Such a style of drainage is consistent with the notion of a patchy film beneath ice sheets Alley (1989), and is also consistent with Engelhardt and Kamb (2013) who made direct borehole observations beneath the Kamb Ice Stream of an ice/till gap of one or two centimetres in their borehole 5.

What we are less able to comment on is the observation by Engelhardt and Kamb of a 1.4 m deep water layer at borehole 9, indicative in their view of a subglacial channel. An alternative possibility is that this layer may represent a subglacial cavity formed by a developing drumlin field following the shutdown of the ice stream, but the issue remains as to the origin of the water. Concentration of an average 5 mm

thick water film into a 1.4 m deep channel represents an amplification of 280, and such a stream of width for example 5 m would drain all the water from subglacial melt from a surrounding width of 1,400 m. While this seems feasible, our theory does not apparently provide the mechanism for such deep streams. On the other hand, the water-saturated till itself contains a large quantity of water: eight metres of till with porosity 0.4 has an effective film depth of 3.2 m! Following the Kamb Ice Stream's shutdown, the basal effective pressure would have risen, and this allows the water to be sucked out of the till. In that case it would be possible to explain the presence of pockets of water, though not within the present theory, which ignores groundwater storage (cf. Christoffersen *et al.* (2014)).

So what perspective does the work in this chapter provide for present-day subglacial drainage? While there are many simplifications made, the work does point towards the possibility that basal water flows through a patchwork of swamps, perhaps with occasional floods opening larger channels, although the dynamics of these are yet to be investigated. Furthermore, there are many paths for future research that emerge from this study given that we have presented a detailed mathematical formulation describing the coupled sediment and water behaviour, but only solved it in one distinct limiting case.

Chapter 6

Coupled ice flow and meltwater drainage

6.1 Introduction

The aim of this chapter is to bring together the work in previous chapters to explicitly consider the interaction between ice flow and subglacial hydrology, in a bid to further understand ice streaming. While using a multivalued flux law at the bed may produce ice-stream flow, as in Chapter 3, it would be beneficial if we could reproduce this behaviour as a more direct consequence of the physical mechanisms governing basal sliding velocities.

It is well known that rapid basal sliding, as observed in Antarctic ice steams, can be attributed to the presence of meltwater at the bed (Engelhardt and Kamb, 1997). More specifically, frictional resistance at the base is intrinsically linked to the water pressure in the meltwater drainage system (Bindschadler, 1983; Iken and Bindschadler, 1986; Clarke, 2005). This effect is usually considered in terms of the effective pressure (4.3)—sliding at the bed can occur when the effective pressure is small and the weight of the ice is largely supported by the underlying water. The dependence of the basal sliding velocity on both basal shear stress and the effective pressure at the bed is given through a sliding law (Budd *et al.*, 1979; Cuffey and Paterson, 2010; Fowler, 2011b). To improve understanding of variations in basal

velocity we must investigate the physical basis and consequences of the sliding law as the basal boundary condition. Since the behaviour of the subglacial hydrologic system governs the effective pressure at the ice-bed interface, this involves coupling together our descriptions of ice and hydrology.

In Chapter 4 we formulated a model for the evolution of a water layer over saturated till. In Chapter 5 we further considered water-sediment interaction, and showed that water may choose to flow in shallow, swamp-like streams incised in the sediment at the bed. In this chapter we therefore adjust our water layer model slightly, to account for the fact that it won't necessarily keep growing in depth evenly, and couple it to the ice-flow model in Chapter 2. This provides a tool for detailed examination of the consequences of the coupling of the subglacial hydrology to the ice, in particular in the context of ice streams. Other recent work looking at ice stream formation over till either disregards water transport all together (Bougamont *et al.*, 2011) or uses a diffusion equation to describe the evolution of a water layer over saturated till, assuming the water 'diffuses' from high to low effective thickness (Bueler and Brown, 2008; Sayag and Tziperman, 2008; Van Pelt and Oerlemans, 2012). This work therefore builds on such studies by using a more physically-motivated and detailed model for the water layer when considering the ice-water coupling.

The chapter is organised as follows. In Section 6.2 we present the fully coupled non-dimensional model of the ice-water system, before briefly considering the behaviour of the water layer with a steady ice flow coupled to it in Section 6.3. In Section 6.4 we present numerical solutions to the fully coupled ice-water model that, under certain conditions, results in ice stream flow. The requirements for ice stream flow are discussed in terms of multivalued flux laws and the chosen parameterisations in Section 6.5. We also comment on ice stream width, spacing and the role topography plays in governing where ice streams form.

6.2 Non-dimensional governing equations

6.2.1 Ice Flow

The ice flow is described by the vertically-integrated hybrid of the SIA and SSA presented in Chapter 2. It takes into account both vertical shear stresses and membrane stresses, providing a valid flow description for all flow regimes within a shallow ice sheet. This is particularly important when modelling the emergence of ice streams. A complete description of the model is presented earlier in the thesis, along with a comparison between this model and similar higher-order approaches (Schoof and Hindmarsh, 2010; Gudmundsson, 2003); here we just re-state the non-dimensional equations. In particular, non-dimensional mass conservation and force balance for the ice are given by

$$\frac{\partial h}{\partial t} + \boldsymbol{\nabla} \cdot \left(h\mathbf{u}_b - \lambda \frac{h^{n+2}}{n+2} \left|\boldsymbol{\gamma}\right|^{n-1} \boldsymbol{\nabla} s_i \right) = a, \tag{6.1a}$$

$$\boldsymbol{\tau}_b = h\boldsymbol{\gamma}, \tag{6.1b}$$

where

$$\boldsymbol{\gamma} = -\boldsymbol{\nabla} s_i + \frac{\varepsilon^2}{\lambda} \boldsymbol{\nabla} \cdot \mathbf{S}, \tag{6.2}$$

$\mathbf{S}$ is the resistive stress tensor (Van der Veen, 1999; Hindmarsh, 2012),

$$\mathbf{S} = \boldsymbol{\tau} + \mathbf{I} \operatorname{trace}(\boldsymbol{\tau}) = \begin{bmatrix} 2\tau_{11} + \tau_{22} & \tau_{12} \\ \tau_{12} & \tau_{11} + 2\tau_{22} \end{bmatrix}, \tag{6.3}$$

and a is the accumulation rate (Kyrke-Smith *et al.*, 2013). $\boldsymbol{\tau}$ is the deviatoric stress tensor, related to strain rate through Glen's flow law for ice (Cuffey and Paterson, 2010). Parameter scales are as in Chapter 4, with τ_0, u_0 and d_0 taken to scale as in

Symbol	Description	Typical value
x_0	horizontal length scale	$500\,\mathrm{km}$
d_0	ice depth	$1000\,\mathrm{m}$
Γ_0	melt rate scale	$10^{-10}\,\mathrm{m\,s^{-1}}$
H_0	meltwater depth scale	$3 \times 10^{-3}\,\mathrm{m}$
N_0	effective pressure scale	$4 \times 10^4\,\mathrm{Pa}$
q_0	meltwater flux scale	$5 \times 10^{-5}\,\mathrm{m^2\,s^{-1}}$
u_0	ice velocity scale	$100\,\mathrm{m\,yr^{-1}}$
a_0	accumulation rate scale	$0.2\,\mathrm{m\,yr^{-1}}$
t_i	ice time scale	$5000\,\mathrm{yr}$
t_w	water time scale	$1\,\mathrm{yr}$
τ_0	basal stress scale	$2 \times 10^4\,\mathrm{Pa}$
ψ_0	hydraulic potential scale	$10^7\,\mathrm{Pa}$
l_0	clast spacing	$0.3\,\mathrm{m}$

Table 6.1: List of variable scales in the governing equations for the coupled ice and water equations (6.1 and 6.6).

(4.21)-(4.23), and so we take the accumulation rate scale as

$$a_0 \sim \frac{u_0 d_0}{x_0} \sim 0.2\,\mathrm{m\,yr^{-1}}. \tag{6.4}$$

These scalings are given in Table 6.1, and λ and ε are introduced in Chapter 2 (2.13,2.12) with values given in Table 6.2.

6.2.2 Subglacial water flow

We consider the subglacial water flow model described in Chapter 4. Mass conservation of water is given by (4.25a) with a local Poiseuille flow in the water film driven by gradients in hydraulic potential (4.25c). There is also an ice closure relation balancing opening rate of the film due to meltback of the ice with a viscous creep closure term (4.25b).

However, now that we are considering the ice and water flow together, we need

to take into account the fact the time-scales of the two flows are orders of magnitude different. More specifically, we have two separate time scales,

$$t_i = \frac{x_0}{u_0}, \tag{6.5a}$$

$$t_w = \frac{H_0 x_0}{q_0}, \tag{6.5b}$$

for ice and water respectively.

Since we will be considering the water flow coupled with the ice flow, we non-dimensionalise the water equations with the larger of these time scales, t_i, and so introduce a non-dimensional parameter $\delta_T = t_w/t_i$. Using these scalings, the dimensionless form of the subglacial flow equations becomes

$$\delta_T \frac{\partial H}{\partial t} + \boldsymbol{\nabla}.\mathbf{q} = \Gamma, \tag{6.6a}$$

$$r\delta_T \frac{\partial H}{\partial t} = \Gamma - \frac{N^n}{\Lambda(H)}, \tag{6.6b}$$

where

$$\begin{aligned} \mathbf{q} &= -H^3 \boldsymbol{\nabla}\psi \\ &= H^3 \left(-\boldsymbol{\nabla} s_i - \omega \boldsymbol{\nabla} b - \omega \delta_{Hh} \boldsymbol{\nabla} H + \nu \boldsymbol{\nabla} N\right), \end{aligned} \tag{6.7}$$

and

$$\Gamma = 1 + \mu \mathbf{u}_b.\boldsymbol{\tau}_b - \kappa u^{1/2} + \chi H^3 \left|\boldsymbol{\nabla}\psi\right|^2. \tag{6.8}$$

Dimensionless parameters are given in Table 6.2 and we consider further the prescription of $\Lambda(H)$.

Symbol	Definition	Typical value
r	ρ_i/ρ_w	0.9
ω	$\Delta\rho_{wi}/\rho_i$	0.1
δ_{Hh}	H_0/h_0	3×10^{-6}
ν	$N_0/\left(\rho_i g \Omega_0 x_0\right)$	4×10^{-3}
μ	$\left(\tau_0 u_0\right)/G$	1
κ	$\left(\frac{\rho_i c_p k u_0}{\pi x_0}\right)^{1/2} \frac{\Delta T}{G}$	0.27
χ	$\left(q_0 \psi_0\right)/\left(x_0 G\right)$	10^{-2}
c_0	$c u_0^{1/3} N_0^{1/3}/\tau_0$	1.7
λ	$(\tau_0 d_0)/(\eta_I u_0)$	0.0625
ε	d_0/x_0	2×10^{-3}
δ_T	t_w/t_i	2×10^{-4}

Table 6.2: Descriptions and typical values of non-dimensional parameters in the coupled ice and water equations (6.1 and 6.6).

The simplest choice of $\Lambda(H)$, as assumed in Chapter 4, is the function

$$\Lambda(H) = \begin{cases} 1 - \frac{H}{H_c}, & 0 < H < H_c, \\ \\ 0, & H \geq H_c, \end{cases} \tag{6.9}$$

as illustrated by the dashed grey line in Figure 6.1.

When H reaches H_c, the ice separates from the bed. From (6.6b) we have that

$$N = \left[\Lambda(H)\left(\Gamma - r\delta_T \frac{\partial H}{\partial t}\right)\right]^{1/n}, \tag{6.10}$$

and it is clear that with the above choice of $\Lambda(H)$, $N = 0$ when $H = H_c$, implying that once the ice separates from the bed there is no basal stress. In this context there is then no reason that H cannot increase further locally, with the effective pressure remaining zero. However, in reality we expect that a sheet flow with depth $H > H_c$ is an unstable configuration (Walder, 1982), and a water layer cannot thicken

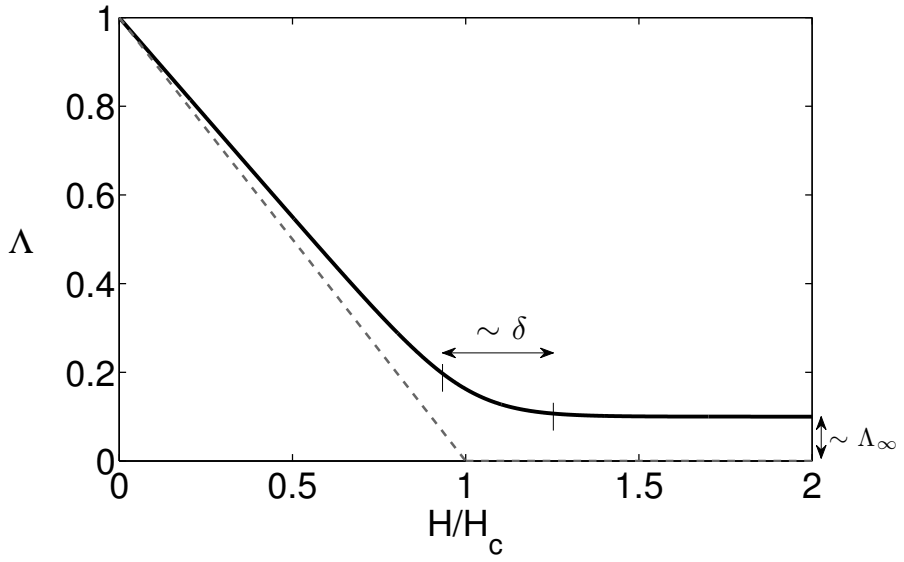

Figure 6.1: Plots of two choices for $\Lambda(H)$. The dashed grey line is given by (6.9) and the solid black line by (6.11) with $\delta = 0.1$, $\Lambda_\infty = 0.1$.

indefinitely. Furthermore, we don't expect that $N = 0$ under ice streams; this would only be the case if there were a subglacial lake. We address this issue by noting that the subglacial flow model has been formulated on the small-scale (of the clast spacing); locally areas of the bed may become submerged but we expect that on the larger scale there will still be areas of the bed providing support to the ice. More specifically, we presume that when H approaches H_c the system becomes unstable to the formation of some kind of locally channelized drainage system at the ice-till interface (Walder and Fowler, 1994), similar also to the subglacial stream formation discussed in Chapter 5. We therefore consider the case where $\Lambda(H)$ decreases to some small limit as H approaches H_c, and specifically we take $\Lambda(H)$ to be a function of the form

$$\Lambda(H) = \Lambda_\infty + \delta\,(1 - \Lambda_\infty) \ln\left[1 + \exp\left(\frac{H_c - H}{\delta H_c}\right)\right], \tag{6.11}$$

where both Λ_∞ and δ are small. The solid black line in Figure 6.1 illustrates this, with $\Lambda_\infty = \delta = 0.1$. From (6.10), we have that $N \sim \Lambda^{1/n}$. This finite limit of $\Lambda(H)$ means that the effective pressure is prevented from reaching zero in the model. Locally we

expect that there are small areas where the effective pressure is zero and $H > H_c$, but on the larger scale (over which we are interested in modelling when investigating ice streams) there are regions of finite support. The choice of $\Lambda(H)$ presented here is meant to represent this globally averaged behaviour in the simplest possible way.

6.2.3 Boundary condition at the ice-water interface

It is necessary to prescribe a boundary condition at the interface between the ice and water in order to couple the subglacial hydraulic flow to the ice flow. This is done through a basal friction law, which relates the basal shear stress, $\boldsymbol{\tau}_b$, to the hydrology, through the general relationship

$$\boldsymbol{\tau}_b = c\,|\mathbf{u}_b|^p\,N^q\frac{\mathbf{u}_b}{|\mathbf{u}_b|}, \tag{6.12}$$

where $\mathbf{u}_b = (u_b, v_b)$ is the sliding velocity of the ice (to be solved for), and p and q are commonly taken as $1/3$ (Budd *et al.*, 1979; Bindschadler, 1983). We furthermore take $c = 6.8 \times 10^4\,\mathrm{Pa}^{2/3}\,\mathrm{s}^{2/3}\,\mathrm{m}^{-1/3}$ to give a sliding speed of the order of $60\,\mathrm{m\,yr}^{-1}$ for typical driving stresses of $10^4\,\mathrm{Pa}$ (Hewitt, 2013).

Non-dimensionalising, this becomes

$$\boldsymbol{\tau}_b = c_0\,|\mathbf{u}_b|^p\,N^q\frac{\mathbf{u}_b}{|\mathbf{u}_b|}, \tag{6.13}$$

where c_0 is defined in Table 6.2.

We now have a complete non-dimensionalised description of the ice-water system. The non-dimensional water flow equations (6.6a,6.6b) can be combined to be written as one equation for H

$$\delta_T\frac{\partial H}{\partial t} - \boldsymbol{\nabla}\cdot\left(H^3(\boldsymbol{\nabla}s_i + \omega\boldsymbol{\nabla}b)\right) = -\nu\boldsymbol{\nabla}\cdot\left[H^3\boldsymbol{\nabla}\left(\Lambda(H)\left(\Gamma - r\delta_T\frac{\partial H}{\partial t}\right)\right)^{1/n}\right] + \Gamma, \tag{6.14a}$$

with N given by

$$N = \left[\Lambda(H)\left(\Gamma - r\delta_T \frac{\partial H}{\partial t}\right)\right]^{1/n} \tag{6.14b}$$

as in Chapter 4. Together with the ice flow equations (6.1a,6.1b) and the basal boundary condition (6.13), we have four coupled equations to be solved for the ice depth, the horizontal ice velocities, and the water layer depth. A description of all the non-dimensional parameters is given in Table 6.2.

6.3 Results for the water layer coupled to a constant ice flow

6.3.1 Hydraulic runaway

Hydraulic runaway is a physical phenomenon that models suggest may occur as a result of a positive feedback between ice velocity and melt rate (Fowler and Johnson, 1995). As ice velocities increase, more meltwater is produced by frictional heating, which results in further ice-bed lubrication and hence faster velocities. We consider whether the basal hydrology model presented here results in such behaviour.

The melting term, Γ in (6.14a), depends on the ice flow. It therefore also has indirect dependence on the water depth, H, since the sliding velocity u_b depends on H through its dependence on N. The ice depth, h, evolves over a long time scale, t_i, through the solution of (6.1a) and (6.1b). We are initially interested in changes in behaviour on a short time scale, so we assume the ice is of constant depth, with constant surface slope, $\boldsymbol{\nabla} s_i = -\hat{\boldsymbol{\imath}}$. Taking the shallow-ice version of basal shear stress

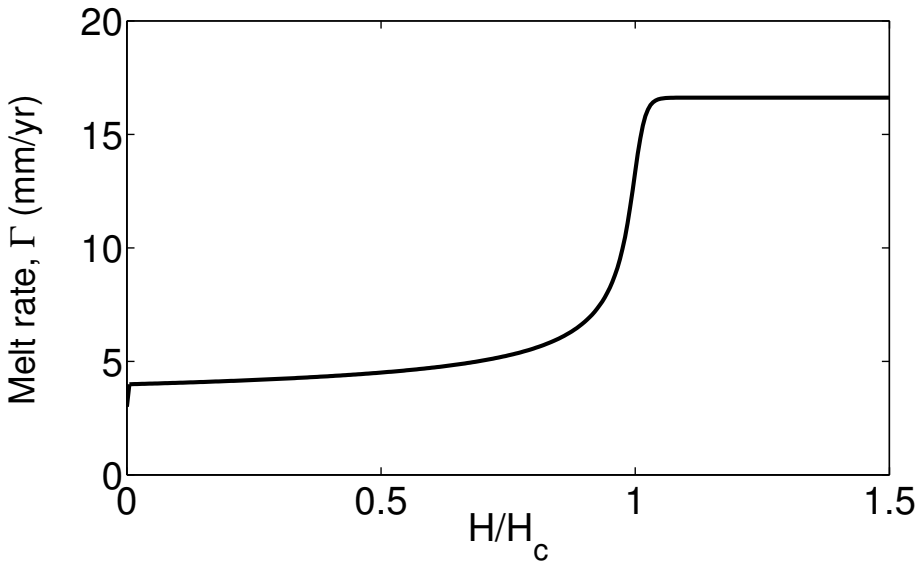

Figure 6.2: $\Gamma(H)$ from (6.15c) with (6.16), and $H_t = 0$, $h = 1$, $\delta = \Lambda_\infty = 0.01$ and other parameter values as given in Table 6.2.

as an approximate sliding law, together with the water equations we then have

$$h = c_0 u_b^p N^q, \tag{6.15a}$$

$$N = \left[\Lambda(H)\left(\Gamma - r\delta_T \frac{\partial H}{\partial t}\right)\right]^{1/n}, \tag{6.15b}$$

$$\Gamma = 1 + \mu h u_b - \kappa u_b^{1/2}, \tag{6.15c}$$

which gives three equations for the three unknowns, u_b, Γ and N.

We seek to eliminate u and N from (6.15a)-(6.15c) to give $\Gamma = \Gamma(H, H_t, h)$. Equation (6.15b) gives us an expression for $N(\Gamma, H)$ and substituting (6.15b) into (6.15a) we have an expression for $u_b(\Gamma, H)$, which is

$$u_b = c_0^{-1/p} h^{1/p} \Lambda(H)^{-q/np} \left(\Gamma - r\delta_T \frac{\partial H}{\partial t}\right)^{-q/np}. \tag{6.16}$$

This can then be substituted into (6.15c) so that we have $\Gamma(H, H_t.h)$.

In Figure 6.2 we plot the quasi-static instance with $\frac{\partial H}{\partial t} \approx 0$ and $\Lambda(H)$ given by

(6.11). As H increases, the melt rate also increases due to an increase in frictional heating. This in turn comes about from an increase in basal velocity by (6.16). From this, it is evident that some kind of hydraulic runaway is inherent in the model, with melt rate increasing rapidly as $H \to H_c$. However, complete runaway is avoided since we do not allow the model to reach zero effective pressure in the subglacial system, which would correspond to no basal stress, and so allow the ice to increase in velocity without limit.

6.3.2 Solutions with a stable water film

We first consider solutions of the water layer equation seperately. We take the ice to have constant surface slope and zero basal slope so that (6.14a) simplifies to

$$\delta_T \frac{\partial H}{\partial t} + \frac{\partial}{\partial x}\left(H^3\right) = -\nu \boldsymbol{\nabla} \cdot \left[H^3 \boldsymbol{\nabla} \left(\Lambda(H) \left(\Gamma - r\delta_T \frac{\partial H}{\partial t} \right) \right)^{1/n} \right] + \Gamma. \tag{6.17}$$

The coupling to the ice occurs through the melt rate term, which, from above, we know increases with both ice depth h and water layer depth H. Rather than considering a constant melt rate, we therefore here take an illustrative Γ function,

$$\Gamma = \frac{h}{H_c^3 - H^3}, \tag{6.18}$$

which both exhibits this behaviour and results in an analytic steady-state solution to (6.17) at leading order. This steady-state solution is given by

$$1 - \left(\frac{H}{H_c}\right)^3 = \left(1 - \frac{x}{x_c}\right)^{1/2}, \tag{6.19}$$

where

$$x_c = \frac{H_c^6}{2h} \tag{6.20}$$

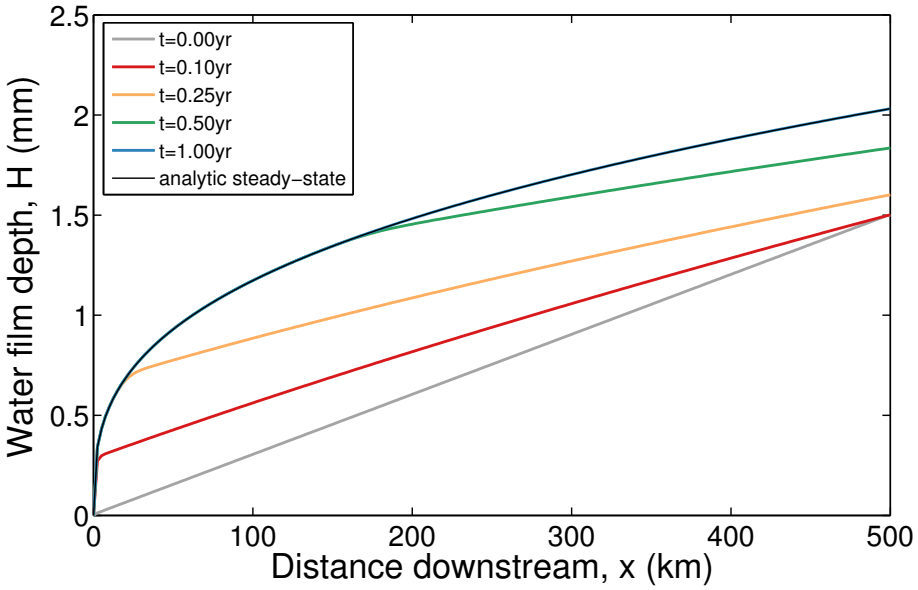

Figure 6.3: Evolution of a solution of the uncoupled water layer equation (4.29) with a melt rate given by (6.18). We take the ice to be of constant depth $h = 1\,\text{km}$ and the critical water depth $H_c = 4.5\,\text{mm}$. $\Lambda_\infty = \delta = 0.01$ and other parameter values for the solution are given in Table 6.2. The solution reaches the steady state solution given by (6.19), plotted in black.

is the non-dimensional position downstream where H reaches H_c. This corresponds to the point at which the bed becomes submerged and the thin film flow becomes a stream. If the bed is sufficiently rough (large H_c) or the ice depth or flux is sufficiently small, then this point would be downstream of the grounding line, and the film flow can exist everywhere.

We ran a suite of simulations solving (4.29) with a melt rate of the form (6.18). As expected, so long as $H_c > (2h)^{1/6}$ then the solutions evolve into the steady state given by (6.19) (plotted in Figure 6.3). However, if $H_c < (2h)^{1/6}$ then the water depth reaches its critical value before the grounding line. The melt rate is no longer defined and an analytic solution does not exist. Our interest therefore now turns to the case where H may reach H_c; we consider the fully coupled water-ice system.

6.4 Results for fully coupled hydrology and ice dynamics

In this section we consider a model with the water layer fully coupled to the ice flow to explore the combined behaviour of the system. The ice flow equations are given by (6.1a) and (6.1b) and we solve them as we did in Chapter 3. The only difference is that in Chapter 3 we used a heuristic triple-valued sliding law together with an equation to describe the relaxation time for the ice to adjust to changes at the bed; these have now been replaced with a sliding law that directly depends on the subglacial conditions (6.13) and the physics-based water layer equation (6.14a).

6.4.1 Model-set up and boundary conditions

We consider a 500 km $\times$ 500 km domain with a uniform bedslope. The upstream end $x = 0$ is a cold-temperate transition line with no water at the bed ($H = 0$). The ice depth satisfies $\partial h/\partial x = 0$ across the boundary, and the inflow is at a constant velocity into the domain ($u_b = u_{in}$ at $x = 0$). Free slip is allowed along this inflow boundary ($\tau_{12} = 0$). To avoid considering grounding-line behaviour, we treat $x = 1$ as an open outflow boundary (Papanastasiou *et al.*, 1992; Sayag and Tziperman, 2009), where the upper surface is free to evolve and $\partial u/\partial x = 0$. Furthermore, a suitable condition for the water layer thickness H, which also avoids the possibility of boundary layers, is $\partial H/\partial x = 0$. The domain is taken to be periodic in the y-direction. With these boundary conditions, we solve (6.14a) coupled to the hybrid ice-flow model outlined in Section 6.2.1. The method for the numerical solution, using the Portable Extensible Toolkit for Scientific Computation (Balay *et al.*, 2013, 2014, 1997), is described in previous work (Kyrke-Smith *et al.*, 2013), and in Chapter 3.

The simulations are initialised with a downstream ice flow that is uniform in the cross-flow direction, i.e. $(u_b, v_b) = (u(x), 0)$. The velocity field $u(x)$ is computed from

the x-component of equation (6.1b) with (6.13). There is no water at the bed and the ice has a constant, uniform thickness, $h = 1.5$. A constant, uniform accumulation rate is applied over the domain. Average accumulation rates in the Siple Coast region of Antarctica are $\sim 140\,\mathrm{kg\,m^{-2}\,yr^{-1}}$ (Joughin and Tulaczyk, 2002), and so we take $a \sim 140\,\mathrm{kg\,m^{-2}\,yr^{-1}}/917\,\mathrm{kg\,m^{-3}} = 0.15\,\mathrm{m\,yr^{-1}}$ as a suitable value. We expect the accumulation rate to be an important parameter in governing the flow behaviour, but do not present a detailed parameter study of the system; here we discuss results that illustrate the basic flow regimes that occur as a result of a realistic accumulation rate applied over the domain.

6.4.2 Flow regimes

6.4.2.1 Laterally uniform flow

We first consider the case where the water film does not get thick enough to submerge all surrounding clasts (i.e. the film depth remains less than the critical depth H_c). If this is the case, the coupled system evolves into a stable steady state. This is illustrated in Figure 6.4, where the critical water depth is $H_c = 2$, corresponding to 6 mm.

The water film evolves rapidly into a quasi-steady-state, similar to that seen in Section 6.3.2, when the water layer is considered alone with a prescribed melt rate. Meanwhile, the ice depth and basal velocities also evolve into a steady state over a longer time scale. Ice depth remains uniform, increasing by $\sim 200\,\mathrm{m}$ over the time of the simulation run. This is due to the downstream ice velocity initially being insufficient to balance the incoming ice flux and accumulation. However, the downstream ice velocity increases and over $\sim 5000\,\mathrm{yrs}$ evolves to put the system in equilibrium. The velocity profile becomes a monotonically increasing function downstream. Over this time, the downstream profile of the water layer remains similar to the profile it reaches within the first year. It does increase in depth by

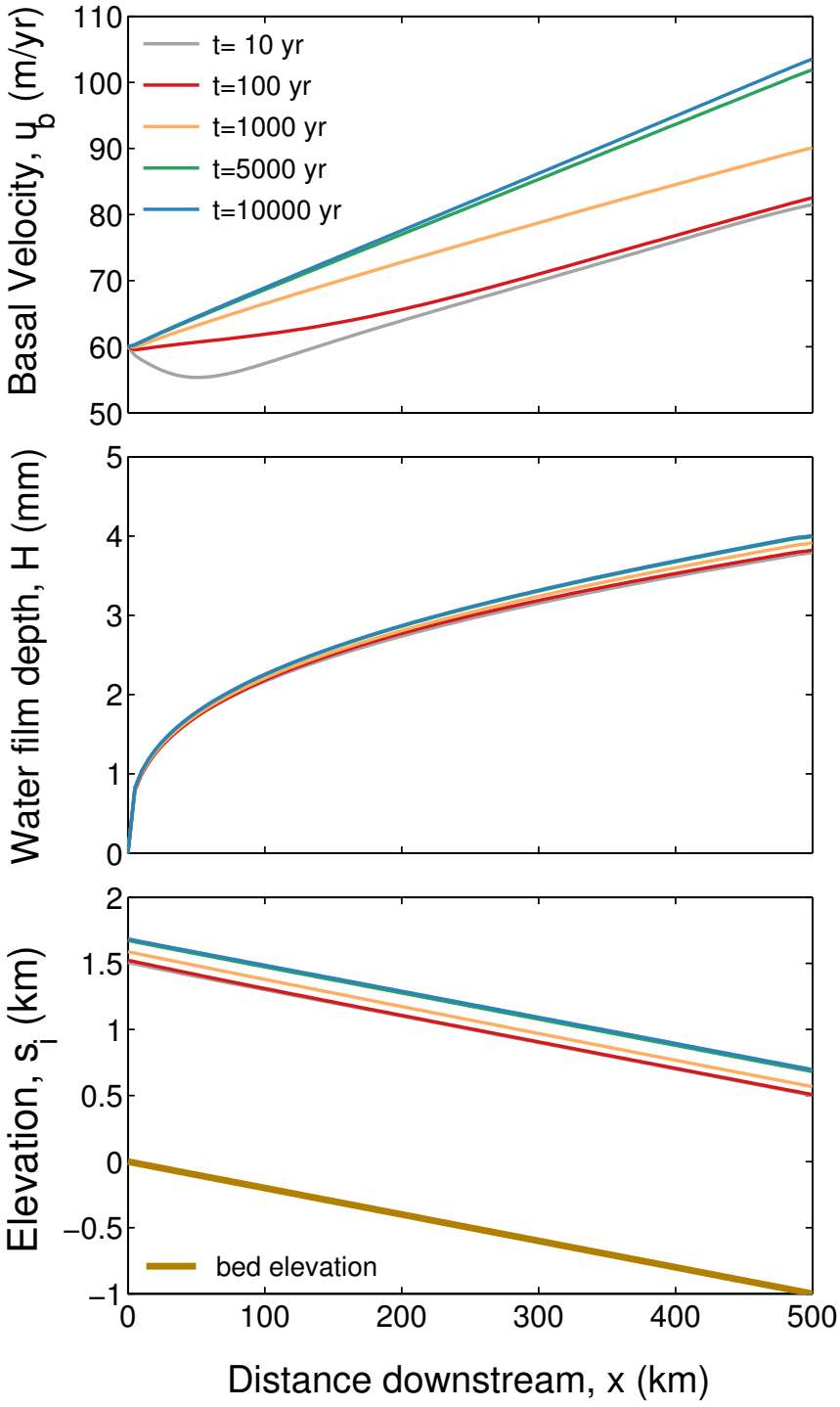

Figure 6.4: Downstream centre-line profiles of basal velocity, water film depth and surface elevation plotted at five different times for the case where the water layer depth does not reach the critical value. Uniform accumulation of magnitude $0.15\,\mathrm{m\,yr^{-1}}$ is applied over the ice sheet and $H_c = 6\,\mathrm{mm}$. There is an inflow of $60\,\mathrm{m\,yr^{-1}}$ into the domain. In (6.11) $\Lambda_\infty = \delta = 0.01$ and other parameter values are given in Table 6.2. The profiles remain uniform across the domain, hence we plot only a downstream profile.

$\sim 0.25\,\mathrm{mm}$ downstream due to increases in ice velocity and ice depth that result in a larger melt rate from frictional heating. The water layer rapidly adjusts for this as the melt-rate increase occurs.

Overall, for the case where there is insufficient meltwater at the bed to submerge all supporting clasts the model is well-behaved and the coupled behaviour is not complicated.

6.4.2.2 Laterally unstable flow

Our interest now turns to the case where the amount of meltwater is sufficient to locally drown all supporting clasts; what effect does the decrease in support provided by the bed have on the ice? Analysis in Section 6.3.1 suggested that melt rate will increase rapidly as the water depth reaches its critical value. In that analysis we assumed that the ice was of constant depth and moving at a constant speed, as we were only interested in behaviour over a short time scale. As a result of that assumption, there is nothing to prevent water depth increasing indefinitely, in turn also allowing the ice velocity to increase (since there is little support at the bed). However, there is a long time-scale feedback that was not taken into account in Section 6.3; over this longer time-scale, the ice depth decreases as a result of increased outflow from the domain. This causes the basal stress, and thus Γ, to decrease. The water depth will start to decrease as a result, therefore decreasing the ice velocity and the total ice flux. This cycle could then repeat once the water depth builds up again to reach the critical depth. In a narrow, confined flow we might expect this to lead to cyclic surging behaviour (similar to Fowler and Schiavi (1998)). However, in a wide flow, a lateral instability that leads to ice streaming occurs; we illustrate this with numerical solutions to the governing equations.

Figure 6.5 shows maps of basal velocity, water depth, and surface elevation at three different times for a simulation run with $H_c = 1.4$, corresponding to a critical

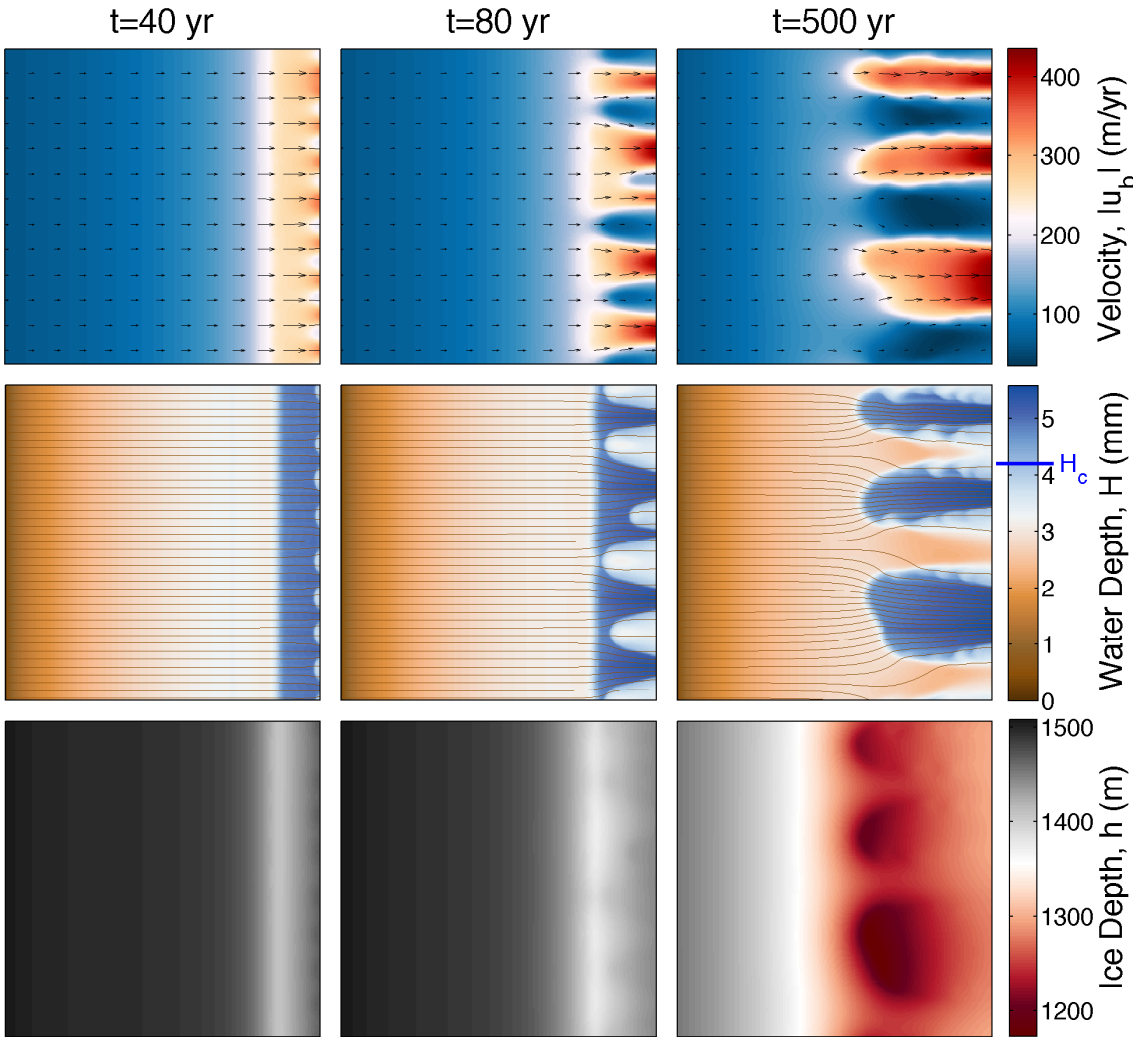

Figure 6.5: Velocity, water film depth and ice depth fields at three distinct times for a simulation run with $H_c = 4.2\,\text{mm}$. Velocity vectors overlie the velocity plots and streamlines for the water flow overlie the water depth plots. Uniform accumulation of magnitude $0.15\,\text{m}\,\text{yr}^{-1}$ is applied over the ice sheet. There is an inflow of $60\,\text{m}\,\text{yr}^{-1}$ into the domain. In (6.11) $\Lambda_\infty = \delta = 0.01$ and other parameter values are given in Table 6.2.

water depth of 4.2 mm. It is evident that this small change in the critical water depth results in dramatic changes in the behaviour of both the water layer and the ice, when compared with the results of the previous section. Initially the flow is stable and uniform cross-stream, but as more water is generated at the bed, H approaches H_c and an instability emerges, as shown in the plots at $t = 40\,\mathrm{yr}$. There is a sudden increase in water depth near the boundary, which results in an increase in ice velocity, since the ice can slip more easily over the bed. A consequential surface lowering of the ice is also evident in the ice depth field. A non-uniformity in the water depth and the ice velocity develops across the domain at this time, as a result of lateral instability (there has been no imposed perturbation to the system). Patches of faster ice flow form, with their positioning corresponding to the discrete areas of deeper water. There is a coarsening of this instability as the system evolves to create distinct stream-like features with a longer wavelength than the initial instability ($t = 80\,\mathrm{yr}$). The streamlines of the water-flow show that water from upstream is drawn toward these water-rich areas, resulting in a positive feedback. These unstable features propagate up the domain, and evolve to create pronounced ice streams, flowing at hundreds of metres per year and of width $\sim$ 50–100 km ($t = 500\,\mathrm{yr}$). The values are of the same order of magnitude as the observed velocity and width of ice streams in Antarctica (e.g. Cuffey and Paterson (2010)), and in other numerical studies (e.g. Bougamont *et al.* (2011); Hindmarsh (2009)). The channelising of water towards these deep-water patches beneath the ice streams is evident from the streamlines of water flow. Moreover, there are depressions in surface elevation at the onset region of the ice streams as a result of the rapid increase in discharge from the region. This is consistent with some observations (Retzlaff and Bentley, 1993). At this point the simulation has reached a quasi-steady-state. The distinct streams do not grow further. There are, however, periodic wave-like features at the edge of the ice streams that propagate along the boundaries (particularly clear in the plots of water depth at 500 yr and in

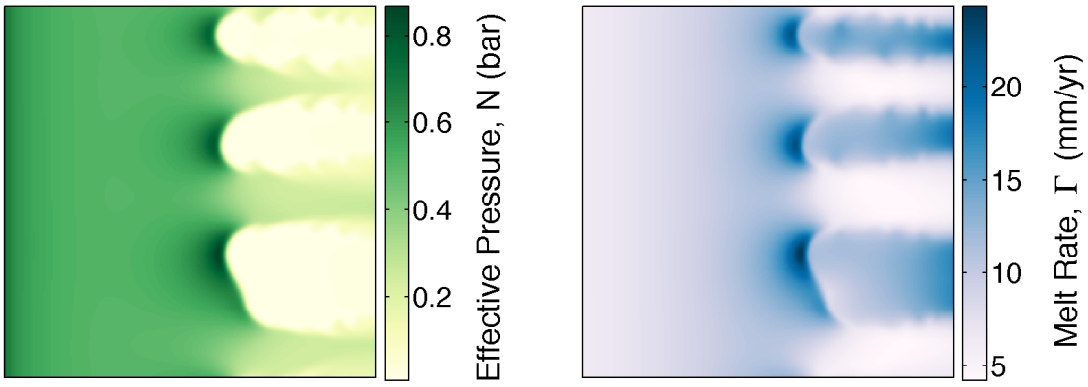

Figure 6.6: Effective pressure and melt rate fields plotted for the simulation shown in Figure 6.5 at $t = 500$ a.

the supplementary online movie of the velocity field in Kyrke-Smith *et al.* (2014)). These could be a result of travelling wave solutions that exist for the water-layer equation (6.14a), although this is purely speculative at present.

Plots of effective pressure and melt rate at $t = 500$ yr are shown in Figure 6.6. The fine scale structures at the edge of the ice streams are evident here as well. We see that the areas of low effective pressure correspond directly to where there is a lot of meltwater, as would be expected from the relationship between N and H (6.14b). Low effective pressure furthermore allows the ice to move more rapidly since there is reduced resistance provided by the bed in these areas (from the sliding law (6.13)). Moreover, the melt rate field illustrates the positive feedback that occurs with more melt being produced underneath the ice streams due to frictional heating from the rapid velocities. The melt rate is, in fact, greatest at the onset zone of the ice streams, due to the large driving stress here from the steep gradient in surface elevation, combined with a higher effective pressure (and therefore higher basal stress), which increases melt rate associated with frictional dissipation. There is consequently enhanced melting at the onset zone—a feedback that will help maintain ice stream flow.

6.5 Discussion

6.5.1 Relationship to multivalued flux laws

We have seen in the previous section that under certain parameter combinations, ice flow can become laterally unstable; this leads to two distinct modes of flow—fast ice streams and slow-moving ice. This is similar to behaviour seen in numerical models that use a triple-valued sliding law as a basal boundary condition (Sayag and Tziperman, 2009; Kyrke-Smith *et al.*, 2013). Can the streaming that emerges in the coupled ice-hydrology model be understood in terms of a triple-valued sliding law, as with the more simplistic model of Fowler and Johnson (1996)?

The water film evolves on a much faster time scale than the ice. Since it is the ice flux we are interested in here, we assume now that the water film is in equilibrium, i.e., we take

$$\frac{\partial}{\partial x}\left(H^3\Omega\right) \approx \Gamma, \tag{6.21a}$$

$$N = \left[\Lambda(H)\Gamma\right]^{1/n}, \tag{6.21b}$$

where $\partial s_i/\partial x = -\Omega$ is the ice surface slope, a constant in the down-flow direction (we also assume there is no cross-flow variation in H or Ω). This is in contrast to the analysis of the water film in Section 6.3.1 when we were interested in the behaviour of the water film over a short time scale and so assumed the ice constant.

Assuming that the melt rate is constant with x in this steady-state water case, and integrating (6.21a) over x gives

$$H^3\Omega = \Gamma x, \tag{6.22}$$

under the assumption that $H = 0$ at $x = 0$, i.e. the inflow boundary is taken to be a divide or a cold-temperature transition line.

We can write the non-dimensionalised sliding law (6.13) as

$$\begin{aligned} h\Omega &= c_0 u_b^p N^q \\ &= c_0 u_b^p \left[\Gamma\Lambda\left([\Gamma x/\Omega]^{1/3}\right)\right]^{q/n}, \end{aligned} \tag{6.23}$$

where

$$\Gamma = 1 + \mu h u_b - \kappa u_b^{1/2}. \tag{6.24}$$

This gives a relationship between ice depth, h, and basal ice velocity, u_b, for ice overlying a water film which is in equilibrium.

Using $\Lambda(H)$ as described by (6.11), we have from (6.23)

$$h\Omega = c_0 u_b^p \left\{\Gamma\left(\Lambda_\infty + \delta\left(1-\Lambda_\infty\right)\ln\left(1+\exp\left(\frac{H_c - (\Gamma x/\Omega)^{1/3}}{\delta H_c}\right)\right)\right]\right\}^{q/n}, \tag{6.25}$$

with Γ once again given by (6.24).

We solve this algebraic relationship between h and u_b (Fowler, 2011a) and plot the solution in Figure 6.7(a) with the same parameter values that produced the ice-streaming behaviour in Section 6.4.2.2. In this case, the relationship between ice depth and ice velocity is multivalued, suggesting that distinct velocity states can occur at the same ice thickness, h. In Figure 6.7(b) we plot this multivalued relationship against a re-scaled version of the triple-valued sliding law derived in Sayag and Tziperman (2009). In their work the sliding law is obtained analytically from a simple one-dimensional (1-D) force balance, based on the cross-flow structure of an ice stream; it has been used for subsequent analysis of ice stream behaviour by Sayag and Tziperman (2011) and Kyrke-Smith *et al.* (2013). We see that the sliding law that arises from a basic coupling of our hydrology model and the ice flow exhibits very similar properties to their triple-valued function. As a result, when solving our coupled model, similar behaviour arises to that seen when using a triple-valued slid-

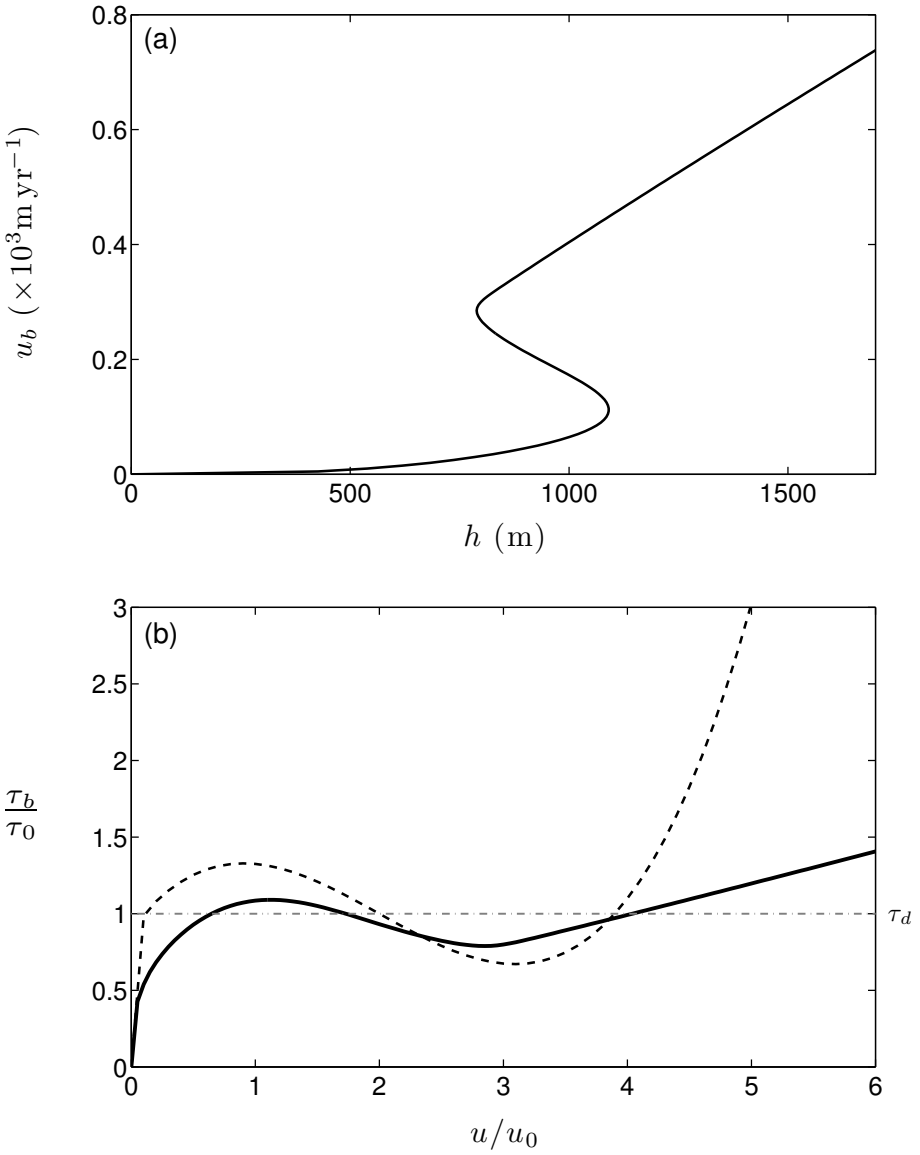

Figure 6.7: (a): Plot of 1D ice velocity versus ice depth from (6.25) with non-dimensional parameter values $H_c = 1.4$, $p = q = 1/3$, $x = 1$, $\Omega = 1.0$, $\Lambda_\infty = \delta = 0.01$, $\mu = 1.0$, $\kappa = 0$ and $c_0 = 1.7$. (b): The corresponding non-dimensional velocity against basal stress plotted alongside a re-scaled triple-valued sliding law from Sayag and Tziperman (2009) (dashed line).

ing law of the form presented in Sayag and Tziperman (2009) as the basal boundary condition.

6.5.2 Stress balances across resultant streams

Figure 6.8 shows cross-stream velocity profiles and the corresponding plots of the magnitude of basal stress and lateral stress for the simulation run is Section 6.4.2.2. Comparing with Figure 3.9, we see that there is a similarity between the stress balances across each stream as there was for an individual stream formed as a result of using a triple-valued sliding law at the bed. The basal stress is at its minimum in the ice stream shear margins, where the lateral shear stress is at its maximum. This is as we would expect from the analysis above in Section 6.5.1, which relates the coupled hydrology-ice model back to the behaviour associated with a triple-valued sliding law.

6.5.3 Dependence of flow regime on parameter choices

6.5.3.1 Critical water depth

The analysis above allows us to investigate what parameters are critical in governing multivalued flux behaviour. Throughout this chapter we have used $\Lambda_\infty = \delta = 0.01$ and have shown in Figure 6.7 that this results in a multivalued flux law when $H_c = 1.4$ (corresponding to 4.2 mm). We used these parameter values to plot Figure 6.7 since we observed multivalued behaviour from a numerical simulation with these parameters in Section 6.4.2.2. Nevertheless, the dependence of the unstable, multivalued behaviour on H_c is of interest. Figure 6.9 shows the relationship between ice depth and ice velocity for four different values of H_c with $\Lambda_\infty = \delta = 0.01$. For very small H_c the relationship is not multivalued, and u_b is simply an increasing function of h. However, as H_c increases the function becomes triple-valued (first becoming so when $H_c \approx 1.1$). For $H_c \gtrsim 1.1$, the function remains triple-valued. The effect of further increasing H_c

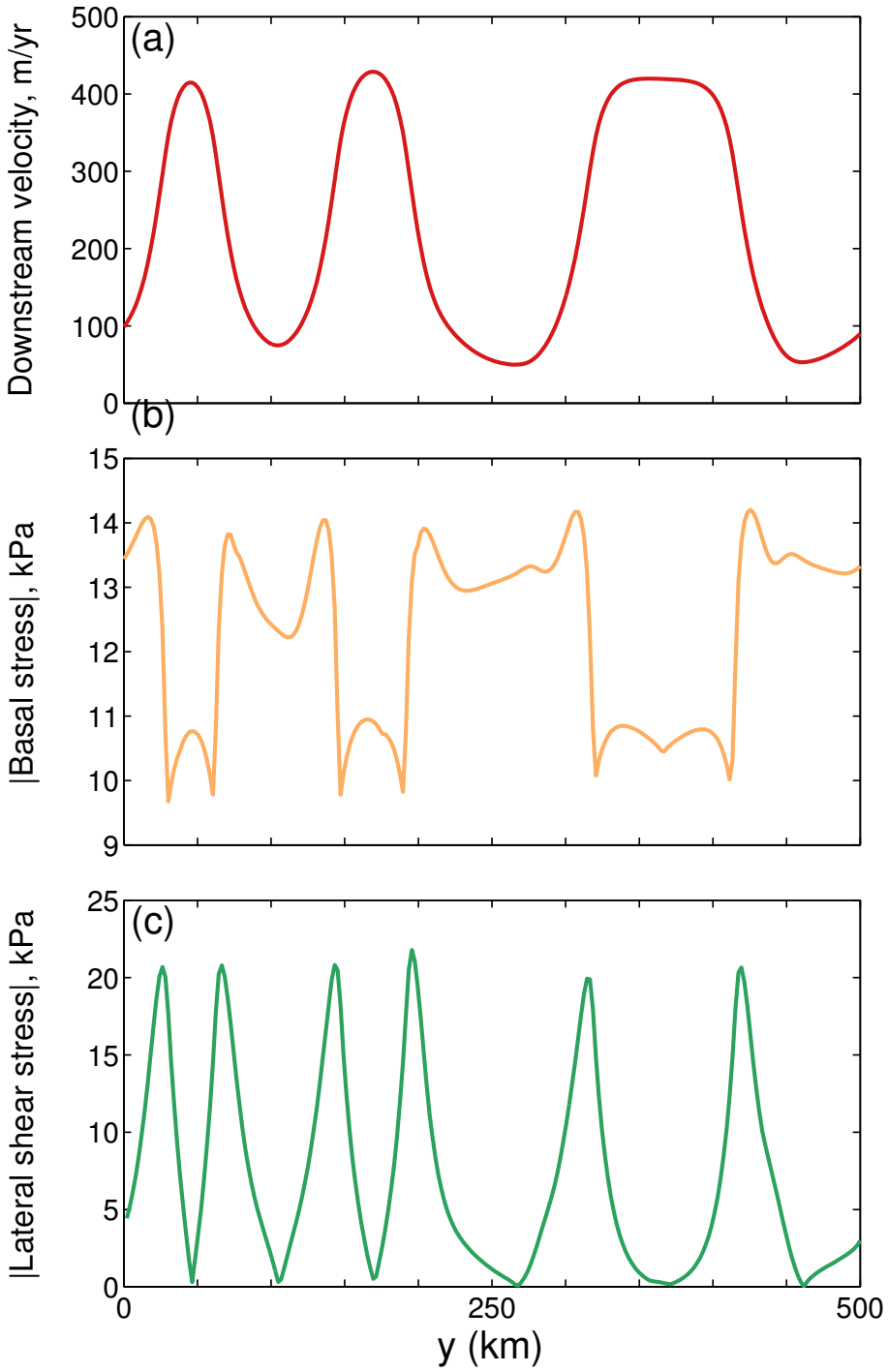

Figure 6.8: Cross-stream velocity and stress profiles for ice streams formed in the simulation discussed in Section 6.4.2.2 and illustrated in Figure 6.5. Cross-sections are taken at the outflow boundary. (a) shows the velocity profile, (b) the corresponding basal stress magnitude, $\sqrt{|\boldsymbol{\tau}_{13}|^2 + |\boldsymbol{\tau}_{23}|^2}$, and (c) the lateral shear stress magnitude, $|\boldsymbol{\tau}_{12}|$.

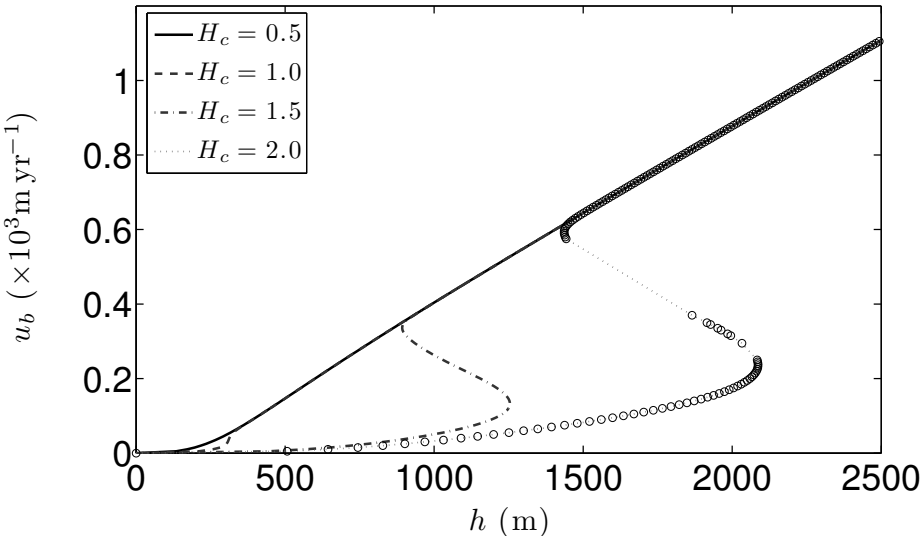

Figure 6.9: Plot of 1D ice velocity versus ice depth from (6.25) with non-dimensional parameter values $p = q = 1/3$, $x = 1$, $\Omega = 1.0$, $\Lambda_\infty = \delta = 0.01$, $\mu = 1.0$, $\kappa = 0$ and $c_0 = 1.7$. Plots for four different non-dimensional values of H_c are given, corresponding to $1.5, 3, 4.5$ and 6 mm. For $H_c = 2$ (6 mm) some solutions are imaginary and we therefore only plot the real solutions (circles), joined together by the dotted grey line.

is that the turning points of the function occur at larger values of h and u_b. This is because more meltwater is required for the water film depth to come close to the critical depth; a larger ice depth results in a larger driving stress that in turn causes more frictional heating. For larger values of H_c (e.g. Figure 6.4) it is necessary to have thicker ice if there is to be sufficient meltwater to initiate the instability. This is in contrast to the behaviour we would expect if H_c were reduced too low; the flux law is no longer multivalued so we would not expect multiple velocity states to coexist in steady state, however large the driving stress.

6.5.3.2 Λ_∞ and δ values

It is also of interest what effect the choice of Λ_∞ and δ in (6.11) has on the multivalued nature of the relationship (6.25). We therefore solve (6.25) over a range of values for these parameters. Figure 6.10 shows a phase diagram of the distinct regions of Λ_∞–δ parameter space where the relationship is triple-valued and single-valued for the

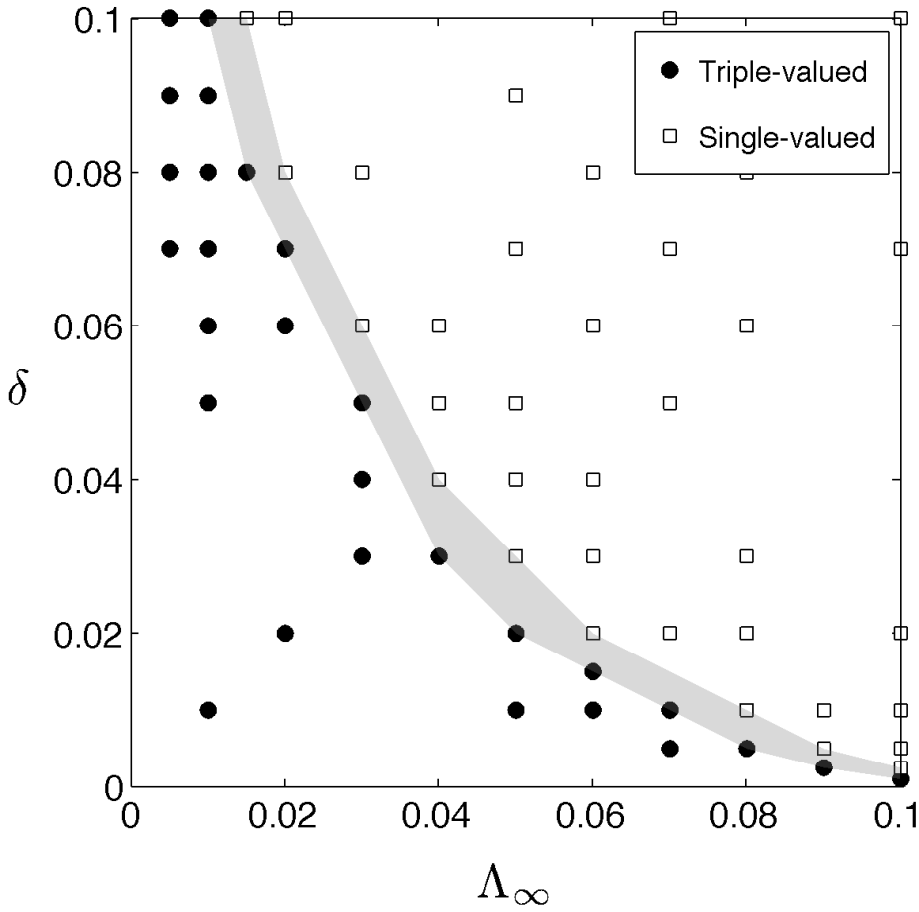

Figure 6.10: A diagram showing discrete regions where the ice depth versus ice velocity relationship is multivalued and where it is single-valued, depending on the values of Λ_∞ and δ. $H_c = 4.2\,\mathrm{mm}$ as for the simulations shown in Figure 6.7.

case with $H_c = 1.4$. It is clear that if both Λ_∞ and δ are sufficiently small then the relationship (6.25) is multivalued and there is therefore the potential for different velocity states to coexist.

6.5.4 Ice stream spacing

In Figure 6.5 it is clear that while the instability develops on quite a short wavelength, there is then a coarsening of the instability so that once the system reaches its quasi-steady-state there are three distinct ice streams with a spacing ~ 60–$80\,\mathrm{km}$ between streams. What determines this spacing?

We return to the mass conservation of water equation (6.14a). In the steady state the principal variation is in the cross-stream direction. We therefore ignore time dependence and downstream variations and consider a balance between lateral diffusion and the melt rate–

$$\nu \frac{\partial}{\partial y}\left[H^3 \frac{\partial}{\partial y}\left(\Lambda(H)\Gamma\right)^{1/n}\right] \sim \Gamma. \tag{6.26}$$

In the Newtonian case, the melt rate terms are balanced and we take $H^3\Lambda(H) \approx$ constant. This is a fair assumption so long as H_c is suitably small, as it must be for us to be in the unstable regime where ice streams develop (see Section 6.5.3.1). We consequently expect the lateral length scale l_y to scale as approximately

$$l_y^2 \sim \nu = 4 \times 10^{-3}. \tag{6.27}$$

This is the length scale for the lateral catchment of water, and in dimensional terms, we expect this to be analogous to the half width of the spacing between streams scaling as $\sim \sqrt{\nu} x_0$. In the case where $\nu = 4 \times 10^{-3}$, as in Table 6.2, this gives a half width spacing of 32 km, which is roughly in line with that observed in simulations (for example, see Figure 6.5).

Physically, the parameter ν corresponds to the ratio of the effective pressure and hydrostatic ice pressure contributions to the gradients in hydraulic potential, i.e.

$$\nu = \frac{[\boldsymbol{\nabla} N]}{[\rho_i g \partial s_i / \partial x]}, \tag{6.28}$$

where square brackets are used to represent the scale of each term. As this ratio increases, we expect the spacing between adjacent streams to widen. With larger ν, the effective pressure gradients play a more dominant role in governing water flow; a smaller gradient in effective pressure between adjacent streams is therefore required

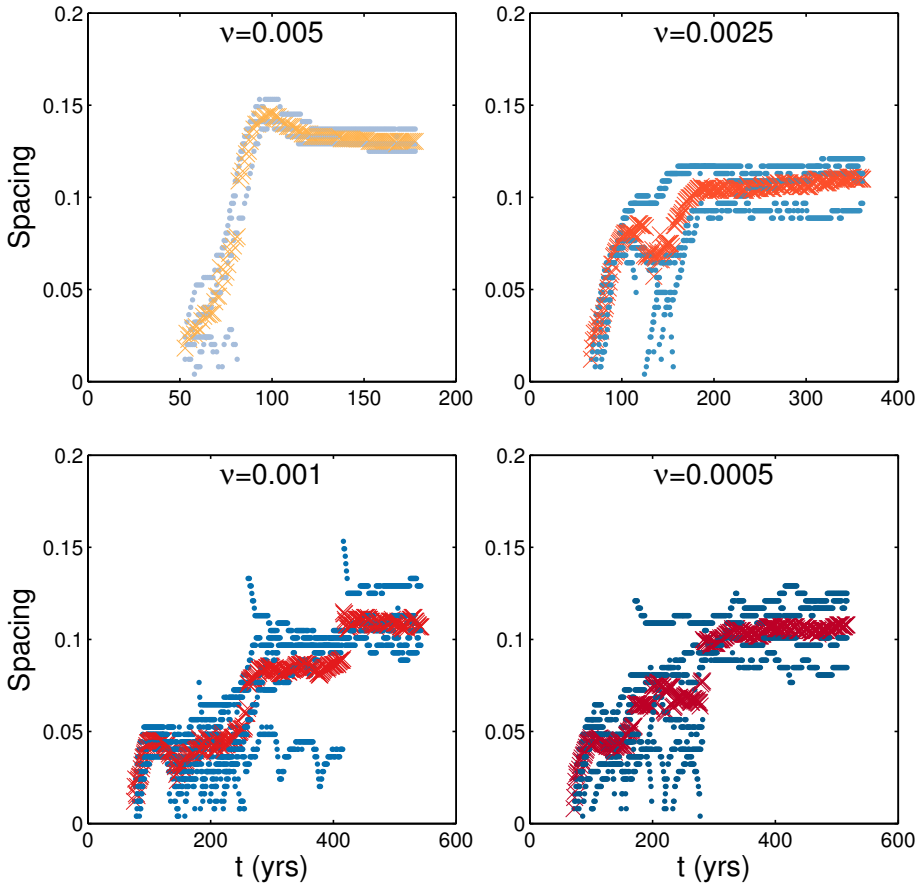

Figure 6.11: The evolution of spacing between streams, for four simulations run with different values of ν. The spacing is measured 10km from the end of the domain, with $u_b < 150\,\mathrm{m\,yr^{-1}}$ defined as being outside of a stream, and $u_b \geq 150\,\mathrm{m\,yr^{-1}}$ defined as being stream velocity. Blue dots represent individual measurements between fast-flowing streams, and the orange/red crosses the mean spacing for each simulation.

for the system to be in balance. A smaller gradient corresponds to a wider spacing, since the change in the effective pressure between the inside and outside of the stream, δN, is approximately constant in all cases, and it is therefore the length scale that adjusts.

Now, to consider whether this argument is consistent, we run a suite of simulations with a range of values of ν, and look at the variation in the magnitudes of separation between streams. Figure 6.11 shows time series of the separation between fast-flowing streams that form in four different simulations, with ν varied over an

order of magnitude. The spacing is estimated using a simple method for which we define $u_b \geq 150\,\mathrm{m\,yr^{-1}}$ to be in an ice stream and $u_b < 150\,\mathrm{m\,yr^{-1}}$ to be outside of an ice stream. Ice streams first develop at a similar time for all values of the parameter ν shown in the figure. However, there is less variation in spacing and the system reaches a state where ice streams are no longer merging or splitting more rapidly for larger ν. For $\nu \gtrsim 0.005$ the instability is suppressed (given the other parameter values used in this study). This is a consequence of the more significant role effective pressure gradients play in driving water flow at higher values of ν. The effective pressure contribution to the hydraulic potential gradient drives water away from ice streams (water flux is in the direction of increasing effective pressures from (4.5,4.8)), while the coupled dynamics of the ice and water means that depressions in surface elevation develop at the onset zone of ice streams (due to the increased outflow from the domain) and these drive water towards the ice streams (again from (4.5,4.8)). At larger values of ν the water is driven away from initial perturbations more rapidly, and over a larger length scale, l_y (6.27). Due to the slower time scale of ice evolution, with larger values of ν the ice does not develop ice streams sufficiently rapidly, and the lateral spreading of the water, which is both faster and over a larger length scale at larger ν, is quick enough to quickly smooth out any perturbations in the water layer.

Two end-member velocity fields are shown in Figure 6.12. These are shown at the late stage where any significant variation in the spacing has died out. For larger ν there are fewer ice streams and they are wider, with wider spaces between adjacent streams, as expected from (6.27).

Furthermore, to relate the spacing to ν more directly, in Figure 6.13 we plot the inter-stream spacing at the onset zone of the streams against $\sqrt{\nu}$. We plot the spacing at the onset zone (in the regions marked by the dashed boxes Figure 6.12) because this is the spacing we believe the parameter ν to actually govern. Streams might

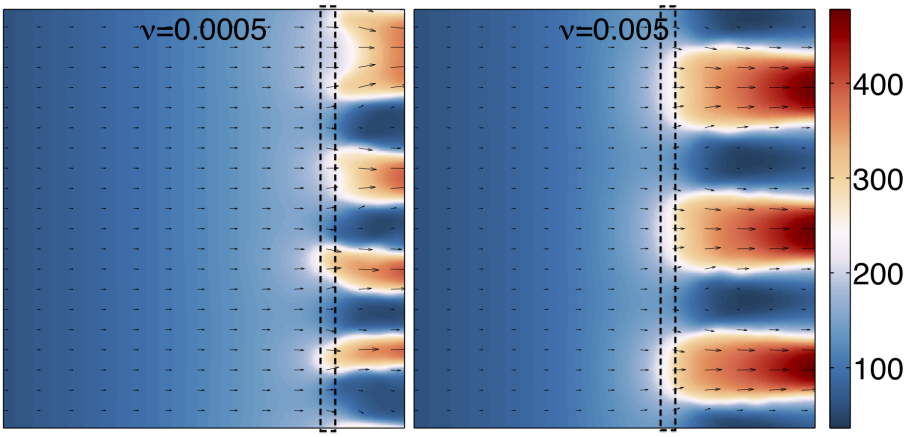

Figure 6.12: Plots of the velocity field, once it has reached a quasi-steady-state, for two values of ν. The value of ν affects the spacing of the streams that form.

widen and evolve downstream, but the catchment area of water for each stream, over which the water is channelised towards individual streams, will govern the distance between onsets of the fast-flowing regions[1].

We observe a positive correlation, as expected, and plot a line with unit gradient through the results. This gives a reasonable fit to the mean data. However, it is important to note the large variation in values of the spacing (individual values plotted with discrete small dots). There are many factors that might contribute to this variation, the most important being the neglect of the coupled behaviour in our analysis above. Although the time scale for the ice flow is longer, the ice responds to what the water is doing, with depressions in surface elevation at the onset of zone also having an influence on the lateral catchment of water, as discussed when discussing the suppression of the instability at larger ν. Furthermore, there is also the issue of the limited size of the domain. This enforces lateral periodicity and may play a role in the large variation of results, since the ice streams have to adjust to fit this restriction on the domain.

[1]For the time series of the spacing in Figure 6.11, the spacing is plotted 10 km from the end of the domain (rather than at the onset region) for ease of calculation—the ice streams propagate upstream as they form and so plotting spacing specifically at the onset would involve tracking this too, something that we deem to be excess to requirements.

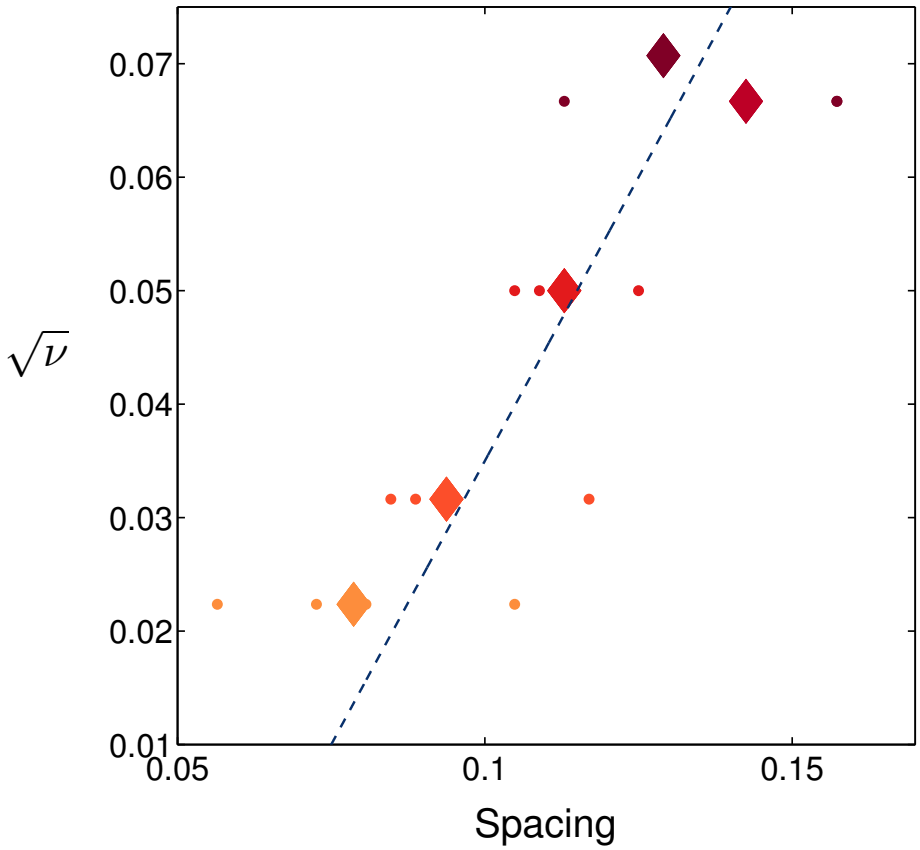

Figure 6.13: A plot of ice-stream spacing against non-dimensional parameter ν, for a suite of simulations run for a range of ν values. All were run at the same resolution with 250×250 grid points. The small dots are values of the space between adjacent ice streams, at the onset zone of the stream (the region illustrated by the dotted boxes in Figure 6.12, picked out individually for each stream). The large diamonds plot the average spacing value for each simulation. A line with unit gradient is also plotted.

6.6 Influence of topography

The unstable stream formation presented in this chapter occurs without any imposed perturbation to the ice–water system. The ice and water are both initialised with a uniform cross-domain flow, and the bed is also smooth with a constant downstream slope and no cross-flow variation. The instability that arises in the system picks out a natural wavelength, which is dependent on certain parameters in the problem, as discussed in the previous section. In terms of relating what we see in our simulations back to what is observed in nature, the ice streams are strictly pure ice streams, where topography plays no role at all in governing where they form.

A question that therefore naturally arises from this study is what effect variations in topography would have on the flow fields we observe. In our coupled ice-water system these pure ice streams may emerge on a flat bed, but if we introduce perturbations to the bed, what role do these variations play in governing where and when ice streams form. What level of topography variation is needed for the pure ice streams to become topographically controlled ice streams, constrained by the variations in topography?

To consider this problem, we apply a perturbation to the bed of the form

$$\hat{b} = B_0 \sin\left(\frac{2\pi n_b y}{y_w}\right) \tag{6.29}$$

where B_0 is the magnitude of the perturbation, n_b/y_w the (integer) frequency across the non-dimensional domain where y_w is the domain width. Table 6.3 summarises results from simulations run with a range of values of B_0 and n_b. A tick mark means that the topography variations govern ice-stream placement (i.e. the fast flowing patches of ice immediately form only in the bedrock troughs), whereas a cross means that ice-stream features form in the domain, independently of the governing topography (i.e. fast flowing patches form, at least temporarily, outside of the bedrock troughs).

	$\mathbf{n_b}$		
$\mathbf{B_0}$	**1**	**2**	**3**
0.1	✓ ✓	✓ ✓	✓ ✓
0.01	× ✓	✓ ✓	✓ ✓
0.001	× ×	× ✓	✓ ✓
0.0001	× ×	× ✓	✓ ✓
0.00001	× ×	× ×	× ✓

Table 6.3: Observations of whether streams form in troughs (tick) or have positioning independent of topography (cross). The entry for each case refers to whether streams initially develop only in the bedrock troughs and the second whether streams remain only in troughs. N.B. dimensionally $B_0 = 1$ corresponds to 1000 m.

There are two entries for each simulation—the first refers to the initial formation of the ice streams, and the second to the point at which the simulation has reached its quasi-steady-state. It is evident that as the frequency of the perturbations decreases, a larger amplitude of perturbation is required to influence the spatial placement of developing ice streams. In the case of there being only one bedrock trough across the domain, only with the largest of perturbations ($B_0 = 0.1$ corresponding to a 200 m difference between the peak and trough of the perturbation) does only one ice stream develop in the domain, in the bedrock trough. With any smaller perturbation, while a larger ice stream develops in the trough, streams do still form in the other half of the domain. In contrast, when $n_b = 3$ and there are three bedrock peaks and troughs cross-domain, even with a perturbation as small as $B_0 = 10^{-5}$ (corresponding to a 2 cm difference between the peak and trough of the perturbation), the streams form in the bedrock troughs. This is not entirely surprising, since the natural wavelength of the instability is three ice streams across the domain (as in Figure 6.5).

To illustrate these results visually, we plot output from the simulations run with

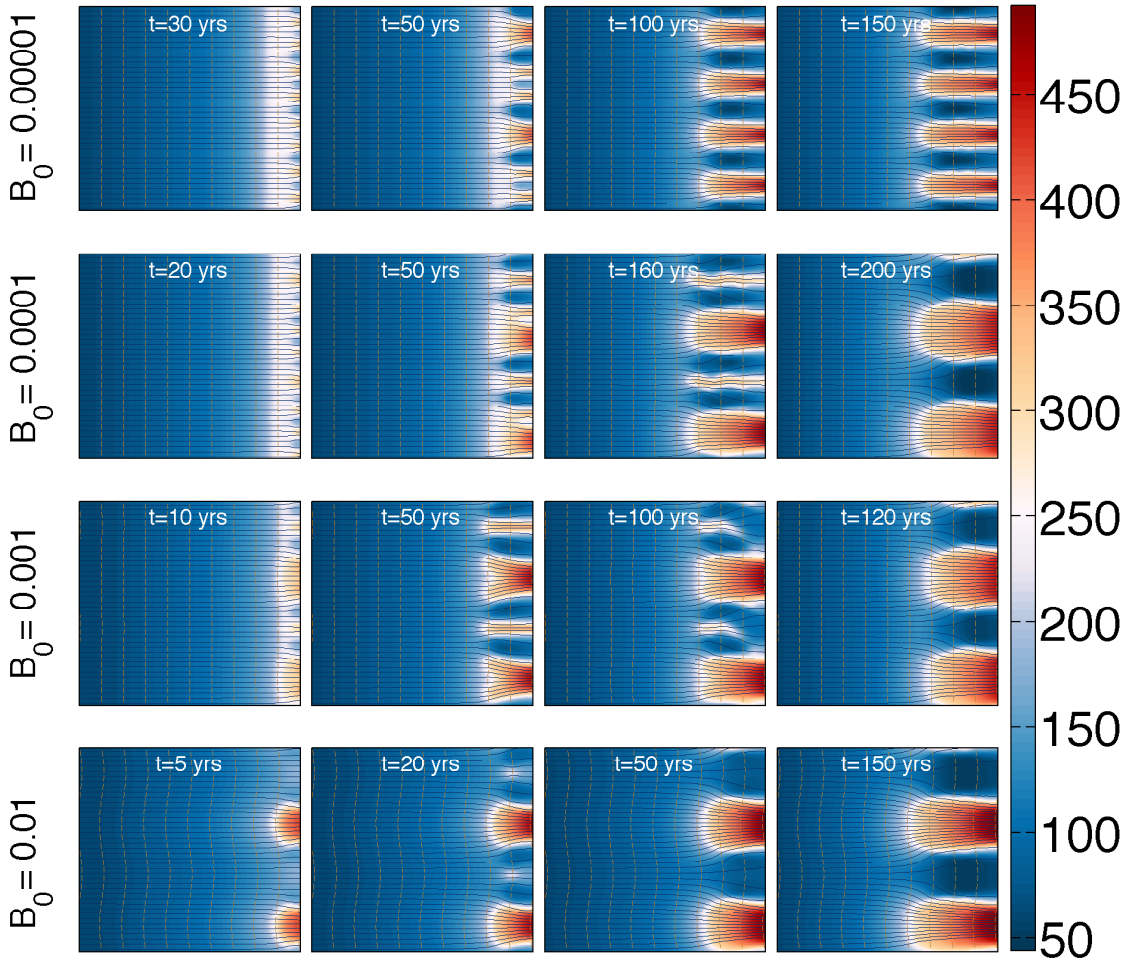

Figure 6.14: Results from a suite of simulations with an applied perturbation in the bed elevation across the domain. The perturbation is of the form (6.29), with $n_b = 2$. Each row shows plots at successive times for a simulation with the magnitude of bed perturbation specified (largest perturbation shown in the bottom row of plots). Colours represent ice speed; solid navy lines are streamlines of water flow in the subglacial hydrologic system; broken brown lines are contours of basal elevation.

$n_b = 2$ in Figure 6.14. For each simulation, snapshots of the solution field are plotted at successive times. The times for which plots are shown are chosen to illustrate the initial onset of the unstable behaviour, the development of distinct fast flowing streams (some of which then merge together in certain cases), and then the final state. Some interesting things to note from these results include

- All but the smallest perturbation case end up with two wide and fast-flowing streams in in the bedrock troughs. In the $B_0 = 0.00001$ case there are also streams overlying the bedrock peaks.

- Streams over bedrock peaks are actually seen in the simulations with larger bed perturbations too, but they are not maintained as the system evolves. The thinner streams located between the topographic lows disappear as the streams lying in the troughs widen. As they widen, the catchment area for water routing towards the troughs increases, limiting the water supply to those thinner streams located on the peaks of the bed perturbations. There is therefore insufficient water to maintain the fast flow in these streams.

- The time for which four streams are maintained is longer for a smaller bed perturbation (the third plot in the $B_0 = 0.0001$ case is shown at $t = 160\,\text{yrs}$, which is long after the extra streams have shut down and the system has settled into a quasi-steady-state with two streams in the $B_0 = 0.001$ case).

- Note that there is also a brief time period where it looks as though a second pair of ice streams located at the bedrock peaks may form in the case with the largest bed perturbation ($B_0 = 0.01$—see plot at $20\,\text{yrs}$).

- The instability develops more rapidly when the bed perturbation is larger (the plots in the first column are at $t = 5, 10, 20$ and $30\,\text{yrs}$ respectively, and these times have been chosen since they illustrate the non-uniformity in the flow first developing for each case).

6.7 Summary and conclusions

The theory developed in Chapter 4 provides a simplified model of subglacial water flow in a Weertman-Creyts-Schoof style rough-bedded film (Weertman, 1972; Creyts and Schoof, 2009) at the base of an ice sheet. In this model, there is some critical water depth H_c at which all supporting clasts become submerged, separating the ice from the bed. After this point, the water layer can theoretically increase in depth without limit. However, in reality, a water sheet with depth greater than H_c is an unstable configuration (Walder, 1982) and we would expect the water film to incise discrete streams into the sediment, as discussed in Chapter 5. In this chapter we have therefore presented a parameterised representation of this idea motivated by the fact that while locally there might be areas of zero effective pressure, at a larger scale (that is still sub-grid scale) there will be regions of finite support at the bed.

Numerical solutions of the fully coupled ice–water system result in distinct flow regimes dependent on whether the water depth reaches the critical depth within the domain. The system evolves into a uniform steady-state if the bed is sufficiently rough (i.e. H_c sufficiently large) that all the melt can flow in the thin film configuration. However, reducing the critical water depth (so that H reaches H_c) results in the ice flow becoming laterally unstable and non-uniform in the cross-flow direction; ice-stream-like features develop.

A basic analysis of the coupled system suggests that the hydrological system can result in a triple-valued flux relationship for the ice. It has previously been shown that a triple-valued sliding law is associated with ice-stream behaviour and such multivalued flux laws have therefore been used to investigate ice-stream dynamics (e.g. Sayag and Tziperman, 2009, 2011; Kyrke-Smith *et al.*, 2013). By showing that this coupling between subglacial hydrology and the ice can result in similar multivalued flux behaviour, this work helps to contextualise analyses of ice-stream flow that result from using a triple-valued sliding law at the bed. Given that the

sliding law is multivalued, however, does not enforce instability in the system for all simulations; it still requires the ice to get sufficiently thick and the water layer to be sufficiently deep. Furthermore, some parameter combinations (we specifically consider variations of Λ_∞, δ and H_c) do not result in triple-valued flux behaviour at all. In these cases, under no circumstances would we expect a lateral instability to occur.

Towards the end of this chapter we have extended on the work presented in Kyrke-Smith *et al.* (2014), and considered the role the non-dimensional parameter ν plays in governing the spacing between ice streams that form in the model. The spacing between streams increases as the ratio between the contribution in effective pressure gradients and ice surface slope gradients to the hydraulic potential increases. We also consider perturbations to the bed, in an effort to understand what level of bed perturbation results in ice-stream positioning being a consequence of the topography. We find that ice streams form in bedrock troughs even with a low level of governing topography. For a more detailed examination of this, we would need to vary other parameters in the model, such as the critical water depth, and also apply more varied topography perturbations.

Chapter 7

Conclusions

This thesis has considered the question of how subglacial water flow interacts with ice-sheet and till dynamics, specifically in the context of ice streams. While observations associate ice streams with the presence of meltwater at the bed, there is little known about the physical processes and feedbacks that may result in ice-stream flow. In large-scale ice-sheet models, water transport at the bed is rarely included, but we have shown in this thesis that it can have profound consequences on the dynamics of the ice sheet.

We refer the reader back to the summaries at the end of Chapters 2–6 for a more detailed overview of their contents. Here, we provide a brief review of the conclusions, before discussing potential for future work.

7.1 Review of conclusions

Ice flow model Chapter 2 focused on deriving a simple, depth-integrated model for ice-sheet dynamics, suitable for describing ice flow both within, and outside of ice streams. Commonly used approximations in large-scale ice sheet models are the shallow ice approximation (SIA) and shallow shelf approximation (SSA); the former is suitable for describing vertical-shear-dominated flow (e.g. for ice frozen to the bed) while the latter provides an accurate flow description for plug flow (e.g. in ice streams, or ice shelves, where there is no velocity variation with depth). Since neither model is

suitable in the transition region between slow ice-sheet and rapid ice-stream flow, we considered a hybrid of the two approximations. The approach outlined in this chapter has many advantages over other ice-flow models. It includes both vertical shear stresses and membrane stresses, allowing us to capture the leading-order behaviour of all flow regimes. Furthermore, solutions are inexpensive compared with solving full Stokes. Moreover, while other hybrid description of ice-flow do already exist in the literature (e.g., Blatter, 1995; Schoof and Hindmarsh, 2010; Bueler and Brown, 2008; Goldberg, 2011; Winkelmann *et al.*, 2011), ours has the advantage that the second non-dimensional parameter has the constraint $0 < \lambda \leq 1$, making it easier to consider the whole range of sliding regimes that the model is capable of describing. The work in this chapter therefore paves the way for investigations of ice-stream dynamics using a vertically-integrated ice-flow model.

Stress balances across ice streams Chapter 3 considered solutions of the hybrid ice flow model with different phenomenological sliding laws at the bed; we showed that ice-streams can exist under distinct stress balances. A triple-valued sliding law results in the minimum value of basal stress in the ice-stream margin, and the stress increases again underneath the ice stream. In contrast, a double-valued sliding law forces a constant minimum in basal stress across the whole width of the ice-stream. Therefore, in the case with a double-valued sliding law, membrane stresses have a more significant role to play in the stress balance across the ice-stream since there is little resistance provided by the bed.

Furthermore, we considered solutions of the hybrid ice-flow model with a range of values of the basal to shear stress ratio (λ). Solutions with low values of λ directly demonstrated the stabilising effect of membrane stresses, since a larger perturbation was needed to initiate ice-streaming behaviour. This result emphasises the important effect membrane stresses can play in inhibiting the emergence of ice-streams, under-

lining the point that any results that predict ice-streaming from a shallow ice model should be re-considered.

Subglacial water layer In a bid to represent processes occurring at the bed more directly, we considered a description of the subglacial water layer in Chapter 4. We presented a model of water flow in a Creyts-Schoof-Weertman style film (Weertman, 1972; Creyts and Schoof, 2009), and examined solutions for the water layer, uncoupled from the ice above it (i.e. with a defined ice flow and melt rate). We showed that shock formation occurs if the water depth decreases in the direction of flow. Furthermore, the $\mathcal{O}(\nu)$ diffusive term in the governing equation for water depth introduces an oscillatory wave train behind the shock front; damping of the wave-train only occurs in the case of non-zero melt rate. The interesting behaviour of the water layer when uncoupled from the ice and sediment makes us expectant of interesting nonlinear feedbacks when the water is coupled with other systems in the subsequent chapters.

Water-sediment interaction beneath ice streams Chapter 5 moved on to look at the coupled behaviour of the water layer with the underlying sediment. As in the previous chapter we neglected ice dynamics and instead coupled the water flow with an equation for sediment evolution. A solution of a simplified form of the equations suggests that we can expect the water to flow in shallow, swamp-like streams, incised in the sediment layer at the bed. Since the bed of the ice-sheet is such an inaccessible area, this is an exciting and intriguing result informing us about what the water flow pattern at the bed may look like. Different subglacial hydrologic systems can have distinct and contrasting effects on ice dynamics, and so it is of utmost importance to be able to predict mechanisms of water flow at the bed; an understanding of the water system will allow accurate predictions of ice flow.

Coupled ice flow and meltwater drainage Finally, in Chapter 6 we coupled our ice-flow model with the description of water flow at the bed. Numerical solutions of the fully coupled model showed that under certain parameter combinations the ice flow becomes unstable to ice-stream formation. We related this behaviour back to that seen with a triple-valued sliding law in Chapter 2, by considering the relationship between basal stress and basal velocity. We have also provided insight on what governs the spacing of ice streams that form in the model by carrying out a simple parameter study; the relative importance of contributions from effective pressure and ice surface slope to the hydraulic potential (the gradient of which drives the water flow) influences the length scale of the instability.

Furthermore, at the end of the chapter we considered how variations in bed topography affect the ice-stream formation. Relatively small amplitude bed perturbations result in the streams choosing to form in bedrock troughs. Streams do form outside of the troughs once the amplitude of the perturbations is reduced down to centimetres, but the topography still has a regularising effect on where the ice streams form and their size and spacing.

7.2 Future work

While this thesis has presented theory and novel, intriguing results associated with a coupling between models of ice and hydrology, there are still questions about the coupled model left unanswered. These provide motivation for future research, and a few paths for this are outlined below.

Energy conservation and temperate ice One important limitation of the current model considered in this thesis is that it neglects energy conservation. The model instead assumes that the bed is always at the melting point. While this might be a fair assumption in the region of ice streams, other work with thermodynamically coupled

ice dynamics has shown that fast flow may begin due to purely thermomechanical feedbacks (e.g. Clarke *et al.*, 1977; Payne and Dongelmans, 1997; Hindmarsh, 2009), as discussed in the introductory chapter to this thesis. It is interesting to observe from these studies that similar ice-stream widths are obtained both in thermal theories and in the hydraulic theory presented here. We expect that this is due to the role of membrane mechanics in resisting ice stream flow, as discussed in our previous work (Kyrke-Smith *et al.*, 2013). Nevertheless, to further understanding of ice stream dynamics, future work will need to include energy conservation, to be able to explore the result of combined thermal and hydraulic feedbacks.

Moreover, the presence of water is not only associated with the bed of an ice sheet; radar measurements suggest that in certain locations it also extends upwards into the overlying ice. For example, measurements taken near Unicorn ridge, Antarctica, mapped a linear diffractor extending to 230 m above the bed, suggestive of the existence of a region of wet, temperate ice (Clarke *et al.*, 2007). Theoretical studies have also suggested meltwater generation may occur within the ice (e.g. Jacobson and Raymond, 1998; Perol and Rice, 2014; Schoof, 2012; Suckale *et al.*, 2014). However, models that incorporate thermal effects generally solve a temperature equation, which is not appropriate once temperate ice is present. In this case, the temperature needs to be pinned at the melting point and the latent heat of liquid water within the ice must be accounted for (e.g. Payne *et al.*, 2000; Bueler *et al.*, 2007). Regions of temperate ice can be treated separately, in a bid to account for this (e.g. Greve, 1997) or an alternative approach is to use the enthalpy method (Aschwanden *et al.*, 2012). In future work we hope to account for regions of temperate ice more accurately using techniques successfully used in the modelling of magma-mantle dynamics (McKenzie, 1984; Katz, 2008).

Presence of subglacial lakes and groundwater storage Recent research has shown that there is a large network of subglacial lakes beneath Antarctica (Smith *et al.*, 2009), which may sporadically drain from one to the other (Wingham *et al.*, 2006; Fricker *et al.*, 2007; Carter *et al.*, 2013). They are therefore an important ingredient of the active drainage system beneath the ice sheet, and can have significant effect on ice-sheet dynamics (Sergienko and Hulbe, 2011).

While work in this thesis suggests basal water may flow slowly through a patchwork of swamps, some observations see the presence of much larger amounts of water, such as Engelhardt and Kamb (2013) who found a 1.4 m deep water layer at the bottom of a borehole drilled to the bottom of the Kamb Ice Stream. They took this to be indicative of a subglacial channel, which would tie in with the idea that occasional floods may open larger drainage channels at the bed. Our model does not currently have the capacity to deal with the formation of such features; one area of development for the future would be to investigate the necessary conditions for a larger-capacity drainage system to develop. A further possibility, and one suggested by the recent work of Christoffersen *et al.* (2014), is that subglacial sediment acts as a storage reservoir that allows expulsion of groundwater under certain conditions. Further examination of this possibility requires a specific inclusion of groundwater storage in the model.

The evolution of subglacial landforms The coupled flow of ice, subglacial water and subglacial sediment is thought to result in the formation of subglacial landforms, such as drumlins, mega-scale glacial lineations, ribbed moraines and eskers (e.g. Boulton and Hindmarsh, 1987; Fowler, 2011a, pg. 686-704). These features are particularly interesting since they can provide constraints for identifying the extent and characteristics of past ice sheets (e.g. Evans *et al.*, 2005). However, there is still much uncertainty surrounding the formation of these landforms. Recent work

considering the stability of coupled ice, water and sediment evolution shows that instability can occur in a range of types, ranging from ribbed moraine through three-dimensional drumlins to mega-scale glacial lineations (Fowler and Chapwanya, 2011). Results largely depend on the granulometry of the till. As computational techniques advance, it will become easier to solve this fully coupled system and learn more about the formation and evolution of landforms.

Application of the model in a real location It would be interesting to implement the model presented in this thesis over the Siple Coast topography. By attempting to match current day velocity and ice depth observations, we could obtain some constraints on unknown parameter values, such as the critical water depth.

Appendices

A1 Discretisation of governing equations

The governing equations for conservation of mass and momentum are given by (2.31a) and (2.31b) in the main text respectively-

$$\frac{\partial h}{\partial t} + \boldsymbol{\nabla}\cdot\left(h\mathbf{u}_b - \lambda\frac{h^{n+2}}{n+2}\left|\boldsymbol{\gamma}\right|^{n-1}\boldsymbol{\nabla}s_i\right) = a, \tag{1}$$

$$\boldsymbol{\tau}_b = h\boldsymbol{\gamma} \tag{2}$$

where

$$\boldsymbol{\gamma} = -\boldsymbol{\nabla}s_i + \frac{\varepsilon^2}{\lambda}\boldsymbol{\nabla}\cdot\mathbf{S}, \tag{3}$$

and $\mathbf{S}$ is the resistive stress tensor,

$$\mathbf{S} = \boldsymbol{\tau} + \mathbf{I}\,\mathrm{trace}\left(\boldsymbol{\tau}\right) = \begin{bmatrix} 2\tau_{11}+\tau_{22} & \tau_{12} \\ \tau_{12} & \tau_{11}+2\tau_{22} \end{bmatrix}. \tag{4}$$

A1.1 Conservation of momentum

The governing equations are discretised onto the staggered gird illustrated in Figure A1.1. Conservation of momentum (2) becomes

$$\left[\tau_b x\right]_{ij} = h_{i+\frac{1}{2},j}\left[\gamma x\right]_{ij}, \tag{5}$$

$$\left[\tau_b y\right]_{ij} = h_{i,j+\frac{1}{2}}\left[\gamma y\right]_{ij}, \tag{6}$$

where $\boldsymbol{\tau_b} = \left(\left[\tau_b x\right], \left[\tau_b y\right]\right)$, and the components are evaluated at the u and v grid points respectively (i and j are the indices of the x and y coordinates). The presence of a

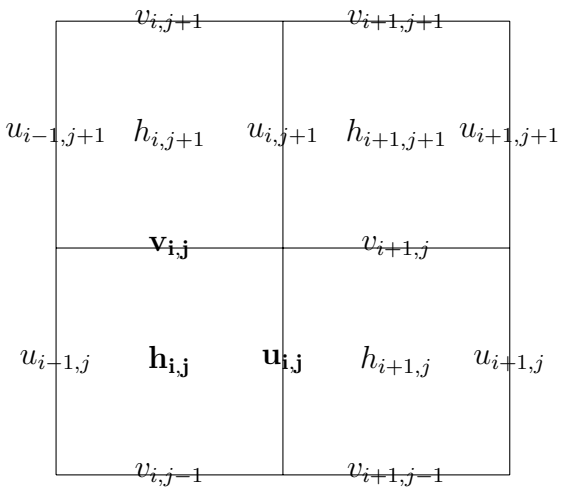

Figure A1.1: The staggered grid used for solution of the two-dimensional flow.

1/2 in the subscript represents averaging e.g.

$$h^k_{i+\frac{1}{2},j} = \frac{h^k_{i+1,j} + h^k_{ij}}{2}, \tag{7}$$

$$h^k_{i+\frac{1}{2},j+\frac{1}{2}} = \frac{h^k_{i+1,j+1} + h^k_{i+1,j} + h^k_{i,j+1} + h^k_{ij}}{4}. \tag{8}$$

$[\gamma x]$ and $[\gamma y]$ are the x and y components of $\boldsymbol{\gamma}$ (given by (3)), evaluated at the u and v grid points respectively,

$$[\gamma x]_{ij} = -[Sx]_{ij} + \frac{\varepsilon^2}{\lambda}[\Gamma x]_{ij}\,, \tag{9a}$$

$$[\gamma y]_{ij} = -[Sy]_{ij} + \frac{\varepsilon^2}{\lambda}[\Gamma y]_{ij}\,, \tag{9b}$$

where Sx and Sy are ice surface gradients in x and y (again evaluated at the u and v grid points),

$$[Sx]_{ij} = \frac{h_{i+1,j} - h_{i,j}}{\Delta x} + \frac{b_{i+1,j} - b_{i,j}}{\Delta x}, \tag{10a}$$

$$[Sy]_{ij} = \frac{h_{i,j+1} - h_{i,j}}{\Delta y} + \frac{b_{i,j+1} - b_{i,j}}{\Delta y}, \tag{10b}$$

and $[\Gamma x]$ and $[\Gamma y]$ are the components of $\boldsymbol{\nabla}\cdot\mathbf{S}$ in (3). To evaluate $[\Gamma x]$ and $[\Gamma y]$, we first introduce μ_{ij} which is the viscosity $(=1/\tau^{n-1})$ evaluated at the h grid points. From (2.33) we have that

$$\mu_{ij}=\left(\frac{1}{S_{ij}+(\varepsilon/\lambda)^2 L_{ij}}\right)^{\frac{n-1}{2n}}, \tag{11}$$

with

$$S_{ij}=\left[\left([Sx]_{i-\frac{1}{2},j}\right)^2+\left([Sx]_{i,j-\frac{1}{2}}\right)^2\right]^n h_{ij}^{2n}, \tag{12a}$$

$$\begin{aligned}L_{ij}=2\left([dudx]_{ij}\right)^2+2\left([dvdy]_{ij}\right)^2+2\,[dudx]_{ij}\,[dvdy]_{ij}\\ +\left[\left(\frac{[u_b]_{i,j+1}+[u_b]_{i-1,j+1}-[u_b]_{i,j-1}-[u_b]_{i-1,j-1}}{4\Delta y}\right)\right.\\ \left.+\left(\frac{[v_b]_{i+1,j}+[v_b]_{i+1,j-1}-[v_b]_{i-1,j}-[v_b]_{i-1,j-1}}{4\Delta x}\right)\right]^2,\end{aligned} \tag{12b}$$

where

$$[dudx]_{ij}=\frac{[u_b]_{i,j}-[u_b]_{i-1,j}}{\Delta x}, \tag{13a}$$

$$[dudy]_{ij}=\frac{[u_b]_{i,j}-[u_b]_{i,j-1}}{\Delta y}, \tag{13b}$$

$$[dvdx]_{ij}=\frac{[v_b]_{i,j}-[v_b]_{i-1,j}}{\Delta x}, \tag{13c}$$

$$[dvdy]_{ij}=\frac{[v_b]_{i,j}-[v_b]_{i,j-1}}{\Delta y}. \tag{13d}$$

Substituting the components of Glen's flow law (2.19) into (4), we are then able to write $[\Gamma x]$ and $[\Gamma y]$ as

$$[\Gamma x]_{ij} = \frac{2\mu_{i+1,j}\left(2\left[dudx\right]_{i+1,j} + \left[dvdy\right]_{i+1,j}\right) - 2\mu_{ij}\left(2\left[dudx\right]_{ij} + \left[dvdy\right]_{ij}\right)}{\Delta x} + \frac{\mu_{i+\frac{1}{2},j+\frac{1}{2}}\left(\left[dudy\right]_{i,j+1} + \left[dvdx\right]_{i+1,j}\right) - \mu_{i+\frac{1}{2},j-\frac{1}{2}}\left(\left[dudy\right]_{i,j} + \left[dvdx\right]_{i+1,j-1}\right)}{\Delta y}, \tag{14a}$$

$$[\Gamma y]_{ij} = \frac{v_{i+\frac{1}{2},j+\frac{1}{2}}\left(\left[dudy\right]_{i,j+1} + \left[dvdx\right]_{i+1,j}\right) - \mu_{i-\frac{1}{2},j+\frac{1}{2}}\left(2\left[dudy\right]_{i-1,j+1} + \left[dvdx\right]_{ij}\right)}{\Delta x} + \frac{2\mu_{i,j+1}\left(\left[dudx\right]_{i,j+1} + 2\left[dvdy\right]_{i,j+1}\right) - 2\mu_{i,j}\left(\left[dudx\right]_{i,j} + 2\left[dvdy\right]_{i,j}\right)}{\Delta y}. \tag{14b}$$

A1.2 Conservation of mass

Using a second-order semi-implicit scheme to discretise (1) gives,

$$\frac{h_{ij}^{k+1} - h_{ij}^{k}}{\Delta t} + \frac{\left(h_{i+\frac{1}{2},j}^{k+\frac{1}{2}}\left[u_b\right]_{ij}^{k+\frac{1}{2}} - h_{i-\frac{1}{2},j}^{k+\frac{1}{2}}\left[u_b\right]_{i-1,j}^{k+\frac{1}{2}}\right)}{\Delta x} + \frac{\left(h_{i,j+\frac{1}{2}}^{k+\frac{1}{2}}\left[v_b\right]_{ij}^{k+\frac{1}{2}} - h_{i,j-\frac{1}{2}}^{k+\frac{1}{2}}\left[v_b\right]_{i,j-1}^{k+\frac{1}{2}}\right)}{\Delta y} - \frac{\lambda}{(n+2)}\frac{\left[\left(h_{i+\frac{1}{2},j}^{k+\frac{1}{2}}\right)^{n+2}\left([Gx]_{ij}^{k+\frac{1}{2}}\right)^{n-1}[Sx]_{ij}^{k+\frac{1}{2}} - \left(h_{i-\frac{1}{2},j}^{k+\frac{1}{2}}\right)^{n+2}\left([Gx]_{i-1,j}^{k+\frac{1}{2}}\right)^{n-1}[Sx]_{i-1,j}^{k+\frac{1}{2}}\right]}{\Delta x} - \frac{\lambda}{(n+2)}\frac{\left[\left(h_{i,j+\frac{1}{2}}^{k+\frac{1}{2}}\right)^{n+2}\left([Gy]_{ij}^{k+\frac{1}{2}}\right)^{n-1}[Sy]_{ij}^{k+\frac{1}{2}} - \left(h_{i,j-\frac{1}{2}}^{k+\frac{1}{2}}\right)^{n+2}\left([Gx]_{i,j-1}^{k+\frac{1}{2}}\right)^{n-1}[Sy]_{i,j-1}^{k+\frac{1}{2}}\right]}{\Delta y} = a_{ij}^{k+\frac{1}{2}}, \tag{15}$$

where superscripts now represent the time step index (and subscripts the spatial step index as before). Gx and Gy are $|\boldsymbol{\gamma}|$ evaluated at the u and v grid points respectively.

More specifically,

$$[Gx]_{ij} = \left[\left([\gamma x]_{ij}\right)^2 + \left([\gamma y]_{i+\frac{1}{2},j-\frac{1}{2}}\right)^2\right]^{\frac{1}{2}}, \tag{16a}$$

$$[Gy]_{ij} = \left[\left([\gamma x]_{i-\frac{1}{2},j+\frac{1}{2}}\right)^2 + \left([\gamma y]_{ij}\right)^2\right]^{\frac{1}{2}}, \tag{16b}$$

and $[\gamma x]$ and $[\gamma y]$ are given by (9). Furthermore, in the case of conservation of mass $[\Gamma x]$ and $[\Gamma y]$ can be discretised as

$$[\Gamma x]_{ij} = \mu_{i+\frac{1}{2},j}\left(4\left(\frac{[u_b]_{i-1,j} - 2[u_b]_{ij} + [u_b]_{i+1,j}}{\Delta x^2}\right) + \left(\frac{[u_b]_{i,j-1} - 2[u_b]_{ij} + [u_b]_{i,j+1}}{\Delta y^2}\right) + 3\left(\frac{[v_b]_{i+1,j} - [v_b]_{i+1,j-1} - [v_b]_{ij} + [v_b]_{i,j-1}}{\Delta x \Delta y}\right)\right), \tag{17a}$$

$$[\Gamma y]_{ij} = \mu_{i,j+\frac{1}{2}}\left(\left(\frac{[v_b]_{i-1,j} - 2[v_b]_{ij} + [v_b]_{i+1,j}}{\Delta x^2}\right) + 4\left(\frac{[v_b]_{i,j-1} - 2[v_b]_{ij} + [v_b]_{i,j+1}}{\Delta y^2}\right) + 3\left(\frac{[u_b]_{i,j+1} - [u_b]_{i-1,j+1} - [u_b]_{ij} + [u_b]_{i-1,j}}{\Delta x \Delta y}\right)\right), \tag{17b}$$

since we can remove the viscosity term $1/\tau^{n-1}$ from inside the derivative, as in (2.32) in Chapter 2. We can furthermore approximate it as just the vertical shearing component (12a) (i.e. $\mu_{ij} = 1/\left(S_{ij}\right)^{(n-1)/2n}$).

A2 Alternative setup with the triple-valued sliding law

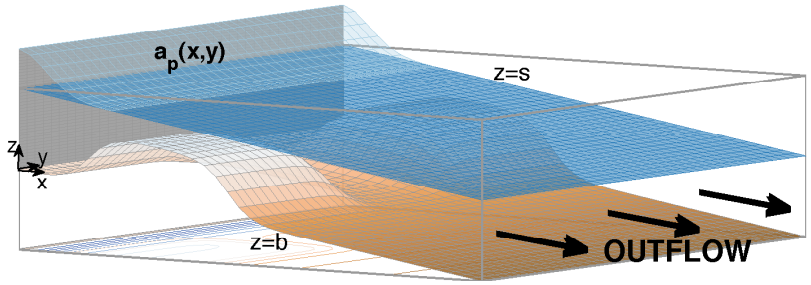

Figure A2.1: Schematic illustrating the model setup. There is zero inflow at the boundary, but instead an accumulation perturbation $a_p(x, y)$ in the form of a Gaussian strip.

An alternative model set up is with bedrock perturbations that channelise the flow in the onset region, as illustrated in Figure A2.1. We again enforce zero inflow to the domain and so apply an accumulation perturbation in a strip along $x = 0$ with a magnitude representing the sum of lesser accumulations from upstream as in Sayag and Tziperman (2011). This results in the same three distinct flow regimes, only with less regularity to them compared to the setup used in the rest of the paper. Figure A2.2 illustrates results from a set of simulations. For the steady-state stream solution, there is an oscillation between which side of the domain 'feeds' the stream—an instability also seen in Sayag and Tziperman (2011) when they use a very similar model set up. Benefits to this set up include the fact that it is possibly more representative of the natural system, since pure ice streams do sometimes have prominent bedrock topography in their onset regions (Anandakrishnan *et al.*, 1998; Bell *et al.*, 1998).

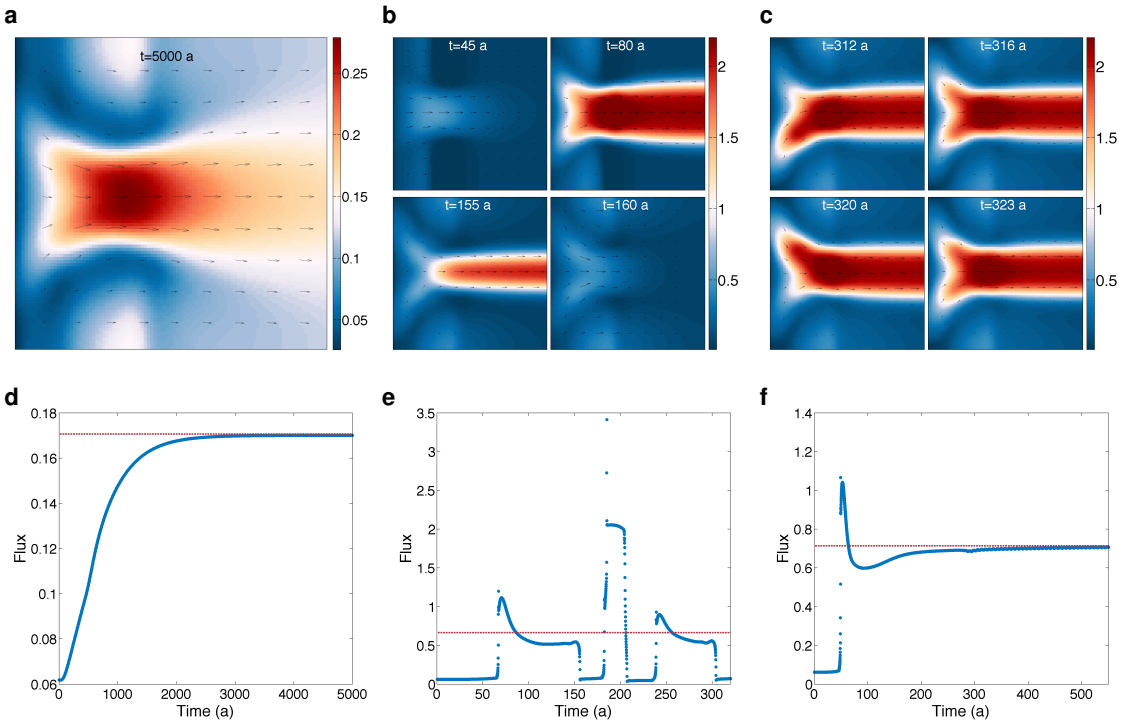

Figure A2.2: Simulation results with three different incoming mass flux values ($A_0 = 15, 30, 45\,\mathrm{m\,yr^{-1}}$ respectively). The plots in the top row are illustrations of the velocity fields and the plots on the bottom row show time series of the total flux out of the solution domain (blue dots plotted at regular time intervals) with the total incoming flux also plotted (red dashed line).

A3 Sensible heat flux into ice

In the expression for the melt rate (4.7), there is a term q_T representing the cooling through a thermal boundary layer. To prescribe this we first consider a simplified temperature equation. In a thermal boundary layer the dominant balance is expected between heat advection and vertical diffusion,

$$u_b \frac{\partial T}{\partial x} = \kappa_T \frac{\partial^2 T}{\partial z^2}, \tag{18}$$

where κ_T is the thermal diffusivity of ice (and lateral heat advection is ignored since we expect $u_b \gg v_b$ in the region of ice streams). With $T = 0$ on $z = b$ and $T \to -\Delta T$ far from the bed, we obtain an error function as a similarity solution of (18), which yields the average basal heat flux in the form

$$q_T = \left(\frac{\rho_i c_p k u_b}{\pi x_0} \right)^{1/2} \Delta T, \tag{19}$$

where the variable x has been replaced with the length scale x_0. Constants are defined in Table 1. This boundary layer approximation is appropriate if the reduced Péclet number $\mathrm{Pe} = \dfrac{u_0 d_0^2}{\kappa_T x_0}$ is large. For velocities $u_0 \sim 100\,\mathrm{m\,y^{-1}}$, length $x_0 \sim 500\,\mathrm{km}$ and depth $d_0 \sim 10^3\,\mathrm{m}$, $\mathrm{Pe} = 5$, and it is larger for ice streaming speeds. Given these values, while the boundary layer approximation is not necessarily a highly accurate approximation, it probably gives a sufficiently accurate representation for the present purpose, and indicates correctly the increase of basal heat flux with basal velocity. Furthermore, the q_T boundary layer formula is inappropriate at large $x \sim \frac{u_0 d_0^2}{4\kappa_T}$, when the temperature profile becomes more conductive, or for small x near divides where $u_b \to 0$ and the x dependence becomes important. The Robin solution which includes vertical but not horizontal advection is often used here, but a better approach uses the Von Mises transformation (Fowler, 1992) which includes the Robin solution, and

allows the similarity solution to approach divides by allowing for the x dependence of u_b. However, we omit such subtleties here.

From these simplified considerations we therefore have that the sensible heat flux increases with $u_b^{1/2}$.

Bibliography

Acheson, D. J. (1990). *Elementary Fluid Dynamics*. Oxford Applied Mathematics and Computing Science Series. Oxford University Press.

Alley, R. B. (1989). Water-pressure coupling of sliding and bed deformation: I. Water system. *J. Glaciol.*, **35**(119), 108–118.

Alley, R. B., Blankenship, D. D., Bentley, C., and Rooney, S. T. (1986). Deformation of till beneath ice stream B, West Antarctica. *Nature*, **322**(6074), 57–59.

Alley, R. B., Blankenship, D. D., Bentley, C. R., and Rooney, S. T. (1987). Till beneath ice stream B: 3. Till deformation: evidence and implications. *J. Geophys. Res. Sol. Ea.*, **92**(B9), 8921–8929.

Anandakrishnan, S. and Alley, R. B. (1997). Stagnation of ice stream C, West Antarctica by water piracy. *Geophys. Res. Lett.*, **24**(3), 265–268.

Anandakrishnan, S., Blankenship, D. D., Alley, R. B., and Stoffa, P. L. (1998). Influence of subglacial geology on the position of a West Antarctic ice stream from seismic observations. *Nature*, **394**, 62–65.

Aschwanden, A., Bueler, E., Khroulev, C., and Blatter, H. (2012). An enthalpy formulation for glaciers and ice sheets. *J. Glaciol.*, **58**(209), 441–457.

Balay, S., Gropp, W. D., McInnes, L. C., and Smith, B. F. (1997). Efficient management of parallelism in object oriented numerical software libraries. In *Modern*

Software Tools in Scientific Computing (eds E. Arge and A. M. Bruaset and H. P. Langtangen), pages 163–202. Birkhäuser Press.

Balay, S., Adams, M. F., Brown, J., Brune, P., Buschelman, K., Eijkhout, V., Gropp, W. D., Kaushik, D., Knepley, M. G., McInnes, L. C., Rupp, K., Smith, B. F., and Zhang, H. (2013). PETSc users manual. Technical Report ANL-95/11 - Revision 3.4, Argonne National Laboratory.

Balay, S., Adams, M. F., Brown, J., Brune, P., Buschelman, K., Eijkhout, V., Gropp, W. D., Kaushik, D., Knepley, M. G., McInnes, L. C., Rupp, K., Smith, B. F., and Zhang, H. (2014). PETSc Web page. http://www.mcs.anl.gov/petsc.

Bamber, J. L. (2000). Widespread Complex Flow in the Interior of the Antarctic Ice Sheet. *Science*, **287**(5456), 1248–1250.

Bamber, J. L. and Aspinall, W. P. (2013). An expert judgement assessment of future sea level rise from the ice sheets. *Nature Climate Change*, **3**(4), 424–427.

Bell, R., Blankenship, D. D., Finn, C. A., Morse, D. L., Scambos, T. A., Brozena, J. M., and Hodge, S. M. (1998). Influence of subglacial geology on the onset of a West Antarctic ice stream from aerogeophysical observations. *Nature*, **394**(6688), 58–62.

Benjamin, T. B., Bona, J. L., and Mahony, J. J. (1972). Model Equations for Long Waves in Nonlinear Dispersive Systems. *Philos. T. R. Soc. Lond. A*, **272**(1220), 47–78.

Bennett, M. R. (2003). Ice streams as the arteries of an ice sheet: their mechanics, stability and significance. *Earth Sci. Rev.*, **61**(3-4), 309–339.

Bindschadler, R. (1983). The importance of pressurized subglacial water in separation and sliding at the glacier bed. *J. Glaciol.*, **29**(101), 3–19.

Bindschadler, R., Chen, X., and Vornberger, P. (2000). The onset area of ice stream d, west antarctica. *J. Glaciol.*, **46**(152), 95–101.

Bindschadler, R. A., Bamber, J. L., and Anandakrishnan, S. (2001). Onset of streaming flow in the Siple coast region, West Antarctica. In *The West Antarctic Ice Sheet: Behaviour and Environment, Antarct. Res. Ser. (eds R. B. Alley and R. A. Bindschadler)*, pages 123–136. AGU, Washington D.C.

Blankenship, D. D., Bentley, C., Rooney, S. T., and Alley, R. B. (1986). Seismic measurements reveal a saturated porous layer beneath an active Antarctic ice stream. *Nature*, **322**(6074), 54–57.

Blankenship, D. D., Bentley, C. R., Rooney, S. T., and Alley, R. B. (1987). Till beneath Ice Stream B 1. properties derived from seismic travel times. *J. Geophys. Res. Sol. Ea.*, **92**(B9), 8903–8911.

Blatter, H. (1995). Velocity and stress fields in grounded glaciers: a simple algorithm for including deviatoric stress gradients. *J. Glaciol.*, **41**(138), 333–344.

Bougamont, M., Price, S., Christoffersen, P., and Payne, A. J. (2011). Dynamic patterns of ice stream flow in a 3-D higher-order ice sheet model with plastic bed and simplified hydrology. *J. Geophys. Res. Earth*, **116**(F4).

Boulton, G. S. and Hindmarsh, R. C. A. (1987). Sediment deformation beneath glaciers: Rheology and geological consequences. *J. Geophys. Res. Sol. Ea.*, **92**(B9), 9059–9082.

Boulton, G. S. and Jones, A. S. (1979). Stability of temperate ice caps and ice sheets resting on beds of deformable sediment. *J. Glaciol.*, **24**(90), 29–43.

Boulton, G. S., Caban, P. E., and Van Gijssel, K. (1995). Groundwater flow beneath ice sheets: Part I—Large scale patterns. *Quatern. Sci. Rev.*, **14**(6), 545–562.

Budd, W. F., Keage, P. L., and Blundy, N. A. (1979). Empirical studies of ice sliding. *J. Glaciol.*, **23**(89), 157–170.

Bueler, E. and Brown, J. (2008). The shallow shelf approximation as a 'sliding law' in a thermomechanically coupled ice sheet model. *J. Geophys. Res.*, **114**(F03008).

Bueler, E., Brown, J., and Lingle, C. (2007). Exact solutions to the thermomechanically coupled shallow-ice approximation: effective tools for verification. *J. Glaciol.*, **53**(182), 499–516.

Carter, S. P., Fricker, H. A., and Siegfried, M. R. (2013). Evidence of rapid subglacial water piracy under Whillans Ice Stream, West Antarctica. *J. Glaciol.*, **59**(218), 1147–1162.

Catania, G. A., Conway, H. B., Gades, A. M., Raymond, C. F., and Engelhardt, H. (2003). Bed reflectivity beneath inactive ice streams in West Antarctica. *Ann. Glaciol.*, **36**(1), 287–291.

Christoffersen, P., Bougamont, M., Cater, S. P., Fricker, H. A., and Tulaczyk, S. (2014). Significant groundwater contribution to Antarctic ice streams hydrologic budget. *Geophys. Res. Lett.*, **41**(6), 2003–2010.

Clark, C. D. (2010). Emergent drumlins and their clones: from till dilatancy to flow instabilities. *J. Glaciol.*, **51**(200), 1011–1025.

Clarke, G. (2005). Subglacial processes. *Annu. Rev. Earth Pl. Sc.*, **33**, 247–276.

Clarke, G. K. C., Nitsan, U., and Paterson, W. S. B. (1977). Strain heating and creep instability in glaciers and ice sheets. *Rev. Geophys.*, **15**(2), 235–247.

Clarke, T. S. and Echelmeyer, K. (1996). Seismic-reflection evidence for a deep subglacial trough beneath Jakobshavns Isbræ, West Greenland. *J. Glaciol.*, **43**(141), 219–232.

Clarke, T. S., Liu, C., Lord, N. E., and Bentley, C. R. (2007). Evidence for a recently abandoned shear margin adjacent to ice stream B2, Antarctica, from ice-penetrating radar measurements. *J. Geophys. Res.- Sol. Ear.*, **105**(B6), 13409–13422.

Cofaigh, C. O., Pudsey, C. J., Dodswell, J. A., and Morris, P. (2002). Evolution fo subglacial bedforms along a paleo-ice stream, Antarctic Peninsula continental shelf. *Geophys. Res. Lett.*, **29**(8), 41–1–41–4.

Collins, D. N. (1979). Sediment concentration in melt waters as an indicator of erosion processes beneath an alpine glacier. *J. Glaciol.*, **23**(89), 247–257.

Creyts, T. T. and Schoof, C. G. (2009). Drainage through subglacial water sheets. *J. Geophys. Res. Earth*, **114**(F4), F04008.

Cuffey, K. M. and Paterson, W. S. B. (2010). *The Physics of Glaciers*. Butterworth Heinemann, 4th edition.

Davis, C. H., Yonghong, L., McConnell, J. R., Frey, M. M., and Hanna, E. (2005). Snowfall-Driven Growth in East Antarctic Ice Sheet Mitigates Recent Sea-Level Rise. *Science*, **308**(5730), 1898–1901.

De Angelis, H. and Skvarca, P. (2003). Glacier Surge After Ice Shelf Collapse. *Science*, **299**(5612), 1560–1562.

Depoorter, M. A., Bamber, J. L., Griggs, J. A., Lenaerts, J. T. M., Ligtenberg, S. R. M., van den Broeke, M. R., and Moholdt, G. (2013). Calving fluxes and basal melt rates of Antarctic ice shelves. *Nature*, **502**, 89–92.

Doake, C., Corr, H., Jenkins, A., Makinson, K., Nichalls, K., Nath, C., Smith, A., and Vaughan, D. (2001). Rutford Ice Stream, Antarctica. In *The West Antarctic*

Ice Sheet: Behaviour and Environment, Antarct. Res. Ser. (eds R. B. Alley and R. A. Bindschadler), pages 221–235. AGU, Washington D.C.

Dodswell, J. A., Cofaigh, C. O., and Pudsey, C. J. (2004). Thickness and extent of the subglacial till layer beneath an Antarctic paleo-ice stream. *Geology*, **32**, 13–16.

Echelmeyer, K. A., Harrison, W. D., Larsen, C., and Mitchell, J. E. (1994). The role of the margins in the dynamics of an active ice stream. *J. Glaciol.*, **40**(136), 527–538.

Engelhardt, H. and Kamb, B. (1997). Basal hydraulic system of a West Antarctic ice stream: Constraints from borehole observations. *J. Glaciol.*, **43**(144), 207–230.

Engelhardt, H. and Kamb, B. (2013). Kamb Ice Stream flow history and surge potential. *Ann. Glaciol.*, **54**(63), 287–298.

Engelhardt, H., Humphrey, N., Kamb, B., and Fahnestock, M. (1990). Physical conditions at the base of a fast moving Antarctic ice stream. *Science*, **248**(4951), 57–59.

Evans, D. J. A., Clark, C. D., and Mitchell, W. A. (2005). The last British Ice Sheet: A review of the evidence utilised in the compilation of the Glacial Map of Britain. *Earth-Sci. Rev.*, **70**(3-4), 253–312.

Fountain, A. G. and Walder, J. S. (1998). Water flow through temperate glaciers. *Rev. Geophys.*, **36**(3), 299–328.

Fowler, A. C. (1981). A theoretical treatment of the sliding of glaciers in the absence of cavitation. *Philos. T. Roy. Soc. A.*, **298**(1445), 637–685.

Fowler, A. C. (1987a). A theory of glacier surges . *J. Geophys. Res. Sol. Ea.*, **92**(B9), 9111–9120.

Fowler, A. C. (1987b). Sliding with Cavity Formation. *J. Glaciol.*, **33**(115), 255–267.

Fowler, A. C. (1992). Modelling ice sheet dynamics. *Geophys. Astro. Fluid*, **63**, 29–65.

Fowler, A. C. (2003). On the rheology of till. *Ann. Glaciol.*, **37**(1), 55–59.

Fowler, A. C. (2009). Instability modelling of drumlin formation incorporating lee-side cavity growth. *Proc. R. Soc. A*, **465**(2109), 2681–2702.

Fowler, A. C. (2010a). The formation of subglacial streams and mega-scale glacial lineations. *Proc. R. Soc. A*, **466**(2123), 3181–3201.

Fowler, A. C. (2010b). The instability theory of drumlin formation applied to Newtonian viscous ice of finite depth. *Proc. R. Soc. A*, **466**(2121), 2673–2694.

Fowler, A. C. (2011a). *Mathematical Geoscience*, volume 36 of *Interdisciplinary Applied Mathematics*. Springer, 1st edition.

Fowler, A. C. (2011b). Weertman, Lliboutry and the development of sliding theory. *J. Glaciol.*, **56**(200), 965–972.

Fowler, A. C. and Chapwanya, M. (2011). The instability theory for the formation of ribbed moraine, drumlins and mega-scale glacial lineations. *Proc. R. Soc. A*. submitted.

Fowler, A. C. and Johnson, C. (1995). Hydraulic run-away: a mechanism for thermally regulated surges of ice sheets. *J. Glaciol.*, **41**, 554–561.

Fowler, A. C. and Johnson, C. (1996). Ice-sheet surging and ice-stream formation. *Ann. Glaciol.*, **23**, 68–73.

Fowler, A. C. and Larson, D. A. (1978). On the flow of polythermal glaciers. I. Model and preliminary analysis. *Proc. R. Soc. A*, **363**(1713), 217–242.

Fowler, A. C. and Schiavi, E. (1998). A theory of ice-sheet surges. *J. Glaciol.*, **44**(146), 104–118.

Fowler, A. C., Kopteva, N., and Oakley, C. (2007). The Formation of River Channels. *SIAM J. Appl. Math.*, **67**(4), 1016–1040.

Fretwell, P., Pritchard, H. D., Vaughan, D. G., Bamber, J. L., Barrand, N. E., Bell, R., Bianchi, C., Bingham, R. G., Blankenship, D. D., Casassa, G., Catania, G., Callens, D., Conway, H., Cook, A. J., Corr, H. F. J., Damaske, D., Damm, V., Ferraccioli, F., Forsberg, R., Fujita, S., Gim, Y., Gogineni, P., Griggs, J. A., Hindmarsh, R. C. A., Holmlund, P., Holt, J. W., Jacobel, R. W., Jenkins, A., Jokat, W., Jordan, T., King, E. C., Kohler, J., Krabill, W., Riger-Kusk, M., Langley, K. A., Leitchenkov, G., Leuschen, C., Luyendyk, B. P., Matsuoka, K., Mouginot, J., Nitsche, F. O., Nogi, Y., Nost, O. A., Popov, S. V., Rignot, E., Rippin, D. M., Rivera, A., Roberts, J., Ross, N., Siegert, M. J., Smith, A. M., Steinhage, D., Studinger, M., Sun, B., Tinto, B. K., Welch, B. C., Wilson, D., Young, D. A., Xiangbin, C., and Zirizzotti, A. (2013). Bedmap2: improved ice bed, surface and thickness datasets for Antarctica. *The Cryosphere*, **7**(1), 375–393.

Fricker, H. A., Scambos, T., Bindschadler, R., and Padman, L. (2007). An Active Subglacial Water System in West Antarctica Mapped from Space. *Science*, **315**(5818), 1544–1548.

Glasser, N. F. and Gudmundsson, G. H. (2012). Longitudinal surface structures (flowstripes) on Antarctic glaciers. *The Cryosphere*, **6**(2), 383–391.

Glen, J. W. (1955). The Creep of Polycrystalline Ice. *Proc. R. Soc. A*, **228**(1175), 519–538.

Goldberg, D. N. (2011). A variationally derived, depth-integrated approximation to a higher-order glaciological flow model. *J. Glaciol.*, **57**(201), 157–170.

Goldberg, D. N. and Holland, D. (2009). Grounding line movement and ice shelf buttressing in marine ice sheets. *J. Geophys. Res. Earth*, **114**(F04026).

Greve, R. (1997). A continuum-mechanical formulation for shallow polythermal ice sheets. *Philos. T. Roy. Soc. A.*, **355**(1726), 921–974.

Greve, R. and Blatter, H. (2009). *Dynamics of Ice Sheets and Glaciers*. Advances in Geophysical and Environmental Mechanics and Mathematics. Springer, 1st edition.

Gudmundsson, G. H. (2003). Transmission of basal variability to a glacier surface. *J. Geophys. Res. Sol. Ea.*, **108**(B5), 2253.

Hart, J. K., Rose, K. C., and Martinez, K. (2011). Subglacial till behaviour derived from in situ wireless multi-sensor subglacial probes: Rheology, hydro-mechanical interactions and till formation. *Quaternary Sci. Rev.*, **30**, 234–247.

Hewitt, I. J. (2011). Modelling distributed and channelized subglacial drainage: the spacing of channels. *J. Glaciol.*, **57**(202), 302–314.

Hewitt, I. J. (2013). Seasonal changes in ice sheet motion due to melt water lubrication. *Earth Planet Sc. Lett.*, **371**, 16–25.

Hindmarsh, R. C. A. (2004). A numerical comparison of approximations to the Stokes equations used in ice sheet and glacier modelling. *J. Geophys. Res. Earth*, **109**(F01012).

Hindmarsh, R. C. A. (2006a). Stress gradient damping of thermoviscous ice flow instabilities. *J. Geophys. Res. Sol. Ea.*, **111**(B12).

Hindmarsh, R. C. A. (2006b). The role of membrane-like stresses in determining the stability and sensitivity of the Antarctic ice sheets: back pressure and grounding line motion. *Philos. Trans. R. Soc. A*, **364**(1844), 1733–1767.

Hindmarsh, R. C. A. (2009). Consistent generation of ice-streams via thermo-viscous instabilities modulated by membrane stresses. *Geophys. Res. Lett.*, **36**(6).

Hindmarsh, R. C. A. (2011). Ill-posedness of the shallow-ice approximation when modelling thermo-viscous instabilities. *J. Glaciol.*, **57**, 1–2.

Hindmarsh, R. C. A. (2012). An observationally validated theory of viscous flow dynamics at the ice-shelf calving front. *J. Glaciol.*, **58**(208), 375–387.

Hindmarsh, R. C. A. and Payne, A. J. (1996). Time-step limits for stable solutions of the ice-sheet equation. *Ann. Glaciol.*, **23**, 74–85.

Hughes, T. J. (1992). On the Pulling Power of Ice Streams. *J. Glaciol.*, **38**(128), 125–151.

Hulbe, C. L. (2001). The contribution of numerical modelling to our understanding of the West Antarctic ice sheet. In *The West Antarctic Ice Sheet: Behaviour and Environment, Antarct. Res. Ser. (eds R. B. Alley and R. A. Bindschadler)*, pages 201–219. AGU, Washington D.C.

Hulbe, C. L. and MacAyeal, D. R. (1999). A new numerical model of coupled inland ice sheet, ice stream, and ice shelf flow and its application to the West Antarctic ice sheet. *J. Geophys. Res. Sol. Ea.*, **104**(B11), 25349–25366.

Hutter, K. (1982). Dynamics of glaciers and large ice masses. *Annu. Rev. Fluid Mech.*, **14**(1), 87–130.

Hutter, K. (1983). *Theoretical Glaciology; material science of ice and the mechanics of glaciers and ice sheets.* D. Reidel Publishing Co., Dordrecht, Holland.

Iken, A. and Bindschadler, R. A. (1986). Combined measurements of subglacial water pressure and surface velocity of Findelengletscher, Switzerland: conclusions about drainage system and sliding mechanism. *J. Glaciol.*, **32**(110), 101–119.

Iken, A., Echelmeyer, K., Harrison, W., and Funk, M. (1993). Mechanisms of fast flow in Jakobshavns Isbræ, West Greenland. I: Measurements of temperature and water level in deep boreholes. *J. Glaciol.*, **39**(131), 15–25.

Iverson, N. R. and Iverson, R. M. (2001). Distributed shear of subglacial till due to Coulomb slip. *J. Glaciol.*, **47**(158), 481–488.

Iverson, N. R., Jansson, P., and Hooke, R. L. (1994). In-situ measurement of the strength of deforming subglacial till. *J. Glaciol.*, **40**(136), 497–503.

Iverson, N. R., Hooyer, T. S., and Baker, R. W. (1998). Ring-shear studies of till deformation: Coulomb-plastic behavior and distributed strain in glacier beds. *Journal of Glaciology*, **44**(148), 634–642.

Jackson, M. and Kamb, B. (1997). The marginal shear stress of Ice Stream B, West Antarctica. *J. Glaciol.*, **43**(145), 415–426.

Jacobson, H. P. and Raymond, C. F. (1998). Thermal effects on the location of ice stream margin. *J. Geophys. Res.*, **103**, 12111–12122.

Jop, P., Forterre, Y., and Pouliquen, O. (2006). A constitutive law for dense granular flows. *Nature*, **441**(7094), 727–730.

Joughin, I. and Alley, R. B. (2011). Stability of the West Antarctic ice sheet in a warming world. *Nat. Geosci.*, **4**(8), 506–513.

Joughin, I. and Tulaczyk, S. (2002). Positive Mass Balance of the Ross Ice Streams, West Antarctica. *Science*, **295**(5554), 476–480.

Joughin, I., MacAyeal, D. R., and Tulaczyk, S. (2004). Basal shear stress of the Ross ice streams from control method inversions. *J. Geophys. Res. Sol. Ea.*, **109**(B9).

Kamb, B. (1987). Glacier surge mechanism based on linked cavity configuration of the basal water conduit system. *J. Geophys. Res. Sol. Ea.*, **92**(B9), 9083–9100.

Kamb, B. (2001). Basal zone of the West Antarctic ice streams and its role in lubrication of their rapid motion. In *The West Antarctic Ice Sheet: Behaviour and Environment, Antarct. Res. Ser. (eds R. B. Alley and R. A. Bindschadler)*, pages 157–201. AGU, Washington D.C.

Kamb, B. and Engelhardt, H. (1991). Antarctic ice stream B: conditions controlling its motions and interactions with the climate system. *IAHS Publication*.

Kamb, B., Raymond, C. F., Harrison, W. D., Engelhardt, H., Echelmeyer, K. A., Humphrey, N., Brugman, M. M., and Pfeffer, T. (1985). Glacier surge mechanism: 1982-1983 surge of Variegated Glacier, Alaska. *Science*, **227**(4686), 469–479.

Katz, R. F. (2008). Magma Dynamics with the Enthalpy Method: Benchmark Solutions and Magmatic Focusing at Mid-ocean Ridges. *J. Petrol.*, **49**(12), 2099–2121.

Knudsen, N., Yde, J., and Gasser, G. (2007). Suspended sediment transport in glacial meltwater during the initial quiescent phase after a major surge event at Kuannersuit Glacier, Greenland. *Danish Journal of Geography*, **107**(1), 1–7.

Kyrke-Smith, T. M. and Fowler, A. C. (2014). Subglacial swamps. *Proc. R. Soc. A*. submitted.

Kyrke-Smith, T. M., Katz, R. F., and Fowler, A. C. (2013). Stress balances of ice streams in a vertically integrated, higher-order formulation. *J. Glaciol.*, **59**(215), 449–466.

Kyrke-Smith, T. M., Katz, R. F., and Fowler, A. C. (2014). Subglacial hydrology and the formation of ice streams. *Proc. R. Soc. A*, **470**(2161), 20130494.

Lemke, P., Ren, J., Alley, R. B., Allison, I., Carrasco, J., Flato, G., Fujii, Y., Kaser, G., Mote, P., Thomas, R. H., and Zhang, T. (2007). Observations: Changes in Snow, Ice and Frozen Ground. In: Climate Change 2007: The Physical Science

Basis. Contribution of Working Group I to the Fourth Assessment Report of the Intergovernmental Panel on Climate Change. *Cambridge University Press*.

Lliboutry, L. A. (1968). General theory of subglacial cavitation and sliding of temperate glaciers. *J. Glaciol.*, **7**(49), 21–58.

Lüthi, M. P. (2010). Glaciology: Greenland's glacial basics. *Nature*, **468**, 776–777.

MacAyeal, D. R. (1989). Large-scale ice flow over a viscous basal sediment- Theory and application to ice stream B, Antarctica. *J. Geophys. Res. Sol. Ea.*, **94**(B4), 4071–4087.

MacAyeal, D. R. (1992). Irregular oscillations of the West Antarctic ice sheet. *Nature*, **359**, 29–32.

McKenzie, D. (1984). The generation and compaction of partially molten rock. *J. Petrol.*, **25**(3), 713–765.

McMeeking, R. M. and Johnson, R. E. (1986). On the mechanics of surging glaciers. *J. Glaciol.*, **32**(110), 120–132.

Morland, L. W. and Johnson, I. R. (1980). Steady motion of ice sheets. *J. Glaciol.*, **25**(92), 229–246.

Murray, T., Corr, H., Forieri, A., and Smith, A. M. (2008). Contrasts in hydrology between regions of basal deformation and sliding beneath Rutford Ice Stream, West Antarctica, mapped using radar and seismic data. *Geophys. Res. Lett.*, **35**(12), L12504.

Papanastasiou, M., Malamataris, N., and Ellwood, K. (1992). A new outflow boundary condition. *lnt. J. Numer. Methods Fluids*, **14**, 587–608.

Payne, A., Huybrechts, P., Abe-Ouchi, A., Calov, R., Fastook, J., Greve, R., Marshall, S., Marsiat, I., Ritz, C., and Tarasov, L. (2000). Results from the EISMINT model

intercomparison: the effects of thermomechanical coupling. *J. Glaciol.*, **46**(153), 227–238.

Payne, A. J. (1995). Limit cycles in the basal thermal regime of ice sheets. *J. Geophys. Res. Sol. Ea.*, **100**(B3), 4249–4249.

Payne, A. J. and Baldwin, D. J. (1999). Thermomechanical modelling of the Scandinavian ice sheet: implications for ice-stream formation. *Ann. Glaciol.*, **28**(1), 83–89.

Payne, A. J. and Dongelmans, P. W. (1997). Self-organization in the thermomechanical flow of ice sheets. *J. Geophys. Res. Sol. Ea.*, **102**(B6), 12219–12233.

Perol, T. and Rice, J. R. (2014). Control of the width of active Western Antarctic Siple Coast ice streams by internal melting at their margins. *J. Geophys. Res.* in review.

Piotrowski, J. A., Mickelson, D. M., Tulaczyk, S., Krzyszkowski, D., and Junge, F. W. (2001). Were deforming subglacial beds beneath past ice sheets really widespread? *Quatern. Int.*, **86**(1), 139–150.

Raymond, C. (1996). Shear margins in glaciers and ice sheets. *J. Glaciol.*, **42**(140), 90–102.

Raymond, C. F., Echelmeyer, K. A., Whillans, I. M., and Doake, C. S. M. (2001). Ice stream shear margins. In *The West Antarctic Ice Sheet: Behaviour and Environment, Antarct. Res. Ser. (eds R. B. Alley and R. A. Bindschadler)*, pages 137–155. AGU, Washington D.C.

Retzlaff, R. and Bentley, C. R. (1993). Timing of stagnation of Ice Stream C, West Antarctica, from short-pulse radar studies of buried surface crevasses. *J. Glaciol.*, **39**(133).

Rignot, E. and Thomas, R. H. (2002). Mass Balance of Polar Ice Sheets. *Science*, **297**(5586), 1502–1506.

Rignot, E., Casassa, G., Gogineni, P., Krabill, W., Rivera, A., and Thomas, R. (2004). Accelerated ice discharge from the Antarctic Peninsula following the collapse of Larsen B ice shelf. *Geophys. Res. Lett.*, **31**(18), L18401.

Rignot, E., Bamber, J. L., Van den Broeke, M. R., Davis, C., Li, Y., van de Berg, W. J., and van Meijgaard, E. (2008). Recent Antarctic ice mass loss from radar interferometry and regional climate modelling. *Nat. Geosci.*, **1**(2), 106–110.

Rignot, E., Mouginot, J., and Scheuchl, B. (2011). Ice Flow of the Antarctic Ice Sheet. *Science*, **333**(6048), 1427–1430.

Ritz, C., Rommelaere, V., and Dumas, C. (2001). Modeling the evolution of Antarctic ice sheet over the last 420,000 years- Implications for altitude changes in the Vostok region. *J. Geophys. Res. Atmos.*, **106**(D23), 31943–31964.

Rommelaere, V. and Ritz, C. (1996). A thermomechanical model of ice-shelf flow. *Ann. Glaciol.*, **23**, 13–20.

Röthlisberger, H. (1972). Water pressure in intra- and subglacial channels. *J. Glaciol.*, **11**(62), 177–203.

Sayag, R. and Tziperman, E. (2008). Spontaneous generation of pure ice streams via flow instability: Role of longitudinal shear stresses and subglacial till. *J. Geophys. Res. Sol. Ea.*, **113**(B5), B05411.

Sayag, R. and Tziperman, E. (2009). Spatiotemporal dynamics of ice streams due to a triple-valued sliding law. *J. Fluid Mech.*, **640**, 483–505.

Sayag, R. and Tziperman, E. (2011). Interaction and variability of ice streams under

a triple-valued sliding law and non-Newtonian rheology. *J. Geophys. Res. Earth*, **116**(F1), F01009.

Schoof, C. (2004). On the mechanics of ice-stream shear margins. *J. Glaciol.*, **50**(169), 208–218.

Schoof, C. (2006). A variational approach to ice stream flow. *J. Fluid Mech.*, **556**, 227–251.

Schoof, C. (2010). Ice-sheet acceleration driven by melt supply variability. *Nature*, **468**(7325), 803–806.

Schoof, C. (2012). Thermally driven migration of ice-stream shear margins. *J. Fluid Mech.*, **712**, 552–578.

Schoof, C. and Hewitt, I. (2013). Ice-Sheet Dynamics. *Annu. Rev. Fluid Mech.*, **45**(1), 217–239.

Schoof, C. and Hindmarsh, R. C. A. (2010). Thin-Film Flows with Wall Slip: An Asymptotic Analysis of Higher Order Glacier Flow Models. *Q. J. Mech. Appl. Math.*, **63**(1), 73–114.

Sergienko, O. V. and Hulbe, C. L. (2011). 'Sticky spots' and subglacial lakes under ice streams of the Siple Coast, Antarctica. *Ann. Glaciol.*, **52**(58), 18–22.

Shabtaie, S. and Bentley, C. R. (1987). West Antarctic ice streams draining into the Ross ice shelf: configuration and mass balance. *J. Geophys. Res. Sol. Ea.*, **92**(B2), 1311–1336.

Smith, B. E., Fricker, H. A., Joughin, I. R., and Tulaczyk, S. (2009). An inventory of active subglacial lakes in Antarctica detected by ICESat (2003–2008). *J. Glaciol.*, **55**(192), 573–595.

Smith, T. R. and Bretherton, F. P. (1972). Stability and the conservation of mass in drainage basin evolution. *Water Resour. Res.*, **8**(6), 1506–1529.

Spiegelman, M. (1993). Flow in deformable porous media. Part 1. Simple analysis. *J. Fluid Mech.*, **247**, 17–38.

Stokes, C. R. and Clark, C. D. (2003). Laurentide ice streaming on the Canadian Shield: A conflict with the soft-bedded ice stream paradigm? *Geology*, **31**(4), 347–350.

Suckale, J., Platt, J. D., Perol, T., and Rice, J. R. (2014). Deformation-induced melting in the margins of the West-Antarctic ice streams. *J. Geophys. Res. Earth*. in press.

Swithinbank, C. W. M. (1954). Ice streams. *Polar Rec.*, **7**(48), 185–186.

Thomas, R. H. (1979). The dynamics of marine ice sheets. *J. Glaciol.*, **24**(90), 167–177.

Truffer, M. and Echelmeyer, K. A. (2003). Of isbræ and ice streams. *Ann. Glaciol.*, **36**(1), 66–72.

Truffer, M., Echelmeyer, K. A., and Harrison, W. D. (2001). Implications of till deformation on glacier dynamics. *J. Glaciol.*, **47**(156), 123–134.

Tulaczyk, S., Kamb, B., and Engelhardt, H. (2000a). Basal mechanics of Ice Stream B. II. Plastic undrained bed model. *J. Geophys. Res. Sol. Ea.*, **105**(B1), 483–494.

Tulaczyk, S., Kamb, W. B., and Engelhardt, H. F. (2000b). Basal mechanics of Ice Stream B, West Antarctica: 1. Till mechanics. *J. Geophys. Res. Sol. Ea.*, **105**(B1), 463–481.

Van den Broeke, M. R., Bamber, J., Lenaerts, J., and Rignot, E. (2011). Ice Sheets and Sea Level: Thinking Outside the Box. *Surv. Geophys.*, **32**, 495–505.

Van der Veen, C. J. (1999). *Fundamentals of Glacier Dynamics*. Taylor and Francis.

Van Pelt, W. J. J. and Oerlemans, J. (2012). Numerical simulations of cyclic behaviour in the Parallel Ice Sheet Model (PISM). *J. Glaciol.*, **58**(208), 347–360.

Vaughan, D. G., Corr, H. F. J., Smith, A. M., Pritchard, H. D., and Shepherd, A. (2008). Flow-switching and water piracy between Rutford Ice Stream and Carlson Inlet, West Antarctica. *J. Glaciol.*, **54**(184), 41–48.

Velicogna, I. and Wahr, J. (2005). Greenland mass balance from GRACE. *Geophys. Res. Lett.*, **32**(18), L18505.

Walder, J. S. (1982). Stability of sheet flow of water beneath temperate glaciers and implications for glacier surging. *J. Glaciol.*, **28**(99), 273–293.

Walder, J. S. (1986). Hydraulics of subglacial cavities. *J. Glaciol.*, **32**(112), 439–445.

Walder, J. S. and Fowler, A. C. (1994). Channelized subglacial drainage over a deformable bed. *J. Glaciol.*, **40**(134), 3–15.

Weertman, J. (1972). General theory of water flow at the base of a glacier or ice sheet. *Rev. Geophys.*, **10**(1), 287–333.

Weis, M. and Greve, R. (1999). Theory of shallow ice shelves. *Continuum Mech. Therm.*, **11**(1), 15–50.

Whitham, G. B. (1973). *Linear and Nonlinear Waves*. Wiley.

Wingham, D. J., Siegert, M. J., Shepherd, A., and Muir, A. S. (2006). Rapid discharge connects Antarctic subglacial lakes. *Nature*, **440**(7087), 1033–1036.

Winkelmann, R., Martin, M. A., Haseloff, M., Albrecht, T., Bueler, E., Khroulev, C., and Levermann, A. (2011). The Potsdam Parallel Ice Sheet Model (PISM-PIK) – Part 1: Model description. *The Cryosphere*, **5**(3), 715–726.

Winsborrow, M. and Clark, C. D. (2010). What controls the location of ice streams? *Earth Sci. Rev.*, **45**, 45–59.

Zwally, H. J., Giovinetto, M. B., Li, J., Cornejo, H. G., Beckley, M. A., Brenner, A. C., Saba, J. L., and Yi, D. (2005). Mass changes of the Greenland and Antarctic ice sheets and shelves and contributions to sea-level rise: 1992–2002. *J. Glaciol.*, **51**(175), 509–527.